9-5-2013

ADVANCED APPLICATIONS OF COSMIC-RAY MUON RADIOGRAPHY

John Perry

Recommended Citation

Perry, John. "ADVANCED APPLICATIONS OF COSMIC-RAY MUON RADIOGRAPHY." (2013).
https://digitalrepository.unm.edu/ne_etds/4

John Oliver Perry
Candidate

Department of Chemical and Nuclear Engineering
Department

This dissertation is approved, and it is acceptable in quality and form for publication:

Approved by the Dissertation Committee:

Dr. Adam A. Hecht, Chairperson

Dr. Cassiano R. E. de Oliveira

Dr. Sally Seidel

Dr. Konstantin Borozdin

ADVANCED APPLICATIONS OF COSMIC-RAY MUON RADIOGRAPHY

BY

JOHN PERRY

B.S., Nuclear Engineering, Purdue University, 2007
M.S., Nuclear Engineering, Purdue University, 2008

DISSERTATION

Submitted in Partial Fulfillment of the
Requirements for the Degree of

Doctor of Philosophy
Engineering

The University of New Mexico
Albuquerque, New Mexico

July, 2013

DEDICATION

I dedicate this dissertation to my wife, Holly R. Perry. She has motivated me through my work selflessly and tirelessly. I struggle to think where I would be today without her. Holly has provided more emotional support throughout these past years than I could ever request. So, to her, thank you and I love you.

ACKNOWLEDGEMENTS

I graciously acknowledge my academic advisor, Dr. Adam A. Hecht, for providing me the opportunity for pursuing my PhD. Dr. Hecht has supported me through my work, education, and transition from academic institutions. I am also grateful for his flexibility in permitting me to pursue my higher education while working at a remote facility full time.

To my mentor Dr. Konstantin Borozdin, I thank you for the many hours that you have invested on my behalf for both this work and many other pursuits that I've had thus far at Los Alamos National Laboratory. I am indebted to you for your constant commitment to improving my work and scientific career. Additionally, I acknowledge, tongue-in-cheek, your profound understanding of the English language, *sans articulos et prolationis*.

To Dr. Oliveira and Dr. Seidel, I thank you for being involved in my dissertation committee. I appreciate the time you have taken out of your schedules so that I may take this next great step in my career!

I want to thank my many colleagues including: Dr. Fesseha Mariam, Dr. Haruo Miyadera, Dr. Edward (Cas) Milner, Dr. Chris Morris, Jeff Bacon, and many others. This team of people, of which I belonged to, has guided and instructed me to the penultimate goal of my academic career. It is because of these types of people that LANL is a world class national laboratory.

I acknowledge Dr. Alexei Klimenko. Dr. Klimenko brought me on to LANL as a post-masters/graduate research assistant and was instrumental in my success as a young scientist.

I thank the many collaborators that I have worked with including: the University of New Mexico, National Security Technologies, and Decision Sciences Corporation.

Finally, I would like to thank my colleague Joseph Fabritius II for assisting in proof-reading my dissertation as well as creating some figures that he allowed me to use.

ADVANCED APPLICATIONS OF COSMIC-RAY MUON RADIOGRAPHY

by

John Oliver Perry
B.S., Nuclear Engineering, Purdue University, 2007
M.S., Nuclear Engineering, Purdue University, 2008
Ph.D., Engineering, University of New Mexico, 2013

ABSTRACT

The passage of cosmic-ray muons through matter is dominated by the Coulomb interaction with electrons and atomic nuclei. The muon's interaction with electrons leads to continuous energy loss and stopping through the process of ionization. The muon's interaction with nuclei leads to angular diffusion. If a muon stops in matter, other processes unfold, as discussed in more detail below. These interactions provide the basis for advanced applications of cosmic-ray muon radiography discussed here, specifically: 1) imaging a nuclear reactor with near horizontal muons, and 2) identifying materials through the analysis of radiation lengths weighted by density and secondary signals that are induced by cosmic-ray muon trajectories.

We have imaged a nuclear reactor, type AGN-201m, at the University of New Mexico, using data measured with a particle tracker built from a set of sealed drift tubes, the Mini Muon Tracker (MMT). Geant4 simulations were compared to the data for verification and validation. In both the data and simulation, we can identify regions of interest in the reactor including the core, moderator, and shield. This study reinforces our claims for using muon tomography to image reactors following an accident.

Warhead and special nuclear materials (SNM) imaging is an important thrust for treaty verification and national security purposes. The differentiation of SNM from other materials, such as iron and aluminum, is useful for these applications. Several techniques were developed for material identification using cosmic-ray muons. These techniques include: 1) identifying the radiation length weighted by density of an object and 2) measuring the signals that can indicate the presence of fission and chain reactions. By combining the radiographic images created by tracking muons through a target plane with the additional fission neutron and gamma signature, we are able to locate regions that are fissionable from a single side. The following materials were imaged with this technique: aluminum, concrete, steel, lead, and uranium. Provided that there is sufficient mass, U-235 could be differentiated from U-238 through muon induced fission.

TABLE OF CONTENTS

LIST OF FIGURES

LIST OF TABLES

PREFACE

This dissertation is submitted in partial fulfillment of the requirements for a Doctorate in Philosophy with a focus on Nuclear Engineering from the University of New Mexico. The majority of the work referenced in the thesis was performed at Los Alamos National Laboratory with a skilled team of scientists, engineers, and technicians. The dissertation was written by the author, John Perry, but there were many contributions from fellow scientists, professors, and advisers. This work would not have been possible without a LANL/UNM team supporting the author, given its scale, challenge, and cost.

CHAPTER 1

Introduction

It is basic human desire to understand, see what is hidden, and discover objects inside of a "black" box; whereas that box might be the human body, a cargo container, a nuclear reactor – or simply – just a box. Beginning with the discovery of X-ray imaging in 1895 by Wilhelm Röntgen [1], many forms of penetrative radiation have proven to be a useful probe for looking inside and discovering the unknown. In particular, cosmic-ray muons are a highly penetrating form of radiation that have been used to successfully image objects with a wide range of geometric scales, atomic properties, and densities.

Prior to the discovery of the cosmic ray, the scientific community believed that background radiation was either terrestrial in origin or due to the presence of the sun. Then in 1912, Victor Hess measured radiation "of great penetrating power" while ballooning with Wulf electrometers, a type of sealed ionization chamber [2]. By performing measurements in darkness to eliminate the effects of solar radiation, Hess discovered that the ionization chambers reported increasing amounts of ionization at several thousand meters above ground. His experimental measurements of the cosmic-ray eventually led to his winning the Nobel Prize in physics for the discovery of cosmic radiation. Street and Stevenson found evidence of a particle with a mass intermediate of the proton and electron in cloud chamber observations of cosmic rays in 1937 [3], which partially confirmed theoretical predictions by Hideki Yukawa [4]. However, this "mu meson" particle did not interact via the strong force as predicted by Yukawa, who actually predicted the pi meson. Additional research revealed that the mu meson had different properties from other identified mesons, which resulted in the mu meson being renamed as a muon.

The cosmic-ray muon belongs to the lepton family which contains three charged particles: electrons, muons, and taus, as well as three corresponding neutrinos. The charged leptons interact through the electromagnetic, weak, and gravitational forces. We are able to utilize these forces, mainly the electromagnetic force, for performing charged particle radiography. The weak force becomes important when considering a different type of imaging known as muon induced fission laminography which is also a focus of this work. Muons are an effective radiography probe having advantages and unique capabilities compared to other imaging probes such as gammas, x-rays, neutrons, and protons. The cosmic-ray muon is highly penetrative due to being minimally ionizing. It is a component of background radiation, and it is suitable for measuring a wide range of materials. Of further interest is the information that can be derived from combining multiple scattering, attenuation, and muon induced fission signatures.

Muons have been used historically to image the interior of thick or large objects. For example, the pyramids that Alvarez et al. [5] studied involved measuring muon transmission through meters of limestone. Recently, we have developed techniques to identify small objects, on the order of centimeters, behind shielding. Measuring properties of these objects, we can determine whether the objects were made of special nuclear material, e.g. uranium or plutonium. A multiple scattering technique was developed based upon established principles of charged particle radiography, e.g. proton radiography [6]. The multiple scattering of the cosmic-ray muon yields better spatial resolution when compared to transmission images. However, different isotopes of special nuclear material look identical for both transmission and scattering radiography because they have the same density and atomic number. In this dissertation work, I discuss a novel technique used to determine isotopic composition of special nuclear material by the tagging of coincident muon induced fission signatures [7]. With the combination of multiple scattering, attenuation, and tagged cosmic-ray muon induced fission, we are able to quantify the amount of special nuclear material, its location, and roughly assess the isotopic composition of the material.

A large fraction of my work was devoted to developing advanced modeling capabilities for muon radiography through validation with experiments. I present my findings on modeling capabilities through the analysis of the imaging of a nuclear reactor at the University of New Mexico [8]. Through this recent work, cosmic-ray muon imaging has been extended to the identification of thick, lower density materials behind heavy amounts of shielding and overburden. In the case of the University of New Mexico Research Reactor, we identified a core consisting of uranium loaded in polyethylene that resided in shielding of concrete, water, steel, and lead. Our team began this work to assist in the cleanup of Fukushima Daiichi following its nuclear reactor meltdown caused by the tsunami in March 2011. The imaging of the remaining core structure is useful for the acceleration of cleanup operations, increasing its efficiency, and reducing radiation dose to the workers. We have now simulated and performed measurements in preparation for a project of this magnitude. Our work at the University of New Mexico research reactor produced useful insight into the obstacles that will be present during a deployment of a muon tomography system at Fukushima, validated simulations pertaining to those efforts, and improved multiple scattering image analysis for radiography of thick, lower density objects behind heavy overburden. Additionally, we develop a coincidence scheme to enable cosmic-ray measurements in a radiation field[1].

---

[1] Appendix B

The Author's Role and this Dissertation

The development of cosmic-ray muon tomography at LANL is a team effort spanning multiple disciplines including: nuclear physics, computer science, and electrical engineering. A portion of the recent muon radiography work involved independent research by the author for the intent of pursuing a doctoral dissertation. The author led the following three broadly defined activities with the support of the Threat Reduction team at LANL.

1. Proposal, experimental execution, simulation, data analysis, and publication of the University of New Mexico Research Reactor measurements
2. High fidelity simulation of the Mini Muon Tomography experimental apparatus
3. Development of methodology for the implementation of muon induced fission and single sided muon radiography and isotopic differentiation between U-235 and U-238

This dissertation focuses on these three topics, but it does include additional team oriented efforts that support the theme of this work. These additional team efforts are referenced through their corresponding publications. The horizontal imaging of the mockup reactor and the Fukushima Daiichi simulations was heavily team oriented. I differentiate my involvement between the earlier reactor work and the UNMRR work as I consider the UNMRR efforts to be largely driven by myself. There was help from my team with the UNMRR research which amounted to: obtaining funding, deploying the experiment, and peer review of the data analysis. The material identification techniques that involved comparing radiation length and attenuation length were a team based effort. Single sided radiography and tagged muon radiography were my own work, but I did receive excellent guidance from senior scientists on my team.

Dissertation Outline

Following the introductory chapter, this dissertation takes a modular approach for explaining the history of muon radiography, the underlying physics, experimental equipment, simulation, and results. Chapter 2 describes the history of muon tomography beginning with the study of muon transmission through tunnels, pyramids, and volcanoes. The imaging technique derived from measuring multiple Coulomb scattering of cosmic-ray muons is explained. The second chapter concludes by showing a tabulated summary of teams that are currently investigating a variety of applications for muon radiography.

Chapter 3 explains the relevant physics behind cosmic-ray muon radiography. The physical origin of the cosmic-ray muon is discussed. An empirical model is shown to accurately approximate the muon momentum spectrum as a function of zenith angle. The three physical processes that effect radiography are detailed in this chapter: energy loss, multiple Coulomb scattering, and muon induced fission. The third chapter concludes with derivations that explain the linear dependence of Z for multiple Coulomb scattering, and the energy loss of muons has a very weak Z dependence.

The experimental apparatus that is used to measure the muon trajectories is discussed in Chapter 4. This apparatus is the Mini Muon Tracker (MMT) detector consisting of aluminum drift tubes with FPGA front end electronics. An overview of the secondary neutron detectors, used for the single sided, tagged muon imaging, is presented in Chapter 4. Chapter 5 includes the algorithms used for the muon track reconstruction from the drift tube signals along with the several radiography algorithms used to generate images from the muon tracks. In Chapter 6, the MMT is simulated with a Monte Carlo computer model showing the intrinsic performance of muon tracking with aluminum drift tubes.

Chapter 7 presents the work leading up to the reactor imaging of the UNMRR and the results of the measurements at the UNMRR. Prior to the UNMRR, the author and his team performed measurements and simulations of horizontal muon radiography at LANL with large concrete blocks and lead to mock up a reactor imaging scenario. Following these measurements, the muon team then proceeded to model the damaged reactor at Fukushima with Geant4 simulations. The experiment at the UNMRR was the first muon radiograph of a nuclear reactor using the multiple scattering technique. Geant4 simulations of the UNMRR measurements were performed for verification and validation purposes. The results from the measurement and simulation present an exciting view into the capabilities of horizontal imaging applications for muon radiography.

Chapter 8 discusses material identification using cosmic-ray muons. This includes several algorithms that compute the radiation length weighted by density of objects that are imaged and the results of single sided imaging using tagged muon radiography. The signal to noise ratio is shown to be improved by using neutron tagged stopped tracks compared to conventional transmission radiography. Finally, fast fission isotopic identification is discussed in detail by comparing data measured from low enriched uranium (LEU) and depleted uranium (DU).

Chapter 9 has the final conclusions and discusses the current state of the art work being performed by the author and muon radiography team at LANL.

CHAPTER 2

History

Following the discovery of X-ray imaging in 1895, physicists were developing new methods and techniques for each identified particle (or wave) of radiation. They determined the capabilities and limitations for each form of radiation that could be measured and used in imaging applications. However, it was not feasible to image objects that were “sufficiently thick” or shielded, .e.g. a lead plate surrounded in concrete. It would be another 50 years until a suitable particle, and method, for imaging larger objects was found. In the 1950s, E.P. George measured the attenuation of cosmic-rays through large structures [9]. George deployed a Geiger counter “telescope” in the Guthega-Munyang tunnel in order to determine the thickness of ice and rock above, also known as overburden. Thus cosmic ray attenuation radiography had been born. George and his colleagues are shown in Figure 1 next to their Geiger counter telescope.

In the 1960s, Luis Alvarez advanced cosmic-ray muon attenuation radiography with his team’s imaging efforts of the Egyptian pyramids. Alvarez imaged the structure of the Second Pyramid of Giza [5]. For several decades prior, cosmic-ray muons had been known to have good properties for measuring large structures, such as pyramids, however; it wasn’t until 1965 that the technology caught up to the theory for such a measurement. The invention of the digital read-out spark chamber allowed Alvarez to proceed, and he deployed his experimental apparatus in a chamber at the bottom of the Second Pyramid of Chephren, a location known as the Belzoni Chamber.

In the Belzoni Chamber, Alvarez deployed two spark chambers, each measuring $0.9\ m$ by $1.8\ m$ in area. An image of the chambers and their deployed location is shown in Figure 2. In an earlier work, low resolution cosmic-ray experiments had shown the existence of the King’s Chamber and the Queen’s Chamber of the Great Pyramid, therefore Alvarez focused on identifying small features over large thicknesses of limestone instead. The Belzoni Chamber was chosen as it was the most suitable point in the pyramid to measure through comparable thicknesses of limestone from each of the Second Pyramid’s faces.

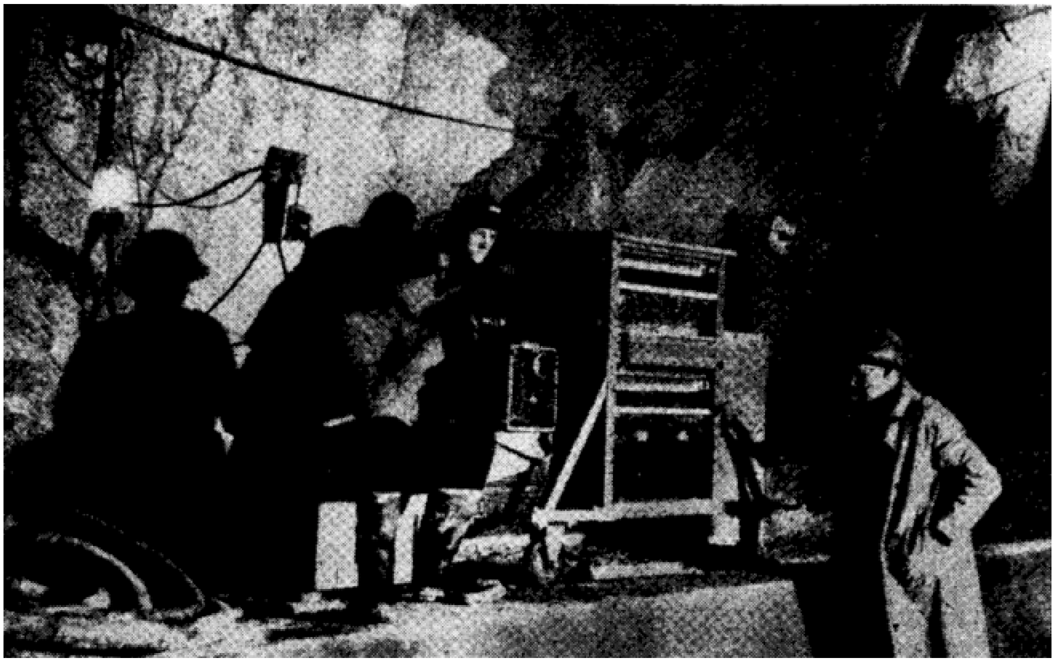

Figure 1 – E.P. George and his colleagues deploying a Geiger counter "telescope" in the Australian mines of Guthega. George determined the thickness of ice and rock overburden in the tunnels from counting the amount of cosmic ray attenuation [9].

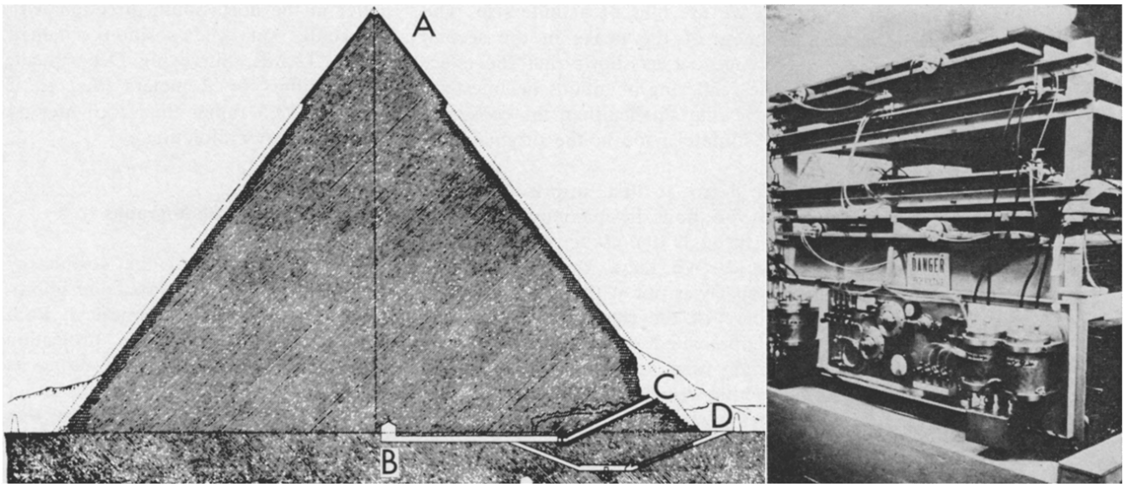

Figure 2 – Cross section of the Pyramid of Chephren (left) and spark chamber cosmic-ray measuring equipment (right). On the left image the four letters refer to: A) Smooth limestone cap, B) the Belzoni Chamber, C) Belzoni's entrance, and D) Howard-Vyse's entrance. The spark chamber detectors were placed in the Belzoni Chamber [5].

He estimated that the cosmic-ray should travel in 2.3 meters less of limestone when passing through the center of the pyramid face as compared to the longer distance from traveling through the corner of the pyramid. This should result in a signal intensity difference of 5 percent. Furthermore, Alvarez also predicted that if a hidden chamber with a height of 5 meters were to be present, the intensity difference in the flux from this particular direction would be increased by 10 percent as compared to solid limestone.

Alvarez's group computed a suite of simulations to model the attenuation of cosmic-rays through the Second Pyramid. The simulations were primarily used to assist in searching for hidden chambers when compared with the data. Over the course of the experiment, the simulations were refined with better models ultimately yielding the conclusion that no "hidden chambers" of sufficient size existed between the spark chamber detectors and the outer walls of the Second Pyramid.

Results from Alvarez's research brought attention to the usefulness of cosmic-ray muon attenuation radiography. Cosmic-ray muon transmission radiography is akin to looking for the shadow of an image due to overburden of the traversed material. In Alvarez's case, he was able to use the attenuated cosmic-rays in order to locate the faces of the pyramid and identify the cap on top of the pyramid as shown in Figure 3 and Figure 4. A stronger signal is found on two of the faces, north and east, due to the Belzoni Chamber being located closer to those faces by several meters.

Several decades later, Nagamine and Tanaka began studying volcanoes and mountains in telescopic mode, which is a moniker for single sided attenuation radiography [10-14]. Initially, their research focused on using the cosmic-ray muon to probe the inner-structure of a mountain. They have expanded upon this technique performing computed tomography with telescopic measurements from multiple angles of Mount Asama, a volcano in Japan. This method is the cutting-edge in muon telescopic radiography, but it also shows the weaknesses in using telescopic cosmic-ray muon radiography for higher resolution applications.

From Alvarez's previous work, it is known that cosmic-ray muons are an effective probe for imaging through many meters of limestone. Another use for these cosmic-ray muons is measuring the inner-structure of volcanoes and their lava conduits as proposed by Nagamine [11]. Prior to performing measurements on a volcano, Nagamine's team demonstrated their method by imaging the inner-structure of Mt. Tsukuba in Ibaraki, Japan. The process for performing this measurement is rather

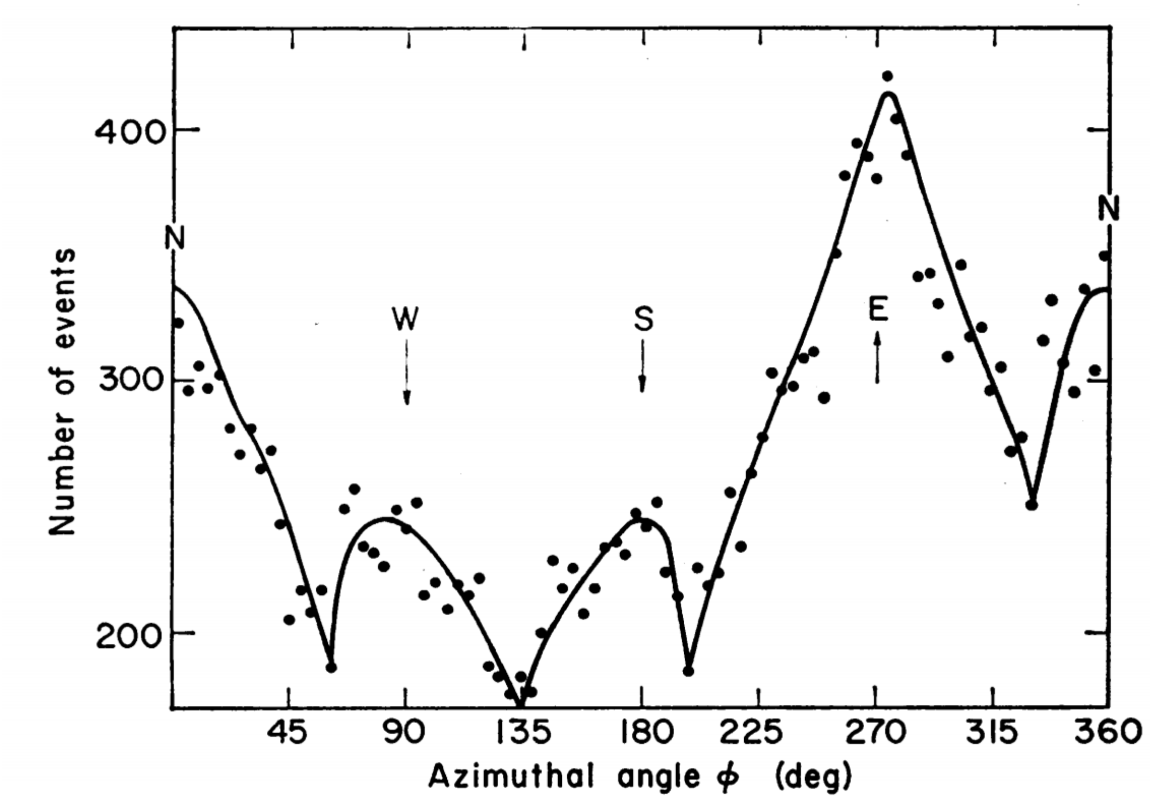

Figure 3 – Azimuthal measurement of cosmic-ray muon flux through all four faces of the pyramid. The zenith angle integrated counts from 20 to 40 degrees. The corners are easily identified as the depressions in the flux where there is a maximum of flux along the center of the pyramid face. The depression of flux near the corners is due to the increase in attenuation due to a greater amount of material [5].

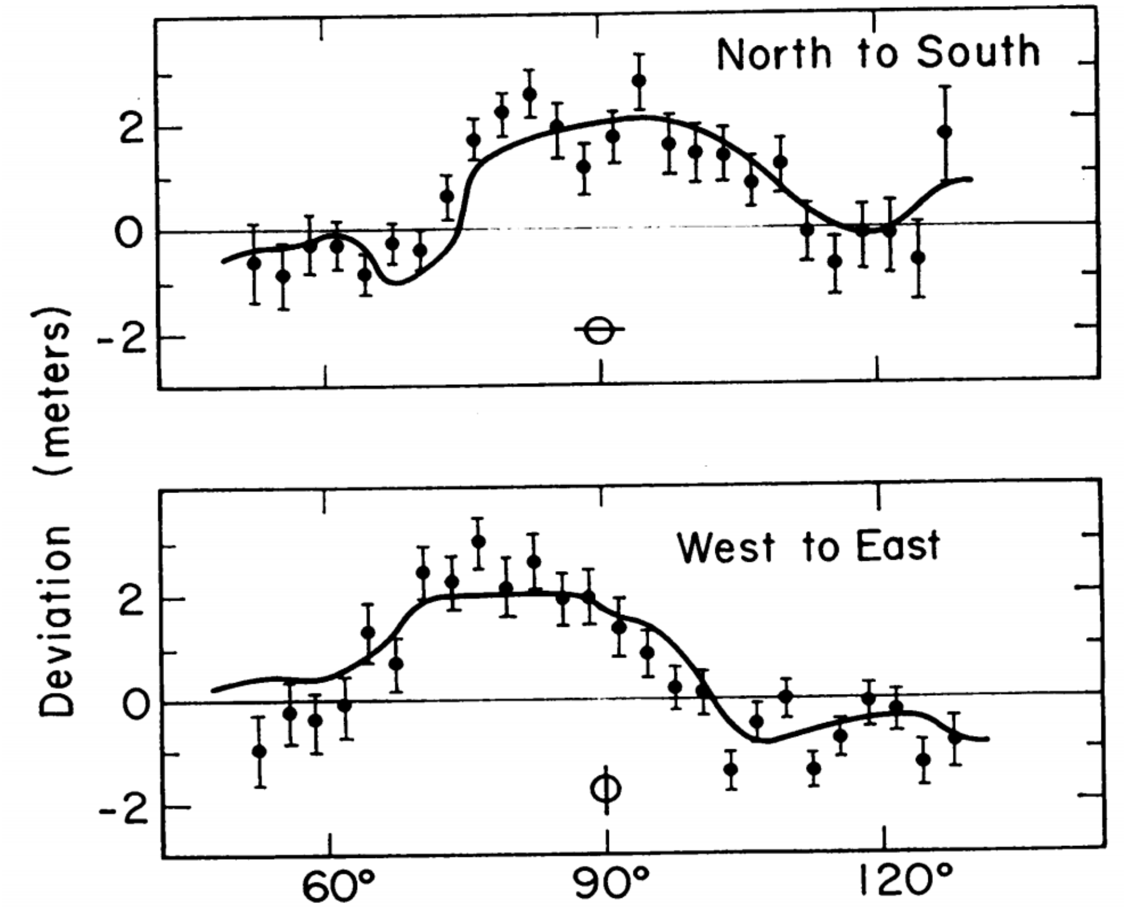

Figure 4 – These two graphs show the difference between the simulation and the measured cosmic-ray muon flux across two 24-degree-wide strips in order to show the cap at the top of the pyramid. In the absence of a cap, we would expect the deviation to lie along the zero line. The data points represent the distances indicated by the cosmic rays (simulation vs. data) and are compared with the solid line, which represents the same distance measured by areal survey [5].

straightforward: 1) determine the energy spectrum of the cosmic-ray muons and their dependence on the zenith angle, 2) find the intensity of cosmic-ray muons penetrating through certain thicknesses of rock, and 3) apply this knowledge to create a density map of Mt. Tsukuba. In order to track the cosmic-ray muons at Mt. Tsukuba, a threefold telescope of plastic scintillators was used. The muons were located in the detector by performing analysis on the time of flight of the muon through each scintillator panel, which resulted in a detector hit location resolution of $\pm 2.5\ cm$. When projected two kilometers to the mountain, the resolution of this method is $\pm 50.0\ m$, which is to be expected when performing a telescopic measurement over the scale of a mountain. A result from this work is an image of the mountain casting a shadow via cosmic-ray muon attenuation as shown in Figure 5. The muons stop throughout the mountain resulting in a lower signal in the detector planes as compared to the horizon above the mountain.

In an attempt to improve the quality of telescopic mode cosmic-ray muon imaging, Tanaka developed a method for performing three-dimensional computed tomography [14]. Over several years, his team had installed two telescopic detector systems at Mt. Asama, an active volcano in Japan. The mountain was measured from these two detector stations, and the data was fitted to a damped least squares method used to solve a density matrix of voxels 100 meters on an edge. By using this method, Tanaka is able to better resolve the density of different locations throughout the volcano’s inner geometry. In Figure 6, three vertical slices of the volcano are reconstructed displaying several features throughout Mt. Asama including: conical procession of slices, a void in the center, and several structures of higher density near the void.

Thus, telescopic cosmic-ray muon imaging has been a useful method for measuring large geometries, however; a new technique developed at Los Alamos National Laboratory has improved the capabilities of muon tomography by measuring the multiple scattering of muons as they pass through an object plane [15-20]. This technique is also capable of being fused with additional cosmic-ray muon radiography methods, such as telescopic measurements and coincident signals from secondary detectors. The usage of multiple scattering in charged particle radiography is well known, e.g. proton radiography [21-28]. Therefore it comes as no surprise to find this method applied for cosmic-ray muon radiography as well. Interestingly, the muon has followed the same evolutionary path of the X-ray community, beginning with attenuation and moving onward into scattering analysis.

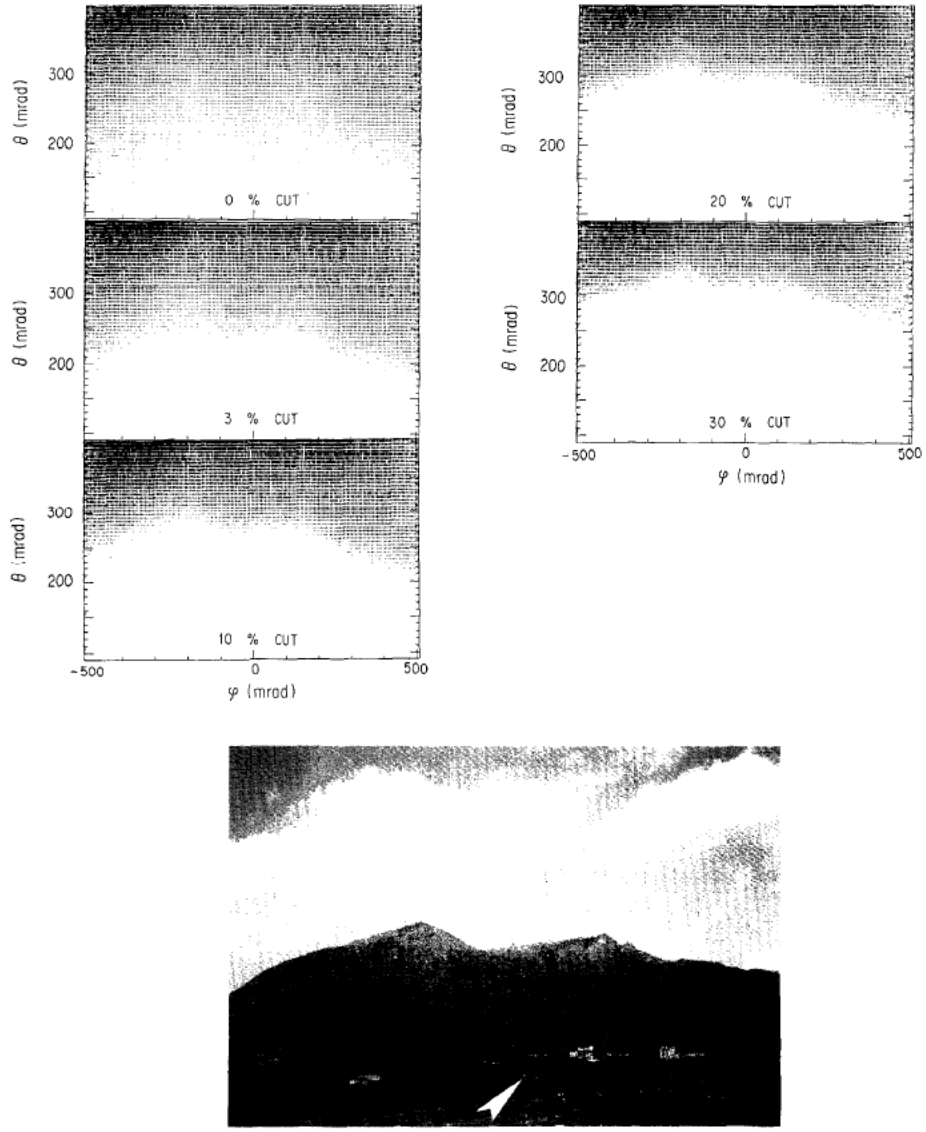

Figure 5 – The five figures above are histograms obtained in the Mt. Tsukuba measurement with different discrimination cuts. The cuts are made based upon the amount of low-rate events allowed. At 20% of the low-event-rate cut, the outer profile of the mountain is clearly visible. The bottom image is a photo of Mt. Tsukuba with an arrow indicating the detector location [11].

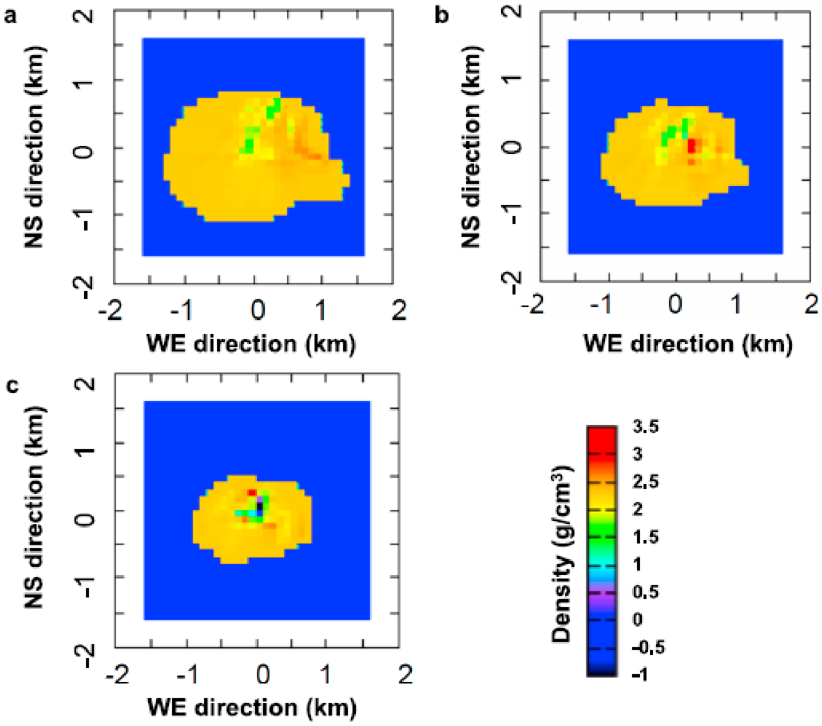

Figure 6 – Damped least squares solution of two-directional muon computed tomography. Three vertical slices are shown: (a) 2170-2270 meters above sea level, (b) 2270-2370 meters above sea level, and (c) 2370-2470 meters above sea level [14].

For example, in the case of X-rays, Röntgen's discovery of X-ray attenuation preceded the development of back-scattering imaging techniques. By using multiple scattering, cosmic-ray muons can be used to image dense objects over ranges of centimeters to meters.

Muon radiography using multiple Coulomb scattering was experimentally validated with a detector stack consisting of four ionizing radiation tracking chambers [29]. The active area of each delay line drift chamber [30] was 3600 square centimeters. After detector calibration, with an empty field of view, the positional precision of this experimental setup was determined to be 400 microns full width half maximum (FWHM). A scintillator was used to trigger the system for recording incident muons, and muon trajectories were measured. The discrimination between low-Z (water, plastic, concrete), medium-Z (iron, copper), and high-Z (lead, uranium) materials, using muon radiography, was achieved with an image reconstruction algorithm that incorporates a point of closest approach (POCA) calculation [18]. In this algorithm, the scattered path of the muon is approximated by a straight line. The momentum is estimated by particle scattering in two known planes. A voxel along the computed straight muon path is selected using POCA, which determines the nearest distance, and corresponding voxel, between the incident and scattered muon path. The momentum and scattering information in each voxel is then used to compute the scattering strength which is defined by eq. 1. This is described in more detail in Chapter 3.

$$\lambda_{mat} = \left(\frac{13.6}{p_0}\right)^2 \frac{1}{L_{0,mat}} \cong \sigma^2_{\theta_0,mat} \qquad \text{eq. 1}$$

Where λ_{mat} is the scattering strength, p_0 is the muon momentum, $L_{0,mat}$ is the material radiation length, and $\sigma^2_{\theta_0,mat}$ is the squared aggregate scattering distribution which is well described as Gaussian.

A tungsten cylinder resting on a Lexan plate supported by two steel rails was reconstructed using this technique showing clear differentiation between the steel and tungsten, shown in Figure 7. An extension of this method was studied using simulations with the same reconstruction method and a cosmic-ray muon source with an appropriate angular and energy spectrum. The simulations established that muon radiography of large objects, e.g. a commercial shipping container, can be performed quickly, in approximately one minute. Additionally, the measurement of muon momentum could also be used to improve image reconstruction and enhance signal to noise ratio.

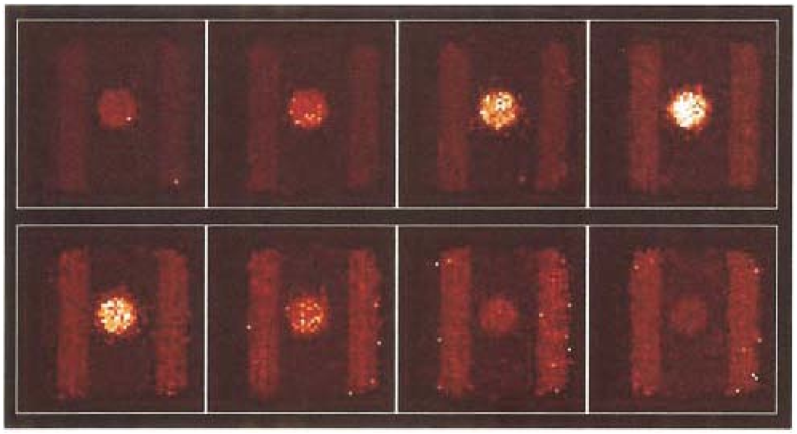

Figure 7 – Reconstruction of test object based on experiment using one hundred thousand cosmic-ray muons. The object in the center is a tungsten cylinder measuring 5.5 cm in radius by 5.7 centimeters in height. The cylinder is resting on a Lexan plate. This assembly sits on two steel rails. The image is reconstructed using 1 cubic cm voxels. The cylinder is clearly identified from the Lexan plate and steel bars [29].

Over 120 million vehicles enter the United States each year. Cosmic-ray muon tomography can be used for monitoring the trafficking of nuclear weapons and special nuclear material in these vehicles. Experimental validation of this application was achieved through measurements from the large muon tracker (LMT) [15]. The LMT consisted of 12 planes of 0.05-m-diameter, 3.65-m-long drift tubes in crossed x-y sets. These detectors measured muons with a positional precision to 400 microns FWHM and an angular precision of approximately 2 mrad FWHM. A robust tracker that fits time zero and eliminates the need for fast trigger was implemented, which increased the solid angle significantly. By using the incident muon flux, the drift tubes of the LMT were also able to be calibrated automatically. A lead brick was mounted next to an automobile engine to demonstrate the speed in identifying a nuclear threat. Muon trajectories were measured for 160 minutes by the LMT and the resulting image reconstruction is shown in Figure 8. Receiver operator curves (ROC), using 40 independent trials, indicated that the lead could be identified with zero false positives in 4 minutes. The required exposure time can be reduced by: including momentum in the track reconstruction and enlarging the solid angle of the detector system. Modeling and simulation with Geant4 [31], a Monte Carlo particle physics simulation package, was used to study additional cases for applying muon tomography for SNM threat identification.

The multiple scattering and transmission of muons have been used to image objects with a variety of size, density, and atomic mass. Recent research of multiple scattering muon tomography shows that it is possible to image small objects on the order of centimeters. As this document will show, multiple scattering is a more sensitive technique, buy attenuation radiography can also yield a useful secondary signal that can improve signal to noise ratio for detecting special nuclear material. Thus, both methods have their uses for specific applications, from high resolution imaging to isotopic identification of enriched uranium. The measurement of near horizontal muon multiple scattering will also allow for the imaging of larger structures, e.g. Fukushima Daiichi reactor, at better resolution than what transmission techniques are able to accomplish. Furthermore, cosmic-ray muon radiography is spreading to the broader scientific community, indicated in Table 1[2], for many purposes including: geophysics, volcano imaging, tunnel imaging, archaeological surveys, fuel canister tomography, port security, safeguards, treaty verification and more.

---

[2] This table was compiled by Dr. E.C. Milner at LANL

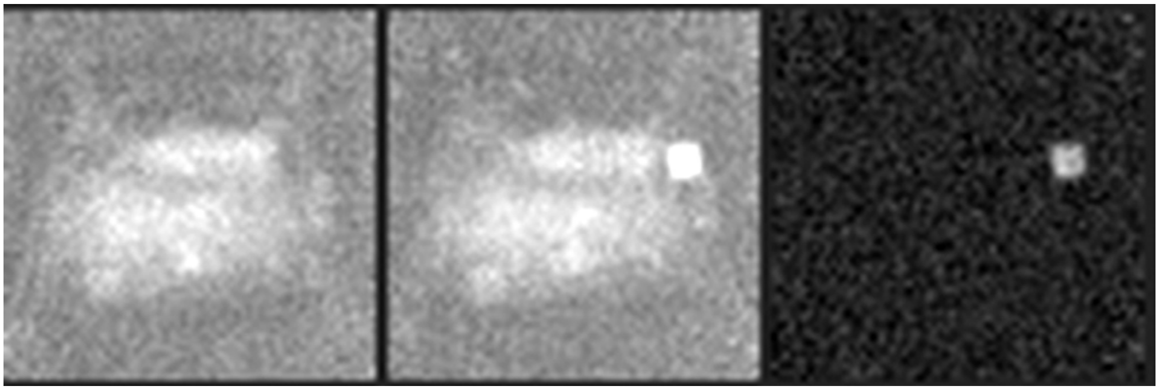

Figure 8 – Mean scattering angle for a slice through the scene 50 cm above the base plate. The left panel shows the engine, the middle panel the engine plus the 10 cm x 10 cm x 10 cm lead cube, and the right panel the difference [15].

Type	Country	Group	Purpose
Transmission Radiography	France	Sorbonne	Geophysics
	Hungary	Eötvös University	Geophysics
	Italy	INFN Napoli	Volcano Imaging
		INFN Trieste	Archaeology
	Japan	Riken	Volcano and Reactor Imaging
		KEK	Reactor Imaging
		Tsukuba University	Reactor Imaging
		Nagoya University	Nuclear Emulsion Technique
		University of Tokyo	Volcano Imaging
		Toshiba	Reactor Imaging
	Mexico	UNAM	Pyramid Imaging
	United States	Univ. of Texas at Austin	Archaeology
Scattering Radiography	Canada	Chalk River Lab	Dry Cask Storage Monitoring
	China	Lanzhou University	Geant4 Simulations
		Tsinghua University	RPC System
	Italy	INFN Padova	CMS Drift Tube System
		INFN Torino	ALICE RPC
	Russia	IHEP	IHEP
	Sweden	Uppsala University	Fuel Canister Tomography
	United Kingdom	AWE	SNM Detection
	United States	Decision Sciences	Port Security
		LANL	Everything
		Florida Institute of Tech.	GEM Detector Development
		University of California	Simulation and Algorithms

Table 1 – This table describes active muon radiography projects by location and group as of 2013. Categories are separated into two types: transmission radiography and scattering radiography.

CHAPTER 3

Theoretical Overview

A well established model for the incident cosmic-ray muon flux is necessary for understanding the radiographic capabilities of muons and their implementation in simulations and experiments. Cosmic-ray muon flux is dependent upon position, angle, and energy. This spectrum is defined by: 1) the incident cosmic-ray proton that generated the muon as a result of pion decay from hadronic showers, and 2) the path that the resulting cosmic-ray muon followed along its course to the surface of the earth. As the muon approaches the earth's surface, it passes through the earth's atmosphere, which is hardening the momentum distribution of the muons and reducing their total flux. Thus, when muons traverse smaller lengths in atmosphere, as is the case of vertical muons at high altitude, the flux is higher and the energy spectrum is softer. The opposite is true for horizontal muons, where the spectrum's average energy is higher and there is less flux. The cosmic-ray muon flux at sea level is about $10^4 \frac{\mu}{m^2\ min}$, and is composed of nearly equal numbers of positively and negatively charged muons.

The cosmic-ray muons have been studied for the greater part of the 20th century, and we make use of the resulting theories and measurements to create models for Monte Carlo simulations. In particular, our simulations rely upon a cosmic-ray muon source that is derived from over 30 years of experimental evidence and theoretical explanations. In this dissertation, it is shown how the knowledge of the cosmic-ray spectrum can improve the material identification capabilities of cosmic-ray muons. For example, the spectrum of the cosmic-ray muon flux can be used to create a multi-group fit for determining radiation lengths of cosmic-ray muon radiography image reconstructions. The theoretical knowledge of the flux allows us to predict the muon rates expected from horizontal muons and determine the impact of overburden from buildings adjacent to an experiment.

The physical processes of charged particle interactions with matter form the basis of cosmic-ray muon imaging. The passage of the muon through the electron cloud of atoms causes ionization resulting in continuous energy loss of the incident muon and potentially leading to muon absorption. This process is the foundation of transmission mode muon radiography. Additionally, the slowing down of negatively charged muons can also lead to muon capture and muon induced fission. Muon induced fission is a useful imaging technique for identifying special nuclear materials with high neutronics gain. The muon interaction with the charged nuclei of atoms in a material results in multiple scattering and angular diffusion of the muon. By measuring the multiple scattering of cosmic-ray muons, we can obtain better spatial imaging resolution as compared to transmission radiography. In the following sections, I discuss the theory behind the cosmic-ray muon spectrum and the three physical processes: ionization, multiple scattering, and muon induced fission, which enable the use of cosmic-ray muons for imaging.

The Cosmic-Ray Muon Spectrum

An accurate model of the cosmic-ray muon spectrum at the earth's surface was developed at LANL. This model implements methods discussed in previous work that parameterized the cosmic-ray muon spectrum as a function of zenith angle [32]. The momentum distribution of vertical muons (with a zenith angle around $\theta = 0°$) at the surface of the earth is well known experimentally. However, the effect that the zenith angle has on the cosmic-ray muon flux energy spectrum and rate is less studied. Reyna suggested a simple approximation for defining the cosmic-ray muon momentum spectrum over all zenith angles, $0° \leq \theta \leq 90°$. By combining empirical data with the angular zenith relationship derived by Reyna, we are able to approximate the cosmic-ray muon momentum spectrum. This model, hereafter referred to as the "Reyna Model", is used in the simulation and analytical computations in this dissertation. I describe this model in more detail below.

The cosmic-ray muon momentum spectrum at the surface of the earth is explained by starting with the cosmic-ray muon's source, e.g. a cosmic-ray proton. The cosmic-ray proton is accelerated in deep space from supernova remnants [33-35], and the proton arrives at the atmosphere of the earth producing hadronic showers shown in Figure 9. These hadronic showers occur due to the highly energetic cosmic-ray proton interacting with atmospheric nuclei forming secondary particles including hadrons and mesons. The delta resonance of this interaction is responsible for most of the pion production in the atmosphere. A high energy cosmic-ray proton interacts with a nucleon in the atmosphere producing a delta baryon and residual nucleus:

$$p + N \rightarrow \Delta + N \qquad \text{eq. 2}$$

The delta resonance produces a group of delta particles, $\Delta^-, \Delta^0, \Delta^+,$ and Δ^{++}. Charged pions and nucleons are obtained commonly from the following two branches:

$$\Delta^- \rightarrow n + \pi^- \qquad \text{eq. 3}$$

$$\Delta^{++} \rightarrow p + \pi^+ \qquad \text{eq. 4}$$

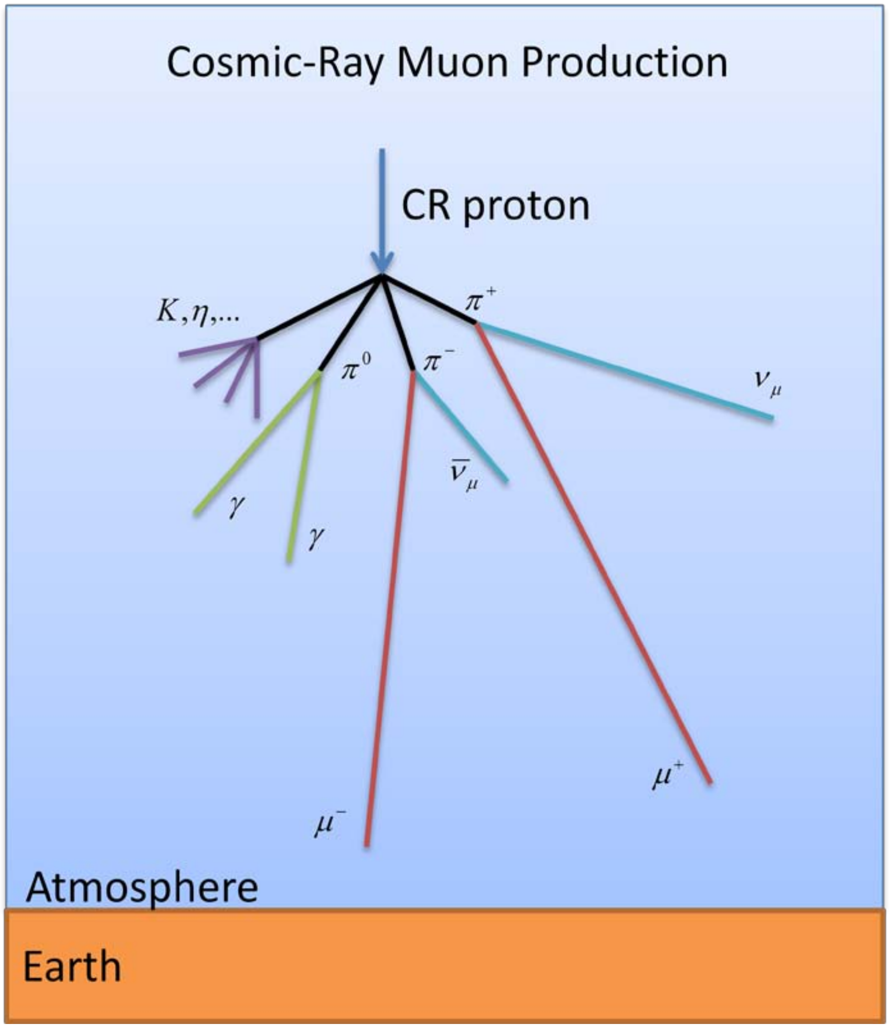

Figure 9 - Diagram of cosmic-ray muon generation in the atmosphere above the earth. The cosmic-ray proton enters the atmosphere creating a hadronic shower, dominated by pions. The charged pions decay into a cosmic-ray muons and neutrinos. Because of their relatively long lifetime and relativistic energies, most of the cosmic-ray muons survive until they interact with the surface of the earth.

With a mean lifetime of $26\ ns$, the pion decays resulting in a muon and neutrino or gammas depending on the parent pion charge (most probable branching ratio is shown here):

$$\pi^- \rightarrow \mu^- + \bar{\nu_\mu} \qquad \text{eq. 5}$$

$$\pi^+ \rightarrow \mu^+ + \nu_\mu \qquad \text{eq. 6}$$

$$\pi^0 \rightarrow \gamma + \gamma \qquad \text{eq. 7}$$

Most cosmic-ray muons originate near an altitude of 15 km [36]. As they pass through the earth's atmosphere, the cosmic-ray muons typically lose ~2 GeV from ionization. The cosmic-ray muon energy spectrum at the earth's surface is at an average energy of $\sim 3 - 4$ GeV. At the surface of the earth, the muons will continue to slow down through additional interactions and either get captured or decay. Upon decay of the cosmic-ray muon, an electron (or positron) and two neutrinos are emitted:

$$\mu^- \rightarrow e^- + \bar{\nu_e} + \nu_\mu \qquad \text{eq. 8}$$

$$\mu^+ \rightarrow e^+ + \bar{\nu_\mu} + \nu_e \qquad \text{eq. 9}$$

In summary, the angular and momentum distribution of the cosmic-ray muon is a convolution of the production spectrum, continuous energy loss in atmosphere, and decay [36]. In order to approximate the cosmic-ray muon momentum intensity at a particular zenith angle, the Reyna Model was derived by analyzing six surface muon measurements. These surface experiments: Nandi and Sinha [37], MARS [38], Kellogg et al. [39], OKAYAMA [40], Kiel-Desy [41], and MUTRON [42], measured the cosmic-ray muon flux as a function of zenith angle and momentum. The OKAYAMA measurements of lower momentum cosmic-ray muons, $p_\mu \leq 250\ GeV$, at multiple angles comprised nearly half of the data analyzed. MARS and Nandi/Sinha measured vertical cosmic-ray muons, and the other three groups measured cosmic-ray muons at the zenith angles within the range of $25.9° \leq \theta \leq 90°$.

In the Reyna Model, the momentum distribution of the vertical muon intensity is described by eq. 10, where p_μ is the momentum of a particular muon.

$$I_V(p_\mu)[cm^{-2}\ sr^{-1}\ s^{-1}\ GeV^{-1}] \quad \text{eq. 10}$$

By plotting the six surface measurements with a simple scaling variable (eq. 11), a similarity in the spectral shape of the differential surface muon intensity is identifiable. A scale factor is then introduced for all cosmic-ray muon momenta $\propto 1/\cos^n(\theta)$, where optimal agreement is reached at $n = 3$. Thus, a relationship exists in the data relating muon intensity at any angle and momentum to the vertical intensity shown in eq. 12. Figure 10 shows this relationship by applying the scaling factor to muon flux defined by the scaling variable ζ.

$$\zeta = p_u \cos(\theta) \quad \text{eq. 11}$$

$$I(p_\mu, \theta) = \cos^3(\theta)\, I_V(\zeta) = \cos^3(\theta)\, I_V(p_u \cos(\theta)) \quad \text{eq. 12}$$

There are several parameterized models that fit the cosmic-ray muon spectrum including: Gaisser [43], Tang et al. [44], Bogdanova et al. [45], and Bugaev et al. [46]. The Gaisser and Bugaev models describe only the vertical muon intensity. The Tang and Bogdanova models include angular dependence for approximating cosmic-ray muon flux at the earth's surface. We chose instead to use empirical data for the incident vertical cosmic-ray muon intensity at the earth's surface, $I_V(p_\mu)$, and then apply Reyna's method, eq. 12. Data from Haino's group [47] was used to sample the low momentum range of the cosmic-ray muon spectrum, and data from the L3 collaboration [48] was used to sample the high momentum range. A smoothing function joined the data sets when they overlapped. The Reyna Model is simple to implement in simulations and is adequate for the full sky simulations that will be discussed further in this dissertation.

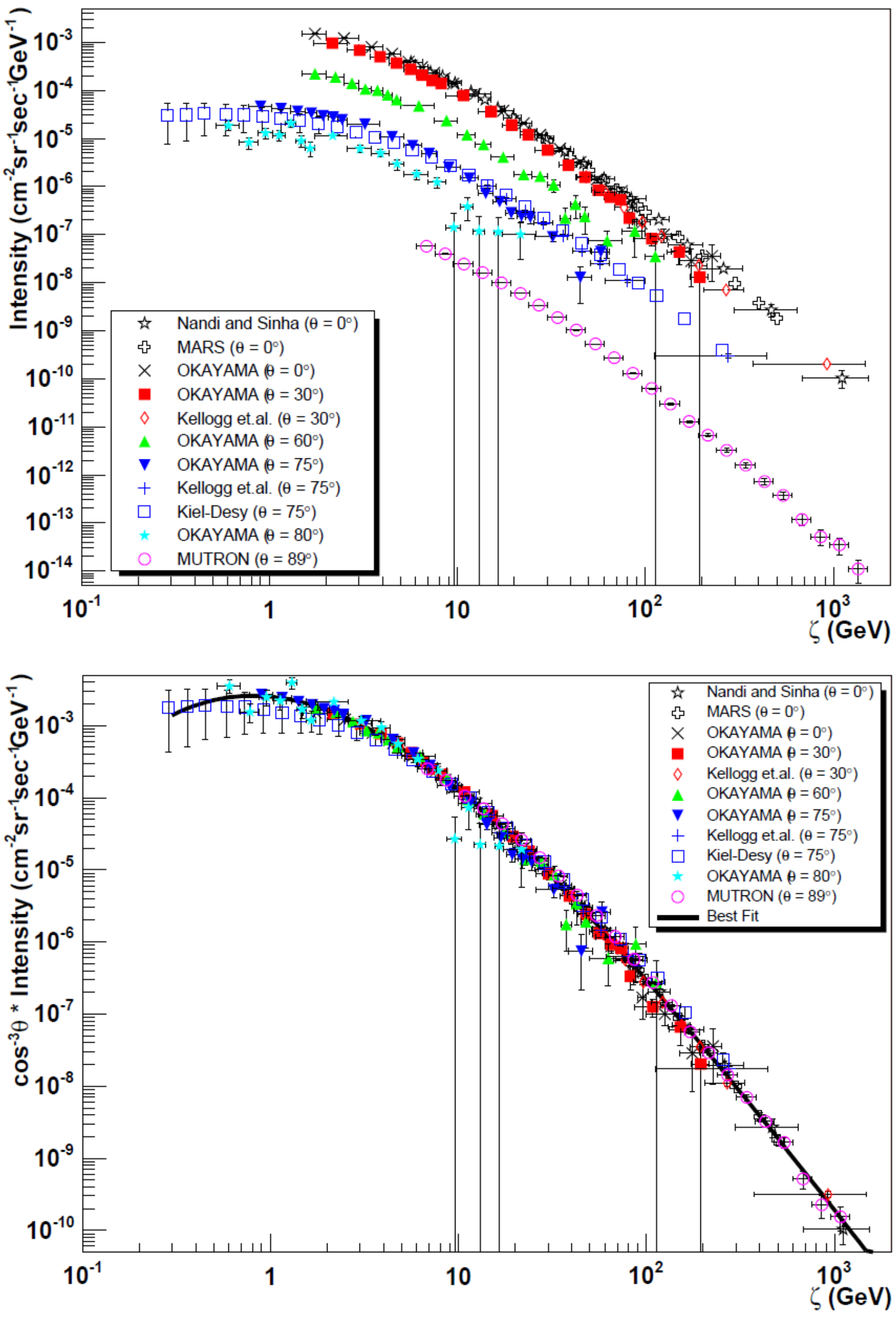

Figure 10 – Differential surface muon intensity (top figure) plotted as a function of ζ. A scaling factor of $1/\cos^3(\theta)$ is applied (bottom figure) resulting in a good fit between momentum and angle for all data sets. The solid black line (bottom figure) is a best fit of the scaled data [32].

Muon Energy Loss

The primary mechanisms for cosmic-ray muon energy loss are ionization and radiative processes. The dominant physical process of energy loss is identified by the critical energy. When the muons momentum is at the critical energy, the amount of energy loss is equivalent between ionization and radiative processes. For most materials, the critical energy is above several hundred GeV, which indicates that ionization is the primary mechanism of energy loss for the majority of cosmic-ray muons given that the average energy of the cosmic-ray muon spectrum is ~3-4 GeV.

The electronic interaction of high momentum muons, with a speed of $v = \beta c$, occurs in singular collisions with energy loss E [49]. The rate that this energy loss occurs is well-described by the Bethe formula [50-52] shown in eq. 13. For a given material the function mainly varies by β unless considering highly relativistic particles where T_{max} becomes more significant.

$$-\frac{dE}{dx} = 4\pi N_A m_e c^2 z^2 \left(\frac{e^2}{4\pi\epsilon_0 m_e c^2}\right)^2 \frac{Z}{A}\frac{1}{\beta^2}\left[\frac{1}{2}\ln\frac{2m_e\beta^2\gamma^2 T_{max}}{I^2} - \beta^2 - \frac{\delta(\beta\gamma)}{2}\right] \qquad \text{eq. 13}$$

Where $\frac{dE}{dx}$ is the change in kinetic energy E over some distance x also known as the "stopping power", N_A is Avogadro's number, $m_e c^2$ is the electron mass, z is the unit charge of the incident particle, $\left(\frac{e^2}{4\pi\epsilon_0 m_e c^2}\right)$ is the classical electron radius, Z is the atomic number, A is the atomic mass, γ is the Lorentz factor, I is the mean excitation energy in eV, T_{max} is the incident particle energy, and $\delta(\beta\gamma)$ is the density effect correction to ionization energy loss.

The change in energy, $\frac{dE}{dx}$, is only weakly dependent of the specific material due to the $\frac{Z}{A}$ ratio. In lower Z materials, the amount of neutrons is similar to the amount of protons. The ratio of neutrons to protons increases for higher Z up to approximately $\frac{3}{2}$ the amount of neutrons when compared to protons. In order to prove that the material has only a small effect on energy loss, I replace the $\frac{Z}{A}$ in eq. 13 with $\frac{Z}{Z+N} \sim \frac{Z}{2Z} \sim \frac{1}{2}$ for lighter Z materials, and $\frac{Z}{Z+N} \sim \frac{Z}{\frac{5}{2}Z} \sim \frac{2}{5}$ for heavier Z materials. The $\ln\frac{2m_e\beta^2\gamma^2 T_{max}}{I^2}$ term is also dependent on Z which affects the mean excitation energy, I. However, when compared to the strong linear Z dependence of multiple Coulomb scattering, the Z dependence of energy loss due to ionization is quite weak.

The high-energy cosmic-ray muon ($\beta\gamma \geq 1$) is highly penetrative and loses energy in small increments. When ionization losses are dominating the energy loss process, the particle is known as minimally ionizing, and its total energy loss is $\sim 2\ MeV\ g^{-1}cm^{2}$. The minimum ionization is similar for most materials and for different charged particles. While the Z dependence is generally weak, the density effect is much stronger and linear for the slowing down process. Additionally, density does typically increase for higher Z materials, this effect is also shared with the multiple Coulomb scattering. The different regimes of muon lethargy in copper are summarized in Figure 11.

It is possible for muons to lose all of their energy in a material and range out, or stop. These ranges are typically on the order of meters for a cosmic-ray muon with an average energy of 4 GeV. This penetrative power of muons enabled the original uses of cosmic-ray muons to measure pyramids and mine shafts. The effects of cosmic-ray muon stopping will be discussed in further detail below as muon induced fission is one resultant of this process.

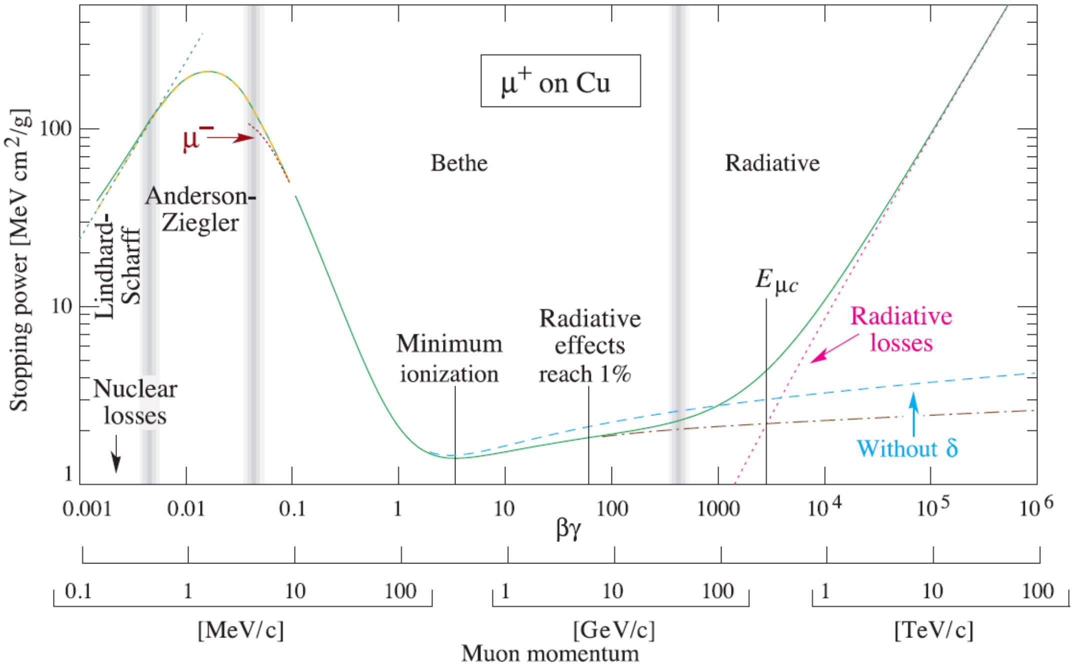

Figure 11 – Stopping power for positive muons in copper over nine orders of magnitude in momentum. The different dominant physical processes, such as radiative losses and ionization, are shown. The critical energy occurs at $E_{\mu c}$. The majority of the slowing down of the cosmic-ray muon spectrum occurs in the Bethe region for muons at the surface of the earth (average energy of 4 GeV) [53].

Multiple Coulomb Scattering

When a muon passes through matter, it is deflected by many small angle scatterings from nuclei. These deflections are due to the Coulomb interaction, which yields the terminology for this process, multiple Coulomb scattering (MCS). The theory of MCS is well described by Molière and Bethe [54]. The cosmic-ray muon undergoes a random walk as it scatters through a material, which results in an aggregate Gaussian angular distribution for the exiting muon [29] shown in eq. 14 and illustrated in Figure 12 [18].

$$\frac{dN}{d\Theta} \propto \Theta \exp\left(-\frac{\Theta^2}{2\Theta_0^2}\right) \qquad \text{eq. 14}$$

The width of this Gaussian distribution, Θ_0, is:

$$\Theta_0 = \frac{13.6\,MeV}{\beta \mathrm{cp}} \sqrt{\frac{L}{L_0}} \left[1 + 0.038 \ln \frac{L}{L_0}\right] \qquad \text{eq. 15}$$

Where L_0 is the radiation length, p is the particle momentum, and βc is the muon velocity (~1 for cosmic-ray muons).

Multiple Coulomb scattering has a linear Z dependence for the Gaussian width, Θ_0, from the inverse dependence of the radiation length, shown in approximated form in eq. 16. The Θ_0^2 parameter is also referred to as the scattering strength, λ_{mat}.

$$\lambda_{mat} = \Theta_0^2 \cong \left(\frac{13.6\,MeV}{\mathrm{p}}\right)^2 \frac{1}{L_{0,mat}} \qquad \text{eq. 16}$$

The Z dependence arises from the definition of radiation length which is the characteristic length of matter that a high-energy charged particle travels through and is defined in eq. 17.

$$\frac{1}{L_0} = \frac{4\alpha r_e^2 N_A}{A} \{Z^2[L_{rad} - f(Z)] + Z L'_{rad}\} \qquad \text{eq. 17}$$

For $A = 1\ g\ mol^{-1}$, $\frac{4\alpha r_e^2 N_A}{A} = (716.408\ g\ cm^{-2})^{-1}$, L_{rad} and L'_{rad} are tabulated values by Tsai [55], and $f(Z)$ is approximated below in eq. 18, where $a = \alpha Z$ [56].

$$f(Z) = a^2[(1 + a^2)^{-1} + 0.20206 - 0.0369a^2 + 0.0083a^4 - 0.002a^6] \qquad \text{eq. 18}$$

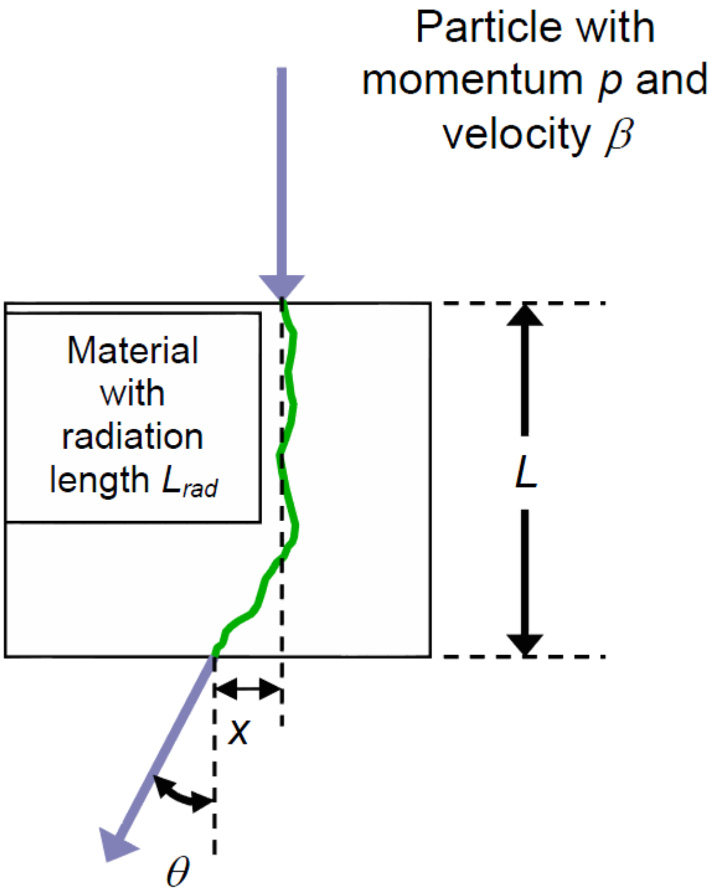

Figure 12 – Multiple Coulomb scattering of a charged particle through material. The magnitude of scattering is exaggerated for illustrative purposes [18].

The radiation length can be simplified as [57]:

$$L_0 = \frac{716.4\ g\ cm^{-2} A}{Z(Z+1)\ln\left(\frac{287}{\sqrt{Z}}\right)} \qquad \text{eq. 19}$$

We can simplify eq. 19 further by approximating $\frac{A}{Z}$ as a constant, and moving the natural log term and leading constant into a total constant K. This results in a radiation length that is inversely proportional to Z with some constant, K, as shown in eq. 20.

$$L_0 = \frac{716.4\ g\ cm^{-2} A}{Z(Z+1)\ln\left(\frac{287}{\sqrt{Z}}\right)} \propto K\frac{1}{Z+1} \propto KZ^{-1} \qquad \text{eq. 20}$$

Where $\frac{A}{Z} = \frac{Z+N}{Z} \sim \frac{Z+KZ}{Z} \sim K$ and $\ln\left(\frac{287}{\sqrt{Z}}\right) \sim K$.

By combining eq. 16 and eq. 20, the scattering strength is linearly dependent and proportional to the Z of the scattering material, eq. 21. The MCS sensitivity to Z enables the discrimination of different materials with similar densities. Additionally, the combination of MCS muon radiography and transmission mode radiography produces a signal that could be used for identifying objects through density measurements and scattering analysis [58].

$$\lambda_{mat} = \Theta_0^2 \cong \left(\frac{13.6\ MeV}{\mathrm{p}}\right)^2 \frac{1}{L_{0,mat}} \propto K\left(\frac{13.6\ MeV}{\mathrm{p}}\right)^2 Z \qquad \text{eq. 21}$$

Muon Induced Fission

The capture of negatively charged muons in heavy materials, e.g. uranium, can lead to fission. The neutrons that result from the fission of heavy materials can be amplified by materials with large fast neutron fission cross-sections. This fission neutron signal can be combined with muon tracking in order to create a single sided, tagged muon radiography image that is particularly sensitive to fast fission materials. By using this technique, special nuclear material can be identified with a high signal to noise ratio from one side.

A slow cosmic-ray muon, $p \ll 100\ MeV/c^2$, is below the point of minimal ionization loss. At this point, each ionization removes increasingly larger amounts of the muon's energy until the muon either decays or is captured in the material. If the muon is negatively charged, and the capturing material is high Z, muon induced fission may occur through either a prompt or delayed process [59].

The negative muon is typically captured in the electromagnetic shell of the atom and quickly de-excites releasing muonic x-rays in the process. As the muon approaches ground state, the probability of it interacting with a proton in the nucleus increases. This is due to the increased mass of the muon pushing its orbit closer to the nucleus as compared to an electron's orbit in the same state. In high Z materials, e.g. uranium, the 1s orbital muon resides inside the nucleus. In prompt muonic fission, the excitation energy of the muonic atom is transferred directly to the nucleus via non-radiative internal conversion. This transition typically overcomes the fission barrier height of most actinides. The prompt muon induced fission process can be represented as:

$$(\mathrm{Z},\mathrm{A})(\mu^-)^* \rightarrow (\mathrm{Z},\mathrm{A})^*(\mu^-) \qquad \text{eq. 22}$$

Alternatively, the muon may interact with a proton through the weak force resulting in a transmutation of the proton to a neutron and a neutrino:

$$\mu^- + p \rightarrow n + \nu_\mu \qquad \text{eq. 23}$$

The neutron generally receives up to 20 MeV of energy and may escape the nucleus. The resulting excited nucleus is prone to fission. The characteristic mean lifetime of this process, which is known as a delayed muon-induced fission, is 70-80 ns in actinides.

CHAPTER 4

Muon Tomography Instrumentation

The cosmic-ray muon is a component of background radiation, which enables us to perform experiments without being tied to expensive source facilities. Though the muons arrive at the experimental apparatus with some variation in flux and energy spectrum, we are not sensitive to the impact of these changes during measurement over long integration times. The experimental facility, where we performed the majority of our measurements, is located at an altitude of ~2200m, which yields more muon flux in contrast to sea level. There was little effect from overburden due to adjacent buildings. The cosmic-ray muon is a probe with the capability of performing charged particle radiography on materials with a variety of thickness, density, and atomic mass; for the detection of these muons, we have implemented arrays of drift tube detectors.

The muon tomography team at LANL decided that sealed aluminum drift tubes were the most suitable detector for cosmic-ray muon radiography. With a well established history in the high energy physics community, due to its use in charged particle detection for accelerator experiments, the drift tubes provided a cost effective, low gamma background alternative to scintillators and photomultiplier tubes. Given that the expected rate of flux through the tubes was low, as compared to an accelerator beamline, the tubes were sealed providing extra robustness and ease of operation. The muon tomography team was able to quickly produce many of these drift tubes for performing cosmic-ray muon imaging.

Aluminum drift tubes have several characteristics limiting the muon radiography resolution. Detector scattering effects amount to several milliradians of angular deflection of the muon probe, which when projected over a meter, can blur reconstructed edge resolution by millimeters to centimeters. This effect can be reduced by replacing the aluminum drift tubes with carbon fiber drift tubes; this lessens the effect of detector scattering. The front end electronics that digitize the drift tube hits have a 200 MHz clock which translates to a 5 ns granularity of the data. Given the speed of the charge migration in the spectroscopic gas, the 5 ns granularity corresponds to a spatial resolution of approximately 400 microns of uncertainty in each aluminum drift tube. A faster clock would improve the spatial resolution in the drift tubes, and that is a more likely option for improvement than finding a slower gas.

Mini Muon Tracker (MMT)

The Mini Muon Tracker uses two muon supermodules to measure incoming and outgoing tracks of individual muons, where the region of interest is contained within the acceptance of the tracker pair. Each supermodule of the Mini Muon Tracker contains drift tubes that measure the trajectories of passing muons. Individual drift tubes have a 5 cm outside diameter, 1.2 m length and 0.9 mm wall thickness; they are sealed on both ends with welded aluminum end-caps[60]. Tubes are filled with a gas mixture of 50 % Ar, 44 % CF_4, and 6% C_2H_6. The anode wire is 30-μm, gold-plated tungsten, installed with 0.49N (50g) tension, and maintained at +2550 V relative to the grounded tube wall during operation.

Drift tubes are arranged in a stacked, dense-pack of double layers, and are able to detect interacting charged particles with high efficiency. For the MMT, each supermodule (one above and one below), is comprised of 3 sets of x-y planes; each plane is 114.3 cm by 114.3 cm (24 tubes at each of two staggered layers in each direction, so 48 tubes for each x and y). The total number of tubes in the system is 576 (96 for each x-y plane; 3 x-y planes per supermodule; 2 supermodules).

Each drift tube in the MMT is a non-proportional avalanche counter. When a muon travels through one of the tubes, it creates a line of electron/ion pairs in the gas. Some electrons and ions may recombine, however when high enough voltage is applied, an “electron cloud” will start drifting toward the wire. The geometry of the electrodes in these tubes creates an avalanche electric field that amplifies the electron cloud as it approaches the wire, near a distance of 1 mm. This results in charge accumulating onto the wire and provides signal for the front end electronics. Figure 13 shows a drift tube schematic and a muon travelling through that tube resulting in an ionized electron cloud moving to the wire.

The drift velocity of the electron charge is an important value for reconstructing the location of the ionizing muon trajectory. The drift time of the electron cloud is defined by the distance of the closest approach of the muon trajectory to the drift tube wire and the electron cloud drift velocity. The drift velocity can be determined either from simulations or measured by using tracking data from the MMT during system calibration. This yields a time-to-radius function for the drift tube, which is used to convert drift times to distance of closest approach for an ionizing muon trajectory. The distance of closest approach, obtained for each hit in an event, is then used for muon trajectory reconstruction. An event is defined as a single muon crossing the MMT detectors whilst hitting multiple tubes in the trackers.

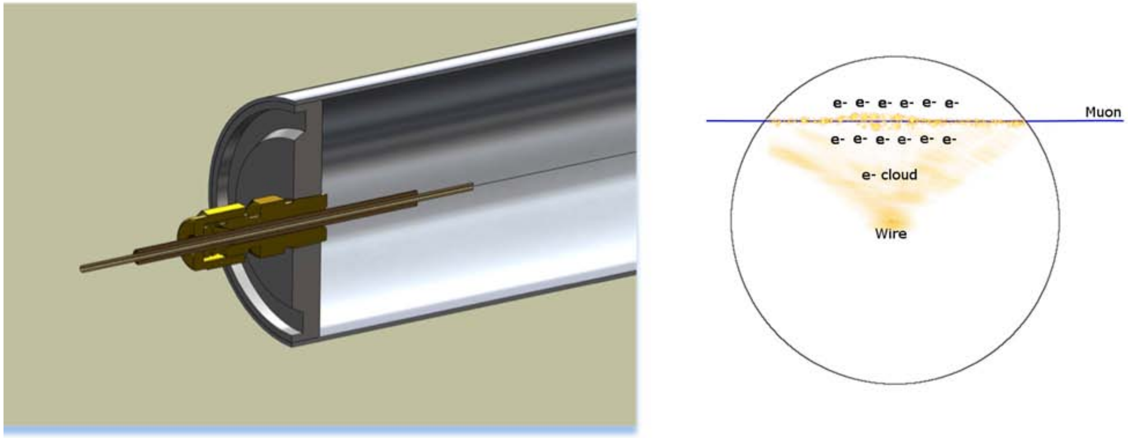

Figure 13 – Drift tube design cutaway (left) [60] and diagram of a charged particle passing through that drift tube (right). This drift tube detector is a gas filled aluminum tube with a Swagelok fitting that anchors a wire between both ends of the tube. When a charged particle passes through the tube, it creates electron and ion pairs (ions omitted in right figure). The cloud of electrons drifts to the wire creating a signal.

In Figure 14, the drift tube radius to time curve is shown for MMT drift tube #270. A datum point is plotted for each hit that occurs in the tube per track. This datum point is converted to a radial distance by using a distance of closest approach between the track vector and a vector that makes up the wire (assumed to be straight). Distance is plotted versus drift time recreating a drift to time (RT) curve for the drift tube #270. Results from a Garfield [61] simulation of the tube are superimposed on the data points. There is a time offset in the data as compared to the simulation, however; the shape of the simulation is similar to the drift tube data. This offset occurs from the tracking reconstruction process, which determines an initial time for track fitting purposes.

The drift tube pulses are amplified by charge sensitive amplifiers, discriminated by multi-threshold discriminators, and digitized in field-programmable gate array (FPGA) time-to-digital converters (TDCs). The data is transferred to a data-acquisition computer through a dedicated Ethernet link. Additional signals are input into the TDC boards for timing coincidence between muons and their induced fission gamma and neutron signatures. Hardware in the form of neutron detectors, gamma detectors, discriminators, and logic level converters are used to provide this signal.

The MMT has been adapted to operate in different modes. In a vertical (standard) orientation, shown in Figure 15, objects are placed between the upper and lower tracker sets. Scattering in the objects deflects the muons, as measured by the difference between track direction vectors measured above and below the objects. The MMT can be rotated by 90 degrees into a horizontal orientation, e.g. for reactor imaging, with the supermodule planes oriented vertically for the reactor experiment in order to measure near horizontal muons. This orientation allows easy set up of the detectors around a large object like the University of New Mexico’s Research Reactor. The MMT system is transportable in a trailer for field work, and this has been demonstrated in several public demonstrations for educational purposes.

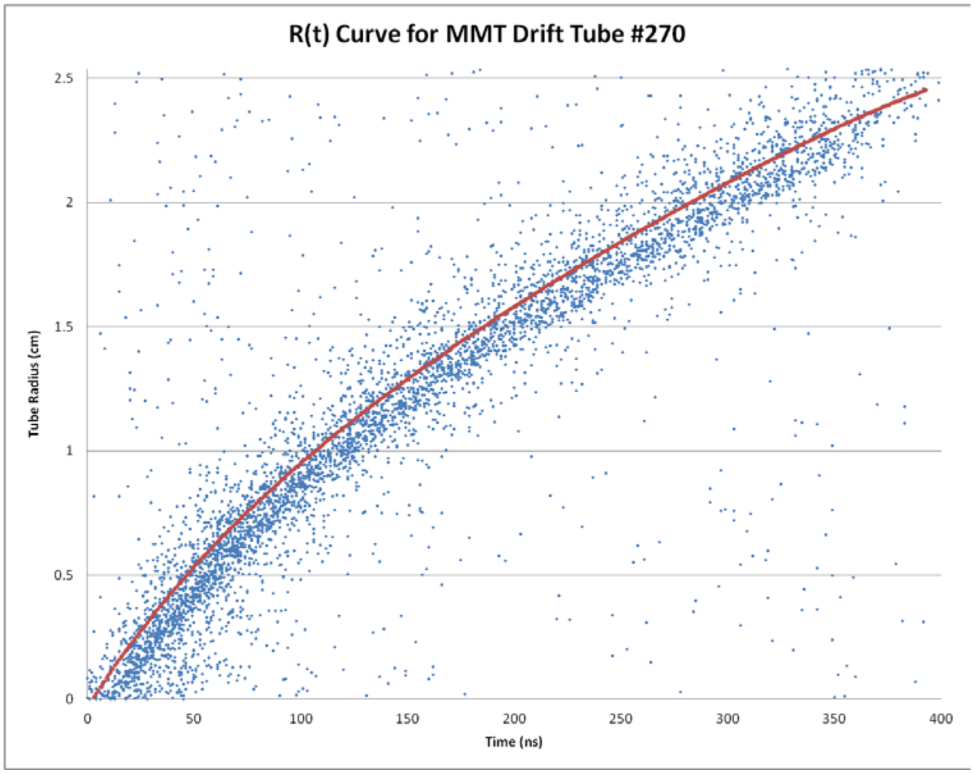

Figure 14 - R(t) curve for MMT drift tube number 270. Data (blue points) consists of a one hour run worth of muon tracks that cross tube 270. The Garfield simulation is the continuous (red) line. The Garfield simulation parameters matched the drift tubes used in the MMT. There is a time offset between the simulation and data due to the track fitting process.

Figure 15 - The mini muon tracker (MMT) in a vertical (standard) orientation. Muon trajectories are measured by drift tubes located in each supermodule. The muon scattering objects in the field of view (e.g., lead blocks seen as blue rectangles in the photo) are reconstructed by the data acquisition computer; their images are displayed on the monitor in real time.

FPGA Frontend Electronics

A field-programmable gate array (FPGA) design[3] was implemented for the frontend electronics for converting the signal from the drift tubes into digital data. There are three printed circuit boards (PCB) for the front end electronics and an additional printed circuit board that provides high voltage to each drift tube. The bottom PCB of the front end electronics magnifies the amplitude of the signal from the drift tubes with a preamplifier and amplifier. Following signal amplification, the bottom PCB applies a discrimination cut on the amplified signal converting the analog signal into a series of logic cuts based on the discriminator threshold. The middle PCB of the front end electronics contains the FPGA components responsible for reading a clock signal, time-stamping the logic from the bottom board with a TDC, and exporting the TDC buffers every second. This middle PCB communicates with the data acquisition computer (DAQ), the 200 MHz clock, and the other frontend electronics cards with Ethernet. A master and slave relationship is used in order to synchronize each of the 24 cards. The top PCB is used to read in additional TTL signals to be combined and timed in coincidence with the muon tracking. This enables the single-sided muon tagged imaging used to study muon induced fission. PCB components are shown in Figure 16.

---

[3] The current iteration of the frontend electronics has been designed by Decision Sciences Corporation (DSC).

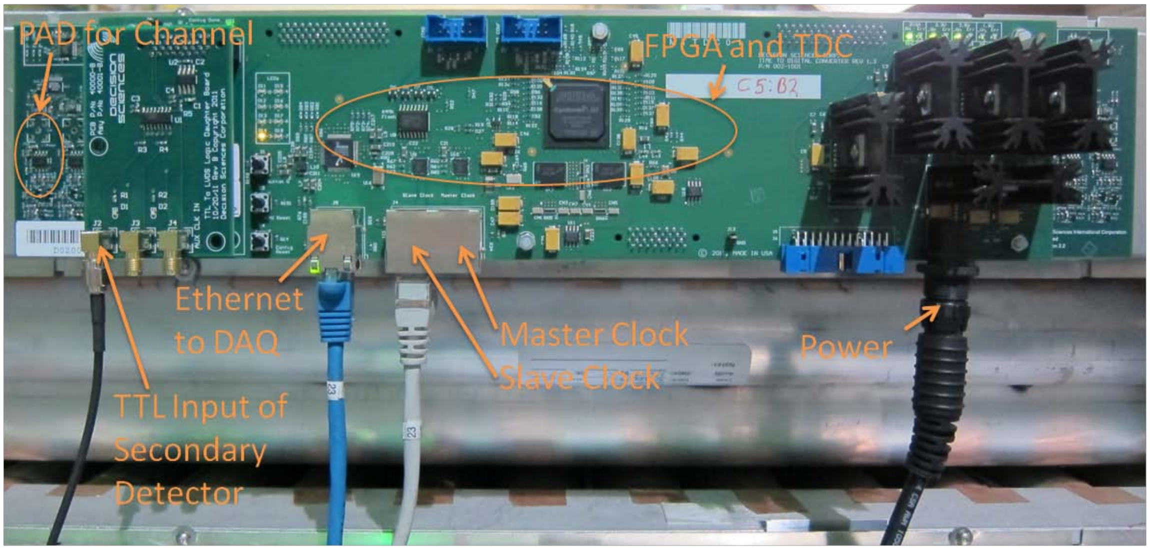

Figure 16 – Frontend electronics for the Mini Muon Tracker. The three printed circuit boards are used to read signal from the drift tubes and convert the signal into logic that is time stamped by the TDC. The drift tube analog signal is converted into logic pulses with a preamplifier, amplifier, and discriminator (PAD). Additional logic signals can be read into the TTL input. Every second, the data is exported to the DAQ via Ethernet.

Secondary Signal Detectors Overview

The secondary signals used to tag muon induced fission for muon radiography result from neutrons and gammas born during the fission process. Several detectors were investigated for measurement of these fission products. There were several criteria used to determine the feasibility of each detector: time until detection, efficiency, and susceptibility to background. As will be discussed in the muon induced fission chapter, the neutron is the best secondary particle to detect for tagged muon induced fission radiography. Thus, the focus on secondary particle detection is specific to the identification of a neutron in coincidence with the incident muon.

Four detectors were evaluated: He-3 tubes wrapped in polyethylene, He-4 tubes, a solid plastic scintillator bar, and EJ-301 liquid scintillators; these detectors are shown in Figure 17. The solid plastic scintillator bars failed at providing a signal of neutron flux due to having poor pulse shape discrimination characteristics and a large gamma background detection rate. The He-4 tubes were also not suitable given that their efficiency was at most 1-2 percent for detection of fast neutrons. The He-3 tubes wrapped in polyethylene performed well; however, their time until detection was too long due to moderation time. The EJ-301 liquid scintillators were the best candidates for identifying neutrons in coincidence with the incident cosmic-ray muon. Further discussion of the EJ-301 detectors, and their usage, is in the muon induced fission chapter.

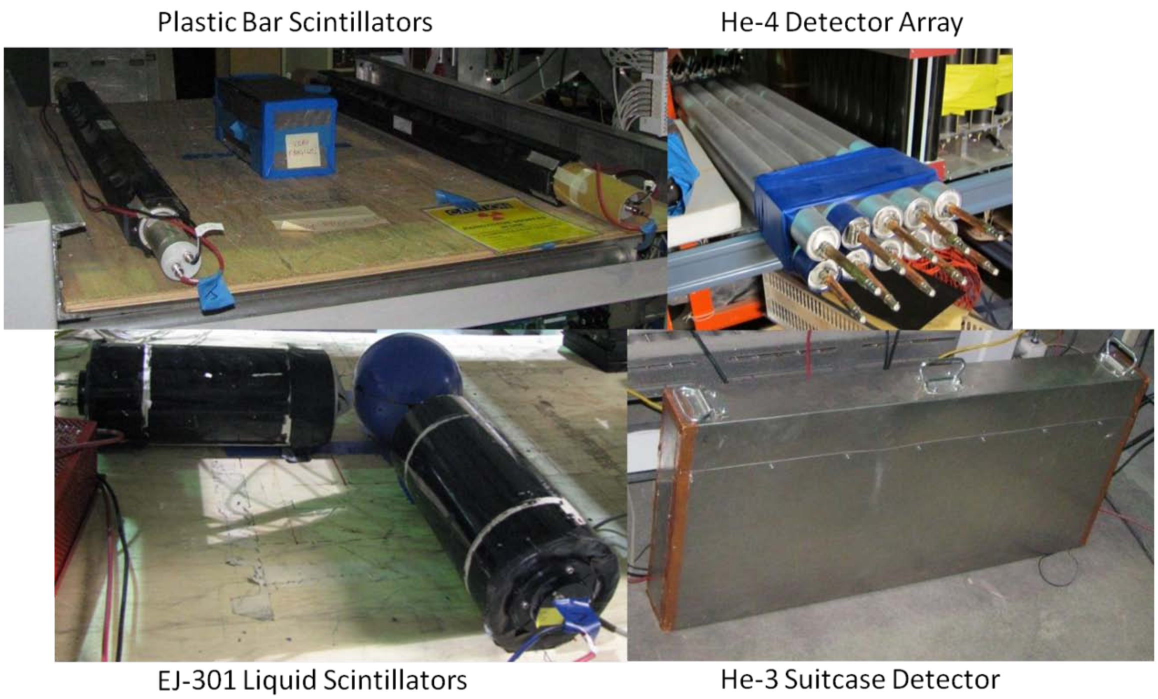

Figure 17 – Detectors used to measure neutrons from muon induced fission. There were several criteria for identifying the best neutron detector: time until detection, efficiency, and susceptibility to background (mainly gamma). The two best detector candidates were the liquid scintillator and the He-3 polyethylene wrapped suitcase detector.

CHAPTER 5

Methodology of Research Overview

The content of this dissertation research evolved over time to include material identification, horizontal reactor imaging, and high fidelity muon tomography simulations. The initial objective of this work was to develop an imaging technique for material identification. A second goal, horizontal reactor imaging, was identified following the tsunami that damaged the nuclear power plant at Fukushima, Japan. Simulations, mostly in Geant4, were studied and improved throughout the course of this work.

The methodology of this work focused on two objectives: 1) measure and analyze muon trajectories for material identification and reactor imaging and 2) improve predictive capabilities through the comparison of measurements and simulations. Experiments and simulations were performed with a standard scientific method, e.g.:

1. Propose the question: Can U-235 be identified using single sided imaging? Is U-235 distinguishable from U-238 using this technique?
2. Background research: Muons stop and scatter in U-235 and U-238 identically and muon induced fission occurs in Uranium. Production of secondary neutrons is higher in materials with neutronics gain (U-235 has a higher fission cross-section at 1 MeV than U-238 for example)
3. Hypothesize: If U-235 has more neutronics gain, then it should be distinguishable from U-238 when measured using single sided muon imaging with muon induced fission.
4. Experimental test: Measured low enriched uranium (LEU) and depleted uranium (DU) blocks with MMT and secondary detectors
5. Data analysis: The measured data suggests that by being sensitive to secondary neutrons, objects can be imaged from one side when imaging is performed in coincidence. Additionally, isotopic information can also be determined with some a priori knowledge (e.g. knowing that the cube is Uranium, but not its isotopes).
6. Peer review: Publications, team review, and review by sponsors of research

There were many additional questions to be asked of the capabilities of muon tomography, some of which are addressed in this dissertation. In general, muon tomography's sphere of influence can be grouped by application to include homeland security, treaty verification, reactor imaging, medical, geophysical, and archaeological. The team that I was involved with performed research primarily in the treaty verification, homeland security, and reactor imaging areas, however; we have also investigated medical imaging capabilities (Appendix C). Though each of these applications is quite different, there is a significant overlap in the experimental techniques. We needed to address several research questions to advance the applications. Is the rate of cosmic-ray flux adequate in order to image objects within a reasonable timeframe for vertical and near horizontal cases? Can the physical interactions of cosmic-ray muons in matter provide measurable data for material identification? Can cosmic-ray muons be detected with sufficient resolution and efficiency?

During the research for this dissertation, several ideas were hypothesized based upon the current understanding of the cosmic-ray muon tomography capabilities. Multiple scattering and single sided imaging, through the measurement of muon induced fission coincidence, can provide information on the material composition of the inspected object. The known cosmic-ray muon horizontal flux could be used to image the interior of thick and complex objects, e.g. a nuclear reactor. These topics, including their experimental measurements, simulations, analysis, and results, are discussed in further detail in the following chapters.

To study the advanced applications of muon tomography, an experimental detector, the MMT, was used to measure muon tracks that passed through objects, e.g. a LEU cube or a nuclear reactor at the University of New Mexico. The single sided imaging used neutron and gamma detectors for measurement of the secondary signals resulting from muon induced fission. Several objects were used in single side imaging mode including: a lead sphere, several lead bricks, an aluminum cylinder, several blocks of steel, a cube of depleted uranium, and a cube of 19.6% enriched uranium (19.6 % U-235/ 80.4 % U-238). In this thesis I focused on the results from the two uranium cubes. For horizontal reactor imaging, we used large concrete blocks and palettes of lead to imitate a mockup reactor and imaged the AGN-201m reactor at the University of New Mexico.

The Reconstruction of Cosmic-Ray Muon Tracks

The creation of cosmic-ray muon tracks was performed with a linear residual fitting routine known as the L1 fitter [62]. The L1 fitter performs a regression of points on a plane by summing the absolute difference between the fitted line and data. Its usage is similar to the well known L2 (least squares) fitting approach, but it is reduced to a linear difference model for suppressing outliers. Both the data and simulation use the L1 algorithm to construct tracks from hit and timing information obtained in the detectors. The primary difference between the data and simulation is the exclusion of time zero fitting in the simulations of the detectors. As the detectors are triggerless, temporal windows are used to group the hits in the measured data. A best fitted track with the lowest residual from a combination of tracking possibilities is computed from the windowed hits. The simulation avoids this issue by recording only the parent particle (a muon or electron), which is tracked from its origin to the end and does not follow secondary particles.

The track fitting is accomplished via a multi-step process. First, incoming and outgoing track information is compiled as two vectors. The tube number, drift time, and distance of closest approach to the tube's wire is stored in the vector for each tube hit in an event. The event is then filtered using the number of drift tube hits and whether they lie within a specified range. If either the number of hits exceeds a specified maximum or the number of activated layers is not achieved, the vector is cleared and the next event information is processed. Once these checks are completed, the event hits are separated into groups corresponding to the top and bottom modules of the MMT based upon the wire positions of the tubes.

The coarse tube fitting creates a track based upon the wire positions of the hit tubes in an event. The XZ and YZ wire planes are fitted independently, where Z is defined as the distance between two supermodules. An iterative process is used to fit the plane of wires, which results in a slope, intercept and L1 fit quality parameter, χ. The intercept position is a projection of that fitted line to a center plane of the detector. The line is chosen by minimization of the χ parameter. The projections are calculated for each of the 'hit' tubes, and the absolute difference is found for each pair and added to χ for every hit. A tracking "story" is created around each of the hit wires, thus the iterations are constrained to the number of hits. The coarse tube fitting results in a trajectory that includes the intercepts, the slopes, and the combined 'χ' for both the x- and y-directions.

After the coarse fitting, the exact fit is initiated. The main difference for the exact fit is the implementation of the drift and the ambiguities matrix. The drift variable is set as the distance of the hit from the center wire of the tube. A Gaussian blur is included to approximate uncertainties in the detector measurements. The ambiguities matrix is used to determine what side the muon passed through the tube. The rest of the fitting process is the same as coarse fitting, with the inclusion of the drift and ambiguities matrix.

We compute and track the hit tube ambiguities in a matrix. Within this ambiguities matrix, each tube fit sets the ambiguities as either 1 or -1, corresponding to the left or right side of the tube. The best track between two points is found using permutations of the hit location point. Each point is rotated around the wire location through all producible tracks, and the one with the least cumulative difference is selected. This least cumulative difference is defined as the summation of the differences between each tube's wire and the drift variable for every hit. Along the projected path, each 'hit' and corresponding 'tube' are identified. The orthogonal distance between the tube's wire and the track found with the drift variable are subtracted. These values are then summed to create the least cumulative difference. The three points within the event that have the lowest drift variable are used. Each possible combination of the three points is permutated, and the least cumulative difference track is located. The ambiguity of each hit is set to either 1 or -1, which is based upon the tracking scenario that has the least residual (least cumulative difference). This ambiguities vector is returned for use in the fine tube fitting.

After all trajectories are compiled for both the x- and y-directed tubes, the final track for each event is created. This is done for both the incoming track and outgoing track information. Once completed, the tracking program proceeds onto the next event. All 'in track' and 'out track' information for the events is stored in the output file in the form of position and direction vectors (direction cosines). The final result is a simulation output that can be compared with data.

Acquisition and Analysis of Data for Muon Tomography

The data in this dissertation was analyzed using image analysis tools along with statistical analysis packages and graphing programs. Several software packages were used for data analysis including: the open source object oriented mathematical toolkit ROOT, a LANL image analysis package NewDisplay [63], and Microsoft Excel. ROOT provided several useful features including: histogram analysis and non-linear, fast storage of data and simulation results. NewDisplay is image analysis software developed at LANL, originally for the proton radiography community. Excel was used for graphing muon trajectories, the output from image analysis projections, and error analysis.

The acquisition and analysis of the MMT data was done in a consistent manner. A hypothesized question was asked; for example, can muon induced photons be identified in coincidence with muon tracks that pass through uranium? The MMT would then be configured by placing uranium in the field of view and surrounding the MMT with sodium iodide detectors. The sodium iodide detectors would be connected to a data acquisition system designed to filter out background photons below 2 MeV. In general, this method was used for data acquisition during material identification purposes regardless of the secondary particle detector type or material that was inspected. At the end of this preparation, data was ready to be measured.

The MMT has a graphical user interface that enables automated run control. This was a useful feature as the data can be automatically separated into small chunks, typically on the order of hourly runs, and then added together during analysis. This method increased the reliability of the data acquisition in the event of occasional hardware failure, e.g. high voltage or low voltage power supplies tripping. A log book was used to record each run. An image of the data acquisition GUI is shown in Figure 18.

The result of a measurement is several ROOT files that contain hit and tracking information measured by the MMT and recorded from the secondary detectors. This data was separated into three file formats for data analysis: full trajectories, stopped trajectories, and secondary detector pulse times. The files were output in a comma separated value format and contained the time of the tracks and the track position and direction components. These values were then processed using software such as Excel or NewDisplay.

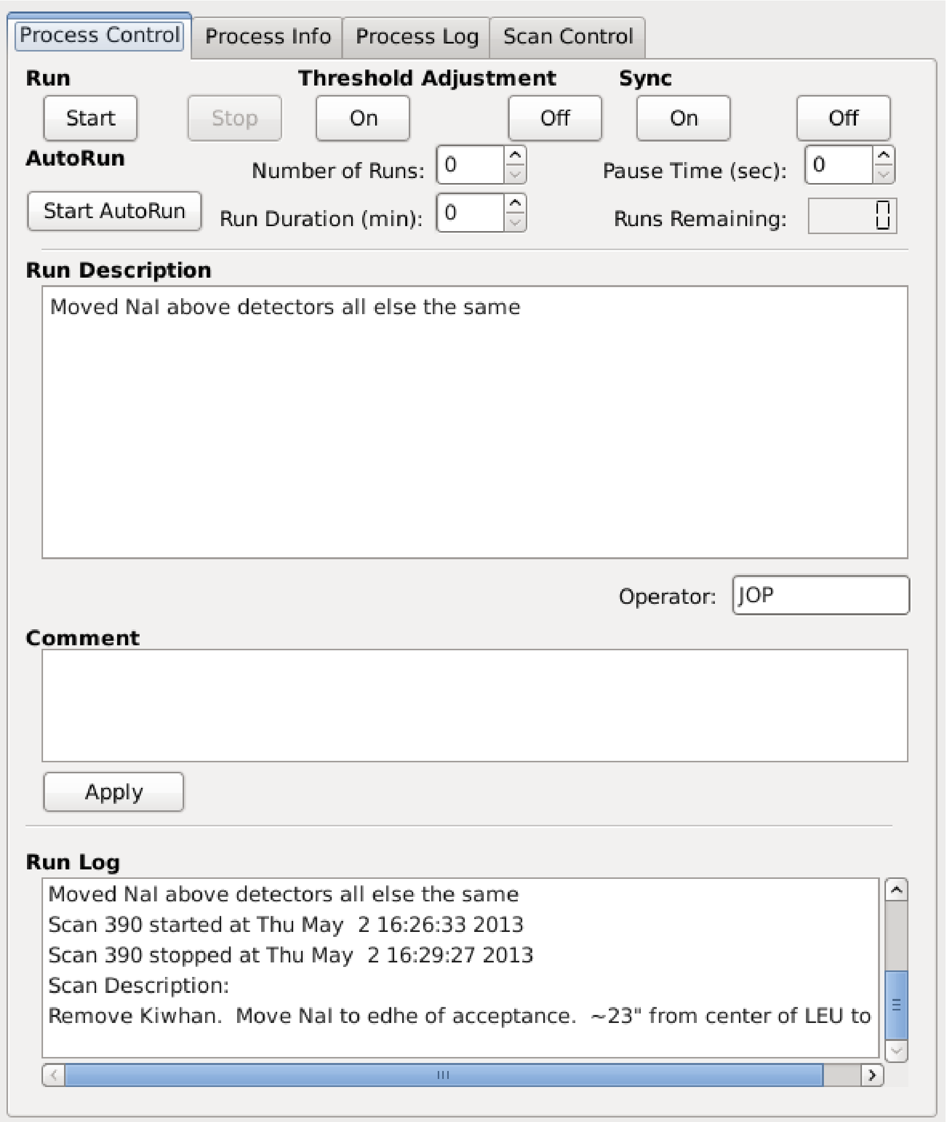

Number of Runs: 0

Pause Time (sec): 0

Run Duration (min): 0

Runs Remaining:

Run Description: Moved NaI above detectors all else the same

Operator: JOP

```
Moved NaI above detectors all else the same
Scan 390 started at Thu May  2 16:26:33 2013
Scan 390 stopped at Thu May  2 16:29:27 2013
Scan Description:
Remove Kiwhan.  Move NaI to edhe of acceptance.  ~23" from center of LEU to
```

Figure 18 – Run control GUI for the MMT. The GUI has several features including a log book, manual start and stop of data acquisition, automated run control, and system health monitoring features.

NewDisplay has many functions for image processing which are primarily oriented toward data analysis. With this software it is possible to open high resolution images and evaluate their contents one pixel at a time. Some of the functionality of this software includes: mathematical operations on images, batch mode image processing, selecting projections (referred to as lineouts), higher order operations such as Abel inversions, and simplified output that is formatted for use in Excel. An example of an image being processed in NewDisplay is shown in Figure 19. The muon induced secondary signals were paired with the stopped or passing muon tracks by using NewDisplay as well.

The final result of the data acquisition and analysis is a set of images and projections that show the behavior of muons passing through an object and the measurement of secondary signals in coincidence with those muons.

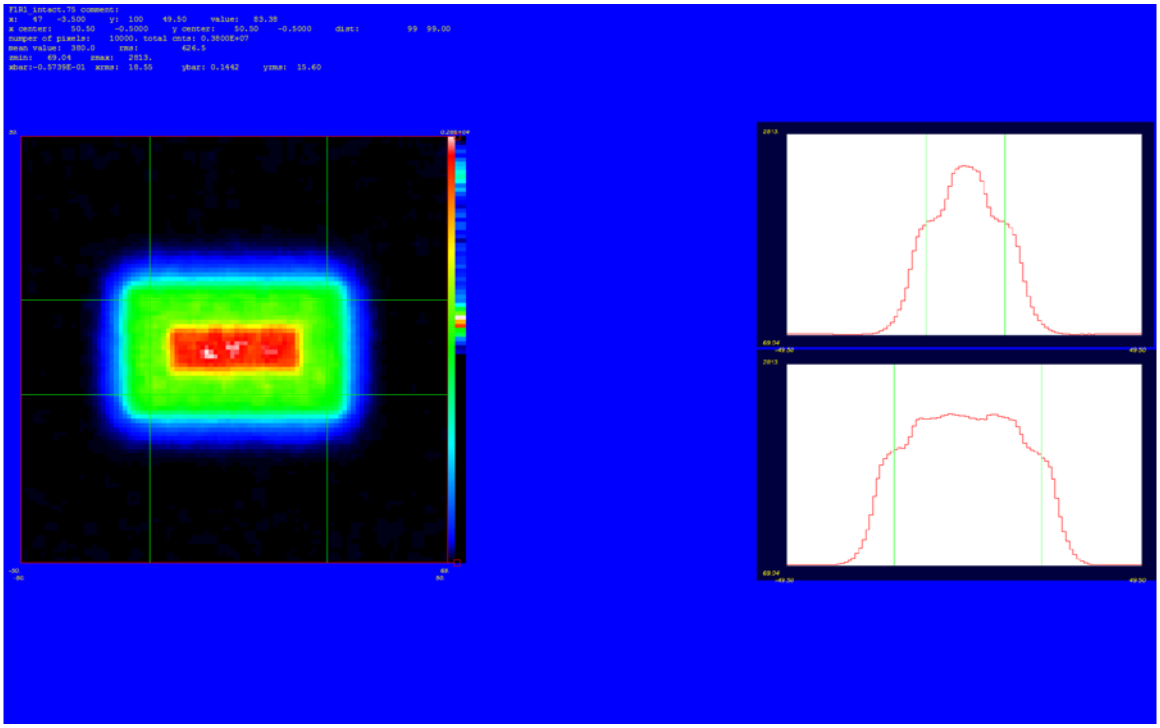

```
F1R1_intact.75 comment:
x:   47   -3.500      y:  100    49.50     value:   83.38
x center:     50.50    -0.5000      y center:     50.50    -0.5000     dist:          99  99.00
number of pixels:     10000. total cnts: 0.3800E+07
mean value:  380.0      rms:          626.5
zmin:   69.04     zmax:   2813.
xbar:-0.5739E-01  xrms:  18.55       ybar: 0.1442     yrms:  15.60
```

Figure 19 – NewDisplay image processing software. A piece of steel embedded in concrete is shown below. A lineout projection of the horizontal and vertical axis are included on the right. The values shown in the projection plots are averaged between the selected green lines.

MMT Detector Resolution

The spatial edge resolution of the MMT is measured by fitting the edge of two lead bricks that are separated by 5.1 cm. The lead brick dimensions are 20.7 cm x 10.2 cm x 5.1 cm with an uncertainty in physical measurement of 1 mm. Cosmic-ray muons passing through the lead bricks were measured for six hours. A multi-group multiple scattering image reconstruction was performed to obtain the edge lineout projections for each brick. The image was reconstructed with a pixel size of 2 mm and using the nearest neighboring pixels for the image smoothing. The pixel size was studied by comparing edge resolution by using several pixel sizes ranging from 2 mm – 2 cm with and without neighboring pixels. I concluded that the pixel size and selection of neighbors did not have a significant impact on the edge resolution provided that the count statistics in a voxel were sufficient. Six of the edges, forgoing the two edges in the center, were used to compute the average of the resolution and its error by using the method of replicate trials [64]. Figure 20 displays the image reconstruction of the lead bricks and the average line projections that are selected.

Several projections are taken through the bricks for computing the average edge resolution. The following edges are labeled and shown in Figure 21. Each edge measurement spans a nine centimeter range and has an offset subtracted to align the edges on the same plot. Edges B, C, and D are flipped for plotting purposes.

The computation of the edge resolution of the lead bricks is accomplished by fitting the edge. Here the edge is defined as a convolution between a step function and a Gaussian with some width. The width of the Gaussian is determined by using a non-linear least squares model. The model minimizes the χ^2 between the data and the fit which is well characterized by an error function. The fitting algorithm includes the three components of the Gaussian, the amplitude A, the mean x_0, and the width σ.

$$\mathrm{erf}(x, x_0, A, \sigma) = A\int_{x_0-x}^{x_0+x} e^{-\frac{(x-x_0)^2}{2\sigma^2}}dx \qquad \text{eq. 24}$$

The fit of the edge is computed by varying the Gaussian variables for the edge in two pieces, to the left of the mean and to the right of the mean. These pieces, which are solved simultaneously, form the two equations used in the non-linear least squares solver. A baseline variable, b, is also included.

$$y_L = \mathrm{erf}(x_L, x_0, A_L, \sigma_L) + b_L, \text{ where } x_L \leq x_0 \qquad \text{eq. 25}$$

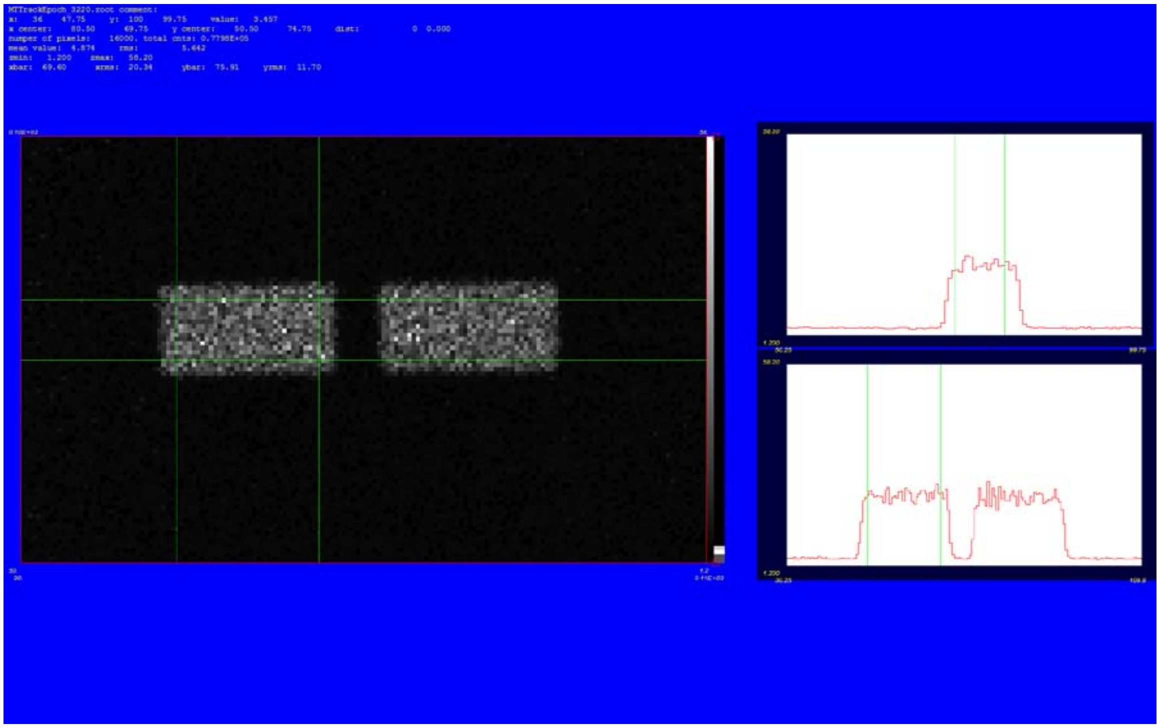

```
MTTrackEpoch 3220.root comment:
x:   36    47.75     y:  100     99.75     value:   3.457
x center:    80.50       69.75      y center:    50.50       74.75     dist:            0  0.000
number of pixels:    16000. total cnts: 0.7798E+05
mean value:  4.874     rms:          5.642
zmin:   1.200    zmax:   58.20
xbar:  69.60      xrms:  20.34      ybar:  75.91     yrms:  11.70
```

Figure 20 - Image reconstruction of two lead bricks using a multigroup algorithm for scattering angle analysis. The edges of these two lead bricks are used to compute the spatial resolution. This image is shown in 5mm pixel sizes for visual purposes only. The plots on the right side are the average projections of the x and y plane which are bounded by the green lines.

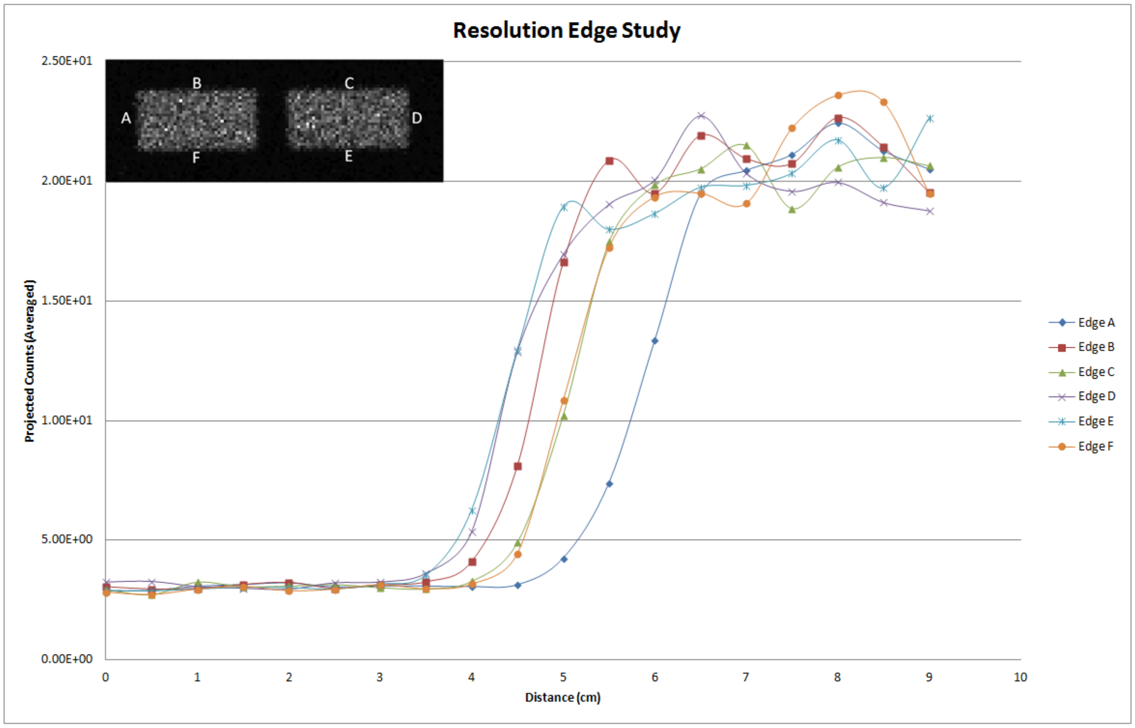

Figure 21 - A plot of the six edges used to measure spatial resolution using two lead bricks. The edges are analyzed with a fitting algorithm designed to compute the Gaussian width of an edge.

$$y_R = \mathrm{erf}(x_R, x_0, A_R, \sigma_R) + b_R, \text{ where } x_R \geq x_0 \qquad \text{eq. 26}$$

The results are two Gaussian widths which represent the edge resolution of the MMT. In this case, the Gaussian widths are forced to be equal during the fitting process to produce a smooth and continuous fit. This width, σ, is used for reporting spatial resolution.

$$\sigma_R = \sigma_L = \sigma \qquad \text{eq. 27}$$

An example of the fitting, for Edge B and Edge F, is shown in Figure 22. The green curve represents the data obtained by taking a projection of the lead brick which bounds Edge F and Edge B. The left curve is the resulting fit of the Edge F and the right curve is the fit of Edge B. This procedure was repeated for the other four edges: A, C, D, and E. The method of replicate trials is used to compute the error. The results are shown in Table 2 which includes the spatial edge resolution of the MMT measured with this method. The full width at half maximum is also computed. However, our convention is to define spatial resolution using σ.

$$FWHM = 2\sqrt{2\ln 2}\,\sigma \approx 2.35482\,\sigma \qquad \text{eq. 28}$$

The following equations are used for the statistical analysis shown in Table 2 including the mean, standard deviation, and standard deviation of the mean (SDOM).

$$\bar{x} = \frac{1}{N}\sum_{i=1}^{N} x_i \qquad \text{eq. 29}$$

$$\sigma_x = \sqrt{\frac{1}{N-1}\sum (x_i - \bar{x})^2} \qquad \text{eq. 30}$$

$$SDOM = \sigma_{\bar{x}} = \frac{\sigma_x}{\sqrt{N}} \qquad \text{eq. 31}$$

The final result of the averaged spatial resolution for the MMT using the lead bricks is $0.63 \pm 0.02\ cm$.

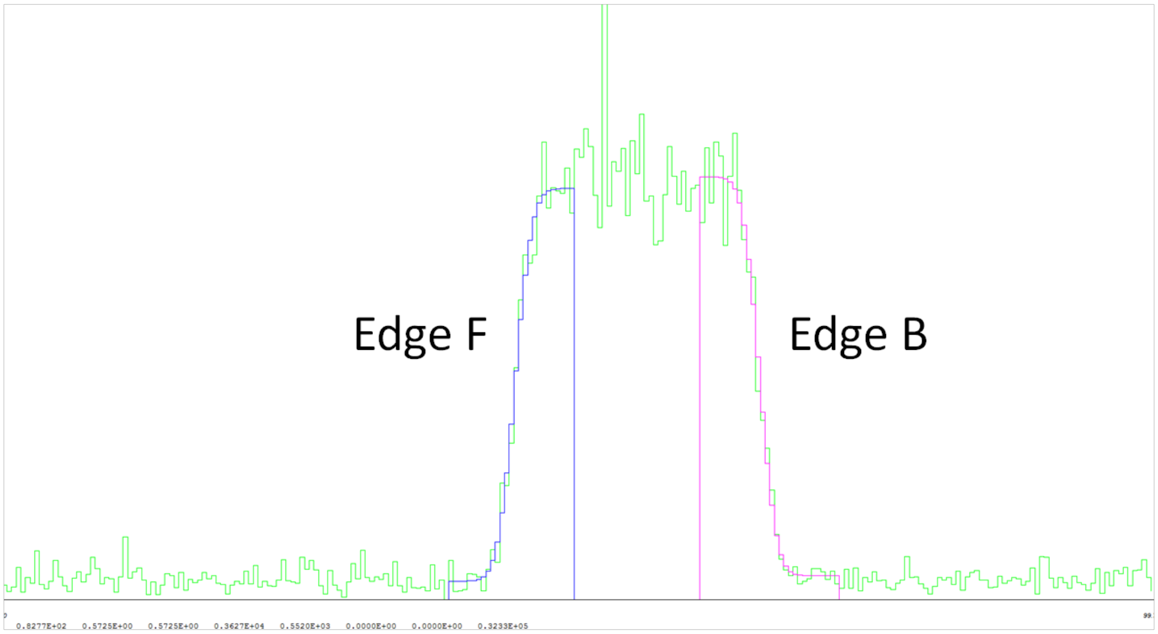

Figure 22 - An edge fitting of the lead brick data. The Edge F (left edge) and Edge B (right edge) are fitted using the error function and varying Gaussian parameters. This function is input into a least squares minimization function to obtain the best fit to data.

	Edge A	Edge B	Edge C	Edge D	Edge E	Edge F	MEAN	StdDev	SDOM
Edge Resolution (cm)	0.722	0.5725	0.6752	0.5942	0.6225	0.5843	0.62845	0.058695	0.023962
FWHM (cm)	1.70018	1.348134	1.589974	1.399234	1.465875	1.375921	1.479887	0.138215	0.056426

Table 2 - Spatial resolution of six edges obtained by measuring muons passing through two lead bricks. The spatial resolution is averaged and an error analysis is performed by using method of replicate trials. The average spatial resolution is 0.63 cm.

The measurement of an edge resolution from a brick, or any other parallelepiped type of geometry has limitations due to the different lengths of muon trajectories that pass near the edge, adding a component of resolution blur. This effect can be removed by performing a resolution study in 1-dimension on a spherical object with the assistance of a regularized Abel inversion. The Abel inversion will be discussed in more detail in Chapter 7, pg. 102.

The advantage of using a sphere is that the distance of closest approach for the track can be used to determine the edge resolution. When the distance of closest approach is used, the muon trajectory passes through the same amount of material regardless of an incident angle (assuming that the muon is sufficiently high in momentum). An Abel inversion is then applied to compute the varying path lengths expected through the sphere and to determine the proper radiation length for a given path length in volumetric space. Thus, the best possible spatial resolution that is obtainable in the MMT is determined from a sphere. Both the lead bricks and sphere provide a useful perspective on the overall spatial resolution that is possible with muon tomography using our current algorithms. Some objects are not spherically symmetric, thus the more conservative value can also be used across many applications for the MMT.

Figure 23 shows that for a spherical cross-section, any muon passing through the sphere has the same distance of closest approach per given track length. An Abel inversion in one dimension is used to obtain path lengths per radiation length from the scattering information in each voxel. This method is performed across the whole spherical domain and a one dimensional plot is obtained. The analysis of the edge resolution is performed similar to that of the lead bricks in the previous section. In order to compute the uncertainty, the method of replicate trials is used.

A lead spherical shell was measured with the MMT to study the spatial resolution of the system. The inside of the sphere is hollow with a diameter of 62 mm and the lead shell has an outer diameter of 202 mm. These measurements were made with an uncertainty of 1 mm. The lead sphere was imaged for 90 hours which yielded 21.31 million muon tracks. Figure 24 displays the lead sphere in two planes which are used to determine the center of the object.

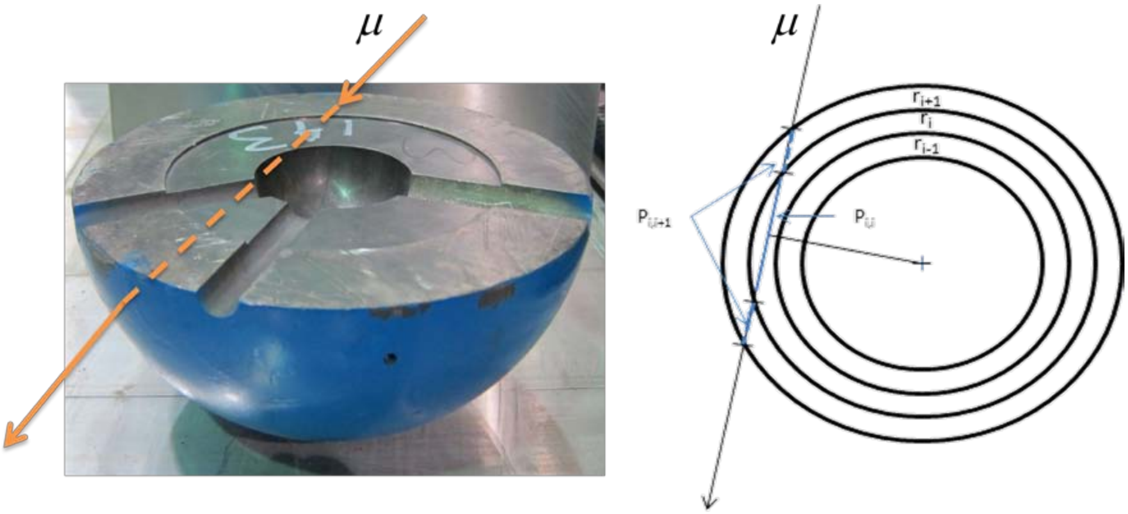

Figure 23 - The figure on the left depicts a muon passing through a hemisphere of the lead spherical shell. On the right is a cross-section illustration of a muon passing through the shell. Path lengths corresponding to the muons trajectory as a function of shell radius are labeled. These path lengths are used for the reconstruction of the 1 dimensional image using an Abel inversion.

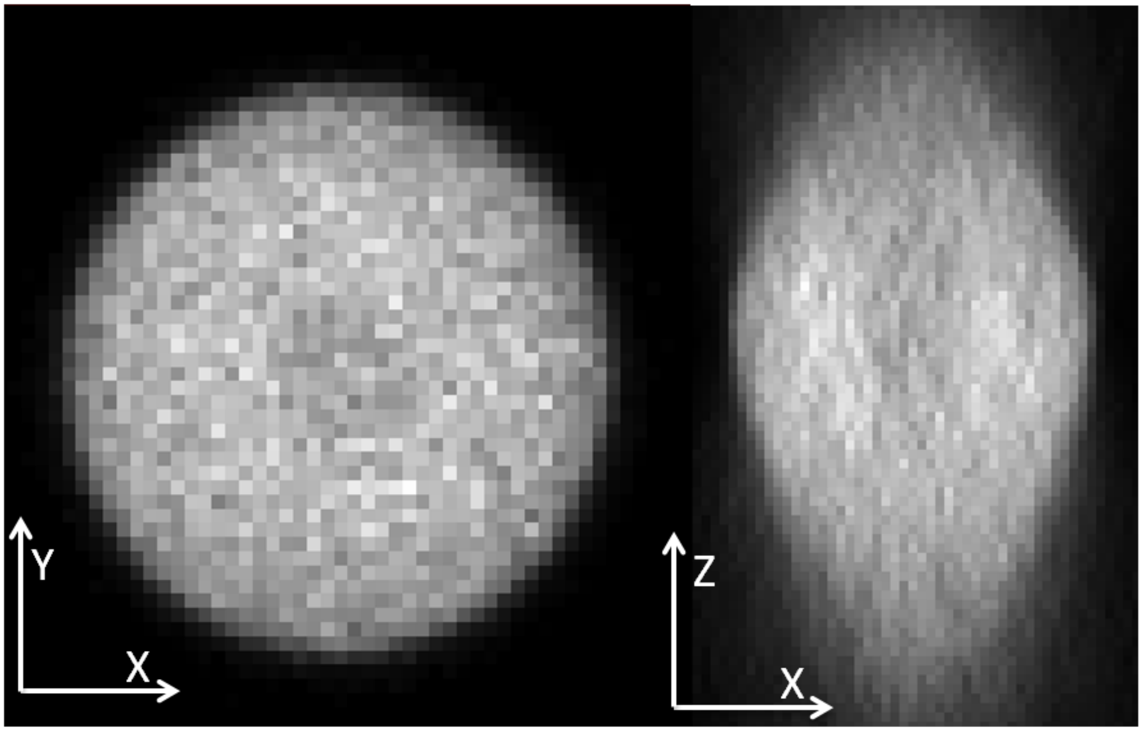

Figure 24 - XY and XZ reconstructions of a lead sphere using a multigroup algorithm to treat the scattering angle analysis. The two images are used to find the center of the sphere to perform the 1 dimensional sphere reconstruction. The image on the right shows that there is some stretching of the image along the Z axis. This is due to vertical blur effects during image reconstruction, as the cosmic-ray muon flux is not measured in this view directly.

Figure 25 shows the Abel inversion, with a small regularization factor, of the 1-dimensional reconstruction of the sphere. The edge resolution is computed with a non-linear least squares analysis of the error function with Gaussian parameters that represent the edge. Each section of the edge analysis corresponds to $1/9^{th}$ of the total data (10 hours, 2.37 million tracks). The nine separate lead sphere runs are reconstructed in one dimension using 2 mm voxels. Each run consisted of ten hours of data. The resolution width, σ, is tabulated for each of the nine runs and the method of replicate trials is used to compute the error. The results for the resolution from using a sphere are shown in Table 3. The mean of the spatial resolution is $0.30 \pm 0.01\ cm$.

The resolution of the MMT has been empirically determined with two measurements. The first measurement involved using lead bricks that returned an edge resolution of $0.63 \pm 0.02\ cm$. This resolution is larger and conservative compared to the lead sphere analysis. The resolution obtained by using a lead sphere was a factor of two better, $0.30 \pm 0.01\ cm$. This is because the spherical symmetry and straight muon tracks enable the computation of track length as a function of radius. This allows for conversion from areal radiation lengths to volumetric (radial shell based) radiation lengths. One conclusion is that an improved tomographic reconstruction algorithm is needed in order to accurately resolve edges of parallel-piped objects. With this improved algorithm, the resolution of the lead bricks would then approach that of the sphere.

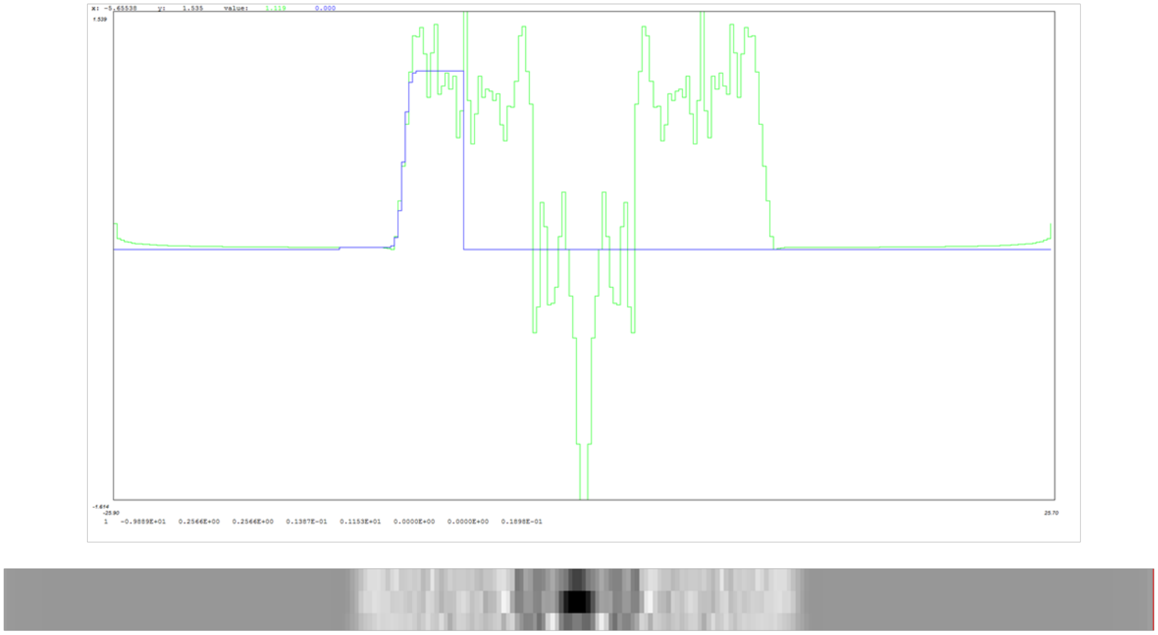

Figure 25 - Lead sphere resolution analysis of an edge with the associated Abel inversion shown below. The Abel inversion is performed on the one-dimensional projection of 10 hours of lead data. There are three layers to the Abel inversion image. These layers, from bottom to top, refer to data obtained from the incident muon tracks, the outgoing/scattered muon tracks, and an average of the two.

	Edge 1	Edge 2	Edge 3	Edge 4	Edge 5	Edge 6	Edge 7	Edge 8	Edge 9	MEAN	StdDev	SDOM
Edge Resolution (cm)	0.2566	0.2945	0.3005	0.3407	0.2744	0.2708	0.2982	0.3043	0.3597	0.299967	0.03291	0.01097
FWHM (cm)	0.604247	0.693494	0.707623	0.802287	0.646163	0.637685	0.702207	0.716572	0.847029	0.706368	0.077496	0.025832

Table 3 - Tabulation of spatial resolution values from measuring the edge of a lead sphere. An Abel inversion is performed to obtain the volumetric radiation length of the edge. The mean spatial resolution of the MMT is 0.3 cm. This is the best value for edge resolution obtainable through analysis of spherical symmetry.

CHAPTER 6

Simulation and Modeling of the MMT

The simulations in this dissertation are created using the Geant4 [31] toolkit, developed at CERN for the simulation of the passage of particles through matter. High statistics simulations are computed on a 64 processor Xeon X7560 monolithic server. Parallelization is done at an individual event level and implemented via explicit message passing (MPI). As the number of primary events is several orders of magnitude greater than the number of processing cores, load balancing is trivially achieved. In order to speed up calculations, secondary particles produced from interactions of primary muons were ignored. Typical simulation runs are performed on 50 cores, and it took approximately a day of computational time to simulate 500 million muon tracks -- 10 million events per core -- during the periods when the server was lightly loaded.

A model of the MMT was created and used to study the effect of detector scattering and other parameters that impact the resolution of reconstructed images. These parameters include detector blur effects and the cosmic-ray muon source. The cosmic-ray muon source used in the Geant4 simulations is modeled from sea-level data that is then extrapolated to Los Alamos's altitude. The cosmic-ray electron flux, primarily below 1 GeV, is also included, which affects the ratio of low angle scattering to high angle scattering. The electron flux causes large angle scattering and increases the tail in the scattering angle distributions, mostly above 50 mrad. The MMT drift tube calibration and detector hardware effects have a significant impact on the resolution of the muon tomography. The sum of these effects is reproduced in simulation by adding a Gaussian blur term to the track fitting of the simulation output.

The Geant4 implementation of the MMT geometry is in XML format, also known as Geometry Description Markup Language, or GDML. The model is modular, which is useful for geometric parameter studies, e.g. changing the aluminum drift tubes to carbon fiber to study detector scattering effects. The geometry was simplified, reducing the drift tubes to two pieces each (an inner gas cavity and a cylindrical shell wall). Several aluminum structural components were included to better model the effects of the scattering from the aluminum structural geometry. Finally, the wooden platform that the imaged objects sat upon was included as well. The final model geometry is shown in Figure 26.

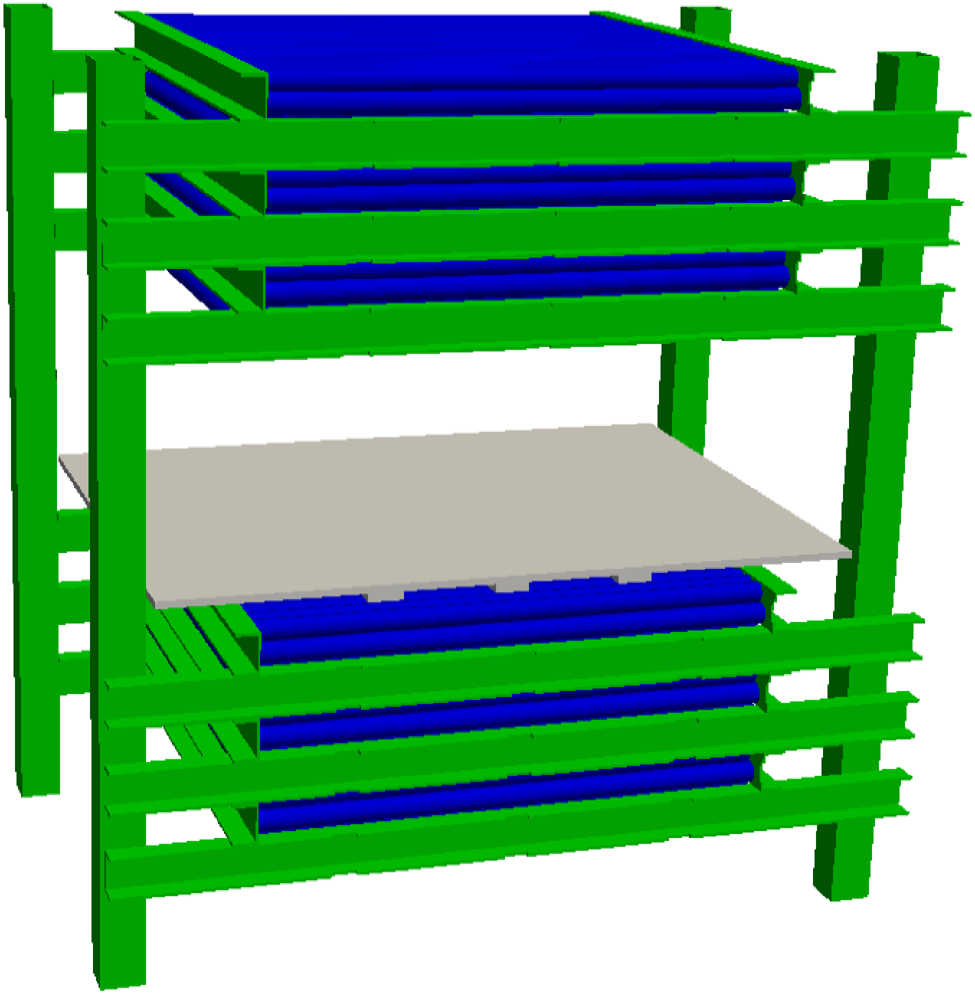

Figure 26 – Modeled MMT geometry for use in Geant4 simulations. This model contains 576 drift tubes that are simplified as a cylindrical shell filled with a gas cavity. Other support structure is included to mock up additional sources of detector scattering. The wooden platform, used to place objects in the MMT without damaging the drift tubes, is also included.

The method of tracking performed in the simulation was designed to reproduce the experimental process of obtaining muon hit information and converting hits into tracks. ROOT was used to store individual tube hit information in the simulation per event. The end result was a collection of events in a data stream where any given event contained a series of tube indices and corresponding distances of closest approach to the tubes' centers (wire locations). This was accomplished by constructing a vector from the muon as it passed through each particular tube shown previously in Figure 13. The distance of closest approach (DOCA) was computed for each simulated hit and was passed into the track reconstruction software.

$$\vec{c} = \overrightarrow{v_W} \times \overrightarrow{v_\mu} \qquad \text{eq. 32}$$

For a simulated hit, there were two direction vectors, the normalized muon vector $\overrightarrow{v_\mu}$ and the normalized wire vector of the tube $\overrightarrow{v_W}$.

$$t_2 = \frac{\vec{c} \cdot \overrightarrow{P_W}}{|\vec{c}|} \qquad \text{eq. 33}$$

$$t_1 = \frac{\vec{c} \cdot \overrightarrow{P_\mu}}{|\vec{c}|} \qquad \text{eq. 34}$$

A point on the muon vector is notated as $\overrightarrow{P_\mu}$, and a point on the wire vector is notated as $\overrightarrow{P_W}$.

$$D = |t_2 - t_1| \qquad \text{eq. 35}$$

The DOCA, D, is defined as the absolute difference between the projections of the wire vector and the muon track vector on the plane that is normal to both of these vectors.

The scattering angle distributions of a bare field of view were compared for the reconstructed data and simulations. Track fitting of both the data and the simulation was performed with the same method, the L1 trajectory fit as described in pg. 47 of Chapter 5. The fit of the simulation results excluded a component of the fitting algorithm, time zero, which is present in the track reconstruction algorithm for the data stream. This is because the simulation's tracks are recorded in increasing time from the origin of the thrown event. We did not study other effects involving generating random noise in the simulation for this work, which affects data measurements due to external background. We focus instead on the understanding of intrinsic MMT detector resolution.

The Cosmic-Ray Muon Momentum Distribution at Los Alamos

In order to extend the well-known cosmic-ray muon momentum spectrum at sea level to higher altitudes, two separate extrapolation methods were investigated. The known sea-level data for the momentum and total flux distributions of cosmic-ray muons [47, 48] were extrapolated to cover a range of approximately 10 MeV to 100 TeV. This distribution was then modified to generate the high altitude muon momentum spectrum. First, the muon momentum was converted to kinetic energy through the energy-momentum relation:

$$T_\mu = \sqrt{\left(p_\mu^2 + m_\mu^2\right)} - m_\mu \qquad \text{eq. 36}$$

where T_μ is the muon kinetic energy, $m_\mu = 105.7\ MeV/c^2$ is the rest mass of the muon, and p_μ is the muon momentum.

In the first method, linear extrapolation was used to extend the distribution of cosmic-ray muon kinetic energies to higher altitudes. This linear extrapolation formula is:

$$T = T_0 + \frac{\frac{dE}{dx_L}\left(E_U - T_0\right) + \frac{dE}{dx_U}\left(T_0 - E_L\right)}{\Delta E} \cdot \frac{\rho_{air}}{\cos\left(\theta\right)} \qquad \text{eq. 37}$$

Where $\frac{dE}{dx_L}$ and $\frac{dE}{dx_U}$, correspond to the energy loss values of the upper and lower energy bin, E_U and E_L. The cosine term accounts for the angles used in the sea level data [47, 48]. From the incremented kinetic energy, the muon intensity was found, with the following equation:

$$I(GeV^{-1}) = \frac{I_0(GeV^{-1})}{\frac{\Delta E_0}{\Delta E}\, e^{-(0.1)/(6.2*E*cos(\theta))}} \qquad \text{eq. 38}$$

Where ΔE_0 is the change in energy from the previous altitude, ΔE is the change in energy at the next altitude step, E is the final energy at the new altitude. This initial method is useful in the high energy region and shows promise with fitting high-energy spectrum behavior, but it fails in the low energy region when energy losses become larger than energy bin size. We used therefore a different method to extend the muon spectrum to Los Alamos altitude.

The second method begins with the same sea level data set [47, 48]. Again, the input momentum is converted to kinetic energy with the momentum-energy relation (eq. 36). The sea level data is fitted with a high order polynomial of logarithms. The intensity in units of inverse energy is then computed for each energy bin. A correction term was applied to account for differences in altitude between sea level and Los Alamos:

$$C_f = \frac{1}{e^{\left(\frac{T+0.1}{m}\cdot\frac{tc}{h}\right)}} \qquad \text{eq. 39}$$

Where *m* is the muon mass, *h* is the height correction for the desired altitude, and *tc* is the relativistic time correction for muon flight. This corrected intensity was then used as our muon source for simulations at Los Alamos altitude. The cosmic-ray muon momentum spectrum for Los Alamos altitude and sea level is shown in Figure 27.

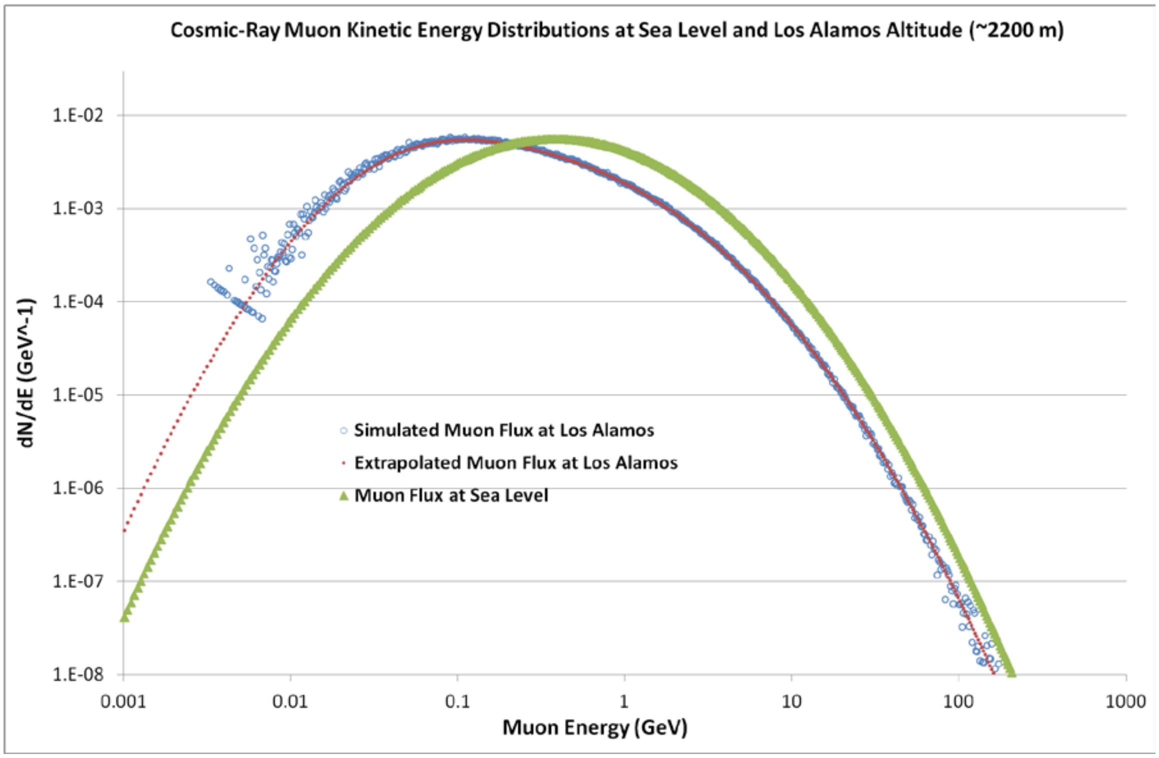

Figure 27 – Cosmic-ray muon flux at two altitudes, sea level and Los Alamos (~2200 m). The muon flux at sea level was obtained by combining two data sets [47, 48] with some additional extrapolation. The muon flux at ~2200 m was obtained with a model applied to the sea level data set to account for energy loss and muon lifetime.

Bare Simulation of the MMT with the Los Alamos Muon Momentum Spectrum

A bare field of view was measured with the MMT, and simulations were performed using the MMT model in Geant4. Both simulation and measurements contained the wooden platform and aluminum drift tubes. The cosmic-ray simulation source was used to generate muons with a momentum distribution corresponding to the extrapolation model used for Los Alamos altitude as described above. The angular distribution of the cosmic-ray muons was computed using the Reyna model. When comparing the simulations with data, there are several differences that are attributed to the cosmic-ray muon source generator and the track fitting algorithm. The following analysis shows that by softening the cosmic-ray momentum spectrum, including electron flux, and implementing a blur component in the track fitting, the simulated cosmic-ray source adequately models the cosmic-ray background.

The bare field data was measured for six hours with the MMT. A full-sky simulation in Geant4 was used to evolve a total of 20 million cosmic-ray muons and electrons and provide simulated tracks for comparison with the data. All simulations were normalized by the same value, derived from matching the peak of the scattering angle distribution of the 900 micron blur tracks to the data. This blur is attributed to several sources including: drift tube resolution (~400 microns), calibration issues, poor performance of a few individual tubes, noise, and time zero fitting. There are two notable regions in the scattering angle distributions, a shoulder and a tail (see Figure 28). This indicates that some tracks are being poorly fit, causing both blur and the resulting scattering angle shoulder. This is reproduced by adding random Gaussian blur during the simulated muon trajectory reconstructions.

The cosmic-ray muon track reconstructions were blurred during the track fitting process to add Gaussian randomness to the distance of closest approach for each simulated drift tube hit. We studied the shoulder by varying the σ (width) of the Gaussian component from 0 up to 900 microns. Several sets of scattering angle reconstructions with different σ are shown alongside the data in Figure 28. As blur increases, the shoulder's center shifts and the FWHM widens. The scattering angle histogram is displayed in the corner of this figure, showing a difference in the tail between data and simulation. The tail of the data and simulation is composed of large angle scattering events caused primarily by electrons and soft

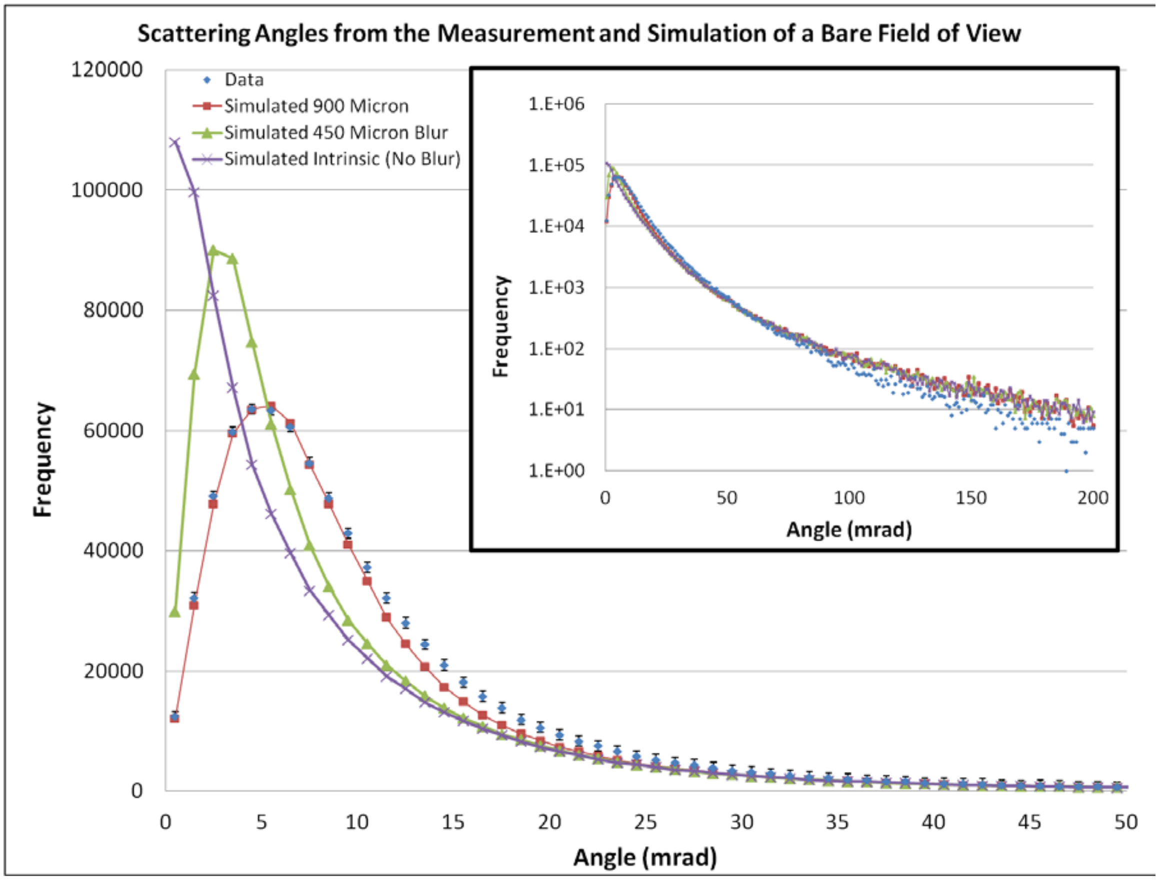

Figure 28 - A comparison of scattering angle distributions from data and simulation. The incident and outgoing cosmic-ray muons pass through an empty field of view in the MMT in all cases. Two features are noticeable; a shoulder below 10 mrad and a tail on the larger scattering angles. The shoulder is due to uncertainties found in the measurement and forced in the simulation during muon trajectory reconstruction. The tail indicates that there are more soft scattering events in the data which is associated with spectral differences in the cosmic-ray muon flux. A Gaussian blur is used to modify the simulated intrinsic tracks creating the shoulder seen in the data.

muons. The impact of the large angle scattering tail is minimal; as it is several orders of magnitude below the majority of the scattering events, which are below 20 mrad.

A random Gaussian blur with $\sigma = 900\ \mu m$, adequately models this “shoulder” effect. The scattering angle distribution of the simulated tracks with this blur component is compared with the data in Figure 29. The error bars are computed with the standard error model. The relative difference is included showing a maximum difference between simulation and data of ~23 percent below 50 mrad. Thus, we can conclude that we are able to model the MMT with sufficient accuracy in GEANT4.

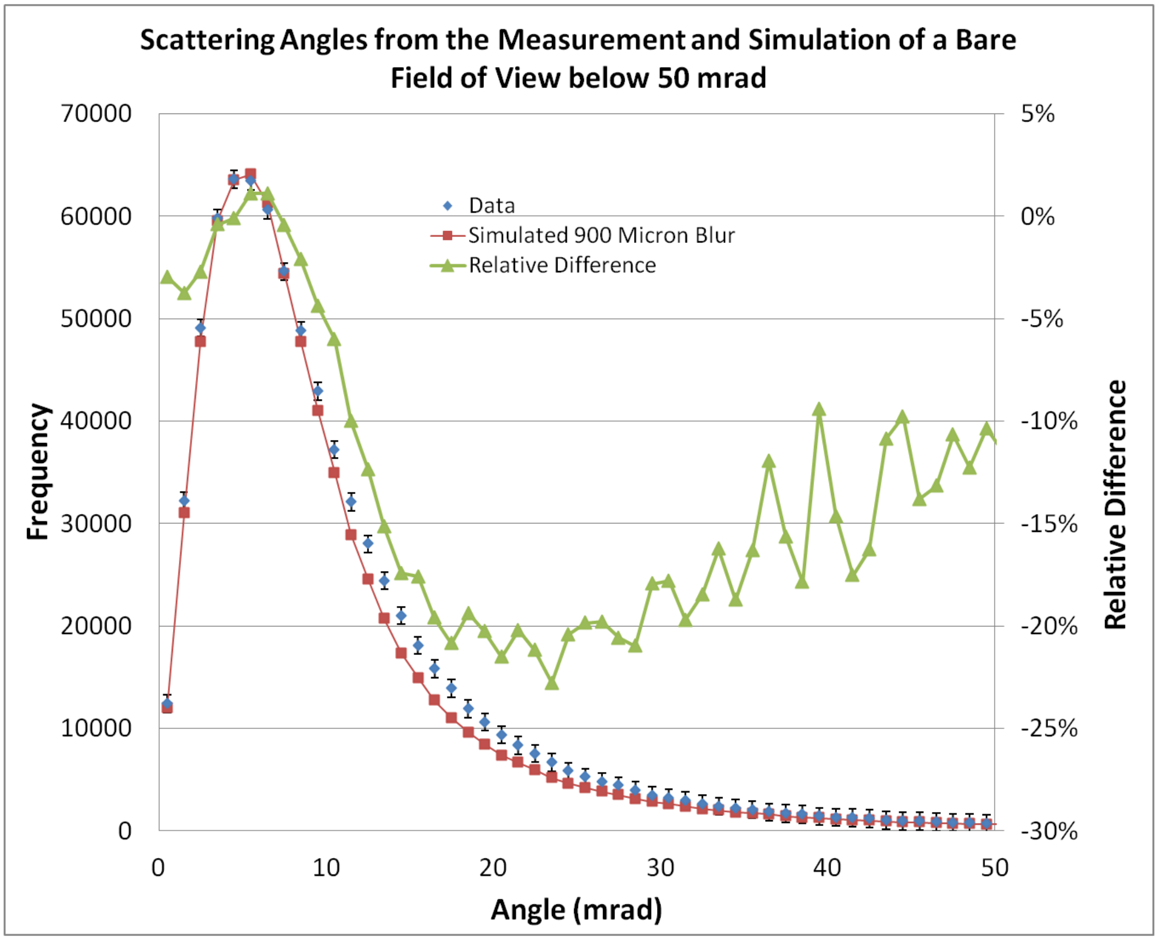

Figure 29 - Cosmic-ray muon scattering angle comparison between data and a simulation blurred with a Gaussian hit uncertainty of $\sigma = 900\ \mu m$. The relative difference is included showing a maximum difference between simulation and data of ~23 percent below 50 mrad.

CHAPTER 7

Reactor Imaging Overview

Muon tomography is a capable technology for imaging objects of different size and material atomic number, Z, which are found in commercial nuclear reactors. A series of experiments and simulations have been undertaken in order to prove the capabilities of muons in nuclear reactor environments. The University of New Mexico Research Reactor measurements uncover the challenges of muon tomography taken in remote environments with external radiation fields. Muon tomography measurements of the UNMRR prove the capabilities of muon tomography for imaging high Z and low Z materials in the same field of view.

A proof of principle experiment was performed at LANL by using the MMT to measure objects in a configuration that utilizes cosmic-ray muons incident from the horizon, also known as horizontal flux. A mockup reactor structure was built out of lead and was surrounded by several meters of concrete blocks. Horizontal muon tomography was accomplished by measuring the incident and exiting muon trajectories. By using the multiple scattering technique, the tomographs of the mock reactor were reconstructed. The experimental results suggested that the horizontal imaging, through the analysis of cosmic-ray muon multiple scattering, would be useful for reactor imaging, e.g. at Fukushima Daiichi. Following this experiment, several simulations, using Geant4, modeled the scenario of deploying a muon tomography system at Fukushima. The results of these simulations confirmed that cosmic-ray muons are a useful probe for imaging the damaged nuclear reactor core. The next step in studying the capability of horizontal cosmic-ray muon radiography was to deploy the MMT at a nuclear reactor, the UNMRR, and validate the Geant4 simulation models with experimental data. The results of this work at the UNMRR validate our models and reconstruction technique. This is the first time that a nuclear reactor has been imaged by measuring the cosmic-ray muon multiple scattering.

Mock Reactor Experiment and Simulation

The reactor mockup tests were performed at LANL to prove the principle of "reactor tomography" and to optimize our muon tomography algorithm to image a reactor core through thick concrete walls [65]. It was a new challenge because the existing muon tomography technique uses downward-going (vertical) muons to study systems with small localized scatterers. This is not the scenario for reactor style imaging, as the flux is more horizontal in nature due to detector placement. As was discussed earlier, the muon flux and energy spectrum are not isotropic: the incident flux of cosmic-ray muons is greatest in the vertical orientation, but the flux of horizontal-going muons is also significant above 1-GeV energy. It is these horizontal-going muons that are well suited to the geometry required for making an image of the uranium inside the pressure vessel of the reactors. A near-horizontal muon loses about 5-GeV when penetrating through a reactor as shown in Table 4.

In our demonstration, we measured cosmic-ray muons passing through a physical arrangement of material similar to a nuclear reactor, with thick concrete shielding and a heavy metal core as shown in Figure 30. Approximately five tons of lead were used to construct a mockup core that is similar to a boiling water reactor (BWR) of the type installed at the Fukushima Daiichi plant. The concrete shielding of the primary containment, which is about 3 m thick, was also part of the experimental mock-up geometry. In terms of scattering length, 0.7 m of lead is equivalent to the uranium fuel in a reactor core (120 radiation lengths), however; the uranium core would be easier to image than the lead target with the muon tomography technique because of larger atomic number.

The reactor mock-up experiment ran for three months continuously. Several configurations of lead block reactor mock-ups were chosen including a full stack of lead bricks and a stack with a conical void. Muon tracks were measured for between 10 to 20 days for the different mock-up scenarios, and the resulting outputs were reconstructed into images. The results of the reconstruction proved that it would be possible to deploy a muon tomography system at a commercial plant or at the Fukushima cleanup site such as in the following example configuration shown in Figure 31.

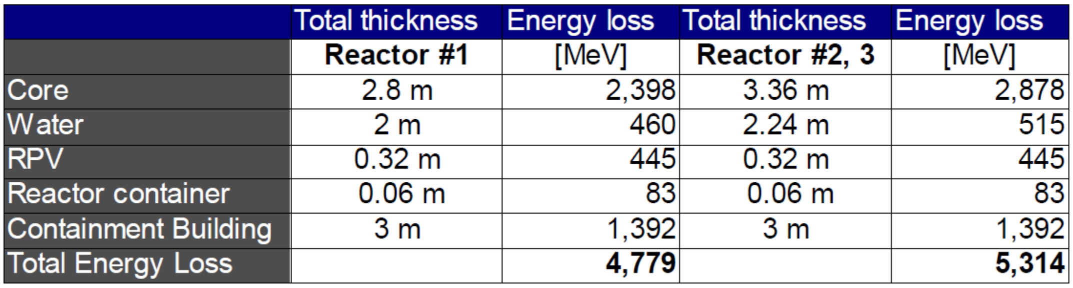

	Total thickness	Energy loss	Total thickness	Energy loss
	Reactor #1	[MeV]	**Reactor #2, 3**	[MeV]
Core	2.8 m	2,398	3.36 m	2,878
Water	2 m	460	2.24 m	515
RPV	0.32 m	445	0.32 m	445
Reactor container	0.06 m	83	0.06 m	83
Containment Building	3 m	1,392	3 m	1,392
Total Energy Loss		**4,779**		**5,314**

Table 4 – Muon energy loss by reactors for a horizontal muon. Energy loss (dE/dx) at 3 GeV was used for the estimation. A mixture of UO_2, Zr, and H_2O with each component assumed to have an average density of 2.6, 2.01, and 0.6 g/cm^3 over the volume of the core assembly.

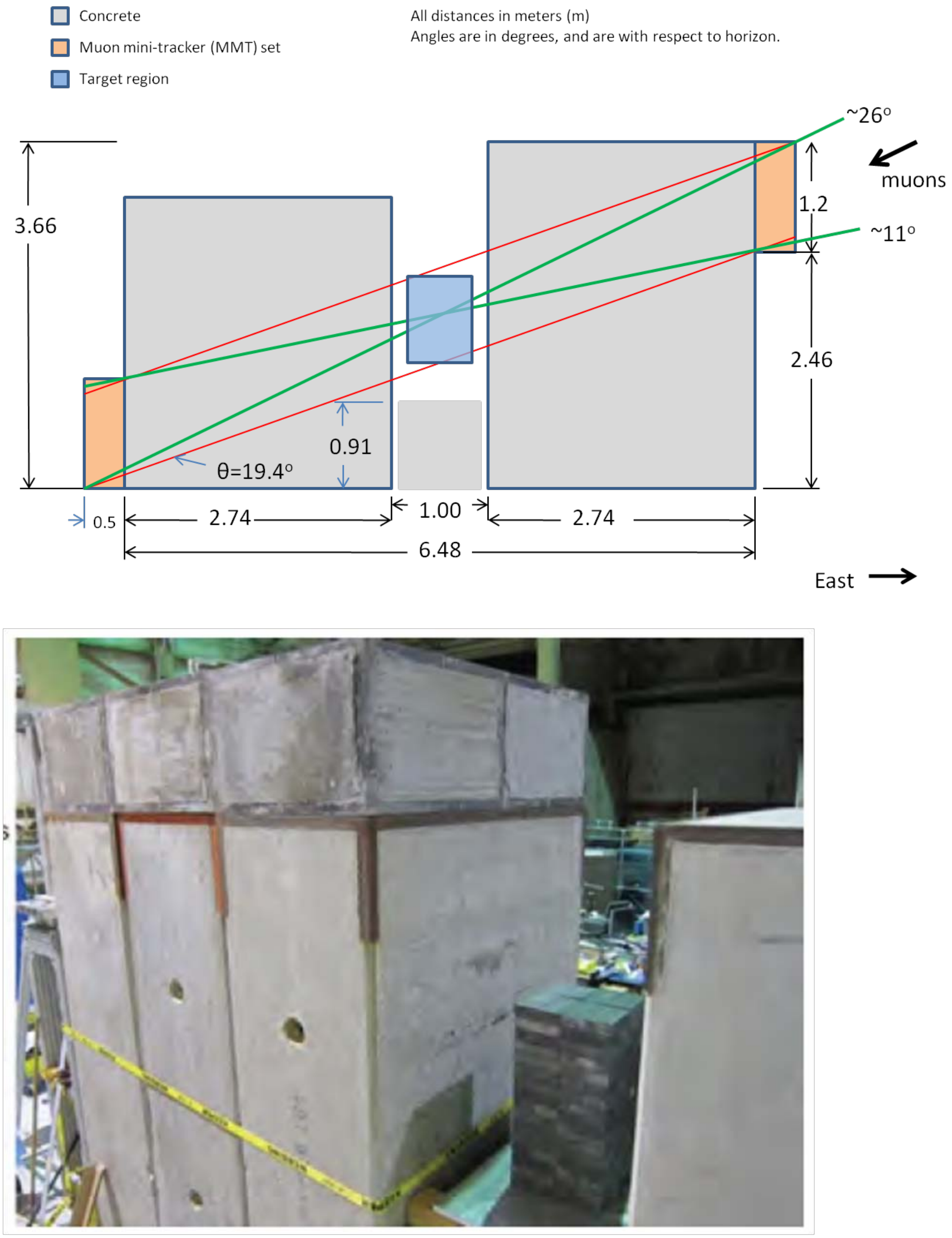

Figure 30 – Experimental drawing of reactor mock-up (top) and photograph (bottom). In the photograph, 2.74 meters of concrete surrounds a stack of lead on each side. The MMT detector planes are oriented on the ends of each slab of concrete (diagramed in orange, top).

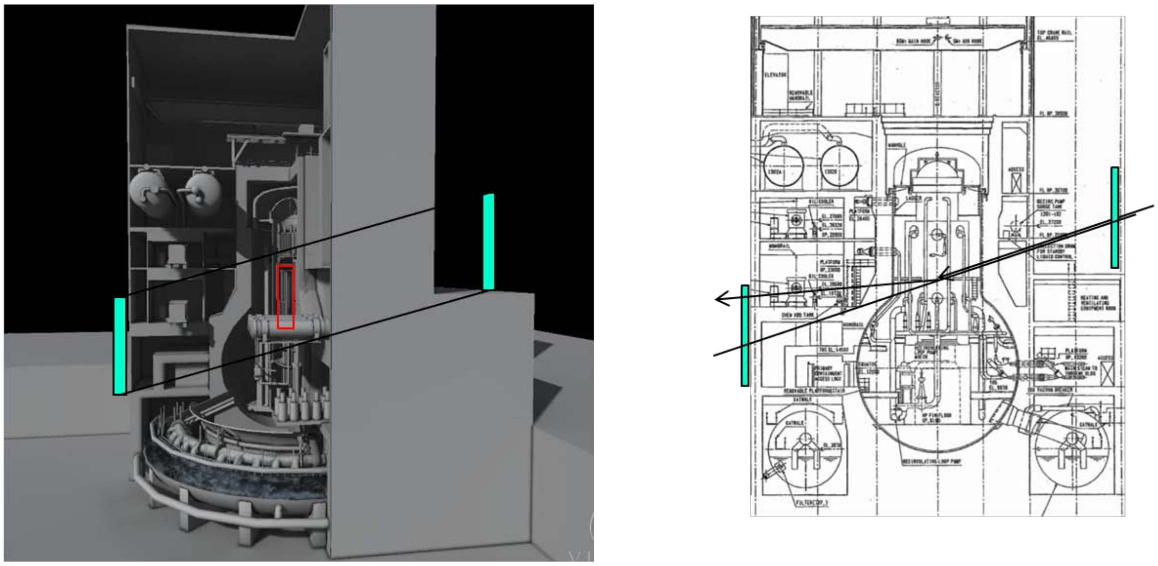

Figure 31 – Deployment of a muon tomography system in a nuclear reactor imaging configuration. The detector planes (teal boxes) are oriented vertically and placed on either side of the reactor. The near horizontal muons are measured as they pass through the reactor. An image is reconstructed showing details of the core and other components that are found in the field of view (red box).

A configuration of lead blocks in a series of thickness measured in the horizontal direction was studied. The lead was arranged in thicknesses of 80 cm, 40 cm, 20 cm, and void, also known as the "80 40 20 measurement". The reconstructed muon image confirms the location of the particular sections of lead. This occurs due to a dependence of muon interaction with length of material as well as Z. The concrete blocks create some additional scattering which does influence the resolution on the order of centimeters. However, the results of this measurement are very clear for establishing the location of the lead stacks. The MMT measured this data set over the course of 210 hours. The results of this configuration are shown in Figure 32.

A second configuration of lead bricks was studied that created a scenario similar to a damaged nuclear reactor. The damage is characterized by a wedge shape due to molten fuel boiling over the sides of the core. To accomplish this, a conical section was removed from the top of a stack of lead bricks. Cosmic-ray muons were measured passing through this configuration for 500 hours. The resulting reconstruction, Figure 33, shows a defined conical shape with a resolution on the order of tens of centimeters.

Following the experiments, several simulations were performed with the 80 40 20 measurement geometry. The results of these simulations show the difference between using the multiple scattering technique as compared to the attenuation method of transmission radiography. The simulations had 1 million cosmic-ray muon events each and are shown in Figure 34. To image a reactor core, the contrast between the uranium and other materials, including large sections of steel, water, and concrete, is required. Muon transmission measures the difference in the muon flux caused by muons stopping in materials after total energy loss. The energy loss of cosmic-ray muons, dE/dx, is comparable between most materials, and given that the effective thickness and volume density of the fuel is similar to that of water found in the reactor, the sensitivity of muon transmission is greatly inhibited. This problem is further complicated by the inclusion of overburden from the concrete buildings and reactor pressure vessel. In contrast, the multiple scattering technique is able to leverage the difference in Z of the materials. This explains why multiple scattering can produce images with better material identification than muon transmission.

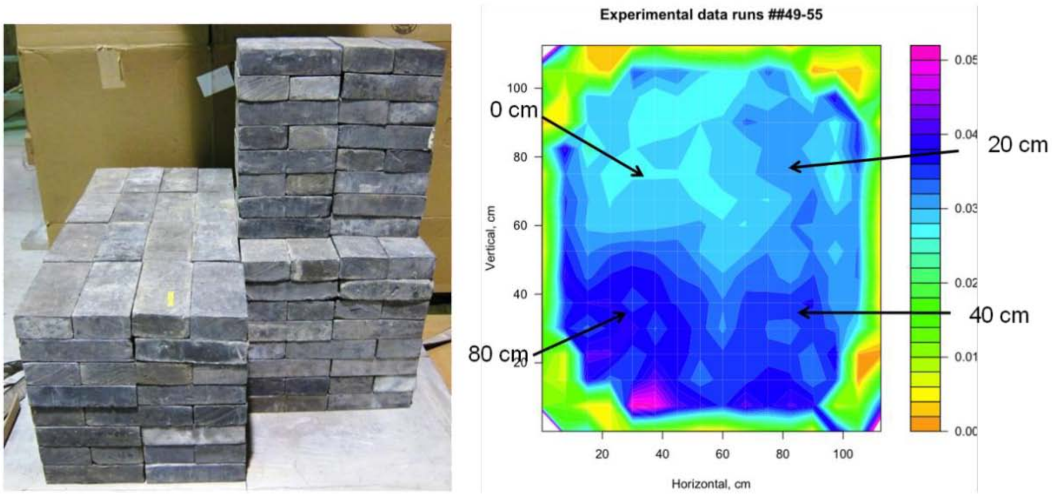

Figure 32 – Lead stack configuration of 80 cm, 40 cm, 20 cm, and void. Cosmic-ray muons were measured passing through the lead stack over a duration of 210 hours. An image reconstruction (right) shows the location of the different thicknesses of lead.

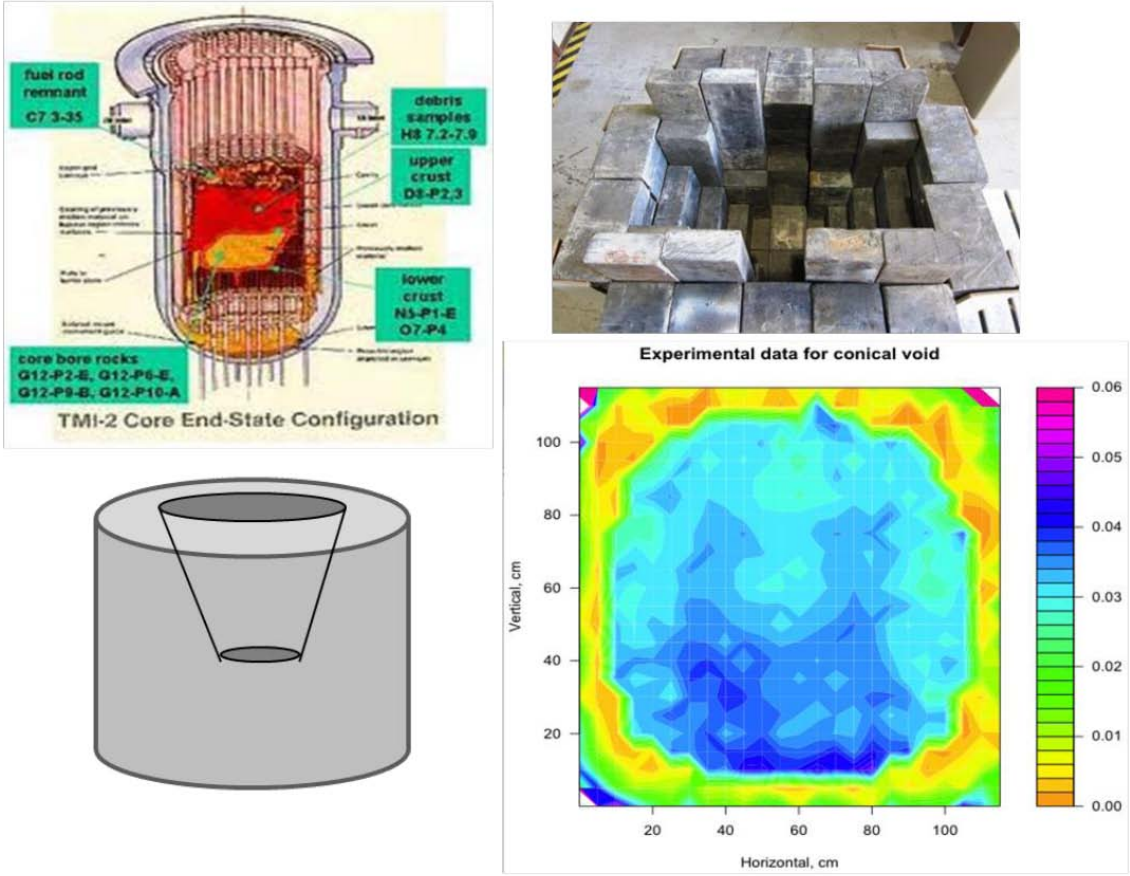

Figure 33 – Conical void configuration for a molten reactor mock-up. Lead bricks are removed from a stack of lead to produce the conical void as shown in the photograph (upper-right) and diagram (lower-left). Muons are measured for 500 hours passing through this geometry and the concrete walls. An image is reconstructed (lower-right) of the lead bricks showing a region indicative of the conical void.

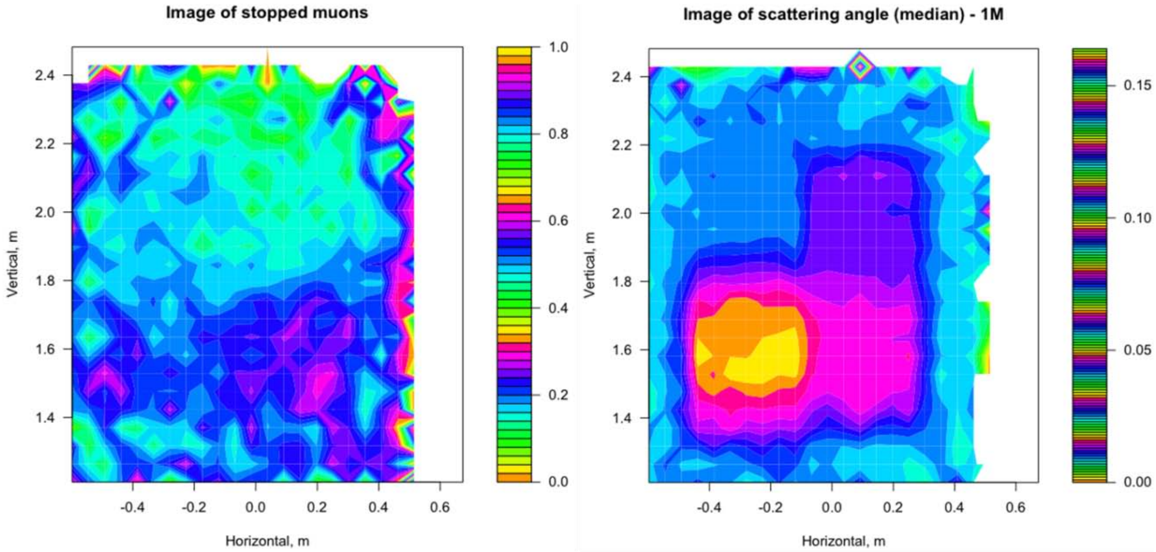

Figure 34 – Geant4 simulation of lead quadrants demonstration for muon transmission (left) and multiple scattering (right) reconstruction techniques. The lead quadrants (thickness of void, 20, 40, and 80 cm) were located between two concrete walls each of 3 m thickness.

Fukushima Reactor Simulations

The cosmic-ray muon imaging of a nuclear reactor was simulated and then compared for both transmission and multiple scattering muon radiography [66]. The simulation code GEANT4 was used to track cosmic-rays through a model of a boiling water reactor similar to Fukushima Daiichi Reactor #1. The model of the reactor included all major structures, the reactor building, the containment vessel, and the pressure vessel. Calculations were performed for an intact core, a core with a 1 m diameter of material removed from the core and placed in the bottom of the pressure vessel, and no core. A schematic view of the detector placement is shown in Figure 35. The placement of detectors outside of the reactor buildings is dictated by very high radiation levels and very limited access to the insides of the buildings.

Several approximations were made to simplify the calculation: structures outside of the field encompassed by the detectors were not included (mainly the turbine buildings); the detectors were assumed to measure position and angles perfectly; there was no gamma shielding added around the detectors; and the energy spectrum was assumed to be independent of zenith angle and was taken from the 75° zenith angle measurements of Jokisch et al. [41], which corresponds to the angle of reactor core from the lower detector. The angular acceptance of the experimental setup is small; therefore, the muon momentum angular dependence is insignificant. The thickness of the gamma-ray shield was not decided upon, but it was assumed to be negligible in the scattering contribution when compared to the reactor walls. A comparison of the spectra given by Jokisch et al. and by Tsuji et al. [40] shows a 50% discrepancy at low momentum and differences in the slope at higher momenta Figure 36. This is indicative of the uncertainty in the normalization of our results.

The output saved from the GEANT4 runs included the input and output vectors, $\vec{X}_{in}$ and $\vec{X}_{out}$, for each incident particle. The incident flux projected to the reactor core location was used to normalize the transmission radiography (attenuation method). The calculations are normalized to the 75° zenith angle flux. The muon angular distribution can be approximated by [36]:

$$\frac{dN}{d\Omega}[\text{ muons/min/sr/cm}^2] = \frac{3}{\pi} cos^2(\theta), \qquad \text{eq. 40}$$

$$\Omega = \frac{sin(\theta)hw}{l^2}, \quad N = \frac{dN}{d\Omega}\Omega\sin(\theta)\,hw$$

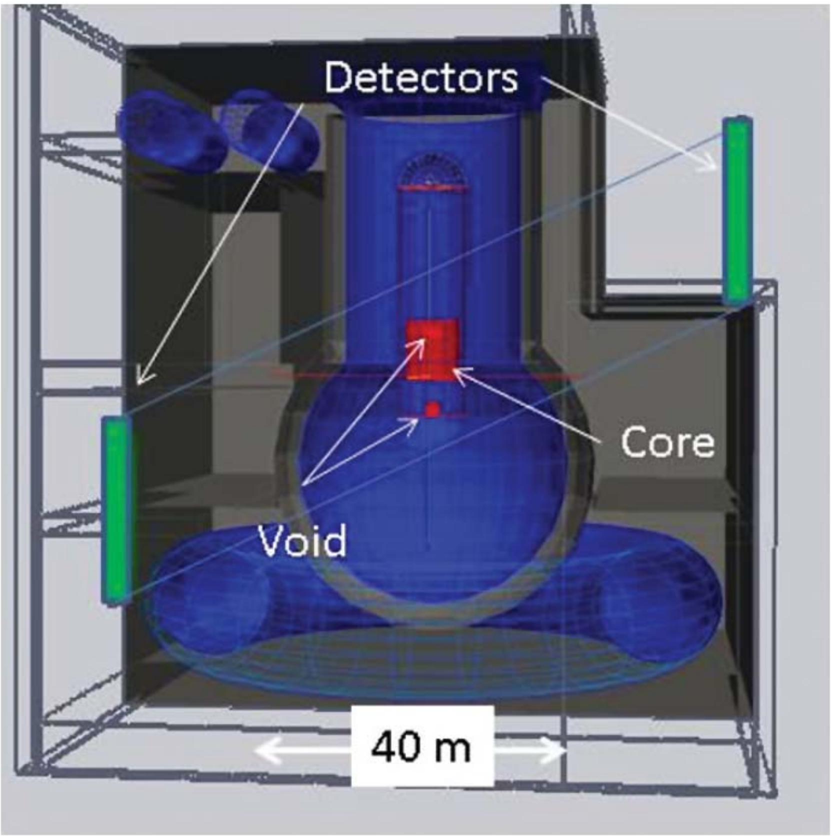

Figure 35 – Cutaway view of a boiling water reactor and a schematic of the detector placement for the Monte Carlo calculation. In the case of attenuation radiography, only trajectory information from the lower detector was used. The location of the 1 m diameter void in the core and its placement in the bottom of the pressure vessel are indicated by arrows.

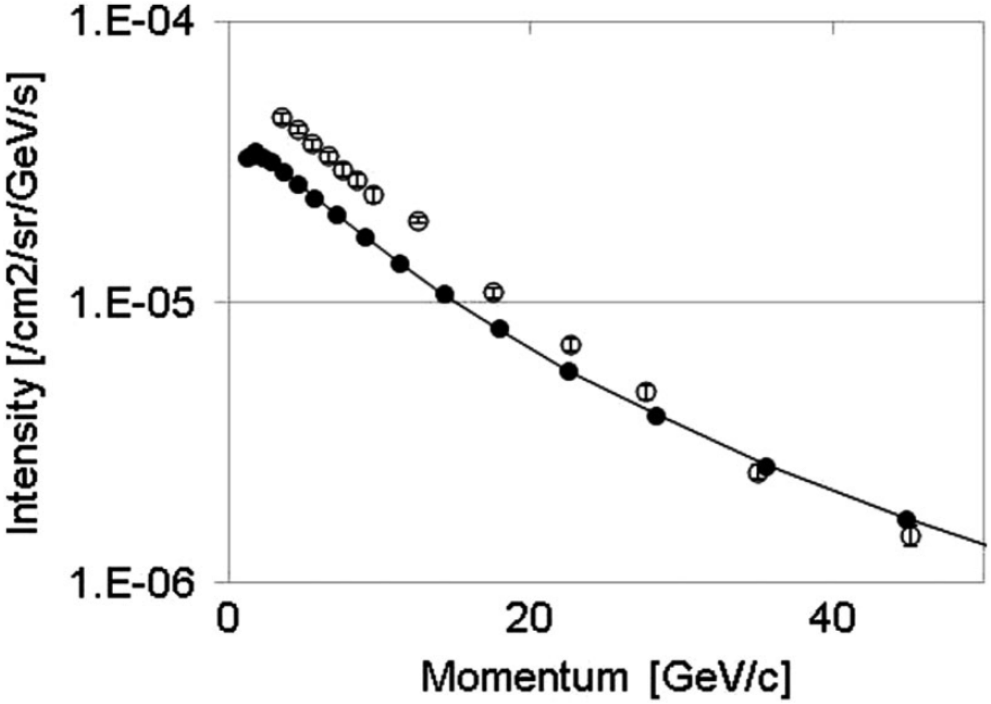

Figure 36 – Cosmic-ray muon energy spectrum at sea level. Solid symbols are from Jokisch [41], and the open symbols are from Tsuji [40]. Muons which penetrate the reactor lose 5-6 GeV.

The normalization of the angular distribution gives a total muon flux of 1/cm^2/min, when it is integrated over 2π steradians. The $\sin(\theta)$ accounts for the fact that the detectors are not normal to the line that connects their centers. The modeled detectors have $h = 10\ m, w = 5\ m,$ and $l = 45\ m$ and are mounted at $\theta = 75°$. For these conditions, we expect $5.3(2.5)\ \times 10^5$ muons per day.

Algorithms were developed to construct images of the core using both the attenuation and multiple scattering of the cosmic rays. The goal is to determine the sensitivity of these techniques for measuring the amount of melted fuel remaining in the reactor core as well as the location of debris. Transmission images were constructed by projecting the outgoing trajectories to a vertical plane centered in the core and histogramming the number of events in 10 x 10 cm^2 pixels. Then, the image was calculated as – $\ln[N(x,y)t_0 / N_0(x,y)/t_N]$, where N_0 was the incident fluence and N was the transmitted fluence in exposure times of t_0 and t_N, respectively. The histogram of incident fluence was smoothed to remove an artifact introduced by the blur of the projection of the output trajectories to the plane of the core.

Plots of both the scattering images and the transmission images are shown in Figure 37 for different exposures starting at 1 h, increasing by near factors of 10 up to 6 weeks. The time scale of several weeks should be considered as “fast” for this particular application, as the timescale of the cleanup is estimated to be between 30-50 yrs. These histograms are displayed with a linear gray scale with a lower value of zero in order to make the combination of contrast and statistical fluctuations clearly visible. The times for the images are for a 50 m^2 detector. For a 1 m^2 detector, these need to be increased by a factor of 50 to obtain the statistics shown at the center of the pictures. The acceptance of this geometry falls to zero at the detector edges. At 1 h, the difference in scattering between the images with and without the core is visible, and by ten hours the reactor core is visible in the scattering image. At 4 days, the 1 m diameter void is visible in the core, and by 6 weeks both the void and the resulting sphere of core material below the core are clearly visible. The low contrast in the attenuation images is apparent when they are compared to the scattering images. The core can be detected by comparing the empty and intact images at the longer exposures, but structure in the images due to the building components shows up as strongly as the core. The void and sphere of material, clearly visible in the scattering radiograph, is not detectable in the attenuation image.

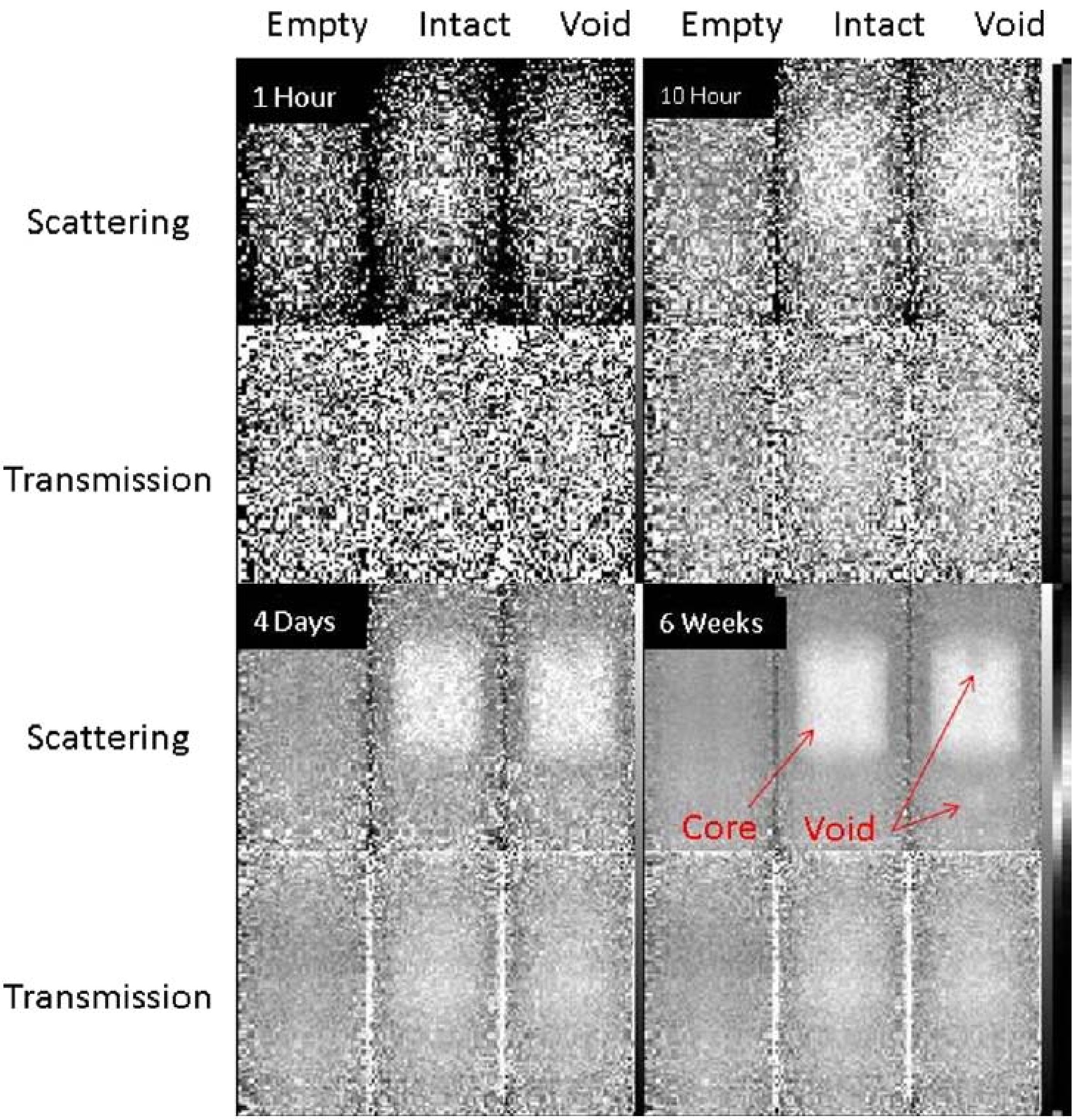

Figure 37 - Reactor reconstructions at different exposure times. In scattering radiography, the reactor core can be detected after about 10 hours of exposure. After four days, a 1 m diameter (1%) void can be detected when compared to an intact core. After 6 weeks, the void is clear and the missing material can be observed. With the attenuation method, the core can be observed when compared to an empty scene in four days. The void is undetectable even after 6 weeks of exposure.

Another major challenge is the engineering of a detector system for muon tomography at Fukushima Daiichi. The site has high radiation levels on the order of 1 mSv/h, primarily from the production of gamma rays from Cs and Sr fission product contamination. Experimental measurements were made at the site with small scale drift tube detectors and have shown that 50 cm of concrete will provide adequate shielding for operating detectors at the locations modeled in this paper. A radiation shield of precast concrete can be quickly installed at the site as well.

In summary, GEANT4 was used to model cosmic-ray radiography of the Fukushima Daiichi reactor unit #1. It is shown that 6 weeks of exposure, with a 50 m^2 detector, is able to produce an image reconstruction where a 1 m diameter sphere can be imaged, which is 1% of the total image resolution. On the other hand, the same exposure in transmission radiography shows much less sensitivity. This analysis shows that high quality data for radiography of the Fukushima core from outside of the buildings can be accomplished with scattering radiography and large detectors. On site tests at Fukushima Daiichi have shown that these measurements are possible with appropriate shielding. For more discussion on this topic, refer to Appendix A.

Imaging of the University of New Mexico Research Reactor

Experimental images of a nuclear reactor, the AGN-201M reactor at the University of New Mexico, were created using data measured with the MMT [8]. The image data are compared with a Geant4 model. In both the data and simulation, specific regions are identified corresponding to elements of the reactor structure, including its core, moderator, and shield. The experimental data is then used to validate simulations of muon tomography which increases confidence in the predictive capabilities of our muon tomography model based on Geant4.

The University of New Mexico Research Reactor, AGN-201M, consists of 10.93 kg of polyethylene loaded with about 3.3 kg of uranium, enriched to 19.75% of U-235. Moderator and shielding consisting of graphite, lead, water, and concrete surround the core. Several access channels pass through and near the core. In Figure 38, the elevated view of the AGN-201M shows components of the reactor geometry. The core profile details how the fuel section is made of stacked cylindrical plates with access ports and control rod channels. The MMT supermodules were offset by 1.9 meters vertically and 3.81 meters horizontally during the reactor measurements. Figure 39 shows the layout for these measurements.

The data collection for muon tomography at the UNMRR ran over several months, though, due to different interruptions, total exposure amounted to 891 hours. The MMT's status was monitored remotely from Los Alamos, located 100 miles from UNM, and the experimental data was collected in 3 hour increments. In Figure 40, the track reconstruction rate and hit rate is shown for the MMT measurements at the UNMRR which details the performance of the MMT as a function of time. There were several periods of data acquisition loss due to failure of the high voltage power supply. The data analyzed in this paper corresponds to the continuous data runs in Figure 40 prior to and immediately following the voltage failure on October 20th, 2012 through October 30th, 2012.

Figure 41 shows a period when the reactor was brought critical indicated by the sharp peaks in the number of detected hits and an absence of detected tracks during the reactor operation. This is due to high counting rates induced by the radiation background produced by the operating reactor which overwhelmed the data acquisition system. Most of these background events can be discriminated by taking time coincidences between multiple drift-tube layers, which can be done in the FPGA. I plan to implement this modification to allow operation in a high radiation environment, e.g. Fukushima Daiichi.

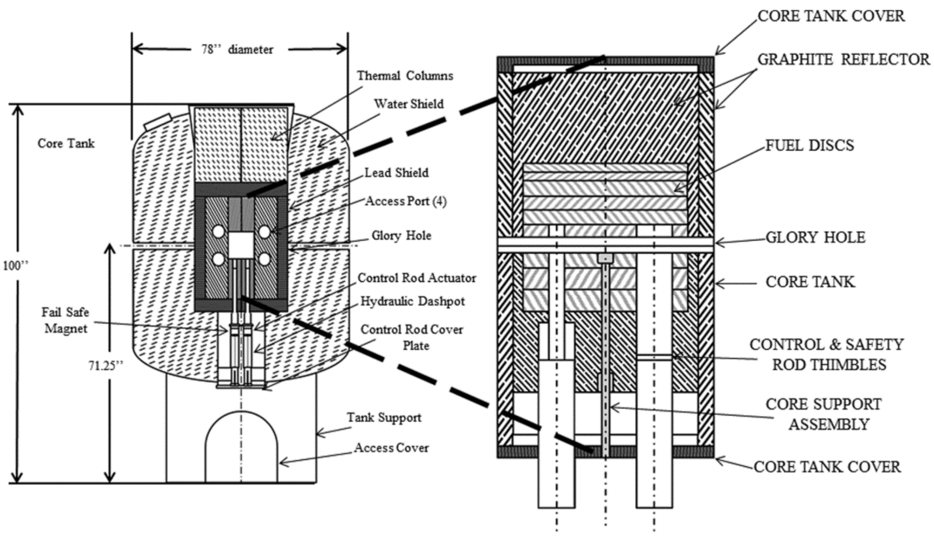

Figure 38 - Elevation view of AGN-201M (left) and core profile (right). The core profile is located in the center of the elevation view [67].

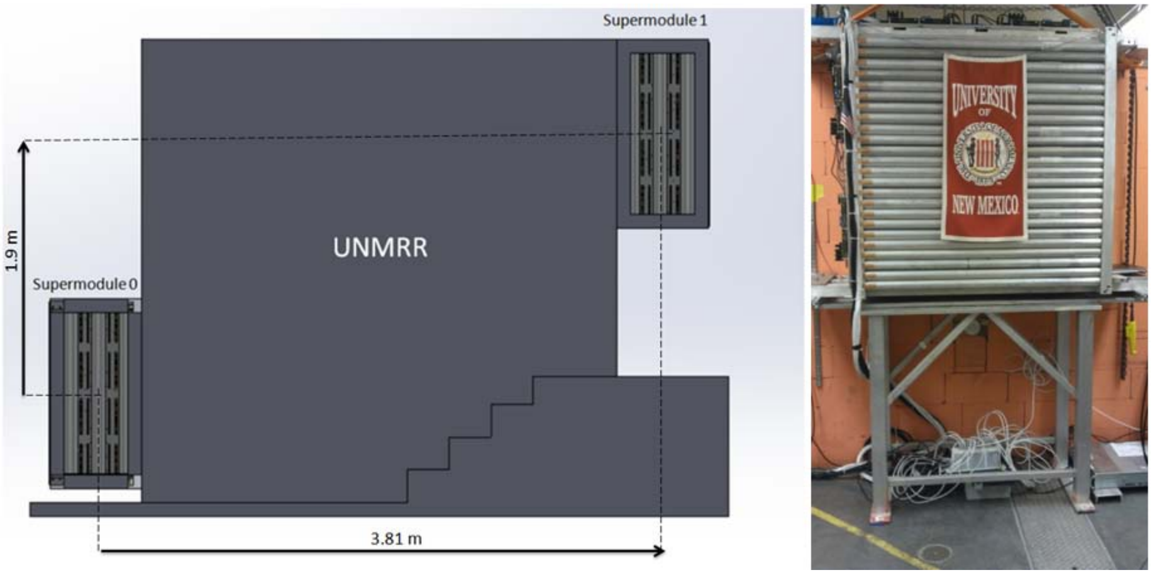

Figure 39 - MMT horizontal mode deployment at UNMRR (left) and supermodule 1 (right)

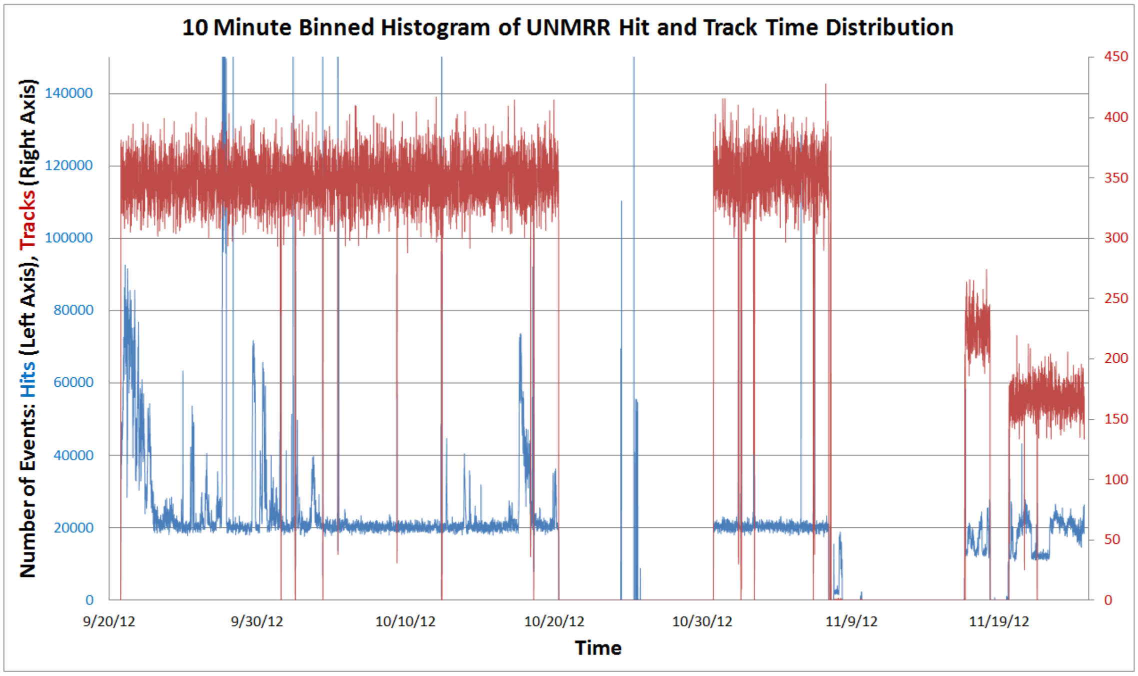

Figure 40 - Track and hit rates from measured data during the UNMRR experiment. The data rates are binned over 10 minute intervals. The blue line corresponds to the number of measured hits. The red line corresponds to tracks that are reconstructed from the hits in the same time bin. The periods of data loss are due to high voltage failures. The last period of observations relates to firmware adjustments designed to improve tracking capabilities in the presence of increased background radiation.

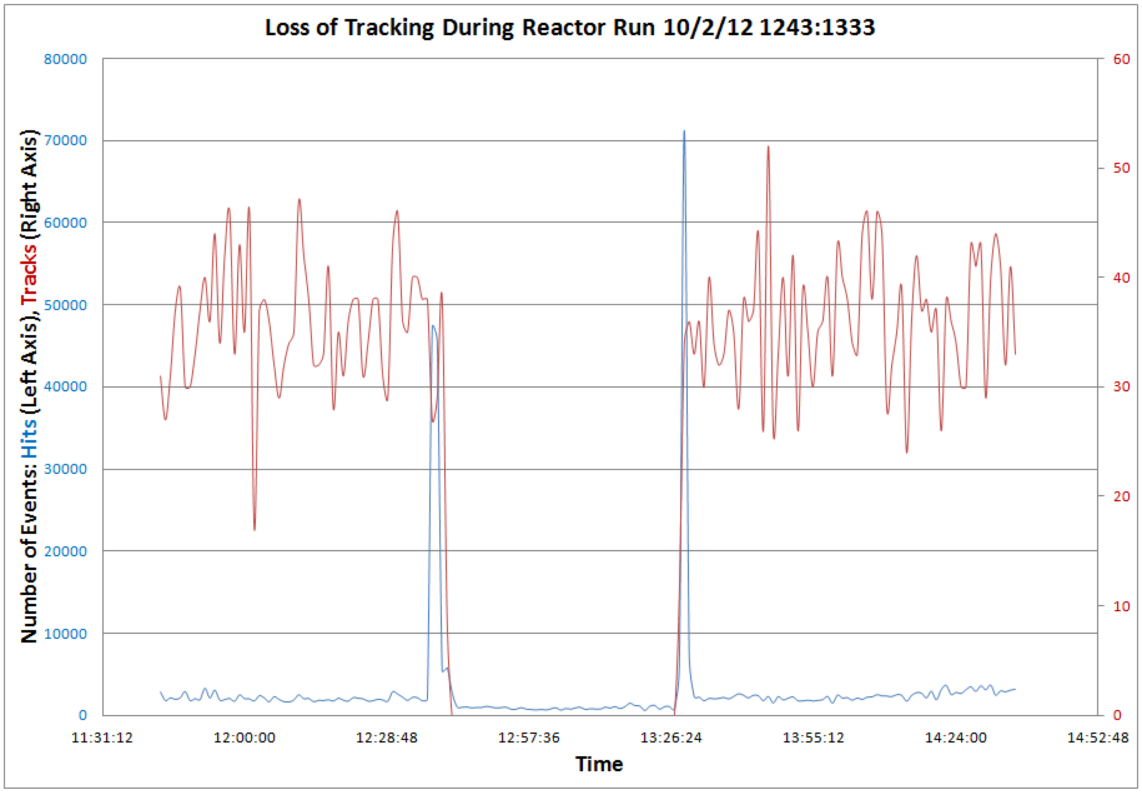

Figure 41 - Tracking failure during the period of reactor operation. The data rates are binned over 1 minute intervals. The blue line shows the number of measured hits. Red line corresponds to tracks that are reconstructed from the hits in the same time bin. The presence of the increased background during reactor operation creates a sharp increase in number of hits, overloading the electronics and disabling the muon tracking.

A model of the UNMRR is created using the GEANT4 toolkit, developed at CERN for the simulation of the passage of particles through matter. The reactor model includes 35 structural components of the reactor. Simulated muons are provided by a cosmic-ray particle source [32]. Muons are sampled uniformly in the azimuthal (horizontal) angle bounded from $(0,2\pi)$. A $\cos^{\mathrm{n}}(\theta)$, where n is 2 except near the horizon, distribution is used to sample muons in the zenith (vertical) angle, where θ is bounded from $(0,\frac{\pi}{2})$. The muon trajectories are recorded in two detector planes located in the positions corresponding to the central planes of the two MMT supermodules. Inscattering, an important component of the data, is modeled by simulating detectors that are half a meter larger on each side.

The geometry of the Geant4 simulation is shown in Figure 42. It shows a number of geometrical shapes representing the uranium loaded polyethylene core, core fuse, empty guide control rod channels, access ports, graphite reflectors, and other structural elements made of aluminum, lead, water, steel and concrete.

Eight hundred and ninety one hours (37 days and 3 hours) of cosmic ray data were collected at the UNMRR. This includes seven hours of cumulative reactor operation during which tracks could not be reconstructed, which reduced our total exposure to 884 hours. Using this data, we validate our modeling and muon transport simulation capabilities.

Tracks were separated into two groups, transmitted and inscattered, for both the simulations and the data. The separation was determined by the incident trajectory’s location projected to the bottom detector. If the track is within the surface area of the bottom detector’s acceptance then the track is considered transmitted otherwise it is inscattered. This is important because the inscattered events are biased to large scattering angles, producing a halo around the image if they are not filtered. We have filtered out most of the inscattering trajectories from the “good” events in our data analysis, but some inscattering remains because of small uncertainties in the reconstructed tracks from data.

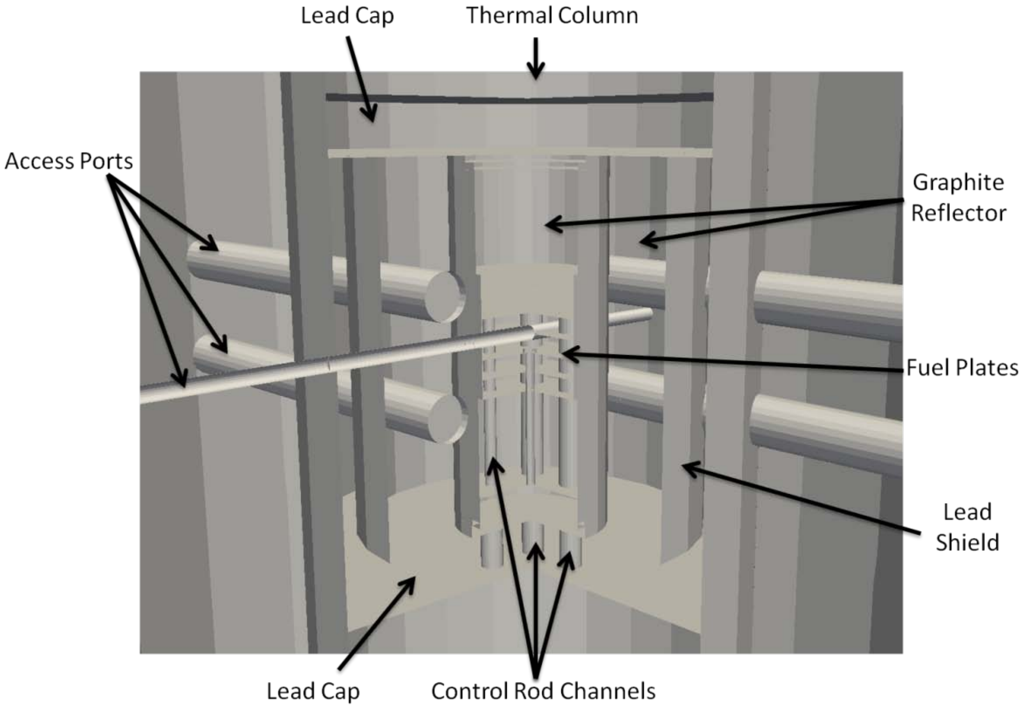

Figure 42 - **Geometry of our reactor model. The fuel plates are located in the center and surrounded by cylinders of graphite. Lead and water cylinders encompass the graphite moderator region. Access ports and drive channels are also included to increase the realism of the simulation.**

The projections of both the height and depth dimension are computed as shown:

$$x_{proj} = x_0 + \left(z_{proj} - z_0\right) * \frac{x_0^{'}}{z_0^{'}} \qquad \text{eq. 41}$$

$$y_{proj} = y_0 + \left(z_{proj} - z_0\right) * \frac{y_0^{'}}{z_0^{'}} \qquad \text{eq. 42}$$

where the projection location is chosen as the bottom detector, and x_0 and y_0 refer to incident tracks measured at the upper detector.

The muon flux from the data and simulation is parsed with this method, diagrammed in Figure 43. The MMT recorded 1.73 million tracks during the course of the run. Of these, 17.6% were filtered as inscatter events, where the initial trajectory is not pointed at the outgoing detector. There were 50.0 million tracks recorded with both detectors in the simulation after evolving one billion events, with 15.3% due to the inscattered flux.

Muon tracking in the MMT also includes detector efficiency and resolution effects, thus the detector edge in the data is fuzzy, rather than the sharp edge we have in our model. Figure 44 shows the flux found in the detectors for both the simulation and experimental measurements. The fine structure in the data is due to differential non-linearities introduced by dead and noisy drift tubes.

The distribution of the incident flux, normalized to the number of incident tracks, is shown in Figure 45 and Figure 46, comparing simulation to data. The method of replicate trials is used to determine the error in the data. Statistical uncertainty in the high-fidelity simulations is significantly smaller than in the data, and is not shown in the plots. There is a maximum discrepancy of 8% between the data and simulation of the azimuthal flux in the top supermodule.

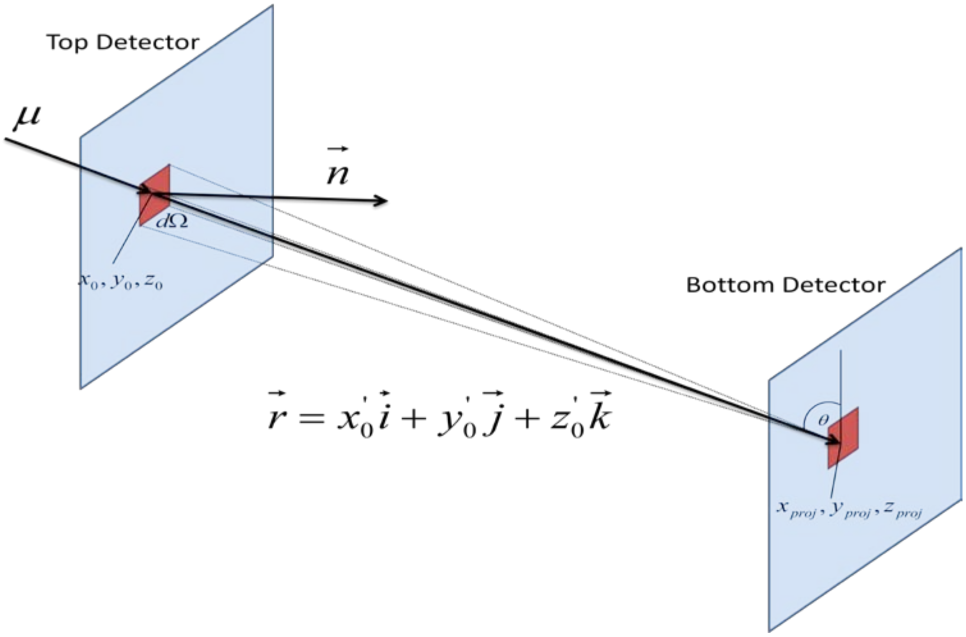

Figure 43 - A conceptual diagram of computing transmission for a muon track. The muon trajectory is determined by the top detector. This incoming trajectory is projected to the bottom detector. If the projection remains within the specified surface area of the bottom detector, the track is considered a transmission track; otherwise it is classified as inscattering.

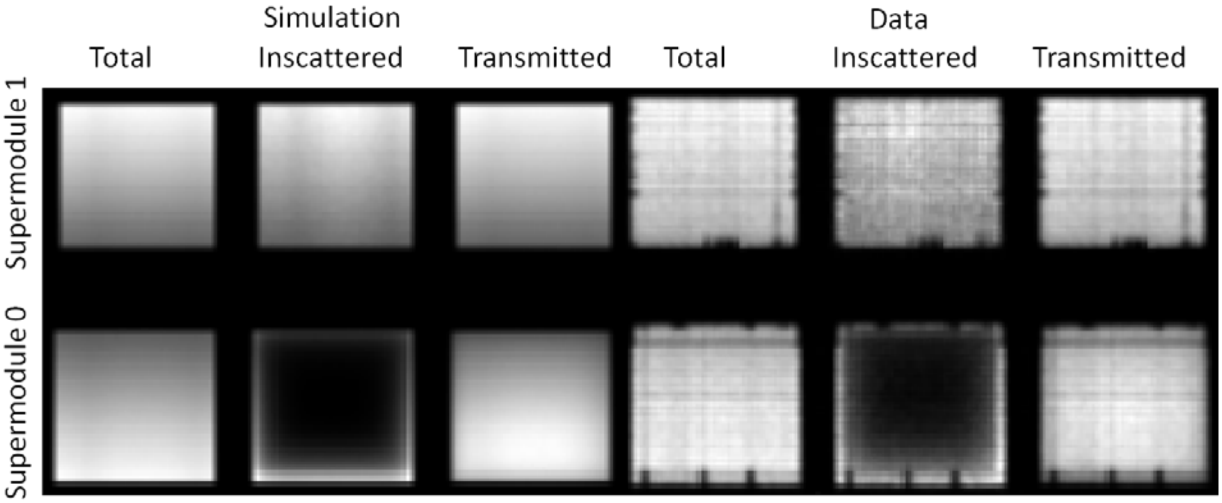

Figure 44 - Flux in simulation (left 6 images) and experimental measurements (right 6 images). The top row is for the muons entering supermodule 1. The bottom row is for muons exiting supermodule 0. For each six images, from left to right, the flux is defined as integrated, inscattered, and transmitted. The images are normalized and shown in a linear brightness grayscale from black to white.

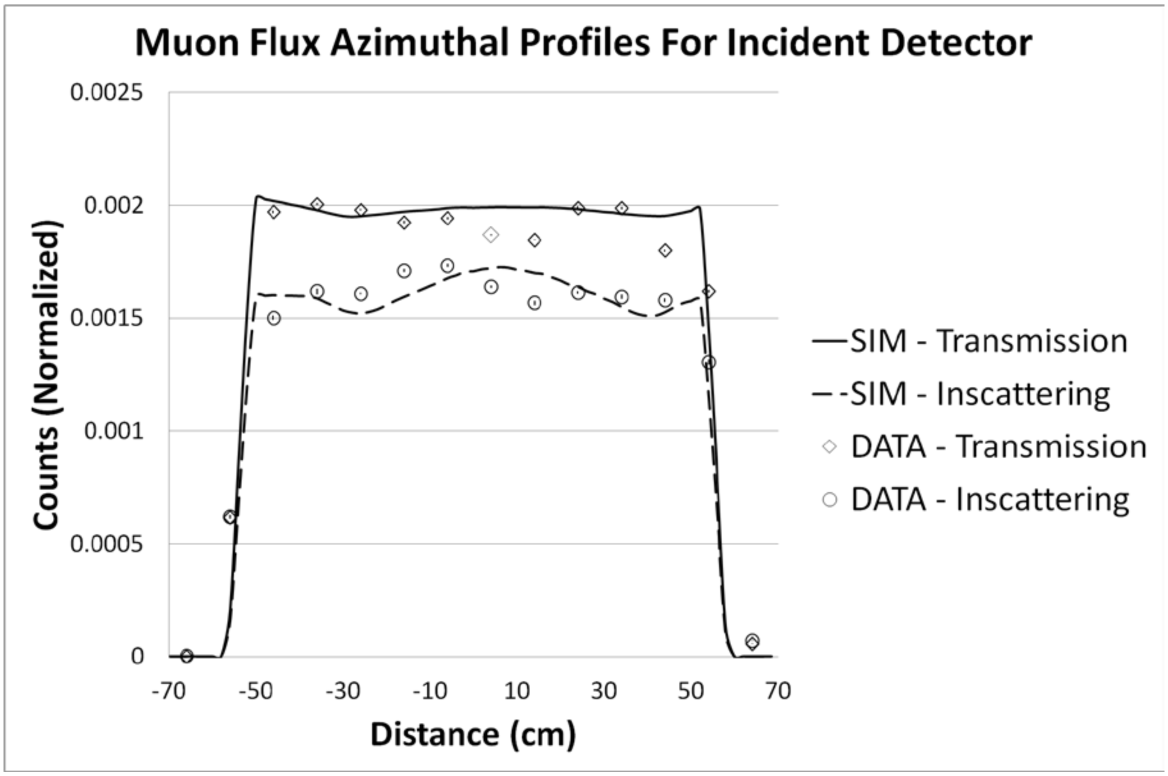

Figure 45 - Azimuthal flux profile in the incident detector. This figure compares the particles thrown in the simulation with muons measured by the MMT. The distance numbers refer to the coordinate system of the MMT (one corner of the bottom supermodule was chosen as the origin).

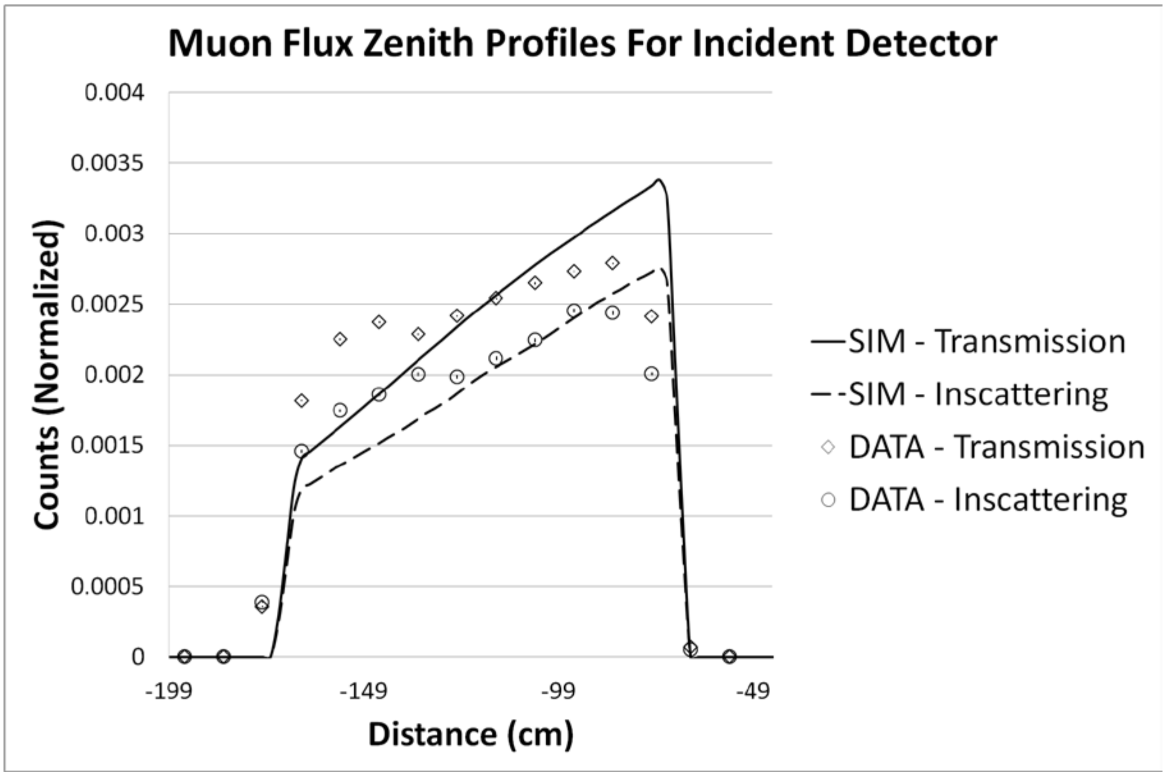

Figure 46 - Zenith flux profile in the incident detector. This figure compares the particles thrown in the simulation with muons measured by the MMT. The distance numbers refer to the coordinate system of the MMT (one corner of the bottom supermodule was chosen as the origin).

The zenith flux in the top supermodule has a shallower slope in the data as compared to the simulation. The zenith flux was investigated with simulations by varying overburden and modifying the cosmic-ray muon source. The overburden, as well as the reactor structure itself, reduces the flux of lower energy muons, which is very sensitive to the zenith angle. Our observations confirm that the higher-energy spectrum of cosmic-ray muons does not decrease with zenith angle as steeply as the lower-energy part of the spectrum. Of course, this fact is very well known from numerous cosmic-ray studies [37-41, 43-46, 68, 69].

Image reconstruction is based on measuring the scattering angle and position between incident and outgoing trajectories of the muons passing through the reactor. The scattering angle distribution for each pixel is fitted to obtain the average radiation length by using a recently developed multi-group description of the muon energy spectrum [58]. The angular distributions are fitted with a sum of Gaussians, with amplitudes corresponding to the distribution of muon energies and the widths depending on the amount and composition of material. The spectrum is calibrated to the integrated radiation length expected for a muon crossing the UNMRR. Figure 47 shows the integration of scattering angles for the MMT in vertical mode (without object), as well as with the UNMRR run. The figure displays that in empty mode the average amount of scattering (due mainly to the detectors) is several mrad. The scattering is on the order of ten times larger for trajectories that penetrate the reactor.

The core and surrounding structure of the UNMRR is nearly symmetric about its azimuthal axis. We exploit this symmetry by performing a regularized Abel inversion. The regularized Abel inversion is a computation of the radial distribution for the materials surrounding the center axis. The regularization term added to the Abel inversion reduces the noise near the symmetry axis by forcing smoothness. This procedure provides density weighted by inverse radiation lengths as a function of radius. It is instructive to mention that the object projection to its central plane is not completely symmetrical in our case, because of different relative heights of the detectors; however, we neglected this effect while performing our reconstructions.

The regularization of the Abel inversion is computed using a linear regularization method[70]. This is done by minimizing the matrix eigenvalue problem:

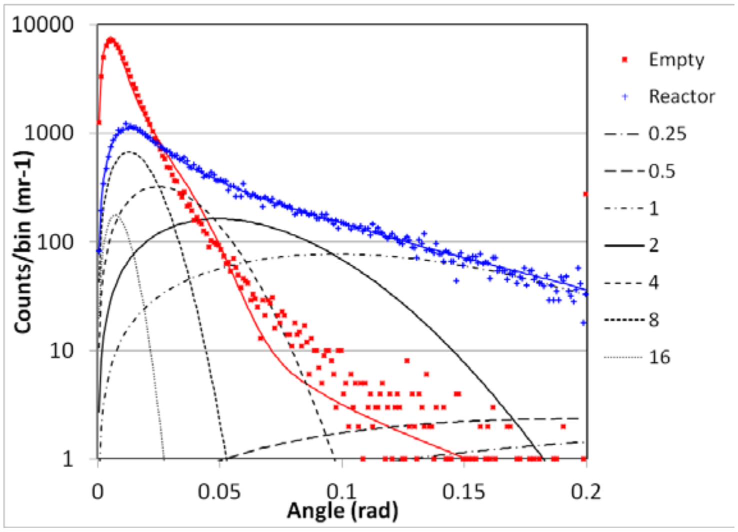

Figure 47 - Muon flux angular distributions and corresponding fits. The red symbols and fitted line show an angular distribution of muons measured with the MMT in a vertical configuration with an empty field of view. The blue points and fitted line are averaged over the horizontal configurations with the reactor. The black curves show the components of the fit (blue line) corresponding to different muon energies.

$$|\boldsymbol{A} \cdot \widehat{\boldsymbol{u}} - \boldsymbol{b}|^2 + \lambda \widehat{\boldsymbol{u}} \cdot \boldsymbol{H} \cdot \widehat{\boldsymbol{u}} \qquad \text{eq. 43}$$

Where $\boldsymbol{A}$ is the functional projection matrix, $\widehat{\boldsymbol{u}}$ is a vector representing the radiation length weighted densities, $\boldsymbol{H}$ is a degenerate symmetric difference matrix, and $\boldsymbol{b}$ is a vector of measurements. We compute the projection (path length) matrix $\boldsymbol{A}$ by averaging the path length for each cylindrical shell over the finite slice thickness.

$$\boldsymbol{A}_{ji} = \frac{\mathbf{1}}{e(i+1) - e(i)} \int_{e(i)}^{e(i+1)} \big(\delta y_1(x) - \delta y_2(x)\big) dx \qquad \text{eq. 44}$$

The index j is the cylindrical shell index and i is the areal slice index. The quantity, e, is the edge boundary of the averaging for the projection. The projected lengths are:

$$\delta y_1(x) = 2\sqrt{MAX[(r_o^2 - x^2), 0]} \qquad \text{eq. 45}$$

$$\delta y_2(x) = 2\sqrt{MAX[(r_i^2 - x^2), 0]} \qquad \text{eq. 46}$$

The shell radii are:

$$r_o = MAX[|e(j)|, |e(j+1)|] \qquad \text{eq. 47}$$

$$r_i = MIN[|e(j)|, |e(j+1)|] \qquad \text{eq. 48}$$

The symmetric difference matrix, $\boldsymbol{H}$, is a product of the first difference matrix transposed, $\boldsymbol{B}^T$, by the first difference matrix, $\boldsymbol{B}$.

$$\boldsymbol{H} = \boldsymbol{B}^T \cdot \boldsymbol{B} \qquad \text{eq. 49}$$

If the rank of $\widehat{\boldsymbol{u}}$ is defined as M, then the first difference matrix, $\boldsymbol{B}$, is $(M-1) \times M$. $\boldsymbol{B}$ is populated with the following conditions:

$$\boldsymbol{B}_{gh} = \begin{cases} -1, \text{ if } g = h \\ 1, \text{ if } g = h + 1 \\ 0, \text{ if } g \neq h \text{ or } g \neq h + 1 \end{cases} \qquad \text{eq. 50}$$

In vector notation, we can determine $\hat{\boldsymbol{u}}$ by solving:

$$(\boldsymbol{A}^T \cdot \boldsymbol{A} + \lambda \boldsymbol{H}) \cdot \hat{\boldsymbol{u}} = \boldsymbol{A}^T \cdot \boldsymbol{b} \qquad \text{eq. 51}$$

The projected measurement vector, $\boldsymbol{A}^T \cdot \boldsymbol{b}_{i1}$, is computed by projecting slices of the image, $\boldsymbol{b}_{i1}$, onto $\boldsymbol{A}^T$. We finish this image processing technique by taking the product of the projected measurement vector with the inverse of the matrix $(\boldsymbol{A}^T \cdot \boldsymbol{A} + \lambda \boldsymbol{H})$.

$$\hat{\boldsymbol{u}} = \boldsymbol{A}^T \cdot \boldsymbol{b} \left(\frac{1}{(\boldsymbol{A}^T \cdot \boldsymbol{A} + \lambda \boldsymbol{H})} \right) \qquad \text{eq. 52}$$

A simulation of the reactor is shown in Figure 48 with arrows relating the regularized Abel inversion reconstruction to the elements of the object geometry. The core of the reactor, which contains polyethylene with traces of uranium, has the lowest effective density (density weighted by radiation length) of the four materials in the reactor. There is more scattering in the graphite moderator surrounding the core (Figure 48, lower right plot). The lead shield is very noticeable as a dominating feature of the images due to the combination of its high atomic number (Z) and density. Some access port features are visible near the lead shield in Figure 48(access ports filled with hydrogenous material and lead slugs). There is also a small depression in the bottom half due to the control rod channels (CRD, which are empty) shown in Figure 48(upper right hand corner). The high fidelity simulation demonstrates the intrinsic imaging capability for muon tomography with the UNMRR. Features are easily distinguished in the reconstruction of this high-statistics simulation.

The reconstructions from the measured muon tracks and the simulated muon tracks are compared for validation purposes. The data is segmented into 9 independent sets of images and regularized Abel inversions are performed for each. Statistical uncertainties are calculated by dividing the rms of the signal in every bin by the number of degrees of freedom (8 in this case). Discrepancies between model and measurements are clearly dominated by systematic errors, resulting from a combination of the model assumptions (e.g., we did not attempt to model overburden that affects both azimuth and zenith distributions of the incoming muon flux, as well as its spectrum), and detector effects (in particular, we ignore a few dead tubes and noisy tubes that are present in MMT).

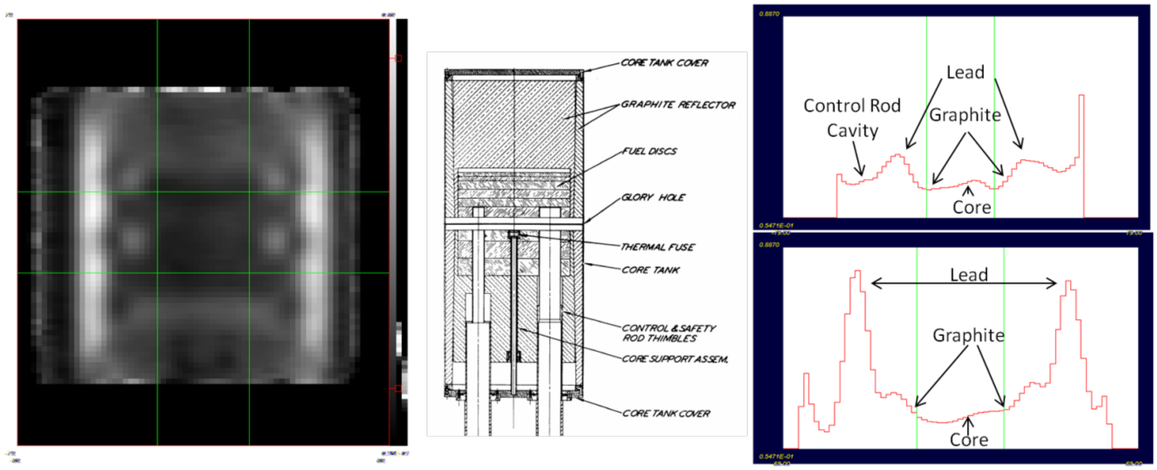

Figure 48 - Regularized Abel inverted reconstruction of simulated muon tomography image showing features of the UNMRR. In the left image, the more prominent features represent the lead cylindrical housing that shields the core, the graphite components in the center, access port materials, and the core itself. The panels on the right are the zenith (top-right) and azimuth (bottom-right) projections of the image integrated over a selected region. The core diagram is shown in the center for reference.

The regularized Abel inversion of the measured data, a simulation with similar statistics as the measured data, and a high statistics simulation are shown in Figure 50. The high statistics simulation amounts to running the MMT at the reactor for 3 years. Therefore, having a validated simulation model becomes very valuable as it only takes several days on 50 CPU to produce high fidelity simulation result.

There are several features that can be identified in both simulation and measurement in Figure 50. The most prominent feature corresponds to the lead cylinder surrounding the core and moderator. The second feature is the water tank surrounding the lead cylinder and seen on the outer edges of the image. There is a void in the lower half of the image which is due to the lack of muon scattering in empty control rod channels. Cylindrical caps of lead above and below the core can also be seen.

The core of the UNMRR is much lower in density and average Z as compared to a commercial nuclear power plant core. Therefore, the core cannot be easily identified in the reconstruction images. We wanted to explore the sensitivity of muon imaging to changes in core composition. In particular, we were interested in whether we could detect the presence of 3 kg of uranium spread homogenously throughout the polyethylene core. Two additional simulations were performed to study this difference.

In the first of these simulations, the uranium was removed from the core resulting in a density of $0.90\ g/cm^3$ of bare polyethylene. Figure 49 shows a comparison of this case with a realistic UNMRR core ($\rho = 1.17\ g/cm^3$). The bare polyethylene core is clearly differentiated from the uranium loaded core.

The two simulations were identical except that in one case the core composition corresponded to the UNMRR, and in the other case, we simulated a bare polyethylene core with the same dimensions. Furthermore, we simulated UNMRR geometry substituting its low density core with core material corresponding to a commercial power plant reactor.

In Figure 51 and Figure 52, we compare regularized Abel inversions of image reconstructions for three cases: 1) simulation of uranium loaded polyethylene core; 2) simulation of bare polyethylene core; and 3) experimental data. There is a scale difference between the simulation and data, of several centimeters at large radii, which is not understood. A correlation of the data points seen in the reconstructed data is due to the forced smoothing from the regularized Abel inversion about the azimuth.

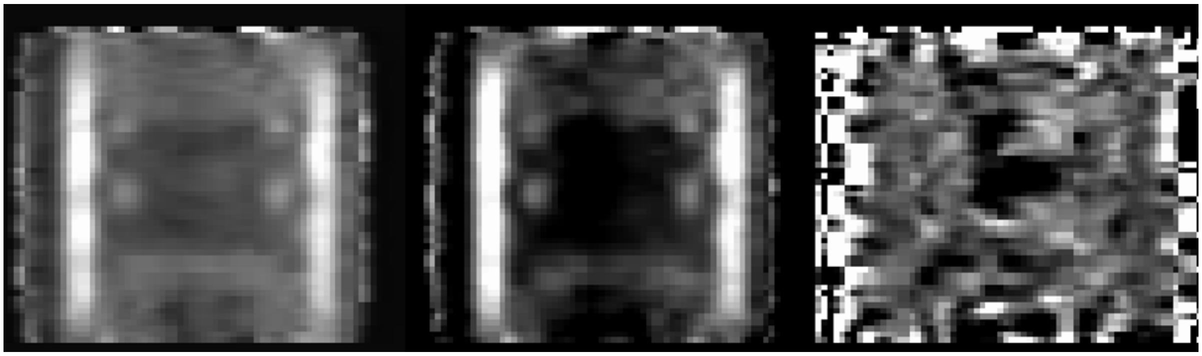

Figure 49 – Comparison of regularized Abel inversions of a uranium loaded polyethylene core on the left, a bare polyethylene core in the middle, and a ratio of the two reconstructions on the right. There are edge effects in the ratio due to division of sparse data.

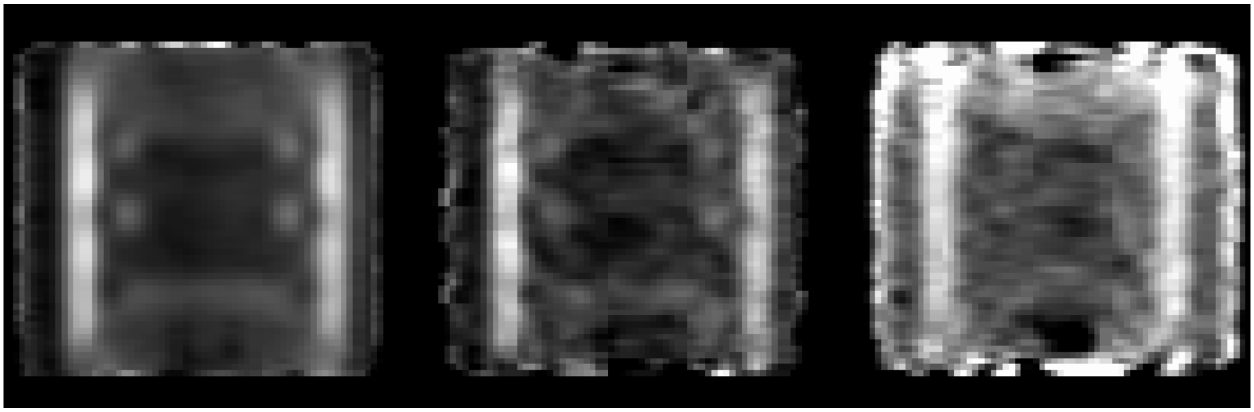

Figure 50 - Regularized Abel inversion reconstructions of the UNMRR at the reactor core plane. A high statistics simulation is shown on the left. A simulation with the same number of transmitted tracks as the data (1.43 million) is shown in the middle. The measurement made at UNM is shown on the right. The high statistics simulation contains approximately 44 times as many tracks as the data. In the images several structures are visible including the core with graphite (center), the lead cylinder shield (outer), and the empty control rod housing (bottom).

eq. 53

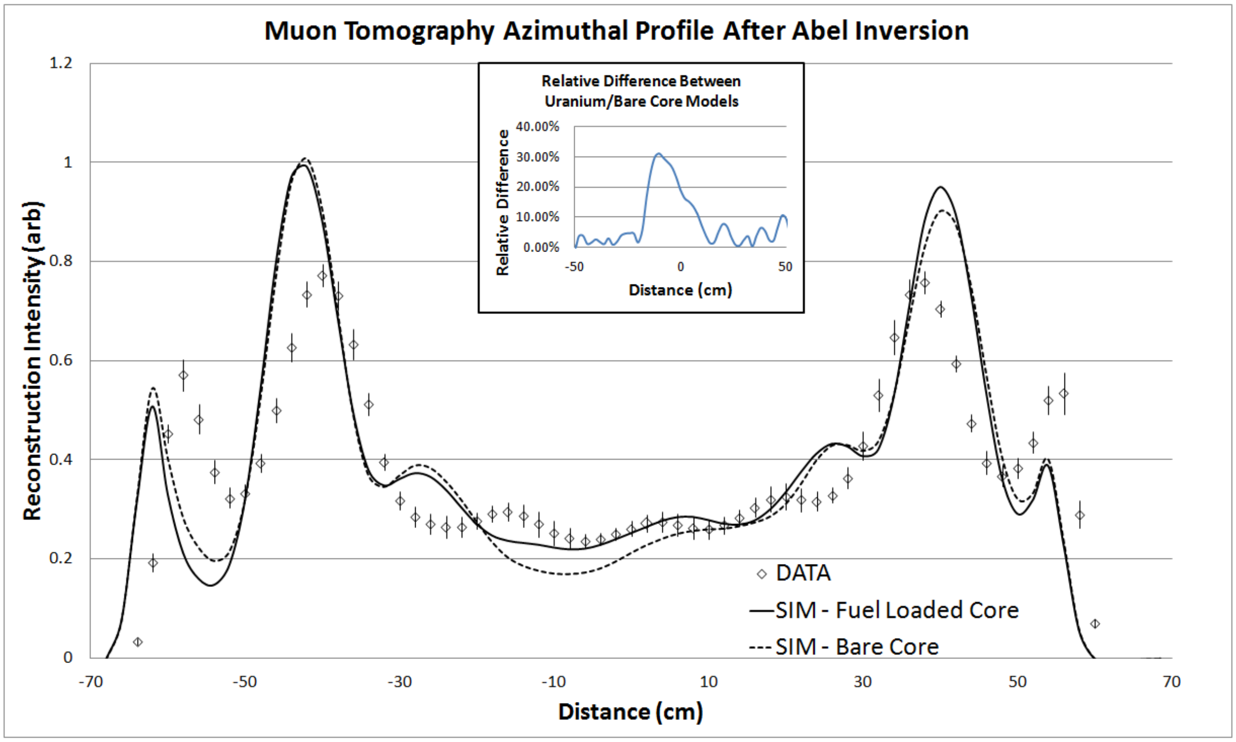

Figure 51 - Azimuthal profiles of data and simulation. Several features are noticeable including the core region, the graphite region, and the lead shield. The water tank outside the lead shield can also be observed.

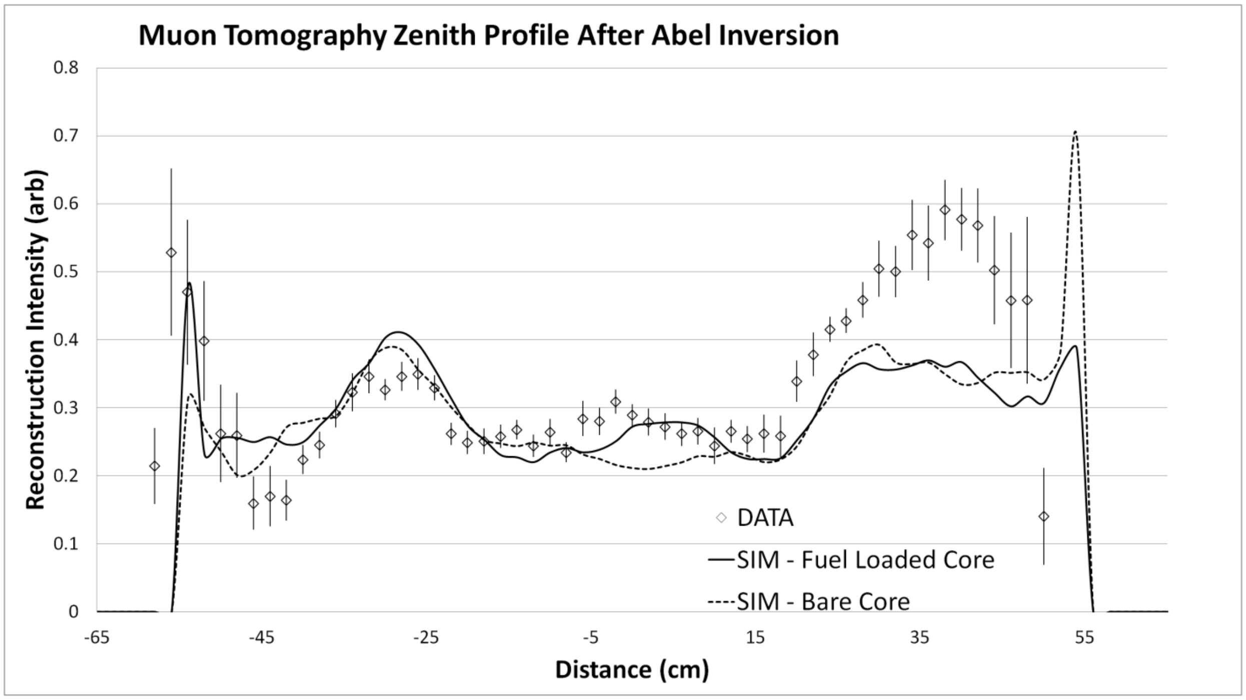

Figure 52 - Zenith profiles of data and simulation for the UNMRR. There is good agreement in the center, but poorly understood discrepancies on the edges.

The center and bottom of the zenith projection corresponds to the lead caps, core/graphite, and control rod region. An increase in scattering at both edges of the zenith projection is much more significant than the inscatter in the azimuthal projection. This is likely due to effects of tracking related to the vertical separation of the detectors; however, these effects are not understood quantitatively at this point.

In Figure 53, the UNMRR core is replaced by a metal homogenous core consisting of uranium, water, and zirconium with a density of $3.75\ g/cm^3$. This composition and density is representative of a core for a commercial nuclear power plant reactor. Our reconstructions clearly show increased signal strength in the core region in this scenario due to the large amount of uranium and high density in the metal core model.

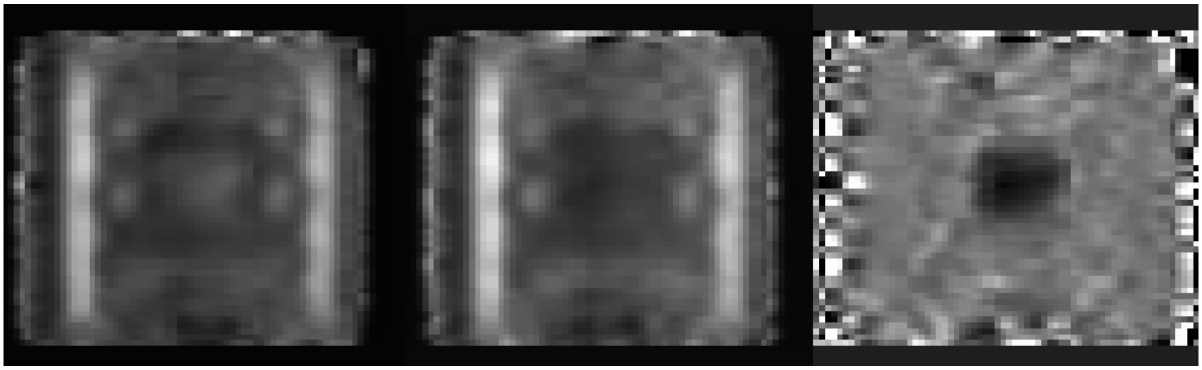

Figure 53 – Comparison of regularized Abel inversion of higher density metallic homogenous core on the left, with a bare polyethylene core in the middle, and a ratio of the two reconstructions on the right.

CHAPTER 8

Material Identification Overview

The identification of materials using cosmic-ray muons can be accomplished through methods that measure density, radiation length, and isotopic composition. These measurements provide data for solving the following inverse problem. What do the multiple scattering of muons, muon attenuation, and muon induced second particles infer for an object in a field of view? By investigating a variety of objects including aluminum, iron, lead, and uranium, we can show that the materials can be identified through density and radiation length analysis. Additional material identification can be obtained from the exploitation of axial or spherical symmetry which can be used to decouple the muon trajectory path length in order to obtain an accurate assessment of radiation length weighted with density. Finally, by using neutron and gamma detectors to measure secondary signals in coincidence with muon trajectories, materials with neutronics gain can be separated from materials with less amplification. For example, differentiating between U-235 and U-238 or well-moderated and un-moderated SNM.

There are several applications for this technology. The research originally began to address treaty verification objectives for the imaging of nuclear weaponry and warheads. Following the preliminary success of the project, additional research goals were established for use in identifying the materials found in objects for homeland security related applications. The majority of this work remained academic in nature, where the bulk of the data was measured from elementary objects interacting with cosmic-ray muons, e.g. the LEU cube or the lead sphere.

Both stopping and scattering measurements are being studied as potential tools to locate the fuel in the melted down reactor cores of the Fukushima reactors. The motivation for this work is the potential cost saving and reduction in human radiation dose for the three-decade long cleanup program at Fukushima Daiichi.

Obtaining Material ID from Transmission and Multiple Scattering of Cosmic-Rays

The passage of muons through matter is affected by their Coulomb interactions with electrons and nuclei [58]. The muon interactions with electrons lead to continuous energy loss and stopping of muons, while their scattering off nuclei lead to angular "diffusion". By measuring both the number of stopped muons and angular changes in muon trajectories we can estimate density and identify materials. This technique has been shown to be useful for locating materials with high atomic number in a contrast with a background of material of low atomic number [20]. The combination of energy loss and scattering has been suggested as a method to determine both material type and density (therefore providing material identification or MID) using focused beams of accelerator produced muons [71]. The combination of nuclear attenuation and Coulomb scattering has also been shown to provide MID in proton radiography [72]. In this paper we demonstrate MID, using the combination of stopping and scattering of cosmic ray muons. Here we demonstrate the material identification using data taken at Los Alamos with the Mini Muon Tracker. An example of a multiple scattering radiographic image obtained with the MMT using overhead muons arriving from directions close to the zenith, is shown in Figure 54.

Transmission (or stopping) imaging with cosmic rays is somewhat different from point source x-ray imaging in that both the intensity and the direction of the cosmic rays can be measured. The trajectory information can be used to generate a focused transmission image at any distance from the detector. Conceptually, the stopping length, λ, of cosmic rays in material is inversely proportional to the stopping rate and can be related to the energy spectrum, $dN(E)/dE$, as shown in eq. 54.

$$\frac{1}{\lambda} = \frac{dN}{Ndx} = \frac{1}{N}\frac{dN}{dE}\frac{dE}{dx} \qquad \text{eq. 54}$$

A plot of the energy spectrum for overhead muons at sea level is shown in Figure 55. The energy loss, $\frac{dE}{dx}$, can be calculated using the Bethe-Bloch formula. Over a wide range of momentum, the energy loss for cosmic ray muons varies only logarithmically with momentum and is approximately proportional to the electron density, $\frac{Z}{A}$. For dense material, where λ is short compared to the muon decay length, $l = \beta c \gamma \tau$, where β and γ are the usual kinematic quantities, c is the velocity of light, and $\tau = 2.2\ \mu s$ is the muon lifetime. The muon stopping can be understood as the shifting of the spectrum shown in Figure 55 to the left, with the loss of muons with energies below some threshold.

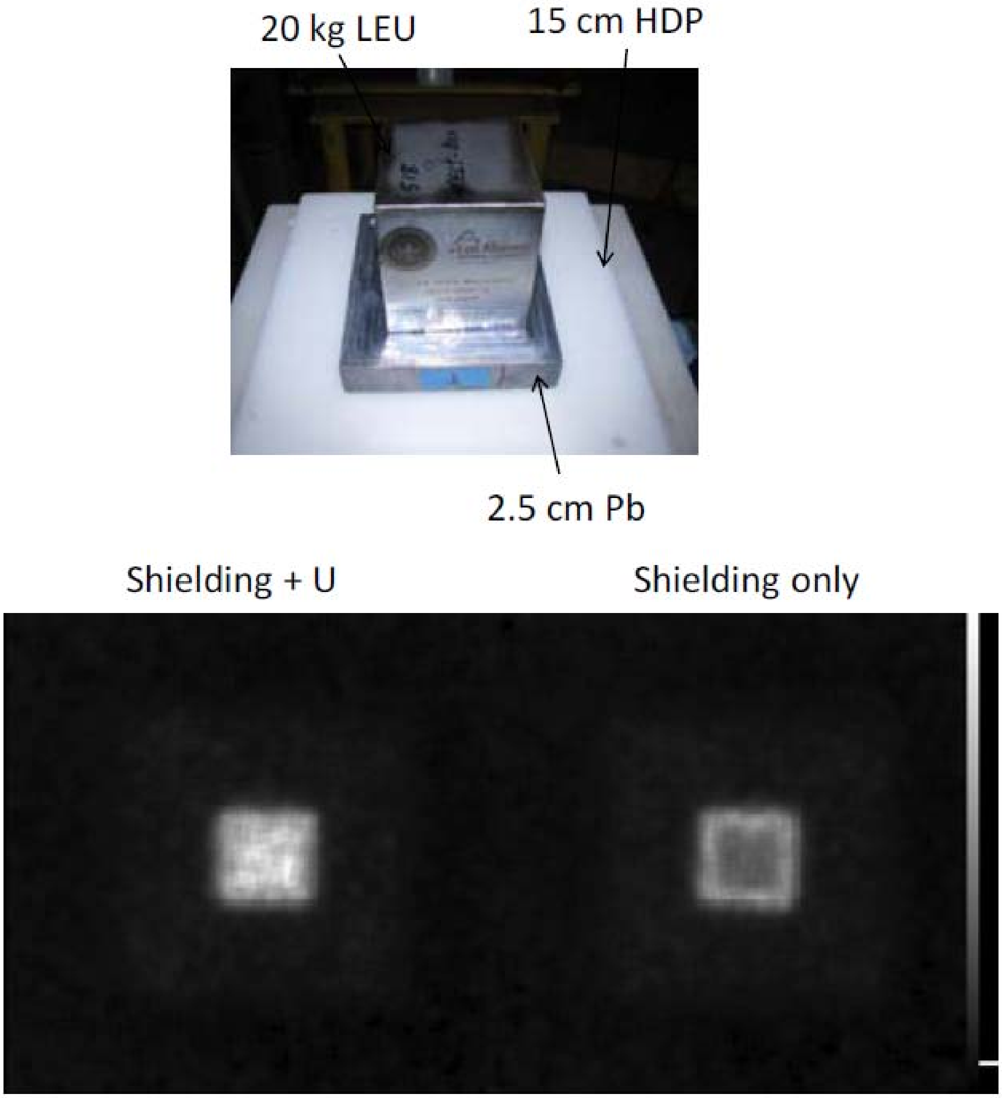

Figure 54 - Top) A photograph of the bottom parts of a layered shielding box with a 10×10×10 cm3 (~20 kg) uranium cube. When fully assembled, the shielding box surrounds the uranium with 5 cm of lead and surrounds the lead with 15 cm of borated polyethylene. Bottom right) a reconstructed image showing a slice at roughly the center of the object from a cosmic ray tomography of the shielding box. Bottom left) an image of the shielding box with the uranium. Grey scale of the image represents the strength of the scattering signal.

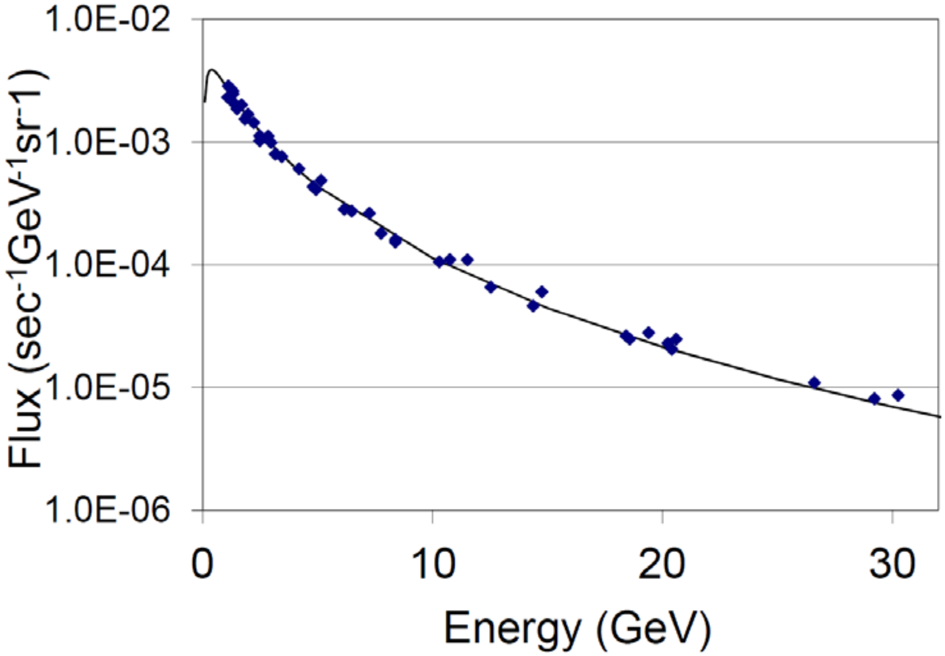

Figure 55 – Spectrum of vertical cosmic ray flux at sea level. Solid symbols are the data [73]. The line is a parameterized fit.

We have measured the transmission through three thicknesses (each) of lead, concrete and steel. The transmission image was obtained by making a ratio of the image of transmitted cosmic rays with the target in place to an image with no target. The bottom and top tracks for transmitted trajectories had to intersect in a horizontal plane at the center of the object to within a radius of 1 cm. This selection criterion was chosen empirically to filter outliers (high energy electrons, delta rays, soft muons) during the image reconstruction process. The resulting radiographs are shown in Figure 56. The negative of the natural log transmission as a function of calculated energy loss is plotted in Figure 5.

The slope of a linear curve constrained to go through the origin fitted to the data in Figure 57 is $1.03\ GeV^{-1}$. This is very close to the value of the peak of $1.2\ GeV^{-1}$ of the normalized spectrum, $\frac{1}{N}\frac{dN}{dE}$, in Los Alamos. The scatter between the different materials is not fully understood, but may be caused by the different geometry of the objects (concrete blocks being much thicker than lead). There is also a considerable uncertainty in the composition of the concrete, while the steel and the lead is well understood.

In addition to energy loss and stopping, cosmic rays also undergo Coulomb scattering from the charged atomic nuclei. Bethe and Moliere [74-77] developed a theory describing the angular distribution of charged particles transported through material foils. The angular distribution is the result of many single scatters. This results in an angular distribution that is Gaussian in shape with tails from large angle single and plural scattering. The scattering provides a novel method for obtaining radiographic information with charged particle beams [72]. More recently, scattering information from cosmic ray muons has been shown to be a useful method of radiography for homeland security applications [15, 17, 29].

The dominant part of the multiple scattering polar-angular distribution is Gaussian:

$$\frac{dN}{d\theta} = \frac{1}{2\pi\theta_0^2} e^{-\frac{\theta^2}{2\theta_0^2}} \qquad \text{eq. 55}$$

The Fermi approximation, where θ is the polar angle and θ_0 is the multiple scattering angle, is given approximately by:

$$\theta_0 = \frac{14.1\ MeV}{p\beta}\sqrt{\frac{l}{X_0}} \qquad \text{eq. 56}$$

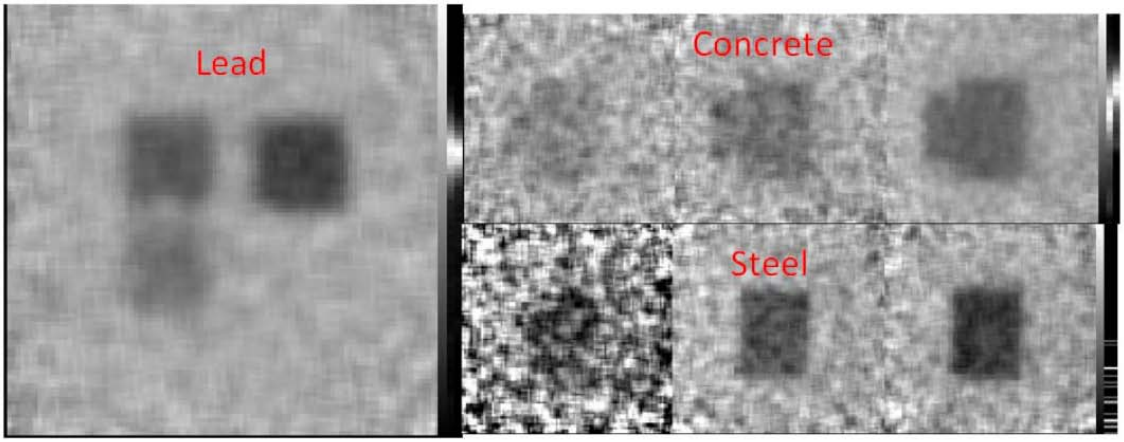

Figure 56 - Transmission images for the lead (left), concrete (top right) and steel (bottom right) targets. The three thickness of lead were radiographed in a single run. The other targets were imaged during individual runs. The grey scale is linear and ranges in value from 0.6 (black) to 1.2 (white) in transmission for all targets.

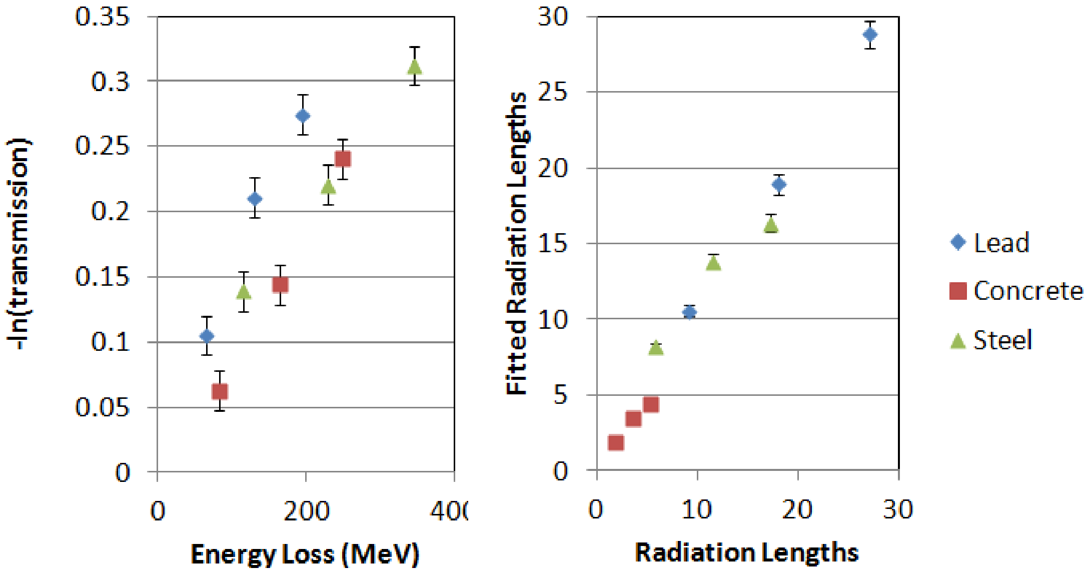

Figure 57 - Left) Negative of the natural log of transmission vs. calculated energy loss for three thickness each of lead, concrete and steel. Right) Fitted radiation lengths vs. radiation lengths.

The muon momentum and velocity are p and β, respectively, and X_0 is the radiation length for the material. This needs to be convolved with the cosmic ray momentum spectrum in order to describe the angular distribution. We have approximated the scattering distribution with a model that uses seven momentum groups, p_i.

$$\frac{dN}{d\theta} = \sum \frac{\mathrm{A_i}}{\sigma_\mathrm{i}} \mathrm{e}^{-\frac{\theta^2}{2\sigma_\mathrm{i}}} \qquad \text{eq. 57}$$

$$\sigma_i = \frac{14.1}{p_i} \sqrt{\frac{l}{X_0}} \qquad \text{eq. 58}$$

The model has been calibrated to data taken through the three thicknesses of lead described above. We fit the amplitudes, A_i, of each energy group, as well as the intrinsic angular resolution and a fixed number of radiation lengths due to the drift tubes and other structural elements of the muon detectors. The model does not account for changes in the shape of the muon spectrum due to stopping. A maximum likelihood fit to the set of lead data is shown in Figure 58. Also shown is the decomposition of one of the data sets into its momentum groups.

The momentum distribution obtained from this fit is compared with previous measurements of the momentum distribution at sea level and a parameterization that has been extrapolated to the altitude at Los Alamos, New Mexico (2231 m) in Figure 59. The agreement is remarkably good above 1 GeV. At lower energies the spectrum is sensitive to stopping and slowing down in the targets and to the electron component of the flux. These effects are not accounted for in this simple model but are important for simulating the tails accurately in the angular distribution as discussed previously.

With the amplitudes fixed by the global fit, described above, a maximum likelihood fit of the angular distribution for each voxel, where l/X_0 was the only parameter that was varied, was used to obtain a radiation length image of each of the data sets used above. A composite of the resulting images is shown in Figure 60. The fitted value for the thickness of the test objects in radiation lengths is plotted vs. actual radiation lengths in Figure 57.

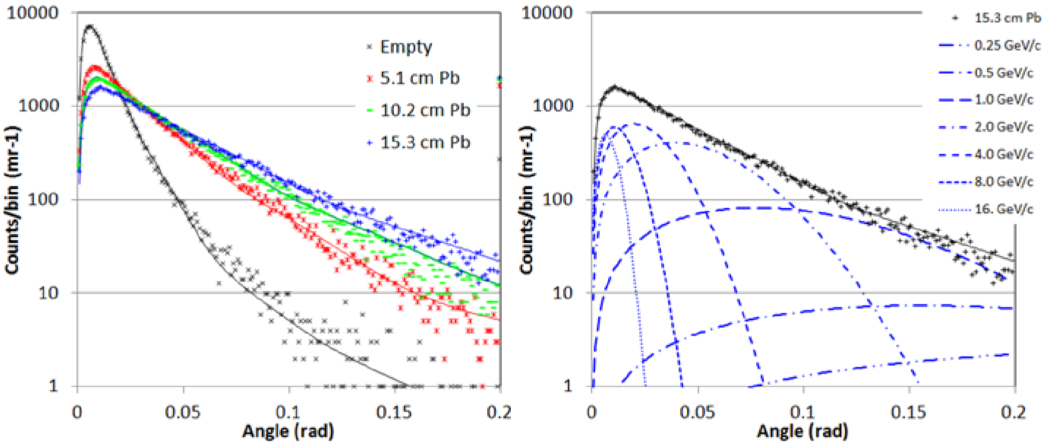

Figure 58 - Left) Measured angular distributions for various thickness of lead (points) and the fit (lines) for various thicknesses of lead. Right) The decomposition of the fit into energy groups. Empty shows the angular distribution with no object in the scanner.

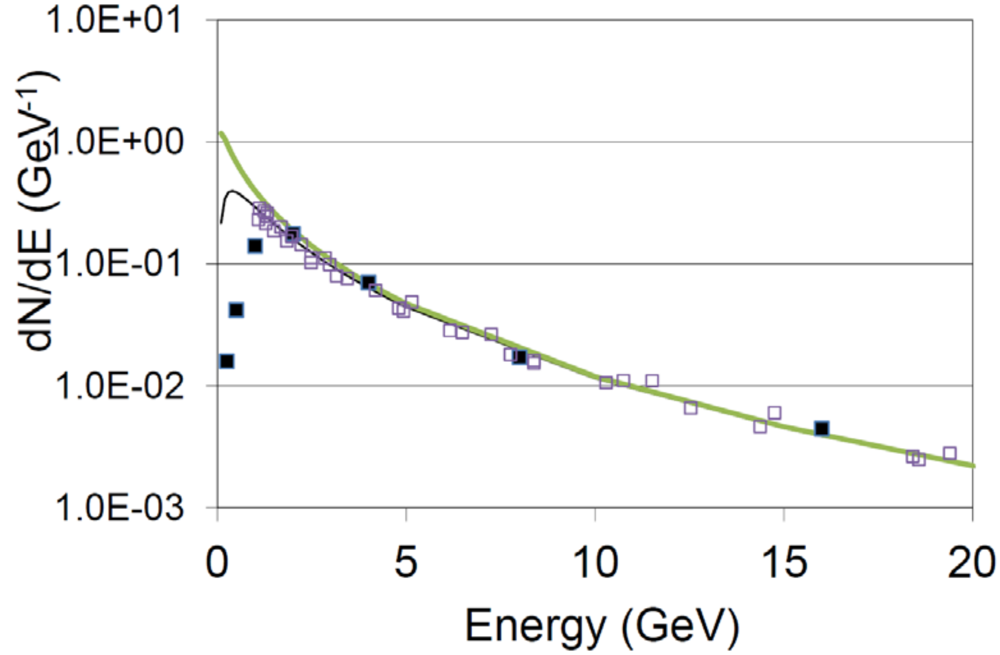

Figure 59 - Fitted spectrum (solid symbols) compared to model and previous data (open symbols). Also shown is the extrapolation of the sea level spectrum (black) to the altitude of Los Alamos (green curve).

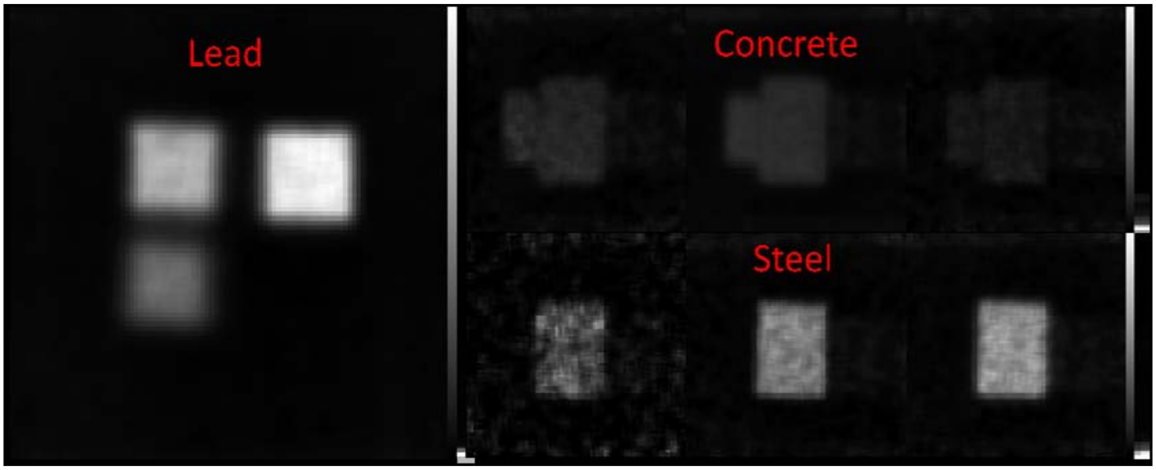

Figure 60 – Radiation length images of the test objects described above.

The same data have been used to obtain the thickness in both radiation lengths and in attenuation lengths. The known thickness and measured thickness agree to ~10-20%. The experimentally measured radiation lengths and attenuation lengths are plotted vs. each other in Figure 61. The fact that the different materials lie on different curves demonstrates material identification.

We have used experimental data collected with the Mini Muon Tracker to validate simple models of cosmic ray muon radiography. The negative of the natural logarithm of transmission was shown to be proportional to material thickness, t, for a given material and approximately proportional to $\frac{dE}{dx}t$ across a range of materials. Similarly, it was shown that l/X_0, the thickness of the object in radiation length units, was measured by fitting the polar angular distribution with a set of Gaussian distributions whose amplitudes were fixed at values fitted to calibration data. The momentum distribution fitted to the cosmic ray data agreed remarkably well above 1 GeV with previously measured data taken with a magnetic spectrometer. The combination of our measurements provided estimates of both the areal density and the material identification.

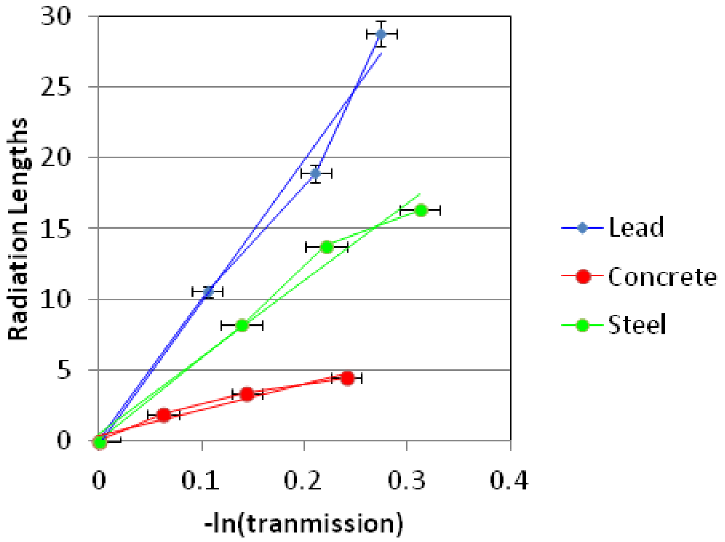

Figure 61 - Radiation lengths vs. attenuation lengths for the different test objects. The different materials lie on lines with different slopes, therefore demonstrating material identification.

Improving Material Identification Capabilities in Muon Tomography through Symmetry

The use of the signal from Coulomb scattering enables three dimensional imaging of complex scenes with high sensitivity to objects composed of materials with high atomic charge (Z). Material identification is determined by obtaining the density weighted radiation lengths of objects in the field of view. While cosmic rays can penetrate significant overburden, the technique suffers from relatively long exposure times and poor resolution because of the low flux and complex algorithms needed for reconstruction. A new method for obtaining improved position resolution and statistical precision for objects with spherical symmetry is demonstrated [78]. This new method improves material identification capabilities by removing the dependence on measuring transmission and instead relying on spherical symmetry and the higher resolution of Coulomb scattering measurements.

Although cosmic rays are highly penetrating and can image through considerable overburden, the flux is limited. The times required for detecting the presence of quantities of uranium or plutonium necessary to create a nuclear explosion are on the order of minutes, and the times needed to image these devices with ~2 cm resolution are on the order of hours. There are several algorithms for generating tomographic images using the input and the output trajectories of the cosmic rays[17]. Here we use a very simple method with a voxelated scene. For each voxel a one-dimensional histogram of scattering angle in 1 mrad steps from 0 to 200 mrad is created. The histogram is incremented for every cosmic ray for which the incident cosmic ray intercepts the voxel and for which the distance between the input and the output cosmic rays in the plane of the voxel is less than 2 cm. For large scattering angles this requirement associates measured scattering events with defined voxels in which most of the scattering occurred.

The scattering distribution for each voxel is fitted with a model that uses seven momentum groups [79], to approximate the muon momentum spectrum. The model has been calibrated with data taken through the three thicknesses of lead, 5.08, 10.16 and 15.24 cm. The amplitudes of each energy group, as well as the intrinsic angular resolution and a fixed number of radiation lengths due to the drift tubes and other structural elements of the muon detectors were fitted to minimize the logarithm of the likelihood function assuming the data were describe by a Poisson distribution. This model does not account for changes in the shape of the muon spectrum due to stopping. A maximum likelihood fit (Appendix D) to the set of lead data is shown in Figure 58. Also shown is the decomposition of one of the data sets into its momentum groups.

Images were constructed by fitting the angular distribution for each voxel to obtain the average number of radiation lengths of material that the ensemble of histogram entries has traversed. This reconstruction algorithm is scalable to large data sets, is simple to compute, and provides near optimal use of the scattering information. However, it doesn't optimally use the vertex information.

We have imaged several spherically symmetric objects: nested spherical shells of copper and tantalum, the copper shell alone, and a hollow lead ball. The outer radii were 6.5, 4.5, and 10 cm and the inner radii were 4.5, 1, and 2.5 cm for the copper, tantalum and lead shells respectively. Cartesian slices through the three dimensional tomograms, centered on the object, are shown in Figure 62.

The center of each object (x_c, y_c, z_c) was estimated by finding the centroid of the signal from the object using the Cartesian slices shown in Figure 62 and these were used for a one-dimensional reconstruction. A trajectory was defined by the line **x**(s) where:

$$x(s) = x_0 + x's \qquad \text{eq. 59}$$

$$y(s) = y_0 + y's \qquad \text{eq. 60}$$

$$z(s) = z_0 + z's \qquad \text{eq. 61}$$

Here (x_0, y_0, z_0) is a point on the line with direction cosines (x', y', z') . The point of minimum distance between (x_c, y_c, z_c) and (x_0, y_0, z_0) is given by $s = s_0$:

$$s_0 = \frac{(x_c - x_0)x' + (y_c - y_0)y' + (z_c - z_0)z'}{x'^2 + y'^2 + z'^2} \qquad \text{eq. 62}$$

The radius of closest approach is:

$$r_0 = \sqrt{(x(s_0) - x_c)^2 + (y(s_0) - y_c)^2 + (z(s_0) - z_c)^2} \qquad \text{eq. 63}$$

A two dimensional histogram of scattering angle versus radius is shown in Figure 63.

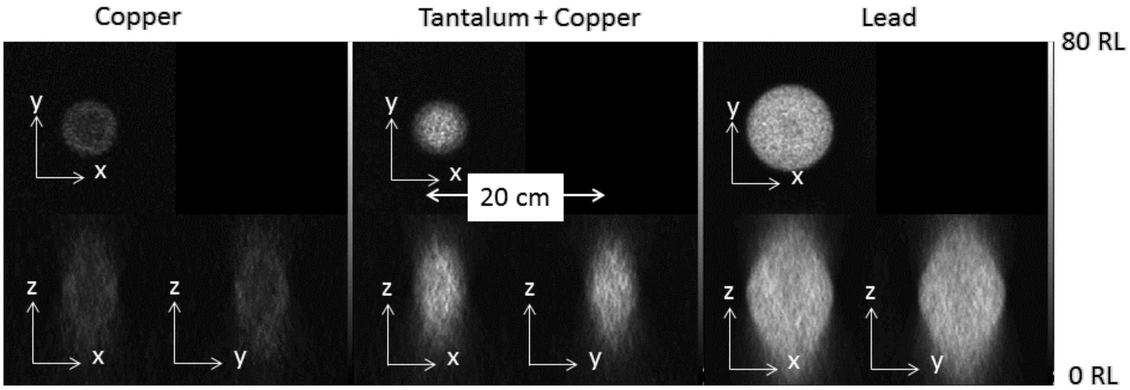

Figure 62 - Cartesian slices through the tomographs of the three objects. They are presented on the same position and grey scales. The grey scale is linear between 0 and 80 radiation lengths from black to white respectively.

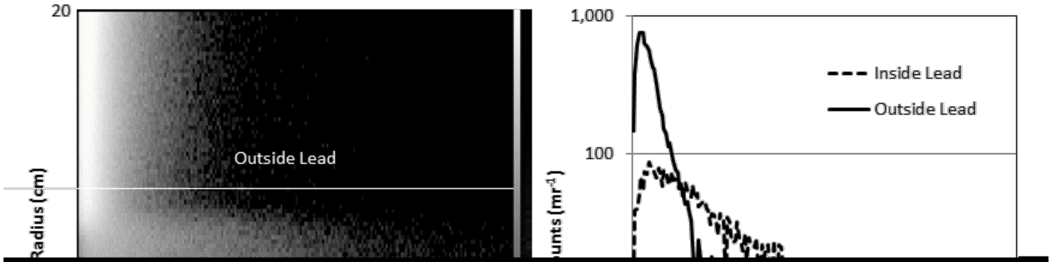

[redacted]

Figure 63 - Left) scattering angle vs. radius for the lead spherical shell. The grey scale is proportional to the logarithm of the number of counts per bin. On the right are plots of counts vs. scattering angle taken along the lines shown in the plot on the left.

A spherically symmetric object can be described by a set of shells at r_i with thickness $dr = (r_{i+1} - r_{i-1})/2$ and of a material with radiation length, X_{0i}, and weighted density ρ_{vi}/X_{0i}. The radiation length weighted path length, L_i, as a function of r_i can be obtained from the data shown in the 2-dimensional histogram by using the multi-group fitting technique described above for each radial bin. The fit to the lead data shown in Figure 58 has been corrected by 12% to account for the average $\frac{1}{\cos(\theta)}$ increase in thickness of the lead in the planar geometry and then used for the spherical symmetry algorithm.

The L_i are related to the set of radiation length weighted volume densities, ρ_{vj}, by a path length vector P_{ij} shown in Figure 64.

$$L_i = P_{ij} \frac{\rho_{vj}}{X_{0j}} \qquad \text{eq. 64}$$

The path length vector is the length a particle at r_i traverses through shell j:

$$\begin{aligned} P_{i,j} &= 0 && \text{, for } i > j \\ P_{i,j} &= 2\sqrt{\left(r_j + \frac{dr}{2}\right)^2 - r_j^2} && \text{, for } i = j \qquad \text{eq. 65} \\ P_{i,j} &= 2\sqrt{\left(r_j + \frac{dr}{2}\right)^2 - r_j^2} - 2\sqrt{\left(r_{j-1} + \frac{dr}{2}\right)^2 - r_{j-1}^2} && \text{, for } i < j \end{aligned}$$

This can be solved for the ρ_{vj}/X_{0i} using the regularization techniques described in Press [70]. This technique dampens the on-axis noise that arises in conventional Abel inversions[80] which is important here because of the poor statistics, especially at small radii.

The results for the three objects, each with 24 hours of exposure, are shown in Figure 65. The ρ_{vj}/X_{0i} for each of the materials studied: copper, tantalum, and lead, are within 10% of the tabulated values [36]. One can easily distinguish the void inside each of the shells, even the 1 cm radius void at the center of the tantalum shell. An analysis of the width of the edges in Figure 65 gives a position resolution of 3 mm which corresponds to our resolution measurements in Chapter 5.

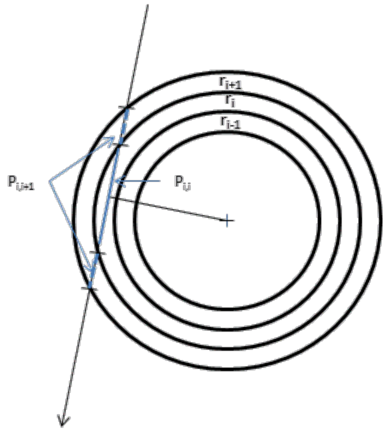

Figure 64) An Illustration of the path-length matrix, $P_{i,j}$.

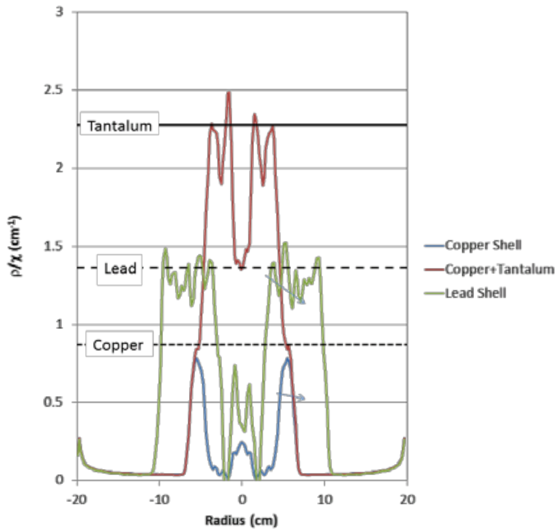

Figure 65) Radiation length weighted density vs. radius. The radii have been mirrored around r=0 (the data at negative *r* are the same as the data for positive *r*). Horizontal lines show the tabulated value of ρ/X.[36]

Cosmic ray scattering data were taken on a set of spherically symmetric objects. The data were analyzed assuming spherical symmetry. The data were stored in a two dimensional histogram of scattering angle vs. radius. The angular distributions were fitted by a sum of Gaussians whose amplitudes were fixed by fits to data taken on a set of planar objects. This resulted in one-dimensional plots of thicknesses in radiation lengths for each of the objects. These were analyzed with a regularized Abel inversion technique yielding radiation-length-weighted volume densities. These results allowed a quantitative evaluation of the material composition of the objects. It is also worth noting that these objects are difficult to study with conventional x-ray radiography due to their opacity from attenuation of the photon flux and large angle Compton scattering. Observing the cavities at the center of the two thicker objects requires high energy x-rays (4 MeV) and good anti-scatter techniques [81].

Muon Induced Fission Overview

Most conventional radiography methods involve measuring the transmission of particles, e.g. x-rays, from attenuation processes. It has been shown that the scattering information, as in the case of muon tomography and charged particle radiography, can be used for imaging as well. The common feature among all of these methods is the requirement for a detector that is located on the opposite side of the imaged object/plane with respect to the source of probing particles. In some scenarios, it may not be feasible to locate a detector in that configuration to measure the flux transmission. Thus, these scenarios require a single sided imaging technique whereupon the detector is placed between the source and the object of desire.

Single sided imaging has been used to look at the surfaces of objects, e.g. in airport security backscattering applications [82]; and single sided imaging has also been used to identify objects through photon backscatter and nuclear resonance fluorescence for homeland security applications [83-90]. These methods are either limited by penetration depth, or the steep increase in radiological dose required for obtaining useful imaging and isotopic information. By using cosmic-ray muons coincident with secondary signals such as fission neutrons, single sided imaging can be performed with high penetration and low dose. The tradeoff is that the natural muon flux is relatively low, ~10000 $\mu/m^2/min$, which requires longer integration time for imaging. Provided that an object is stationary, the use of cosmic-ray muons in these applications is an attractive alternative. Tagging cosmic-ray muons coupled with μ^- induced fission neutrons in coincidence enables us to detect and image SNM for warhead counting and treaty verification.

Our method is based on the use of signatures provided by interactions of cosmic-ray muons with an inspected object. As negatively charged muons stop, they are captured into atomic orbits in the stopping medium. In high-Z atoms, a stopped negative muon has a large probability of combining with one of the protons in a nucleus through the weak interaction forming an excited neutron and neutrino. In a fissionable material, stopped negative muons can trigger small fission chains, depending upon the effective multiplication of the neutronics system. Each fission reaction produces several gamma rays, 2-3 neutrons, and fission fragments. Products of this muon-induced fission create a distinctive signature that we can couple to muon trajectories in the target in order to create a tagged image within a coincidence window. In addition, cosmic-ray muons that pass through the target undergo Bremsstrahlung and pair-production resulting in potential photonuclear interactions.

The rate of stopped muons in small cubes (e.g. $1000\ cm^3$) of uranium that cause muon-induced fission is at most several a minute. The stopping rate varies with time, altitude and latitude, but in general is stable enough to produce a reliable probe. The rate of the secondary signal is directly proportional to the neutronics gain in the target. When compared to other sources of background, such as terrestrial gamma flux ($\sim 26000\,\frac{\gamma}{m^2 s}$), the rate is low. Different detectors and techniques can be applied in order to see the muon-induced fission signal. These include: neutron detectors, e.g. liquid scintillators, gamma-ray detection with high energy thresholds, pulse-shape discrimination, and establishing a coincidence window.

The amount of fast and thermal fission events depends upon the geometry of the object, the quantity of fissile material, as wells as other materials that may reflect, absorb, or moderate neutrons. The Boltzmann transport equation defines these components through a series of losses and gains in the neutronics system [91]:

$$\begin{aligned}\left[\frac{1}{v}\frac{\partial}{\partial t} + \Omega\cdot\nabla + \Sigma_{\mathrm{t}}(r,E,t)\right]\phi(r,\Omega,E,t)\\ = \int_0^\infty dE' \int_{4\pi} d\Omega' \Sigma_s(r,\Omega'\cdot\Omega,E'\to E)\phi(r,\Omega',E',t)\\ + \frac{\chi(E)}{4\pi}\int_0^\infty dE' \int_{4\pi} d\Omega' \nu(E')\Sigma_f(r,E',t)\phi(r,\Omega',E',t)\\ + Q(r,\Omega,E,t)\end{aligned} \qquad \text{eq. 66}$$

If the system geometrical size is small, the neutron population will be dominated by losses due to leakage current, $[\Omega\cdot\nabla]\phi(r,\Omega,E,t)$. Losses can also include absorption through nuclear resonances and scattering out of a particular energy group, $\Sigma_{\mathrm{t}}(r,E,t)\phi(r,\Omega,E,t)$. If the resulting neutrons from fission are not fast enough, then fast fission neutronics gain is also diminished. These effects can have a significant impact on reducing the fast fission signal component that is being observed in coincidence with muon tracks. Of course, if neutrons of sufficient speed can remain in the fissile material for a long enough period of time, because of a large object size or adequate reflection, fast fission will occur, resulting in chain reactions that may be measured with neutron detectors. The source of these neutrons is defined by the scattering kernel

$\int_0^\infty dE' \int_{4\pi} d\Omega' \Sigma_s(r, \Omega' \cdot \Omega, E' \to E)\phi(r, \Omega', E', t)$, the fission source term,

$\frac{\chi(E)}{4\pi} \int_0^\infty dE' \int_{4\pi} d\Omega' \nu(E')\Sigma_f(r, E', t)\phi(r, \Omega', E', t)$, and any additional external sources, $Q(r, \Omega, E, t)$.

There is a practical challenge in measuring signals from fast or thermal fission. A fast signal resulting from muon-induced fission consists of neutrons and gammas emitted in a narrow time window on the order of hundreds of nanoseconds. However, if neutrons from thermal fission are to be measured, the timing coincidence window must be extended by hundreds of microseconds to account for the moderation time. The wider coincidence gate results in higher rate of accidental coincidences due to random background. This issue is further compounded if the neutron or gamma detectors are intrinsically slow.

There are several neutron energy regions that are important to consider for uranium isotope identification. A muon induced fission in uranium produces neutrons with energies that are well described by the Watt spectrum [92], with an average energy of 1-2 MeV and a tail above 10 MeV (see Figure 66). At the lower end of this fast spectrum (~1 MeV), the difference between fission cross-sections of uranium isotopes, U-238 and U-235, is almost two orders of magnitude, $\sigma_{f,U238} = 0.014\ b$ and $\sigma_{f,U235} = 1.2\ b$. At the higher end of the spectrum (above ~5 MeV), the difference in fission cross-section becomes smaller, e.g. at 15 MeV $\sigma_{f,U238} = 1.2\ b$ and $\sigma_{f,U235} = 2.1\ b$. Another neutron energy region to consider is the thermal one, where the difference between isotopes becomes dramatic, with U-235 fission cross-section being over 7 orders of magnitude larger than U-238, e.g. $\sigma_{f,U238} = 1.7 \cdot 10^{-5}\ b$ and $\sigma_{f,U235} = 590\ b$ at 0.025 eV. The U-235 and U-238 total fission cross-sections are shown in Figure 67.

The fast and thermal energy regions can both be used for material identification. The challenges associated with the fast energy region is that the mean free path of a neutron in uranium is large (order of centimeters). This implies that without reflection, or large geometrical size, it is difficult to obtain several chain reactions for a good secondary signal measurement. The thermal energy region produces a fission reaction within an object proportional to its U-235 enrichment, but this requires longer coincidence times as the thermal neutrons are slow (~2200 m/s).

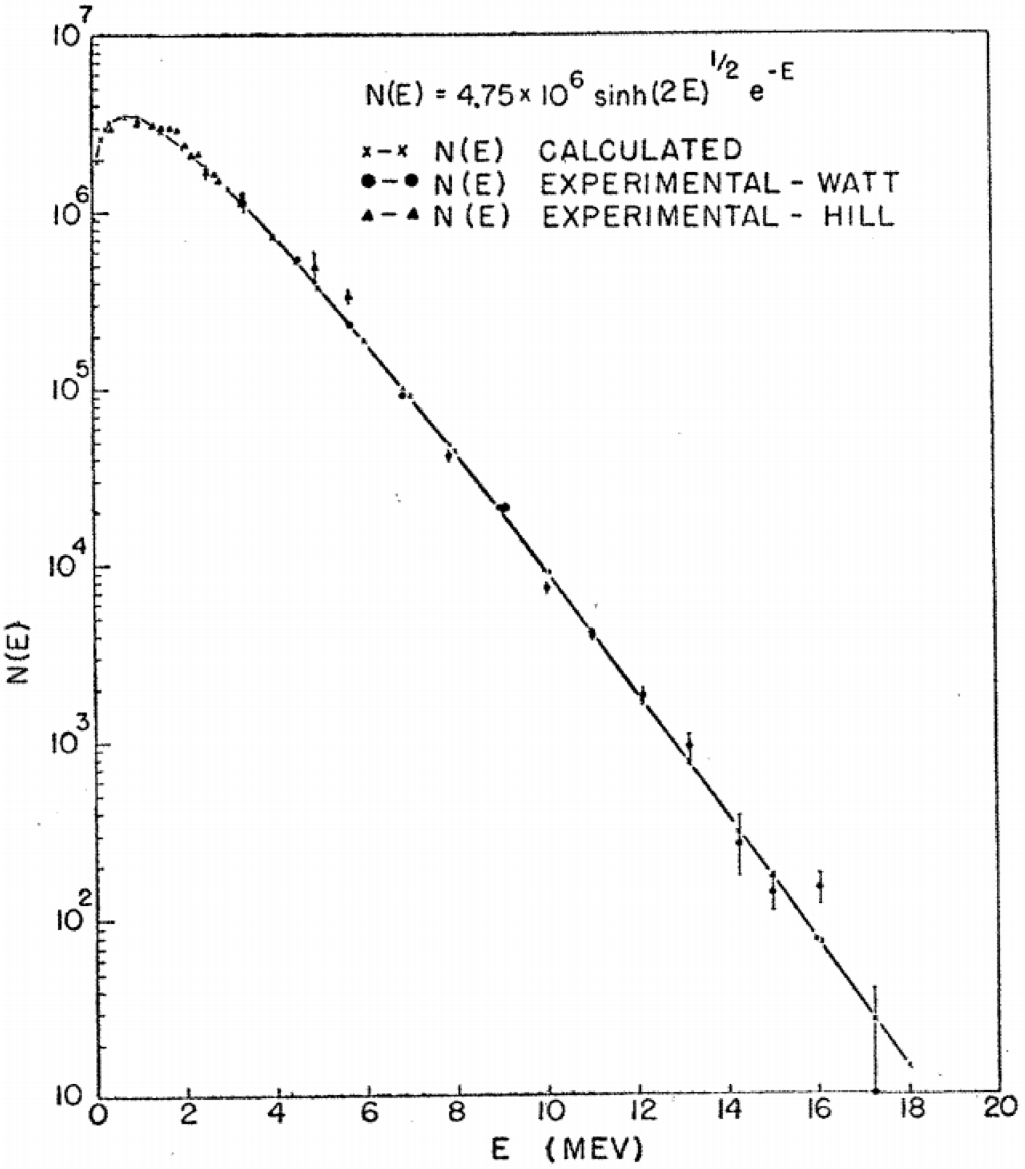

Figure 66 – Energy spectrum of fission neutrons. The calculated curve is based on the assumption of a Maxwellian distribution in the center-of-mass system for the neutrons emitted by a fission fragment [92].

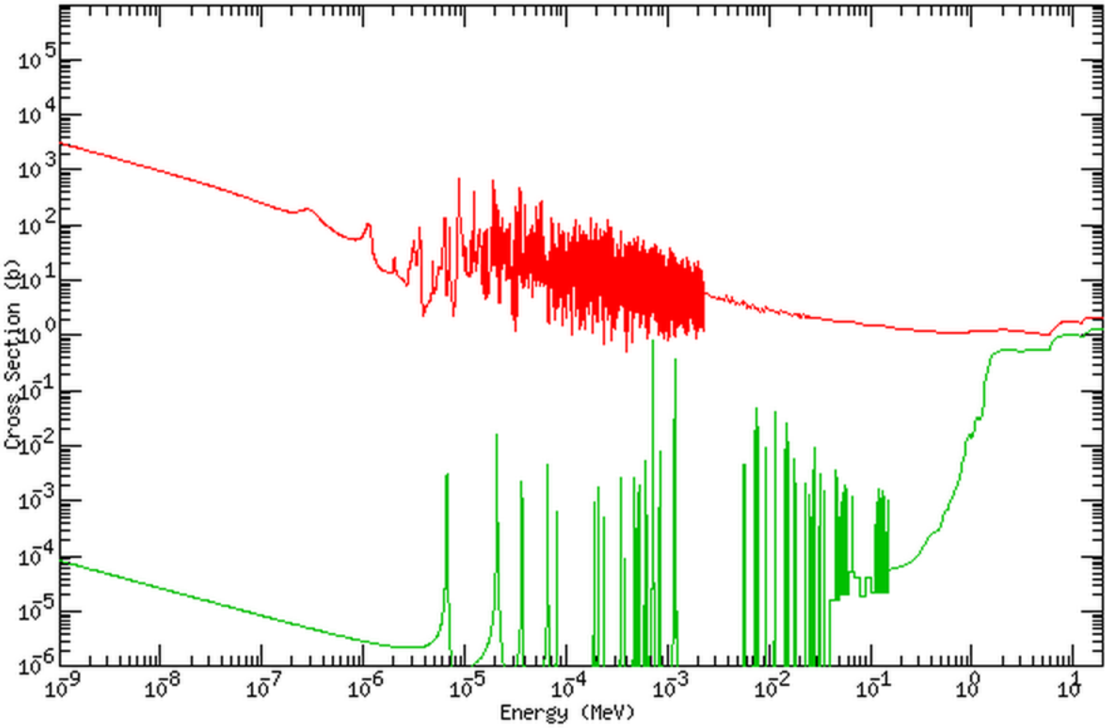

Figure 67 – Total fission cross-sections of uranium. U-235 is shown in red and U-238 is shown in green. There are three regions of interest for muon induced fission. The first is the region above 10 MeV where the difference in fission cross-section is small between U-235 and U-238. The second is the region around 1-2 MeV where the U-235 cross-section begins to become larger than U-238. Finally, the third region is at thermal energies where the U-235 cross-section is very large (data from ENSDF [93]).

Geant4 HEU, LEU, and DU Cube Simulation Study for Muon Induced Fission

Geant4 is used to understand the multiple physical processes that occur in muon induced fission. This is done by separating the muon induced fission process into several stages. First, the neutronics of three bare cubes, HEU, LEU, and DU are investigated. The HEU, LEU, and DU cubes have a side length of 10cm. The neutronics study is performed using fast and thermal neutrons in order to understand the outgoing neutron and gamma flux from fission. Second, a simulation is performed on the LEU cube surrounded by an inch of high density polyethylene moderator (HDPE). The HDPE affects the timing distribution of secondary signal neutrons, spreading them over several milliseconds and ultimately reducing the effectiveness of tagged muon radiography. Finally, the interactions of μ^+ and μ^- with the three cubes tie together the neutronics with the muon induced fission.

Neutrons of different energies are simulated within a cube of HEU, LEU, or DU. The output of the simulations is plotted to show the energy and time distributions in order to better understand the detector coincidence window sizes and rates. Several energy regions are investigated corresponding to the expected neutron energies that occur from muon-induced fission. The fission simulations produce a Watt spectrum in uranium that contains U-235 with a spatial distribution proportional to the neutron mean free path. A 4π spherical detector covering the entire solid angle with a radius of 30 cm is used to measure the distribution of particles emitted from each cube (see Figure 68). The high-precision *Neutron_HP* model is used to simulate the neutrons below 20 MeV accurately in Geant4 [94-98].

The following simulation runs used 1 million particles per case in order to study the energy and timing distribution of secondary signals with adequate statistics. Simulations were performed with an isotropic neutron source located at the center of the uranium. Neutron source energies were monochromatic at either 15 MeV or 0.025 eV. The uranium cubes were bare. The integrated results of the simulation are shown in a table following individual discussions of each component of the flux.

The gamma energy spectra for the bare cube simulations are shown in Figure 69. The HEU signal is stronger than the signal found in either the LEU or DU, which is to be expected due to the higher fission cross-section found in U-235. The average energy of the exiting gamma rays from fission and capture processes is between 1-2 MeV, with the spectrum extending beyond 8 MeV.

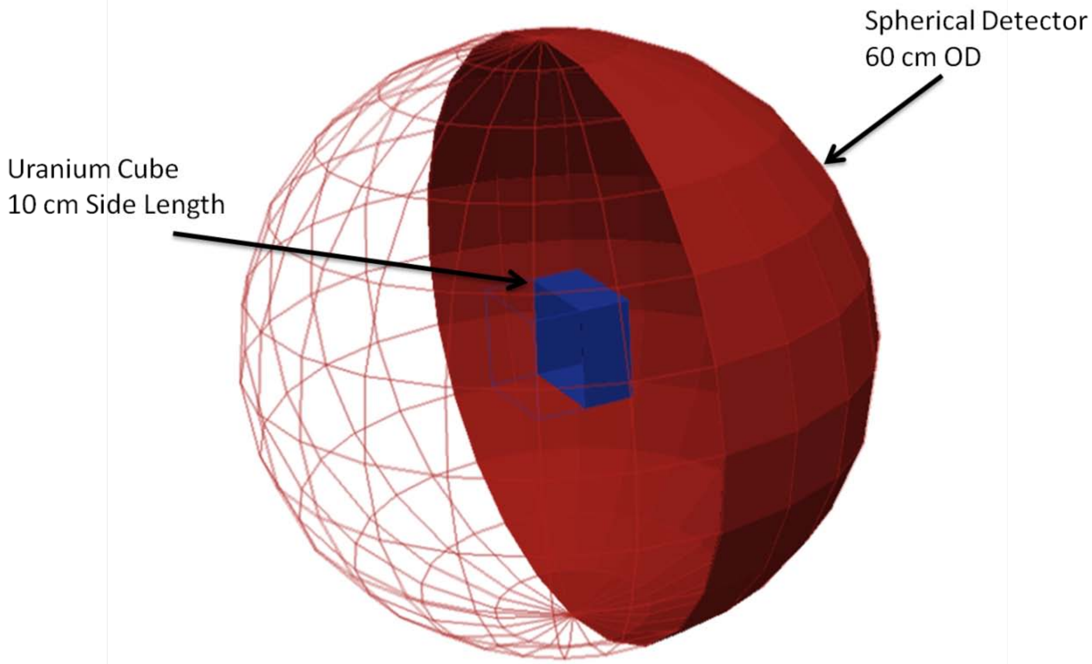

Figure 68 – Geant4 simulation geometry of a uranium cube with a 4π spherical detector surface. The spherical detector is sensitive to gamma and neutron flux that results from fission and other processes. This was used to study the neutronics output of different uranium enrichments with muon and neutron sources.

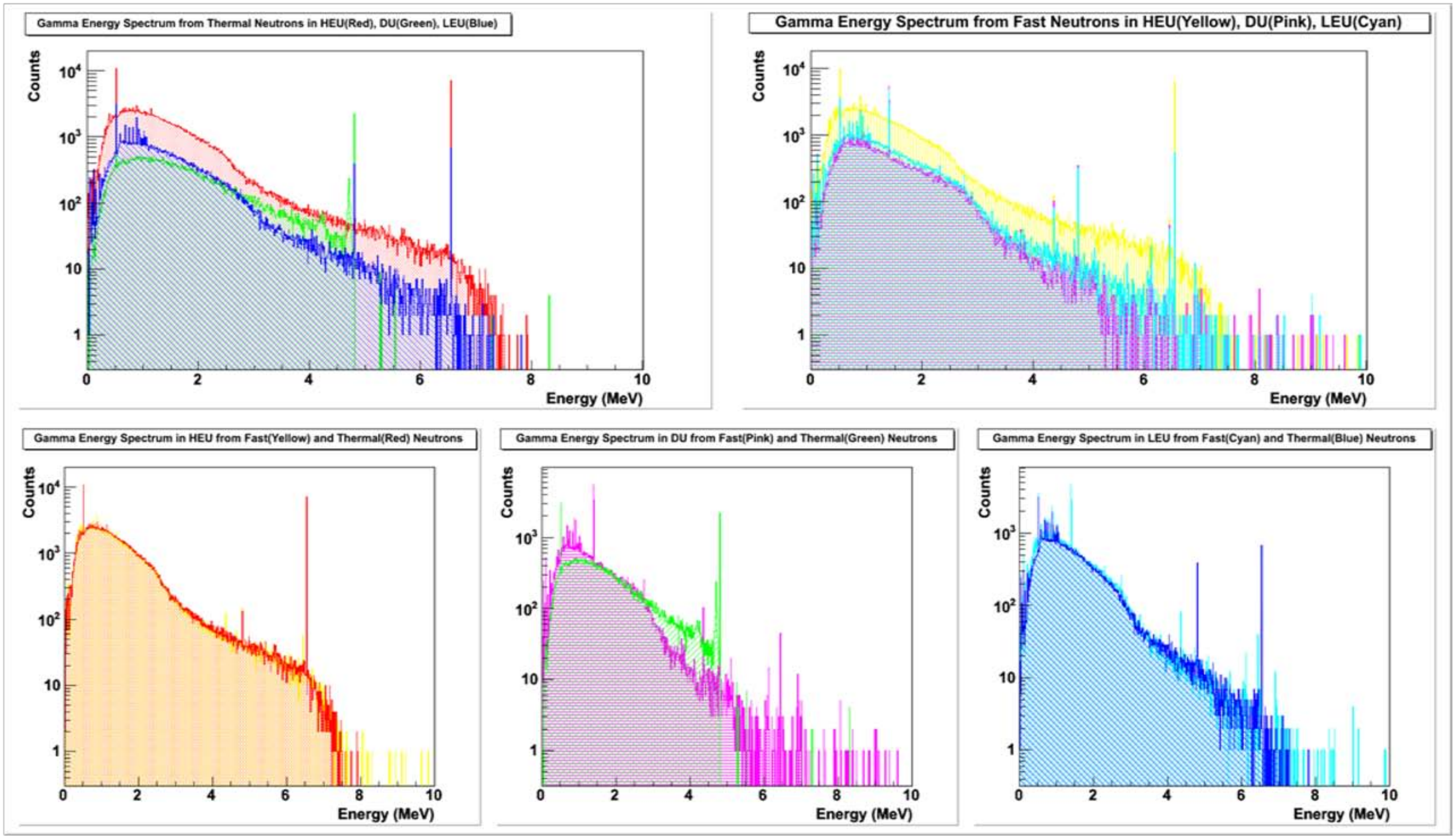

Figure 69 – Neutronics simulation of three uranium cubes consisting of depleted uranium, 19.5% U-235 low enriched uranium, and 90% U-235 high enriched uranium. A thermal neutron and fast (15 MeV) neutron point source was used in each cube. The secondary gamma energy spectra are compared. Several differences are immediately noticeable, first the overall yield of the gamma is larger in the HEU as would be expected by the larger fission cross-section of U-235. In DU, there is a significant amount of gamma resulting from neutron capture as indicated by thermal neutrons starting in DU (where no fission would be expected).

The temporal distribution of the gamma events resulting from the capture and fission of thermal and fast neutrons is shown in Figure 70. The thermal neutrons stimulate fissions quickly in LEU and HEU, producing secondary gamma-rays at the times shorter than 10 microseconds. The thermal neutrons in DU scatter for a longer period of time prior to their capture and release of gamma rays. In the fast energy range, the gammas can be seen largely as a result of fast fission. Delayed gammas are also visible, but they are not useful for muon tagged radiography due to their much later occurrence in time. A coincidence window for prompt gamma detection from muon induced fission should be set below 10 microseconds.

The energy spectra of the neutron flux resulting from the capture and fission of thermal and fast neutrons in the LEU, DU, and HEU cubes are shown in Figure 71. In DU, the escaping thermal neutrons have a broadened energy from upscattering and downscattering. The LEU and HEU show a typical Watt spectrum resulting from thermal fission. The fast neutrons also show a Watt fission spectrum that is softened by the DU in the cube. Additionally, the 15 MeV neutron source escape peak is also present in the energy plot. The secondary neutron detection from muon induced fission involves measuring polychromatic neutrons, covering the Watt spectrum.

The timing spectra of the neutron flux resulting from fission of thermal and fast neutrons in HEU, LEU, and DU cubes are shown in Figure 72. In DU, the thermal neutrons that escape reach the detector much later than the fission neutrons in the LEU and HEU cube. For both fast and thermal fission in the LEU and HEU cubes, the prompt neutrons are measured within several microseconds. The measurement of delayed neutrons is possible, but according to the timing distribution, this measurement would require a prohibitively large coincidence window. For the accidental background suppression the coincidence window for measuring secondary neutrons from muon-induced fission must be closed within several microseconds of the fission event.

The neutronics analysis is concluded with one final study that describes the timing spectrum of secondary gammas and neutrons when moderation is present. The geometry consists of the LEU cube (10 cm on a side) surrounded by 5 cm of high density polyethylene (HDPE). Neutrons are generated as an isotropic point source in the center of the cube with thermal or fast energies. The timing and energy spectra of the secondary neutrons and gammas from the moderated LEU cube are shown in Figure 73. The HDPE extends the time until neutron detection from several microseconds to milliseconds. This

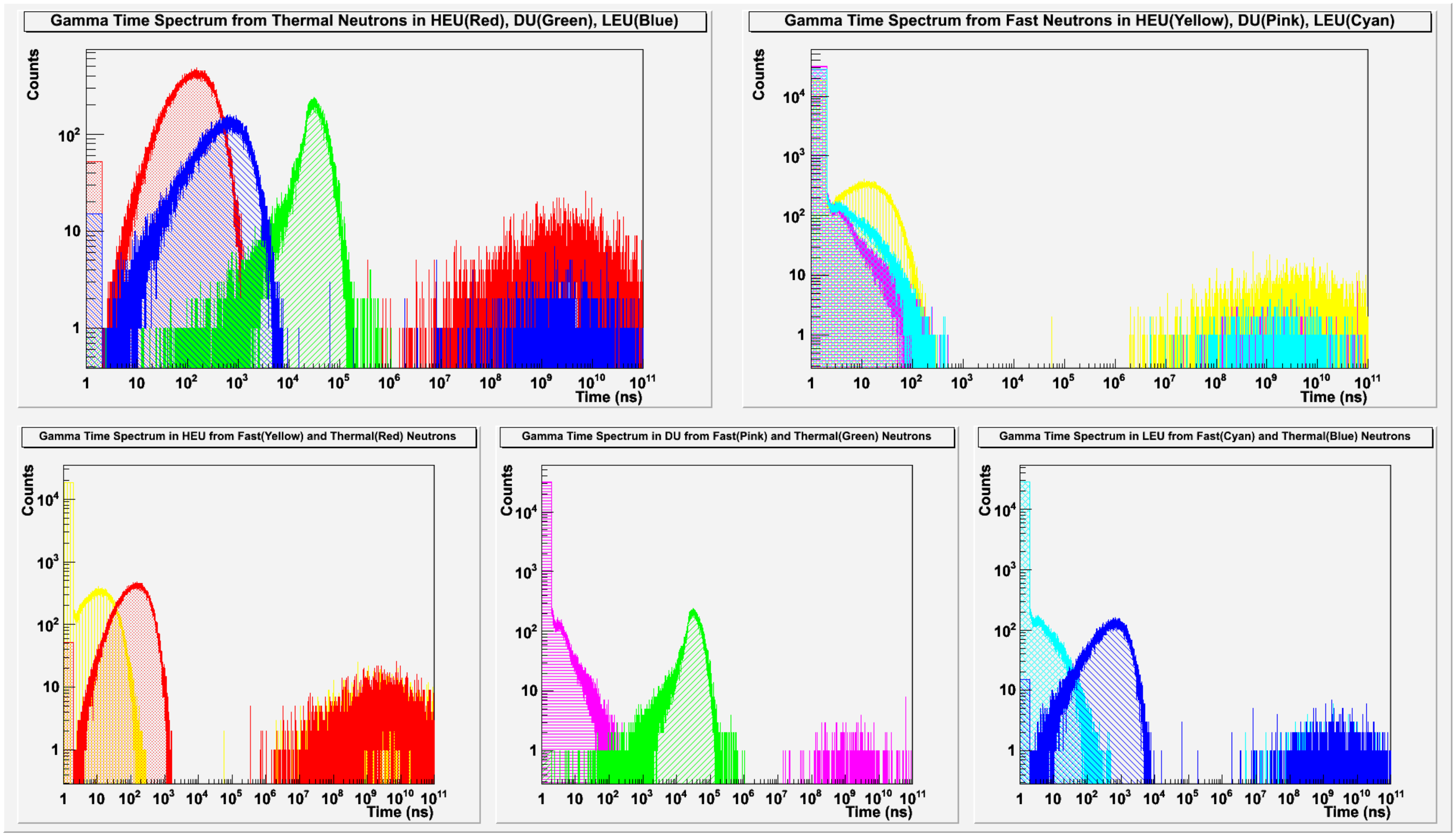

Figure 70 – Neutronics simulation of three uranium cubes consisting of depleted uranium, 19.5% U-235 low enriched uranium, and 90% U-235 high enriched uranium. A thermal neutron and fast (15 MeV) neutron point source was used in each cube. The secondary gamma time distributions are compared. The thermal neutrons fission quickly in LEU and HEU, which results in secondary gamma time distributions below 10 microseconds. The thermal neutrons in DU scatter for a longer period of time prior to capturing and releasing gamma rays. In the fast energy range, the gammas can be seen largely as a result of fast fission. Delayed gammas are also visible, but are not important for this analysis.

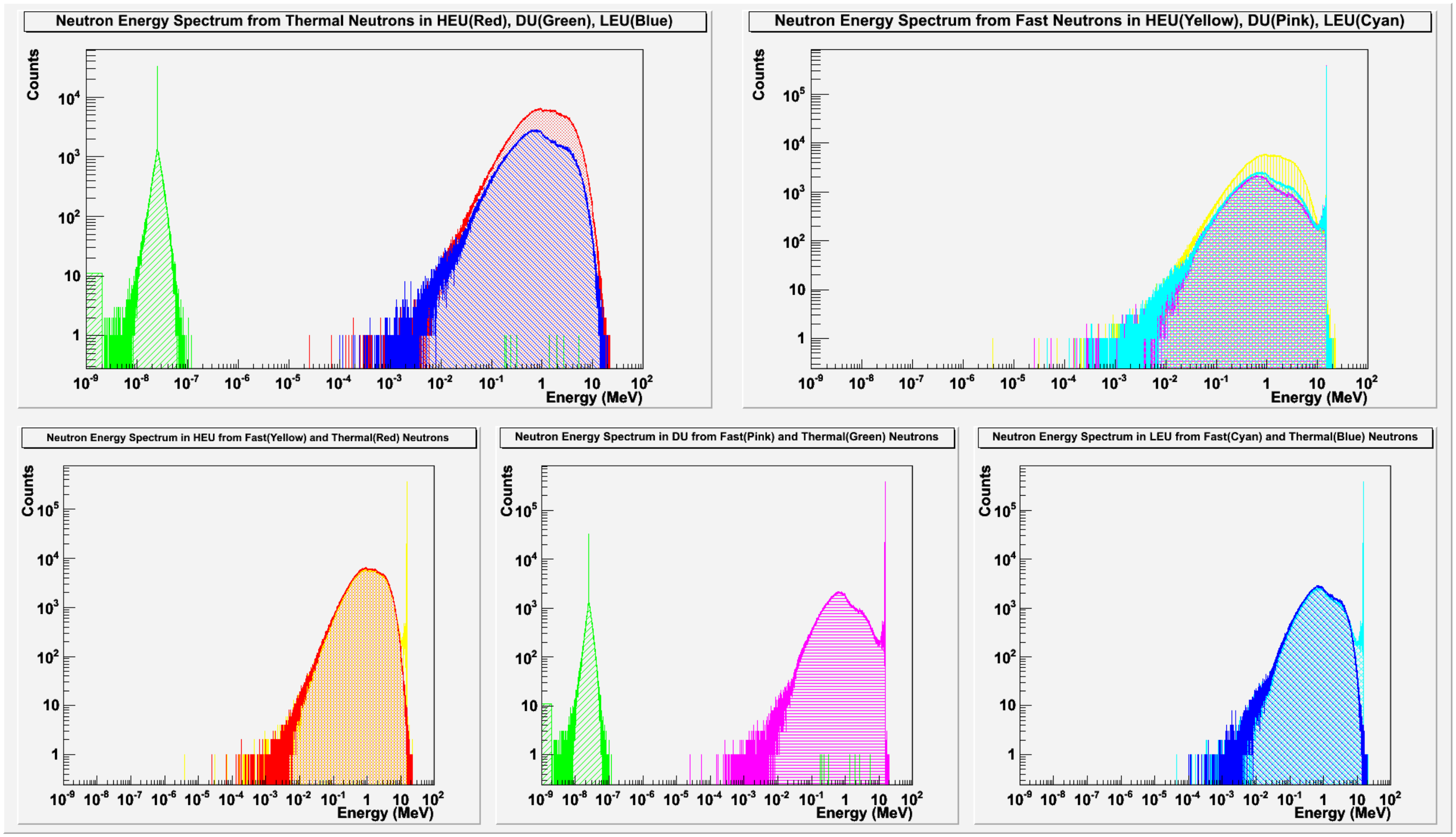

Figure 71 - Neutronics simulation of three uranium cubes consisting of depleted uranium, 19.5% U-235 low enriched uranium, and 90% U-235 high enriched uranium. A thermal neutron and fast (15 MeV) neutron point source was used in each cube. The secondary neutron energy spectra are compared. In DU, the thermal neutrons that escape have a broadened energy from upscattering and downscattering. The LEU and HEU show a typical Watt spectrum resulting from thermal fission. The fast neutrons also show a Watt fission spectrum that is softened by the concentration of DU in the cube. Additionally, the 15 MeV source neutron is also seen at the upper part of the energy plot.

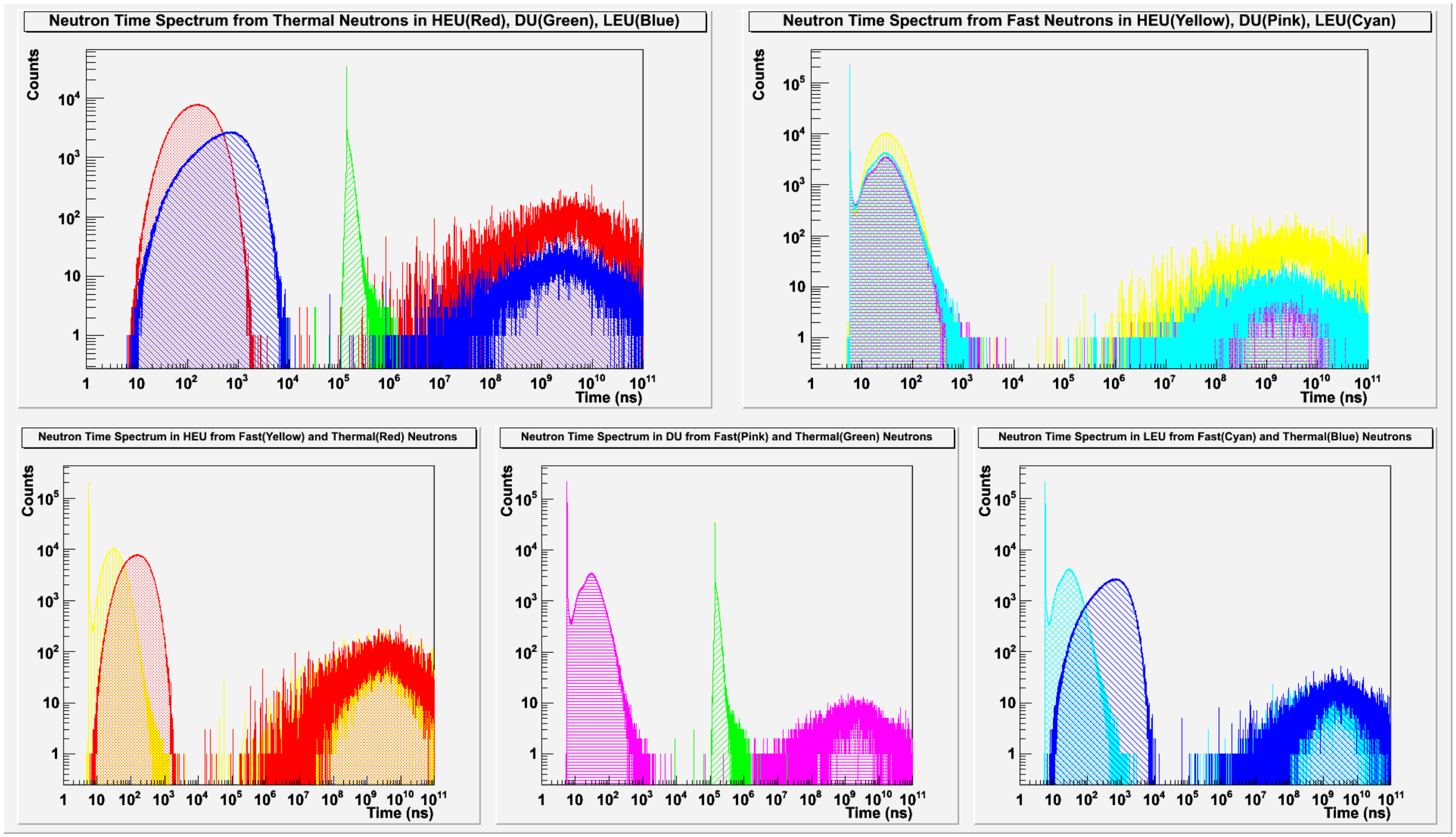

Figure 72 - Neutronics simulation of three uranium cubes consisting of depleted uranium, 19.5% U-235 low enriched uranium, and 90% U-235 high enriched uranium. A thermal neutron and fast (15 MeV) neutron point source was used in each cube. The secondary neutron timing distributions are compared. In DU, the thermal neutrons that escape reach the detector much later than the fission neutrons in the LEU and HEU cube. For both fast and thermal fission in the LEU and HEU cubes, the prompt neutrons are measured within several microseconds. Additionally, the delayed neutrons are visible but not important for purposes of measuring muon induced fission.

implies that a coincidence window would need to span several milliseconds, significantly increasing the background count rate and therefore decreasing the signal-to-noise ratio of muon induced fission and tagged radiography. For the same reason the signal-to-noise ratio is also reduced in moderated neutron detectors, such as HDPE wrapped He-3. The most promising solution to this problem is to utilize fast liquid scintillators with good pulse-shape discrimination characteristics in order to measure fast neutrons. This was done after several experimental studies that investigated several detectors including: HDPE moderated He-3, He-4, lithium, and liquid scintillators. The experimental results shown in this dissertation are from the EJ-301 liquid scintillators.

Following the neutronics study in the different uranium cubes, several simulations were performed using μ^- and μ^+ distributed uniformly throughout cubes of DU, LEU (19.5% U-235), and HEU (90% U-235). A parametric study of two muon energies, 2 GeV and 1 MeV, was performed. The higher muon energy approximately represents the average energy of the cosmic-ray muon spectrum. These muons lose energy in matter slowly, primarily through ionization. In the lower energy range, the muons stop in thin layers of material due to the increase in their energy losses, dE/dx. The output of the parametric simulation predicts the secondary neutron and gamma-ray rates measured in a 4π detector per muon generated. By using Geant4, it is shown that both μ^- and μ^+ produce secondary particles in uranium. At lower energies, the μ^- slows down rapidly and stops with a high probability of capture in the uranium. This process is simulated by the *muMinusCaptureAtRest* process in Geant4, and produces secondary particles and additional fissions. Secondary particles in uranium can also be created by photonuclear processes caused by cosmic-ray muon Bremsstrahlung.

The stopping of μ^- in uranium cubes (10 cm side length) is shown in Figure 74. This primarily results in muon induced fission with secondary neutrons and gammas that are released proportional to the amount of U-235 enrichment, which enhances the neutronics gain of the cube. The muon induced fission that occurs from stopped μ^- produces a signal that is dependent on neutronics gain. This signal can be useful for treaty verification applications. The signal rates per stopped muon are shown in the table at the end of this section.

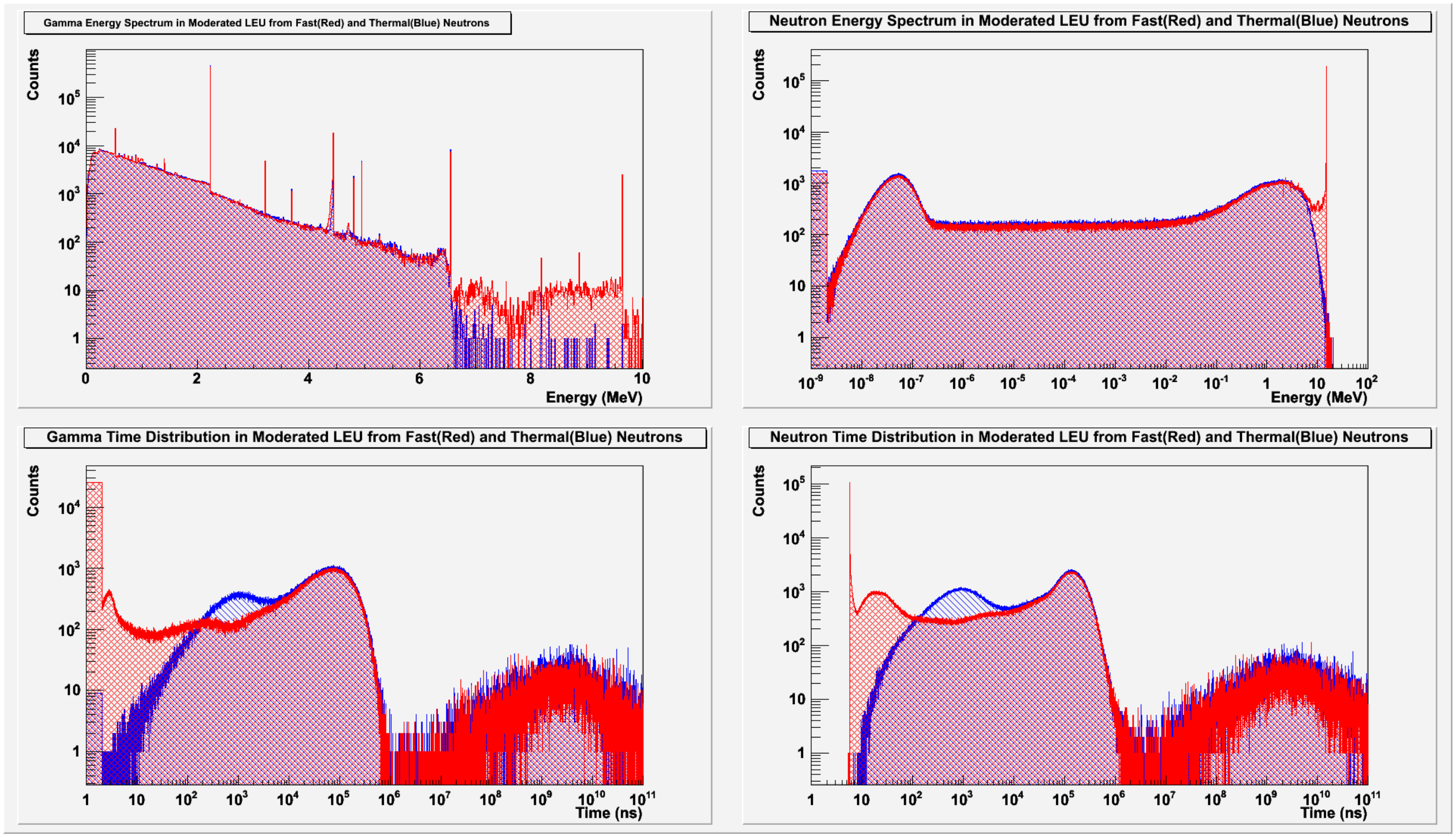

Figure 73 – A study of moderation times for fission in LEU using Geant4. A point source of thermal and fast (15 MeV) neutrons was simulated in the center of the LEU (10 cm side) cube. The LEU was surrounded by 5 cm of HDPE on each side. The most significant issue is that the secondary signals are stretched out to several milliseconds from the initial event. For muon induced fission tagged radiography purposes, this results in a coincidence window that is too large.

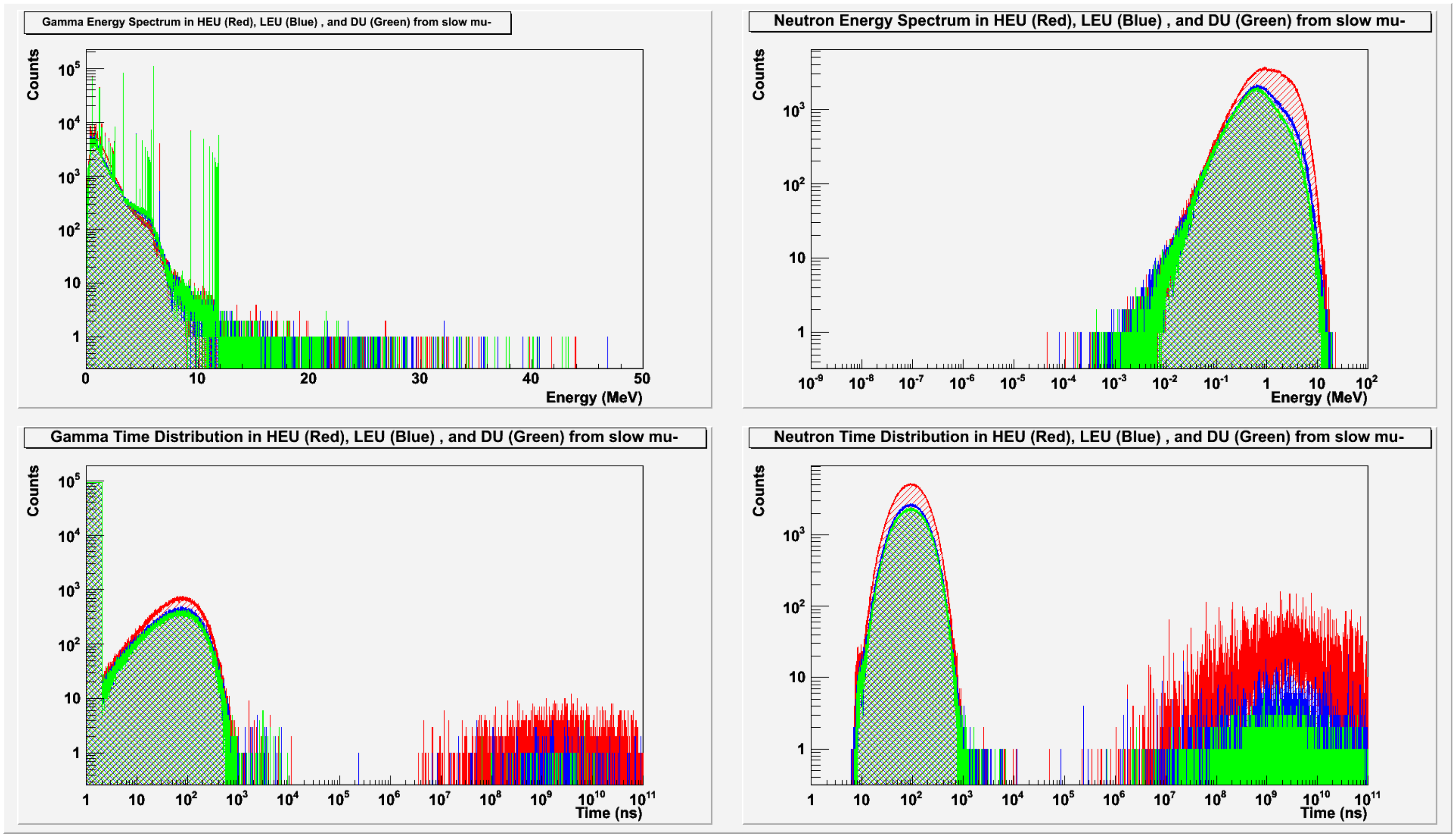

Figure 74 – Secondary neutron and gamma energy spectrum that result from μ^- stopping in cubes of uranium: HEU (red), LEU (blue), and DU (green). The primary mode of neutron generation is due to muon induced fission from μ^- capture. Two important features are 1) more gain for increasing U-235 concentration and 2) the secondary prompt signals occur below 1 microsecond.

Fast cosmic-ray muons of both charges and slow μ^{+} generate secondary neutrons at much lower rates compared to μ^{-} induced fission. For example, if a slow μ^{+} stops in uranium it decays releasing a fast positron and neutrinos. The positron creates photons through Bremsstrahlung, which may result in photonuclear production of neutrons. Additionally, fast muons may also radiate photons from Bremsstrahlung in high-Z targets. The rates of these effects are much smaller (by several orders of magnitude) when compared to μ^{-} induced fission. Figure 75, Figure 76, Figure 77 show that prompt neutrons are produced by these processes, but at a much smaller frequency.

The conclusion of this study is that the μ^{-} induced fission produces a dominant source of neutrons as compared to the other processes. Additionally, the increased neutronics gain found in the HEU provides increased secondary signal that is useful for tagged radiography. By using this additional signal, materials with high neutronics gain can be tagged and located. As was shown, both neutrons and gammas are useful signals for this method. We have determined that neutrons are a more desirable secondary signal to measure for several reasons: 1) the gamma background is large, 2) low-energy gamma-rays are self-shielded in SNM, and 3) the majority of the secondary neutron signal is the result of μ^{-} fission events.

The rates of secondary neutrons in the three different cubes are shown below. These rates refer to the prompt neutrons measured within 1 μs of the muon either passing through or stopping in the uranium cubes. As will be shown in the next section, this time frame corresponds to the prompt signal measured by the EJ-301 liquid scintillator detectors. The rates were determined by using the simulations mentioned previously in this section: 1 million incident muons, uniform source distribution, three types of uranium cubes, two muon speeds, two muon charges, and a 4π detector. The majority of the secondary neutron signal is emitted from the muon induced fission process induced by slow μ^{-}. The HEU U-235 enrichment results in an increase of neutron output by a factor of two compared to the LEU. The difference between neutron output in DU and LEU is much smaller. Theoretically, it may be possible to differentiate DU from LEU as there is a 15 percent difference in the neutronics gain.

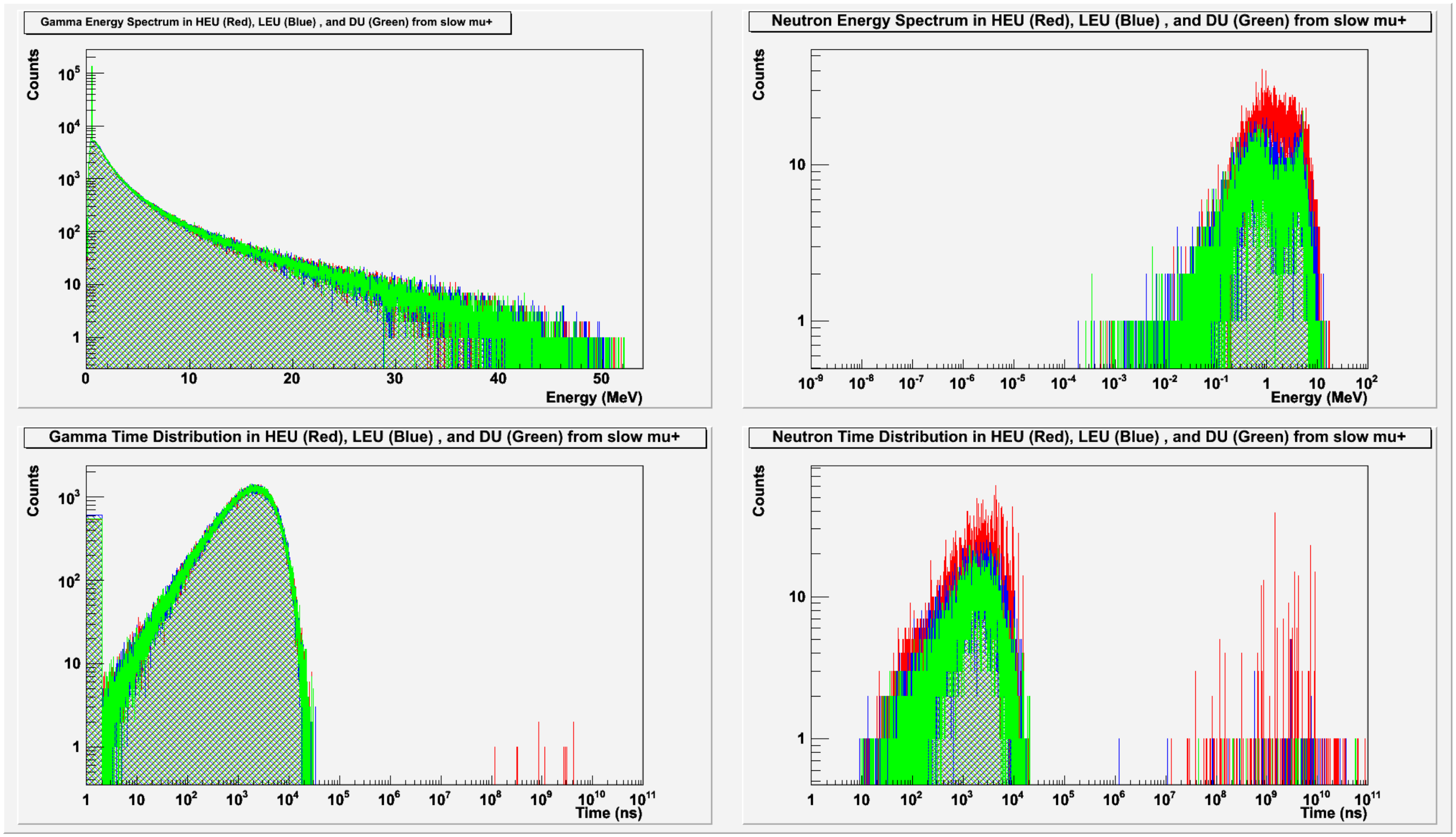

Figure 75 - Secondary neutron and gamma energy spectrum that result from μ^+ stopping in cubes of uranium: HEU (red), LEU (blue), and DU (green). The primary mode of neutron generation is due to μ^+decay resulting in a fast positron that yields a Bremsstrahlung photon and subsequent photonuclear processes. There is a small increase in neutronics gain when comparing the HEU to the other cubes.

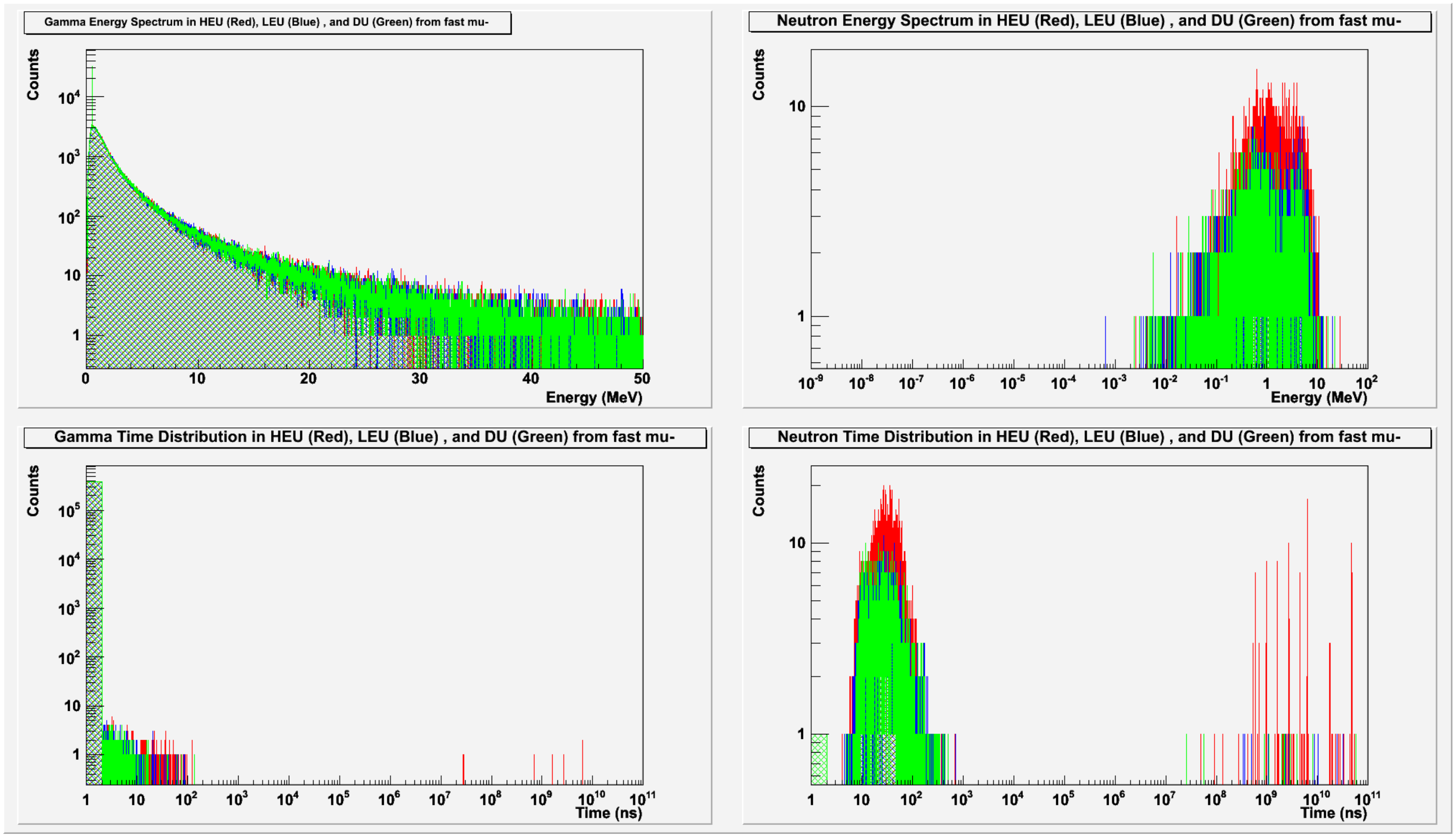

Figure 76 - Secondary neutron and gamma energy spectrum that result from fast μ^- passing through cubes of uranium: HEU (red), LEU (blue), and DU (green). The primary mode of neutron generation is due to direct μ^- Bremsstrahlung photon production and subsequent photonuclear processes. There is a small increase in neutronics gain when comparing the HEU to the other cubes.

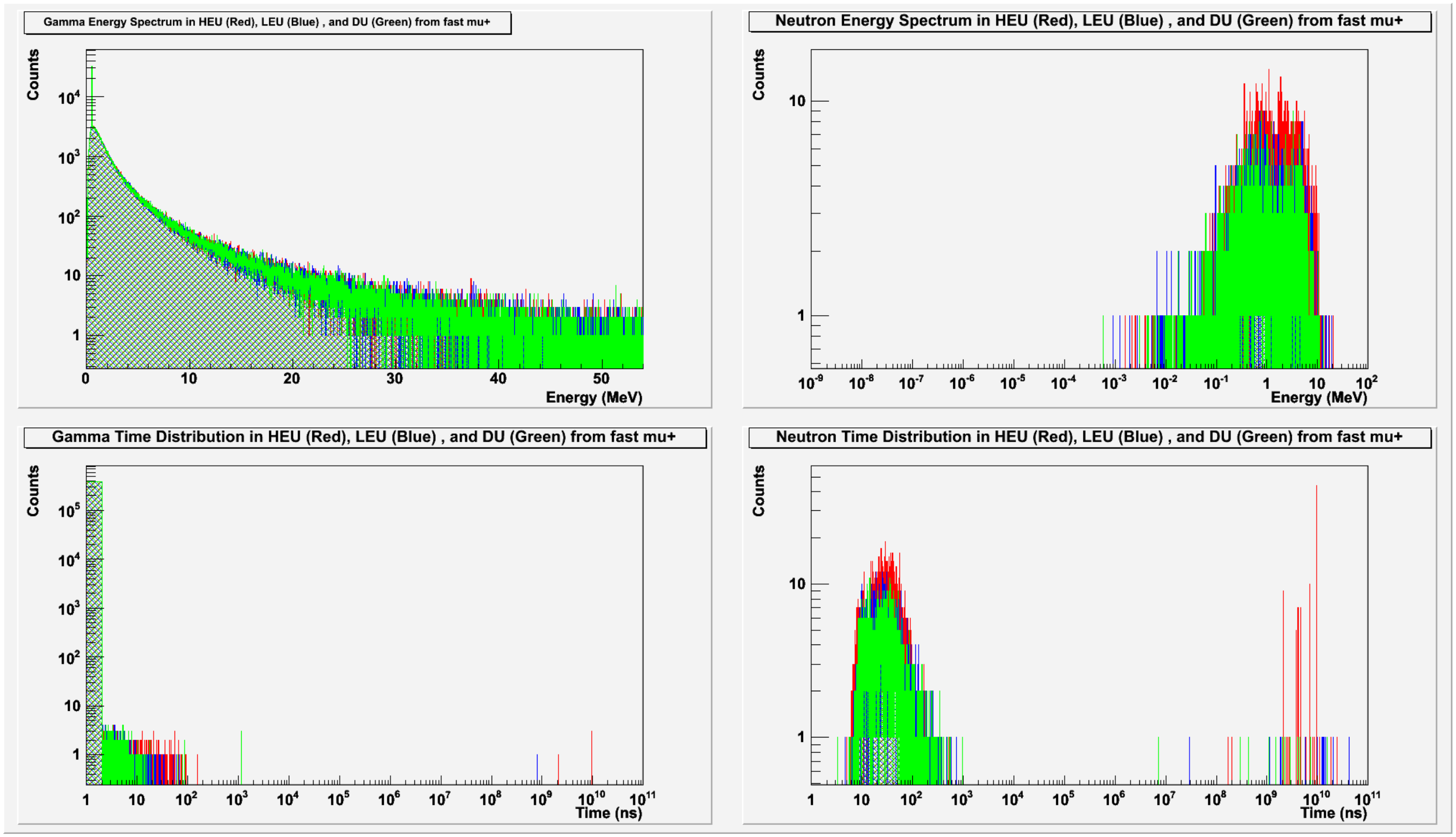

Figure 77 - Secondary neutron and gamma energy spectrum that result from fast μ^+ passing through cubes of uranium: HEU (red), LEU (blue), and DU (green). The primary mode of neutron generation is due to direct μ^+ Bremsstrahlung photon production and subsequent photonuclear processes. There is a small increase in neutronics gain when comparing the HEU to the other cubes. The difference between μ^+ and μ^- neutron production is minimal.

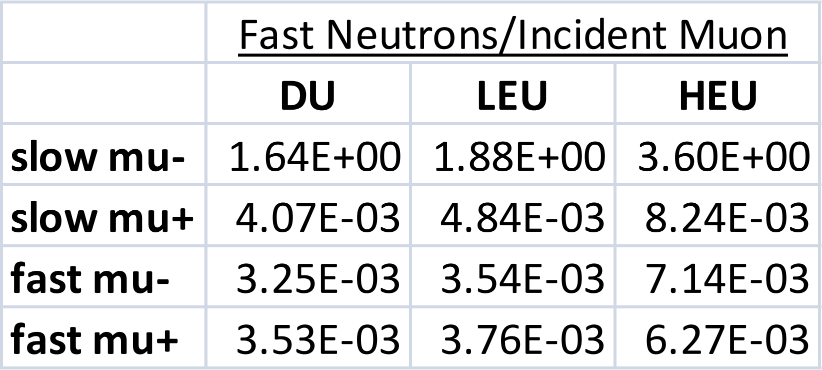

	Fast Neutrons/Incident Muon		
	DU	**LEU**	**HEU**
slow mu-	1.64E+00	1.88E+00	3.60E+00
slow mu+	4.07E-03	4.84E-03	8.24E-03
fast mu-	3.25E-03	3.54E-03	7.14E-03
fast mu+	3.53E-03	3.76E-03	6.27E-03

Table 5 – Rate of fast neutrons that are emitted from bare cubes of uranium (10 cm on a side): HEU (90% U-235), LEU (19.5% U-235), and DU (0% U-235). The majority of secondary neutron signal is emitted from the muon induced fission process induced by slow μ^-. The HEU results in an increase of neutron output by a factor of two compared to the LEU. The difference between DU and LEU is much smaller.

Measuring Muon Induced Fission in Uranium: LEU and DU

We used the MMT for experimental measurements of muon induced fission in 1 liter uranium cubes. Two cubes were studied including a depleted uranium cube (DU) and a 19.5% U-235 enriched uranium cube (LEU). The LEU cube consists of 4 uranium plates bound in a thin steel structure for criticality safety purposes. Two EJ-301 liquid scintillator detectors were located approximately 10 centimeters from the face of the uranium cube. A Mesytec MPD-4 pulse shape discriminator separated neutrons from the gamma background, and the discriminated neutron TTL signal was injected into the MMT data stream. The cubes were measured individually: 23.5 hours for the DU cube and 48 hours for the LEU cube. Multiple scattering reconstructions show the experimental setup in Figure 78.

The stopped track radiography is created before the tagged coincidence image. This is done by measuring events that do not create hits in the bottom supermodule of the MMT. Both of the stopped images are shown in Figure 79. The stopping image has poorer edge resolution when compared to the resolution of multiple scattering. This is due to the wide angle scattering that occurs in softer, high dE/dx muons. There is also a large penumbra due to having many events that miss the bottom supermodule at the edge of the field of view. The stopped track radiography is filtered with a coincidence window containing secondary signals which enables the tagging of muon induced fission.

Two EJ-301 liquid scintillator detectors were used for the measurement of fast neutrons resulting from muon induced fission. This liquid scintillator, made by Eljen Technology, has excellent pulse shape discrimination properties, and it is identical to the well recognized liquid scintillator, NE-213. The scintillator is packaged in a right cylinder with an outer diameter of 12.7 cm and a 2.54 cm thickness. Each scintillator was connected to a Hamamatsu photomultiplier tube (PMT) with a voltage between -1300 V and -1400 V. Both detectors were gain matched with a Cs-137 source photopeak of ~50 mV. The pulse shape discrimination was tested with several gamma sources (including the Cs-137 source) and a Cf-252 neutron source. Following detector calibration, the output of the detectors' neutron discrimination was injected into the MMT data stream. The secondary signals measured by the EJ-301 were clocked with a 200MHz frequency (a temporal resolution of 5 ns).

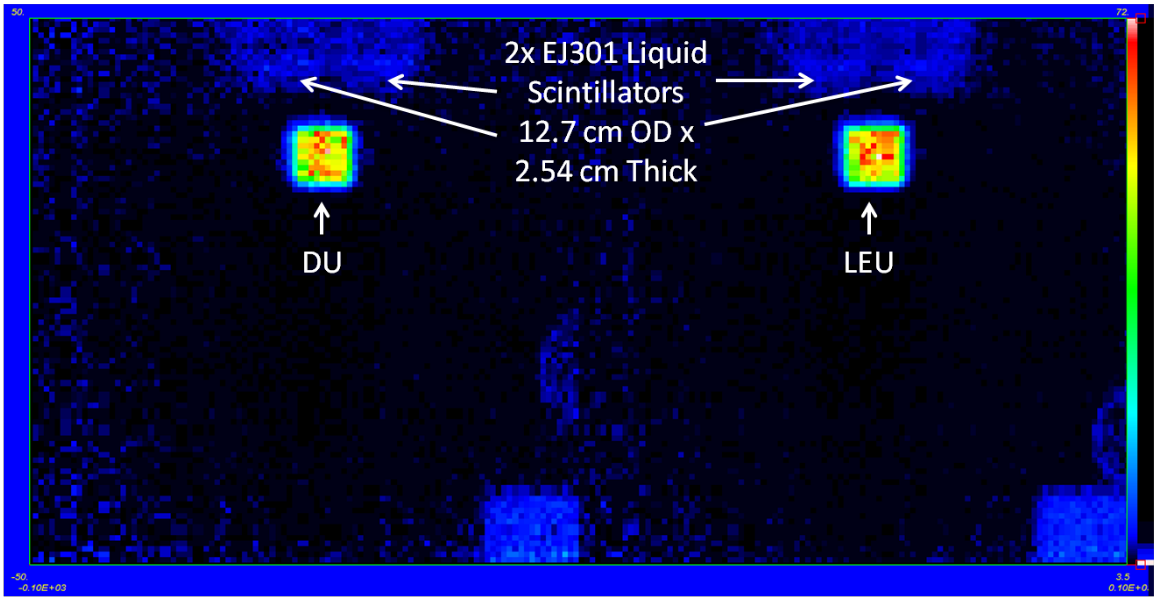

Figure 78 – Multiple scattering measurement of DU (23.5 hours, left) and LEU (48 hours, right). The cubes were placed in a nearly identical location for purposes of comparing stopped tracks and tagged stopped tracks. Several objects in the bottom right corner are extraneous to the scene.

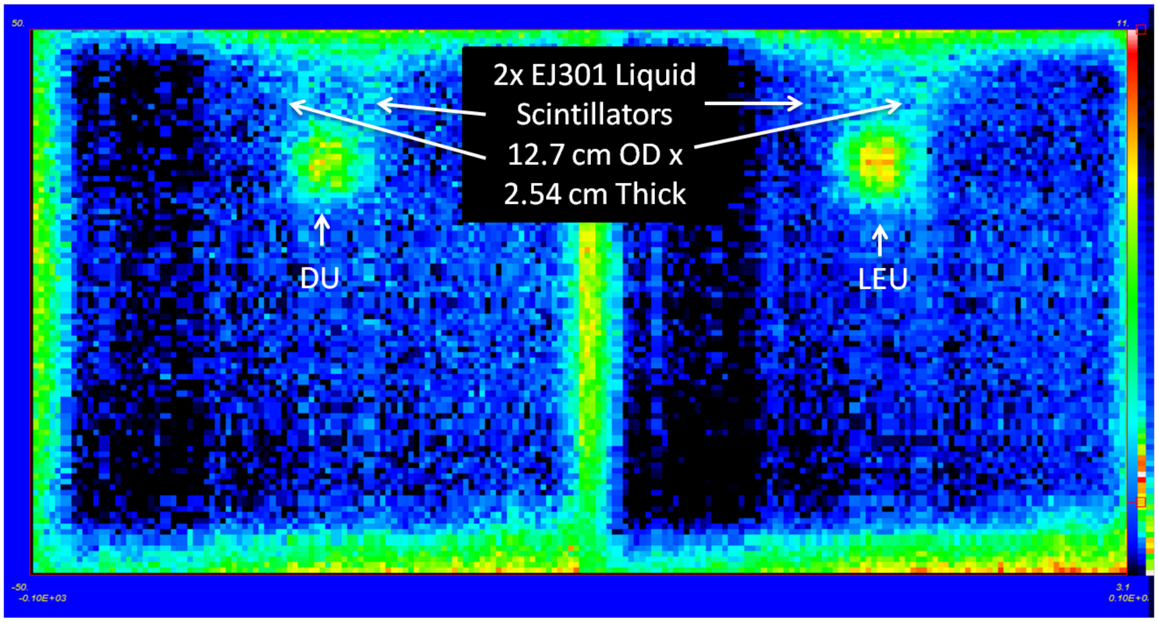

Figure 79 – Stopped track radiography of DU (23.5 hours) and LEU (48 hours) cubes. Both images are normalized to the duration of measurement. The stopped track radiography is the first step in performing coincidence tagged radiography.

The coincidence signal gate width was set between 350 ns and 650 ns for both the LEU and DU runs. This was determined by recording the difference in time stamps between each EJ-301 detector hit and the stopped muon track within a microsecond. Only the first and nearest event was included. Given that the measured rate of coincidence is low, $\sim 10^{-3} \frac{\mathrm{n}}{stopped\ \mu}$, the probability of consecutive non-related coincidences occurring in the window is negligible, $10^{-3} * 10^{-3} \rightarrow 10^{-6}$. This ensures that looking for the first, nearest event is adequate for short time windows with infrequent events. The results of the timing spectrum are shown in Figure 80 and Figure 81. For both cube measurements, the detectors returned a peak of hits between 350 ns and 650 ns. It was assumed that the timing distribution was composed of prompt and delayed components of muon induced fission. With this model, the prompt component was fitted with a Gaussian with a width corresponding to system time resolution. The delayed component, which indicates the lifetime of the muonic atom, was fitted using the exponential. The total temporal distribution of events was fitted using a sum of three components: exponential decay, Gaussian, and constant background.

$$y = B + Pe^{-\left(\frac{t-t_0}{\tau}\right)} + Ae^{-\frac{(t-t_0)^2}{2\sigma}} \qquad \text{eq. 67}$$

Where B is a constant background, P is an amplitude at some peak time of the exponential decay, t_0 is the peak location for both the Gaussian and exponential curve, τ is the exponential lifetime associated with the muon capture lifetime, and σ is the Gaussian width.

The lifetime of the muon capture in uranium was measured for each cube. In the literature, the lifetime of muonic U-235 is ~72 ns and in U-238 is ~77 ns [99]. A Poisson distribution was assumed for the data, and the temporal distribution was fitted. The fitting parameters were varied in order to minimize a summed log likelihood ratio, which accounts for statistical weightings near zero counts. This was done using Excel's solver function while the peak time location, t_0, was fixed. Eighty-seven degrees of freedom were used in the summation that was minimized by the solver.

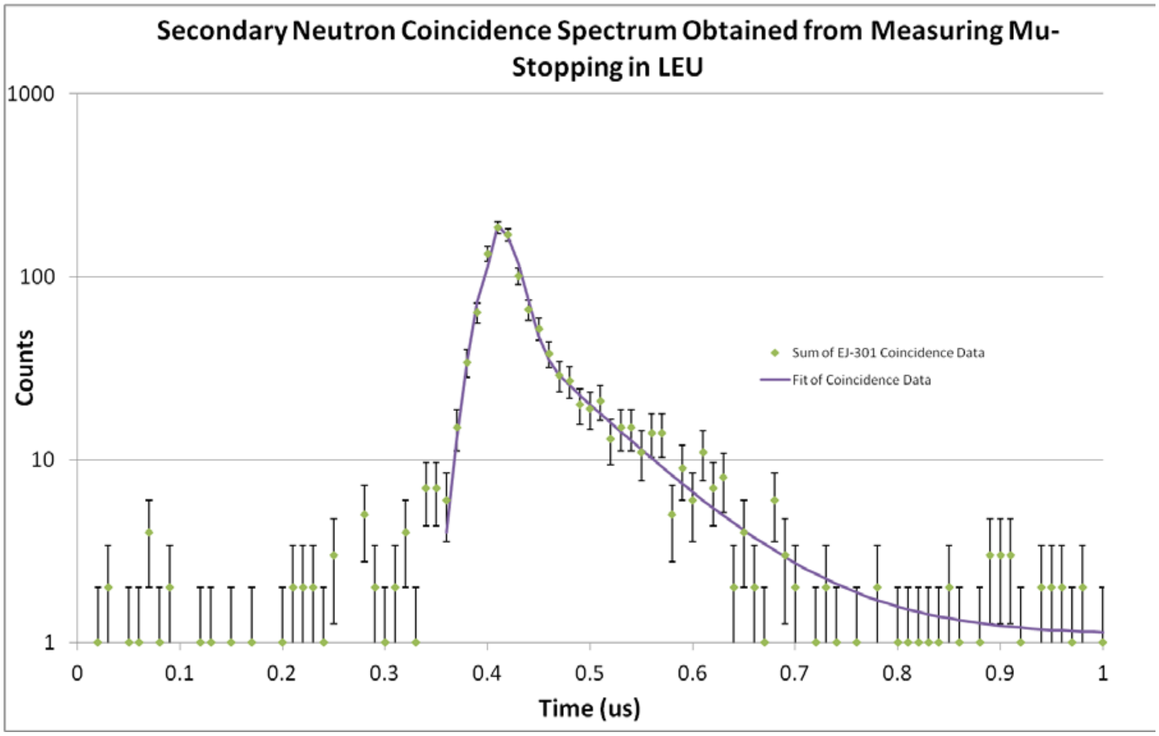

Figure 80 – Secondary neutron coincidence spectrum obtained from a coincidence window of EJ-301 neutron detection and stopped muon tracks in LEU. The data from both detectors is summed (green diamonds) and a log likelihood fit (purple line) is performed on the tail of the coincidence spectrum. The lifetime of the muonic LEU, which is measured by this fit, is $82 \pm 34\ ns$.

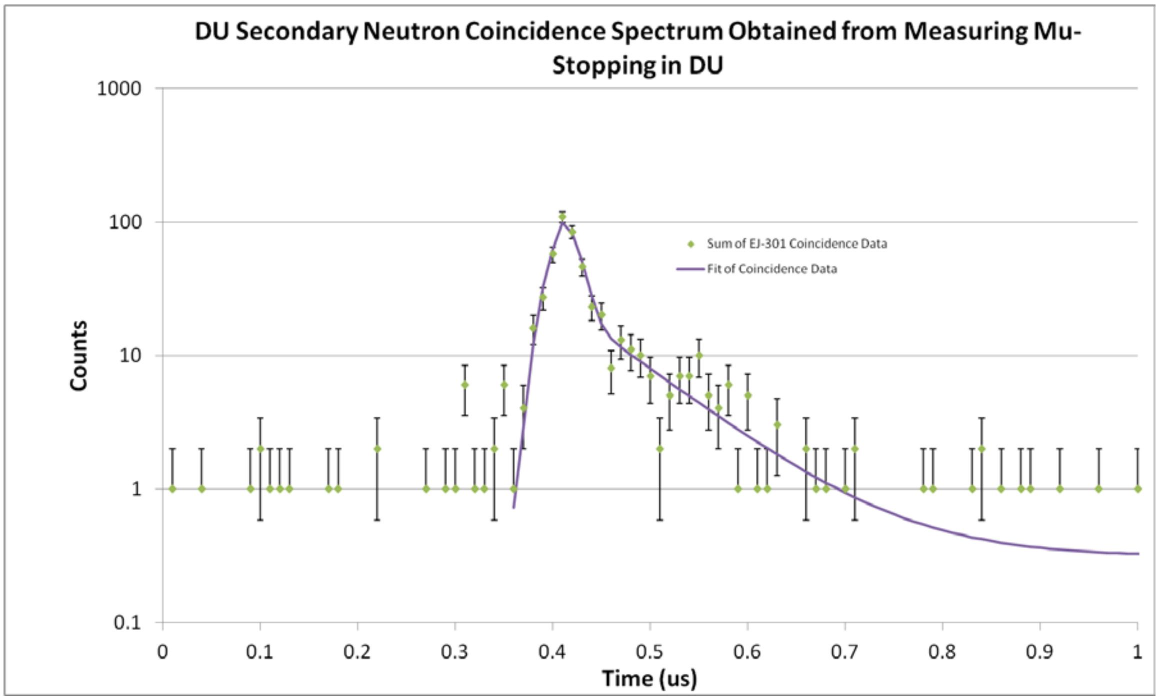

Figure 81 - Secondary neutron coincidence spectrum obtained from a coincidence window of EJ-301 neutron detection and stopped muon tracks in DU. The data from both detectors is summed (green diamonds) and a log likelihood fit (purple line) is performed on the tail of the coincidence spectrum. The lifetime of the muonic DU which is measured by this fit, is $80 \pm 57\ ns$.

The fitted lifetime for the LEU cube was $82 \pm 34\ ns$, and the fitted lifetime for the DU cube was $80 \pm 57\ ns$. The error was determined by computing the 1σ equivalent of a log-likelihood ratio and subtracting the difference between this new lifetime value and the minimized log-likelihood value. Both fits agreed well within the data, with a summed log likelihood (Appendix D) that was approximately equal to the 87 degrees of freedom. Table 6 shows the fitting parameters for both cubes.

The tagged radiography of the LEU and DU cubes are shown in Figure 82. The tagged images were normalized to the total number of stopped tracks, 1.041E+5 stopped tracks in the LEU cube over 48 hours and 4.991E+4 tracks in the DU over 23.5 hours. The total tagged stopped tracks, determined from the neutron detection in coincidence with stopped muons, were 846 ± 29 tracks in the LEU and 376 ± 20 tracks in the DU. This signal contributed statistical error of approximately 4% in LEU and 6% in DU. Following normalization, this amounted to $(7.53 \pm 0.45) \cdot 10^{-3} \frac{\mathrm{n}}{stopped\ \mu}$ in DU and $(8.13 \pm 0.33) \cdot 10^{-3} \frac{\mathrm{n}}{stopped\ \mu}$ in LEU. The relative difference between these two quantities is ~8 percent (see Table 7). This is consistent with our expectation that there should be more neutronics signal from the LEU cube following a stopped muon induced fission. The results of our simulations indicate that if HEU was compared to DU or LEU the signal would be dramatically increased. The tagged muon-induced radiography greatly improves the signal-to-noise ratio of the uranium in the image while being more sensitive to materials with neutronics gain. This feature enables SNM to be identified from inert high-Z materials which is indistinguishable with multiple scattering and transmission radiography.

A simulation was performed using Geant4 of the LEU and DU cube to check agreement between the simulation and data of muon induced fission. The geometry of the simulation is shown in Figure 83. One million isotropic 1 MeV μ^- were generated uniformly in each cube, and the neutrons were recorded passing through each cylindrical detector plane. The results of this simulation were used to estimate the efficiency of the EJ-301 detectors by comparison with the measured, tagged data (see Table 8). The number of neutrons observed per μ^- in the simulation was $0.106\ \frac{\mathrm{n}}{\mu^-}$ in DU and $0.120\ \frac{\mathrm{n}}{\mu^-}$ in LEU.

	DU - Minimized Fit	DU - 1 Sigma	LEU - Minimized Fit	LEU - 1 Sigma
Background (counts)	0.3	0.3	1.1	1.1
Gaussian Amplitude (counts)	75	75	133	133
Gaussian Width (ns)	16	16	18	18
Exponential Amplitude (counts)	24	24	57	57
Exponential Lifetime (ns)	80	137	82	116
Peak Center (ns)	410	410	410	410
Degrees of Freedom	87	87	87	87
Summed Log-Likelihood	81	168	87	164
Lifetime Uncertainty (ns)	57	57	34	34

Table 6 – Fit parameters of temporal distributions for a liquid-scintillator measuring neutrons in coincidence with stopped muons. The measured lifetime of the muon capture in uranium was $82 \pm 34\ ns$ in LEU and $87 \pm 57\ ns$ in DU. The DU measurement had nearly half the total counts of the LEU measurement.

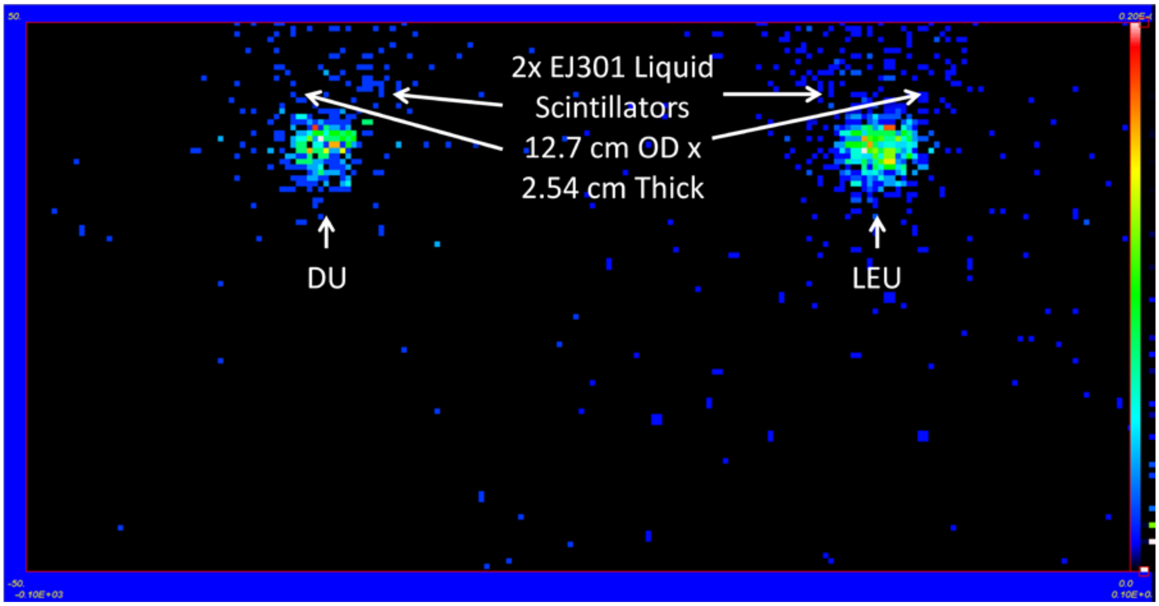

Figure 82 – Tagged radiography in coincidence with muon induced fission neutrons. The signal in the LEU cube is approximately 8 percent stronger which indicates the presence of neutronics gain from the U-235 enrichment. The detectors are barely present in the field of view after performing the tagged radiography.

Cubes	**DU**	**LEU**
Measurement Duration (min)	1410	2880
Stopped Tracks (counts)	4.99E+04	1.04E+05
Stopped Tracks (counts/min)	3.54E+01	3.61E+01
Tagged Stopped Tracks (counts)	376	846
Tagged Stopped Tracks (counts/stopped)	7.53E-03	8.13E-03

Table 7 – Two measurements of uranium cubes were made with the MMT. For each cube, the number of stopping tracks in the cube's location is shown. The tagged stopped tracks are shown as well and are normalized by the total amount of stopped tracks in the cube. Thus, we measure a fission neutron signal of smaller than 1 percent of the stopped muons in the uranium cubes.

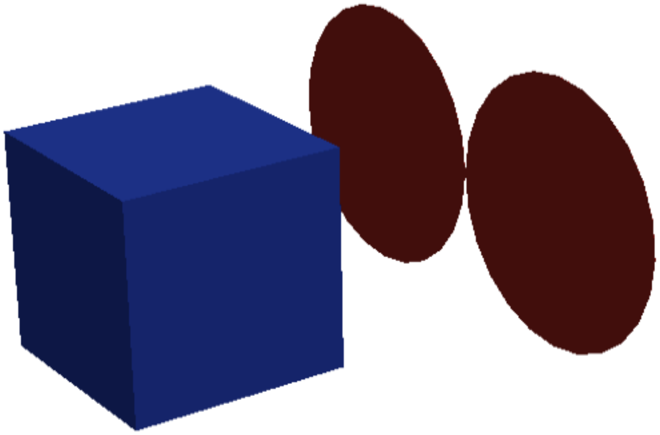

Figure 83 – Simulation geometry used in Geant4 to model muon induced fission measured by two cylindrical detector planes representing EJ-301 liquid scintillators.

Cubes	DU	LEU
Sim: Neutrons Detected (counts)	1.06E+05	1.20E+05
Sim: Neutrons Detected (counts/mu-)	1.06E-01	1.20E-01
Mu Minus Ratio (mu-/mu)	0.45	0.45
Sim: Neutrons Detected (counts/mu)	4.78E-02	5.38E-02
Tagged Stopped Tracks (counts/mu)	7.53E-03	8.13E-03
Predicted Detector Efficiency	1.58E-01	1.51E-01

Table 8 – This table contains the results of a Geant4 simulation used to check the approximate amount of neutrons expected. The geometry of the simulation is shown in Figure 83. The table shows the normalized amount of neutrons detected as a function of the stopped μ^- flux. This value is then renormalized to compare to the total stopped flux measured in data to approximate a detector efficiency of ~15-16 percent.

These values were then normalized assuming that the μ^{-} constituted 45 percent of the total cosmic-ray muon flux. The detector efficiency for the EJ-301 detectors was then computed to be ~15-16 percent. This compares well with published literature values (i.e. NE-213 efficiencies) [100-103].

For practical implementation of one sided imaging, we cannot rely on the knowledge of whether the cosmic-ray muon was stopped in the object. Therefore, the total signal of single sided imaging is composed of both stopped and transmitted muons. The results of the cosmic-ray muons stopping in cubes of LEU and DU have been shown along with the tagged component associated with stopped muon induced fission. The transmission of cosmic-ray muons has also been analyzed, shown in Figure 84; there are $2.29 \cdot 10^{5}$ muons transmitted through the LEU cube and $1.13 \cdot 10^{5}$ muons through the DU cube (see Table 9). A coincidence window was established with the transmitted tracks between 350 ns and 460 ns. The temporal distribution of the coincidence data between the transmitted muons and secondary signal is prompt (see Figure 85 and Figure 86). This is expected due to the prompt nature of muon Bremsstrahlung induced secondary neutrons. The measurement of the prompt width is similar to that of the prompt component seen in the stopped μ^{-} temporal distribution which was fit with a Gaussian model. The lack of a tail in the transmitted muon coincidence spectrum reinforces our explanation of the lifetime observed from measuring the stopped muon coincidence spectrum.

There were 141 ± 12 neutrons measured in coincidence with the LEU cube and 60 ± 8 neutrons measured in coincidence with the DU cube. This amounts to a coincidence rate of $(5.3 \pm 0.7) \cdot 10^{-4} \frac{\mathrm{n}}{trans.\ \mu}$ in DU and $(6.1 \pm 0.5) \cdot 10^{-4} \frac{\mathrm{n}}{trans.\ \mu}$ in LEU. The simulations predict that the transmitted signal should be closer to 1 percent of the stopped tracks instead of the 10 percent measured in the data. This difference is not understood at this point and will be explored in the future, requiring more accurate simulation of the physics and geometry. The combined tagged radiography, containing both the stopped and transmitted components, is shown in Figure 87. Figure 87 is similar to Figure 82 because the majority of the muon induced fission signal arises from stopped μ^{-}. The tagging of stopped and transmitted tracks proves that muon induced fission imaging is possible.

We developed a methodology for single sided imaging using cosmic-ray muons in coincidence with secondary signals. Simulations were studied of the neutronics in uranium, muon induced fission output, and experimental geometry. The experimental data was consistent with our expectations derived from the simulations. Our study confirms the feasibility of single sided imaging in coincidence with muon induced fission for identifying and imaging SNM.

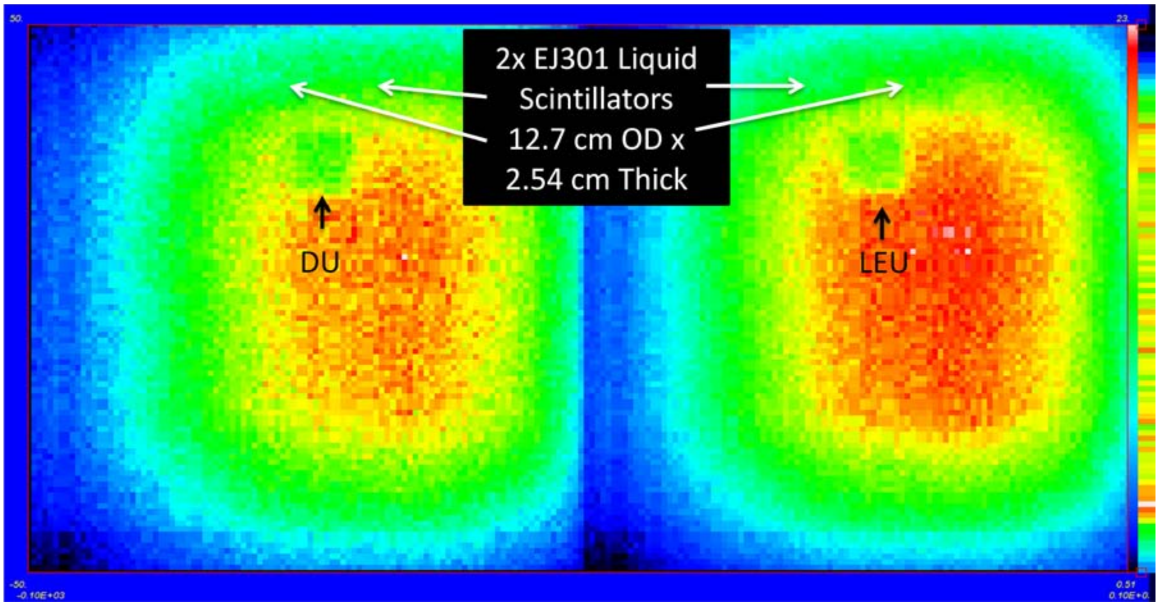

Figure 84 – Cosmic-ray muon transmission reconstruction of the DU and LEU cubes. This image shows the shadow of each cube where the missing flux is due to muons stopping in the uranium. The DU was measured for 23.5 hours and the LEU was measured for 48 hours. Both images have been normalized to the time measured, and the difference in statistics between the two measurements is noticeable when comparing the smoothness of the LEU data to the DU data.

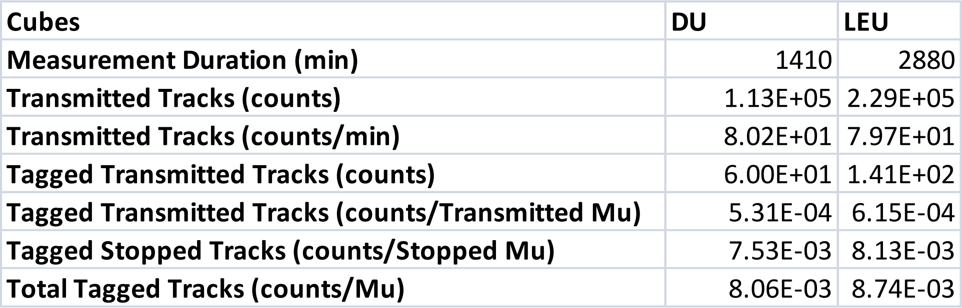

Cubes	**DU**	**LEU**
Measurement Duration (min)	1410	2880
Transmitted Tracks (counts)	1.13E+05	2.29E+05
Transmitted Tracks (counts/min)	8.02E+01	7.97E+01
Tagged Transmitted Tracks (counts)	6.00E+01	1.41E+02
Tagged Transmitted Tracks (counts/Transmitted Mu)	5.31E-04	6.15E-04
Tagged Stopped Tracks (counts/Stopped Mu)	7.53E-03	8.13E-03
Total Tagged Tracks (counts/Mu)	8.06E-03	8.74E-03

Table 9 – This table summarizes the amount of tagged tracks seen in the data for the uranium cube measurements. The total tagged tracks are a summation of the tagged tracks observed from both muon stopping and transmission. There is ~8 percent increase in signal found in the normalized total tagged tracks from the LEU.

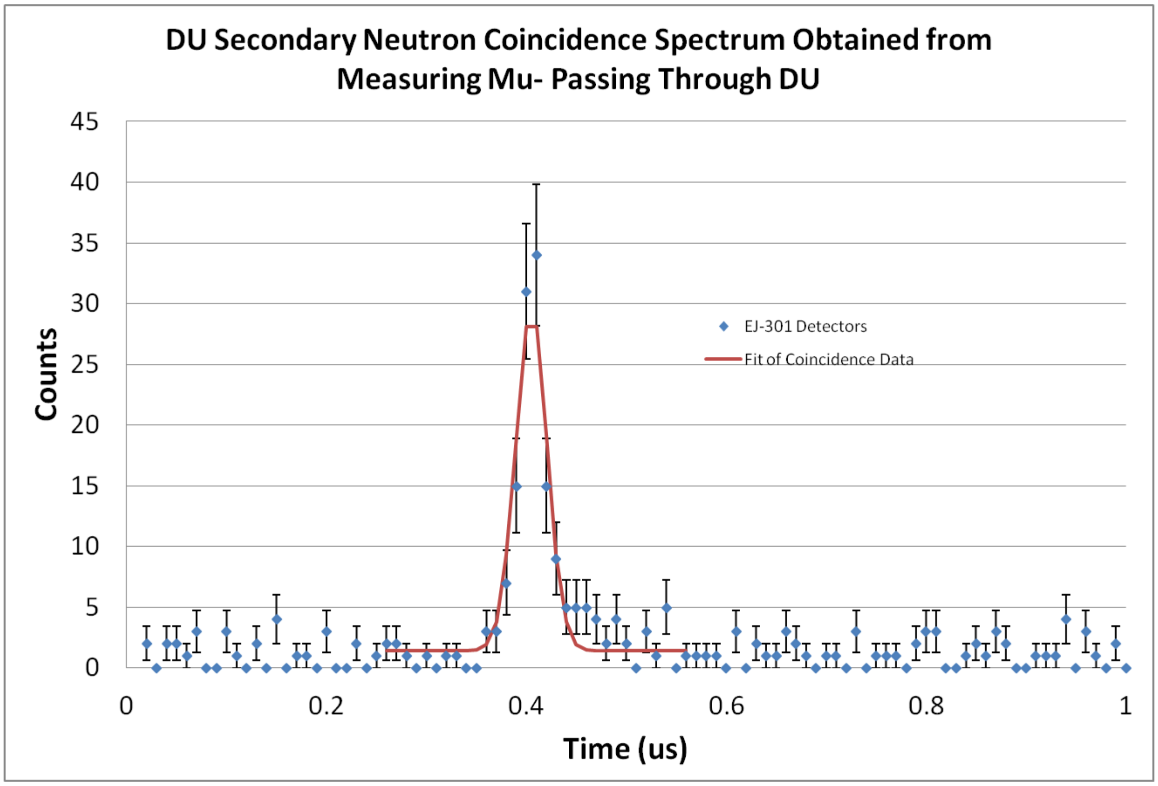

Figure 85 – Secondary neutron coincidence spectrum obtained from a coincidence window of EJ-301 neutron detection and transmitted muon tracks in DU. The data from both detectors is summed (blue diamonds) and a log likelihood fit (red line) using a Gaussian model is applied to the data. The width of the Gaussian is 16 ns.

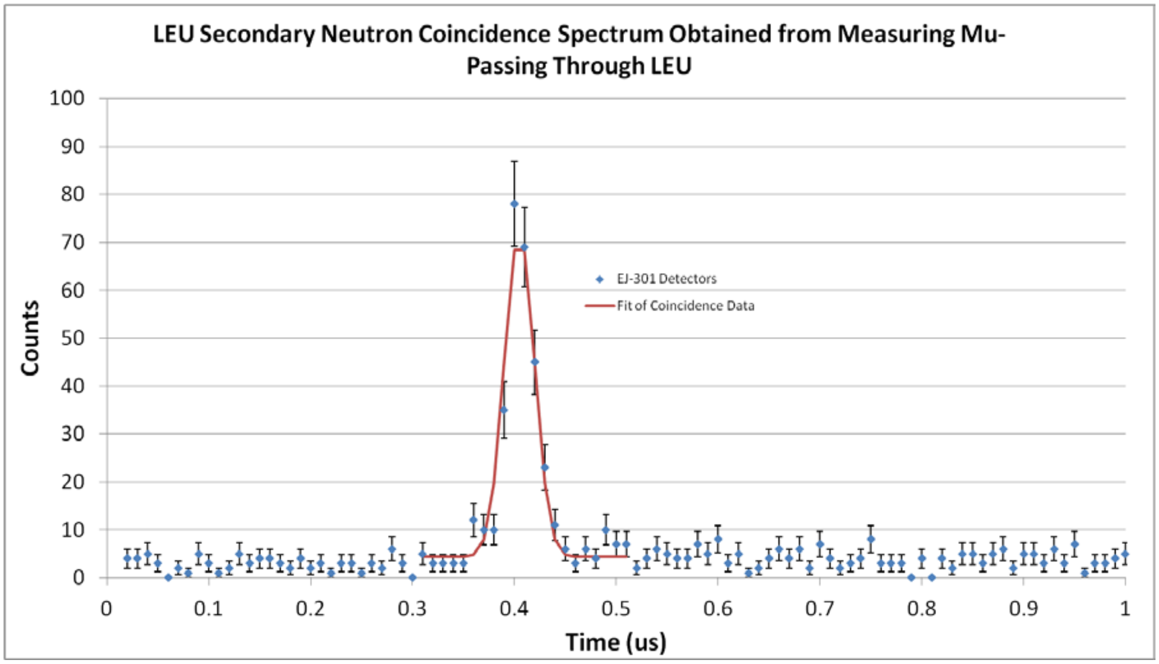

Figure 86 - Secondary neutron coincidence spectrum obtained from a coincidence window of EJ-301 neutron detection and transmitted muon tracks in DU. The data from both detectors is summed (blue diamonds) and a log likelihood fit (red line) using a Gaussian model is applied to the data. The width of the Gaussian is 15 ns.

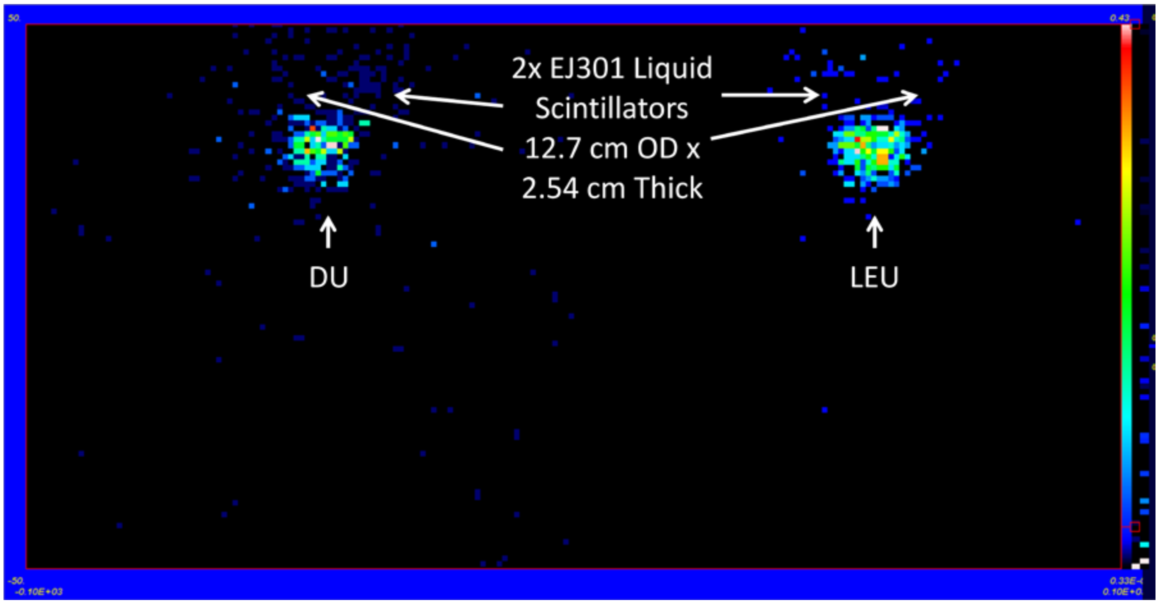

Figure 87 - Tagged radiography in coincidence with cosmic-ray muons that stop and transit through the uranium cubes. The total signal in the LEU cube is approximately 8 percent stronger which indicates the presence of neutronics gain from the U-235 enrichment. The detectors are barely present in the field of view after performing the tagged radiography.

CHAPTER 9

Conclusions

Cosmic-ray muons are a useful probe for measuring and imaging materials. In the 20th century, these muons were used to measure tunnel overburden, the Egyptian pyramids, and volcanoes using a transmission technique. Recently, scientists at Los Alamos developed the multiple scattering method to measure materials with a greater degree of accuracy and sensitivity. It is shown in this dissertation, that a combination of muon transmission, stopping, and multiple scattering is useful for advanced applications of muon radiography. The focus of the research presented here is two-fold: 1) near horizontal imaging of large structures, such as a nuclear reactor and 2) material identification using scattering in combination with secondary sources of information. During the span of the research, simulations using Geant4 were developed to confirm measured results of muon radiography and predict future experimental capabilities.

The accident at the Fukushima nuclear power plant motivated the research of near horizontal imaging, where we used two detectors to measure the multiple Coulomb scattering. Two experiments prefaced the work at the UNMRR: 1) simulating and measuring a mockup reactor geometry and 2) simulating the nuclear reactor at Fukushima Daiichi.

The mockup reactor experiment proved that images could be made of lead bricks in different geometrical orientations, e.g. a conical void or stacks of bricks, when behind a large concrete overburden of 6 m. By using cosmic-ray muons near the horizon, imaging could be performed on stationary large structures in a few weeks of cumulative exposure. Geant4 simulations verified the measurements of the mockup reactor and have been expanded to the simulations of measurements planned at Fukushima Daiichi.

A model of a boiling water reactor similar to Fukushima Daiichi Reactor #1 was simulated using Geant4 to pass cosmic-ray muons through the geometry. The model of the reactor included all major structures, the reactor building, the containment vessel, and the pressure vessel. We determined that 6 weeks of exposure, with a 50 m^2 detector, were needed in order to produce an image reconstruction where a 1m diameter sphere can be imaged. This small sphere amounted to only 1% of the total fuel in the reactor. On the other hand, the same exposure in transmission radiography showed much less sensitivity. These results proved that high quality data for radiography of the Fukushima core from outside of the buildings can be accomplished with scattering radiography and large detectors. On site tests at Fukushima Daiichi have also proven that these measurements are possible with appropriate shielding.

Tomographic images of the University of New Mexico Research Reactor were constructed using cosmic-ray muons measured over an effective 884 hour period. These images were processed with a regularized Abel inversion allowing us to identify different components of an AGN-201 m reactor structure. The core with access port structures, the graphite reflector, lead shielding, and the water tank were observed in both the experiment and Geant4 simulations. The muon flux distribution in the detectors and the reconstruction of the reactor and surrounding geometry were compared between the data and simulation. The flux showed good agreement along the azimuthal axis for both data and simulation. The flux also showed agreement in the center of the detectors along the zenith axis. There was a poorly understood discrepancy in the flux near the edges of the detectors along the zenith axis. We investigated images and projections from reconstructed simulations and measurements. The regularized Abel inversion was utilized in order to measure the density of the reactor as a function of radial distribution. The azimuthal profile of the reconstructed data has good agreement with the simulations. We have shown that given a measurement of sufficient duration, our technique is sensitive to different materials in the core region of a reactor.

Cosmic-ray muons are an effective tool for identifying materials of various atomic number and mass. The material identification was performed using a transmission and multiple scattering technique that exposed the density weighted radiation length. For symmetric cases, such as a sphere, the multiple Coulomb scattering can be used to identify materials with good spatial resolution (on the order of millimeters). The identification of SNM is also achievable through another technique that involves measuring cosmic-ray muon induced fission signatures.

We have used experimental data collected with the Mini Muon Tracker to validate simple models of cosmic ray muon radiography. The negative of the natural logarithm of transmission was shown to be proportional to material thickness, t, for a given material and approximately proportional to $\frac{dE}{dx}t$ across a range of materials. Similarly, it was shown that l/X_0, the thickness of the object in radiation length units, was measured by fitting the polar angular distribution with a set of Gaussian distributions with amplitudes fixed at values fitted to calibration data. The momentum distribution fitted to the cosmic ray data agreed remarkably well above 1 GeV with previously measured data taken with a magnetic spectrometer. The combination of our measurements provided estimates of both the areal density and the material identification.

Cosmic ray scattering data were taken on a set of spherically symmetric objects. The data were analyzed assuming spherical symmetry. The data were stored in a two dimensional histogram of scattering angle vs. radius. The angular distributions were fitted by a sum of Gaussians with amplitudes fixed by fits to data taken on a set of planar objects. This resulted in one-dimensional plots of thicknesses in radiation lengths for each of the objects. The plots were analyzed with a regularized Abel inversion technique yielding radiation-length-weighted volume densities. These results allowed a quantitative evaluation of the material composition of the objects. It is also worth noting that these objects are difficult to study with conventional x-ray radiography.

We developed a methodology for single sided imaging using cosmic-ray muons in coincidence with secondary signals. Simulations were studied of the neutronics in uranium, muon induced fission output, and experimental geometry. Both the prompt and delayed temporal neutron coincidence distributions were measured from muons interacting in uranium. The delayed component of the stopped μ^- induced fission was measured at ~80 ns in uranium. The prompt component of this coincidence timing spectrum was measured for muons that stopped and transmitted in the cubes of DU and LEU. The experimental data was consistent with our expectations derived from the simulations. Our study confirms the feasibility of single sided imaging in coincidence with muon induced fission for identifying and imaging SNM. It was shown that for single sided imaging, with our EJ-301 secondary detector configuration, we measured an SNM tagging rate of $8.06 \cdot 10^{-3} \frac{\mathrm{n}}{\mu}$ in DU and $8.74 \ \cdot 10^{-3} \frac{\mathrm{n}}{\mu}$ in LEU. Simulations suggest that HEU would show an increase in secondary neutrons by a factor of 2 as compared to the LEU or DU.

Future Work

The muon tomography team at Los Alamos is currently undertaking several projects that are exciting and hope to bring more exposure to this useful technology, as well as help our fellow man. The first, and most critical task at hand, is the continued work that one day may lead to the imaging of Fukushima Daiichi. We partner with TEPCO, Toshiba, KEK, and others in order to make the Fukushima imaging a reality. The next step in this process is to deploy the MMT, in a configuration similar to the UNMRR measurements, at a critical assembly facility in Japan. The objective of this work is part operational and part continued proof of our method. Provided that these sponsors are satisfied, the measurements at Fukushima should become reality, which is exciting. From a humanitarian aid perspective, it is estimated that by measuring Fukushima Daiichi with muons, we can reduce the cumulative radiological dose to over several thousand workers by at least 50,000 rem.

A path of medical research is being investigated by measuring the tissue density of a human phantom (see Appendix C). The original goal of this research is to use cosmic-ray muons to measure the tissue loss in non-ambulatory patients over time. By measuring the phantom, we are establishing a baseline capability for muon tomography to be used in medical applications. Provided that resolution could be improved and sensitivity to low Z materials increased (through the use of carbon fiber drift tubes), an additional application of muon tomography is to measure the brain density of non-ambulatory patients for swelling near the skull following head trauma. If this were possible, it would provide a low dose alternative to multiple CTs of the brain, for vehicular accident patients.

The work involving material identification continues for homeland security, treaty verification, and other purposes not mentioned in this dissertation. Tagged muon radiography in coincidence with high energy gamma rays (>2 MeV) and slow neutrons are being investigated. Additionally, we will perform a muon capture lifetime measurement of materials for comparison with uranium and existing literature, e.g. lead, iron, and tungsten. We will also investigate other techniques for quantifying the difference between simulations of muon tomography and measurements. Finally, we will simulate the UNMRR with the MMT detector geometry to study contribution of detector effects in the model.

REFERENCES

1. Roentgen, W.C., *On a New Kind of Rays.* Nature, 1896. **53**: p. 274.
2. Hess, V.F., *Observations in low level radiation during seven free balloon flights.* Physikalische Zeitschrift, 1912. **13**: p. 1084-1091.
3. Street, J.C. and E.C. Stevenson, *New evidence for the existence of a particle of mass intermediate between the proton and electron.* Physical Review, 1937. **52**(9): p. 1003-1004.
4. Yukawa, H. and S. Sakata, *Mass and mean life-time of the meson.* Nature, 1939. **143**: p. 761-762.
5. Alvarez, L.W., et al., *SEARCH FOR HIDDEN CHAMBERS IN PYRAMIDS.* Science, 1970. **167**(3919): p. 832.
6. Gavron, A., et al., *Proton Radiography*, in *Los Alamos National Laboratory document*1996, Los Alamos National Laboratory: Los Alamos.
7. Borozdin, K.N., et al. *Passive Imaging of SNM with Cosmic-Ray Generated Neutrons and Gamma-Rays*. in *2010 IEEE Nuclear Science Symposium and Medical Imaging Conference (2010 NSS/MIC)*. Piscataway, NJ, USA: IEEE.
8. Perry, J., et al., *Imaging a nuclear reactor using cosmic ray muons.* Journal of Applied Physics, 2013. **113**(18): p. 184909.
9. George, E.P., *Cosmic rays measure overburden of tunnel.* Commonwealth Engineer, 1955: p. 455–457.
10. Nagamine, K., *Geo-tomographic Observation of Inner-structure of Volcano with Cosmic-ray Muons.* Journal of Geography 1995. **104**(7): p. 998-1007.
11. Nagamine, K., et al., *Method of probing inner-structure of geophysical substance with the horizontal cosmic-ray muons and possible application to volcanic eruption prediction.* Nuclear Instruments & Methods in Physics Research, Section A (Accelerators, Spectrometers, Detectors and Associated Equipment), 1995. **356**(2/3): p. 585.
12. Tanaka, H., et al., *Development of a two-fold segmented detection system for near horizontally cosmic-ray muons to probe the internal structure of a volcano.* Nuclear Instruments & Methods in Physics Research, Section A (Accelerators, Spectrometers, Detectors and Associated Equipment), 2003. **507**(3): p. 657.
13. Tanaka, H., et al., *Development of the cosmic-ray muon detection system for probing internal-structure of a volcano.* Hyperfine Interactions, 2001. **138**(1/4): p. 521.
14. Tanaka, H.K.M., et al., *Three-dimensional computational axial tomography scan of a volcano with cosmic ray muon radiography (vol 115, B12332, 2010).* Journal of Geophysical Research-Solid Earth, 2011. **116**.
15. Morris, C.L., et al., *Tomographic imaging with cosmic ray muons.* Science and Global Security, 2008. **16**(1-2): p. 37-53.
16. Klimenko, A.V., et al., *Exploring signatures of different physical processes for fusion with scattering muon tomography.* IEEE Transactions on Nuclear Science, 2007. **54**(1): p. 228-235.
17. Schultz, L.J., et al., *Statistical reconstruction for cosmic ray muon tomography*. IEEE Transactions on Image Processing, 2007. **16**(8): p. 1985-93.
18. Schultz, L.J., et al., *Image reconstruction and material Z discrimination via cosmic ray muon radiography*. Nuclear Instruments & Methods in Physics Research, Section A (Accelerators, Spectrometers, Detectors and Associated Equipment), 2004. **519**(3): p. 687.
19. Borozdin, K.N., et al., *Scattering Muon radiography and its application to the detection of high-Z materials.* IEEE Nuclear Science Symposium ConferenceCRecord, 2004: p. 3444.
20. Borozdin, K.N., et al., *Surveillance: Radiographic imaging with cosmic-ray muons.* Nature, 2003. **422**(6929): p. 277.
21. Hogan, G.E., et al. *Proton radiography.* 1999. Piscataway, NJ, USA : IEEE, 1999.
22. King, N.S.P., et al., *An 800-MeV proton radiography facility for dynamic experiments.* Nuclear Instruments & Methods in Physics Research Section A-Accelerators Spectrometers Detectors and Associated Equipment, 1999. **424**(1): p. 84-91.

23. Cookson, J., *Radiography with protons.* Naturwissenschaften, 1974. **61**(5): p. 184-191.
24. STEWARD, V.W. and A.M. KOEHLER, *Proton radiography as a diagnostic tool.* Physics in Medicine and Biology, 1973. **18**(4): p. 591.
25. Ellard, G.A., et al., *Radiography with 160 MeV protons.* Nature, 1972. **239**(5368): p. 157-9.
26. Cookson, J.A., B.H. Armitage, and A.T. Ferguson, *Proton radiography.* Non-Destructive Testing, 1972. **5**(4): p. 225-8.
27. KOEHLER, A.M., *PROTON RADIOGRAPHY.* Physics in Medicine and Biology, 1970. **15**(1): p. 181-&.
28. KOEHLER, A.M., *Proton radiography.* Science, 1968. **160**(3825): p. 303-4.
29. Priedhorsky, W.C., et al., *Detection of high-Z objects using multiple scattering of cosmic ray muons.* Review of Scientific Instruments, 2003. **74**(10): p. 4294.
30. Atencio, L., et al., *Delay-line readout drift chambers.* Nuclear Instruments and Methods in Physics Research, 1981. **187**(2-3): p. 381-386.
31. Agostinelli, S., et al., *GEANT4-a simulation toolkit.* Nuclear Instruments & Methods in Physics Research Section a-Accelerators Spectrometers Detectors and Associated Equipment, 2003. **506**(3): p. 250-303.
32. Reyna, D., *A Simple Parameterization of the Cosmic-Ray Muon Momentum Spectra at the Surface as a Function of Zenith Angle.* arXiv:hep-ph/0604145, 2006.
33. Helder, E.A., et al., *Measuring the Cosmic-Ray Acceleration Efficiency of a Supernova Remnant.* Science, 2009. **325**(5941): p. 719-722.
34. Scott, J.S. and R.A. Chevalier, *Cosmic-Ray Production in Cassiopeia-a Supernova Remnant.* Astrophysical Journal, 1975. **197**(1): p. L5-L8.
35. Enomoto, R., et al., *The acceleration of cosmic-ray protons in the supernova remnant RX J1713.7-3946.* Nature, 2002. **416**(6883): p. 823-826.
36. Nakamura, K., et al., *Review of Particle Physics.* Journal of Physics G: Nuclear and Particle Physics, 2010. **37**(7A): p. 075021.
37. Nandi, B.C. and M.S. Sinha, *The momentum spectrum of muons at sea level in the range 5-1200 GeV/c.* Journal of Physics A: General Physics, 1972. **5**(9): p. 1384.
38. Ayre, C.A., et al., *Precise measurement of the vertical muon spectrum in the range 20-500 GeV/c.* Journal of Physics G: Nuclear Physics, 1975. **1**(5): p. 584.
39. Kellogg, R.G., H. Kasha, and R.C. Larsen, *Momentum spectra, charge ratio, and zenith-angle dependence of cosmic-ray muons.* Physical Review D, 1978. **17**(1): p. 98-113.
40. Tsuji, S., et al., *Measurements of muons at sea level.* Journal of Physics G: Nuclear and Particle Physics, 1998. **24**(9): p. 1805.
41. Jokisch, H., et al., *Cosmic-ray muon spectrum up to 1 TeV at 75° zenith angle.* Physical Review D, 1979. **19**(5): p. 1368-1372.
42. Mitsui, K., et al., *Cosmic-ray muon spectrum derived from the transferred energy spectrum of bursts observed by the Mutron calorimeter.* Journal of Physics G: Nuclear Physics, 1983. **9**(5): p. 573.
43. Gaisser, T.K., *Cosmic rays and particle physics*1990, Cambridge England ; New York: Cambridge University Press. xiv, 279 p.
44. Tang, A., et al., *Muon Simulations for Super-Kamiokande, KamLAND and CHOOZ.* arXiv:hep-ph/0604078, 2006.
45. Bogdanova, L.N., et al., *Cosmic muon flux at shallow depths underground.* arXiv:nucl-ex/0601019, 2006.
46. Bugaev, E.V., et al., *Atmospheric Muon Flux at Sea Level, Underground, and Underwater.* arXiv:hep-ph/9803488, 1998.
47. Haino, S., et al., *Measurements of primary and atmospheric cosmic-ray spectra with the BESS-TeV spectrometer.* Physics Letters B, 2004. **594**(1-2): p. 35-46.
48. Achard, P., et al., *Measurement of the atmospheric muon spectrum from 20 to 3000 GeV.* Physics Letters B, 2004. **598**(1-2): p. 15-32.
49. Bichsel, H., *A method to improve tracking and particle identification in TPCs and silicon detectors.* Nuclear Instruments & Methods in Physics Research Section a-Accelerators Spectrometers Detectors and Associated Equipment, 2006. **562**(1): p. 154-197.
50. Bethe, H., *Theory of passage of swift corpuscular rays through matter.* Annalen der Physik, 1930. **5**(3): p. 325-400.

51. Livingston, M.S. and H.A. Bethe, *Nuclear dynamics, experimental.* Rev. Mod. Phys., 1937. **9**(3): p. 245-390
52. Allison, S.K. and S.D. Warshaw, *Passage of Heavy Particles through Matter.* Reviews of Modern Physics, 1953. **25**(4): p. 779-817.
53. Beringer, J., et al., *Review of Particle Physics Particle Data Group.* Physical Review D, 2012. **86**(1).
54. Bethe, H.A., *Moliere Theory of Multiple Scattering.* Physical Review, 1953. **89**(6): p. 1256-1266.
55. Tsai, Y.S., *Pair Production and Bremsstrahlung of Charged Leptons.* Reviews of Modern Physics, 1974. **46**(4): p. 815-851.
56. Davies, H., H.A. Bethe, and L.C. Maximon, *Theory of Bremsstrahlung and Pair Production .2. Integral Cross Section for Pair Production.* Physical Review, 1954. **93**(4): p. 788-795.
57. Yao, W.M., et al., *Review of particle physics.* Journal of Physics G-Nuclear and Particle Physics, 2006. **33**(1): p. 1-+.
58. Morris, C.L., et al., *Obtaining material identification with cosmic ray radiography.* Aip Advances, 2012. **2**(4).
59. Oberacker, V.E., *Prompt muon-induced fission: a probe for nuclear energy dissipation.* Acta Physica Hungarica New Series-Heavy Ion Physics, 1999. **10**(2-3): p. 221-230.
60. Wang, Z., et al., *Inexpensive and practical sealed drift-tube neutron detector.* Nuclear Instruments and Methods in Physics Research Section A: Accelerators, Spectrometers, Detectors and Associated Equipment, 2009. **605**(3): p. 430-432.
61. Veenhof, R., *GARFIELD, recent developments.* Nuclear Instruments & Methods in Physics Research Section a-Accelerators Spectrometers Detectors and Associated Equipment, 1998. **419**(2-3): p. 726-730.
62. Hampel, F., et al., *Robust Statistics: The Approach Based on Influence Functions*1986: Wiley.
63. Morris, C.L. and A. Saunders, *NewDisplay*, in *Los Alamos Computer Code*2004.
64. Taylor, J.R., *An introduction to error analysis : the study of uncertainties in physical measurements*. 2nd ed1997, Sausalito, Calif.: University Science Books. xvii, 327 p.
65. Milner, E., et al., *Fukushima Daiishi Muon Tomography.* LA-UR-11-12002, 2011.
66. Borozdin, K., et al., *Cosmic Ray Radiography of the Damaged Cores of the Fukushima Reactors.* Physical Review Letters, 2012. **109**(15).
67. Busch, B., *The University of New Mexico AGN-201M Reactor: REACTOR OPERATION and TRAINING MANUAL.*
68. Eidelman, S., et al., *Review of particle physics.* Physics Letters B, 2004. **592**(1-4): p. 1.
69. Babson, J., et al., *Cosmic-ray muons in the deep ocean.* Physical Review D, 1990. **42**(11): p. 3613-3620.
70. Press, W., et al., *Numerical recipes in Fortran*. Second ed. Vol. 3. 1992: Cambridge university press Cambridge.
71. Nagamine, K., *Advanced muon radiography with compact accelerator system.* Proceedings of the Japan Academy, Series B (Physical and Biological Sciences), 2004. **80**(4): p. 179.
72. Morris, C., J.W. Hopson, and P. Goldstone, *Proton Radiography.* Los Alamos Science 2006. **30**.
73. Grieder, P.K.F., *Cosmic rays at Earth: researcher's reference manual and data book*2001: Elsevier Science & Technology Books.
74. Bethe, H.A., *MOLIERE THEORY OF MULTIPLE SCATTERING.* Physical Review, 1953. **89**(6): p. 1256.
75. Lynch, G.R. and O.I. Dahl, *Approximations to multiple Coulomb scattering.* Nuclear Instruments & Methods in Physics Research, Section B (Beam Interactions with Materials and Atoms), 1991. **B58**(1): p. 6.
76. Moliere, G., *THEORIE DER STREUUNG SCHNELLER GELADENER TEILCHEN-II MEHRFACHSTREUUNG UND VIELFACHSTREUUNG.* Zeitschrift fur Naturforschung Section A-A Journal of Physical Sciences, 1948. **3**(2): p. 78.
77. Moliere, G., *THEORIE DER STREUUNG SCHNELLER GELADENER TEILCHEN .1.* Zeitschrift fur Naturforschung Section A-A Journal of Physical Sciences, 1947. **2**(3): p. 133.
78. Morris, C.L., et al., *A new method for imaging nuclear threats using cosmic ray muons.* arXiv:1306.0523, 2013.
79. Morris, C., et al., *Obtaining material identification with cosmic ray radiography.* arXiv preprint arXiv:1210.6102, 2012.

80. Abel, N.H., *Résolution d'un problème de mécanique.* J. Reine u. Angew. Math, 1826. **1**: p. 153-157.
81. Watson, S., et al. *Design, fabrication and testing of a large anti-scatter grid for megavolt/spl gamma/-ray imaging*. 2005. IEEE.
82. Kaufman, L. and J. Carlson, *An evaluation of airport x-ray backscatter units based on image characteristics.* Journal of Transportation Security, 2011. **4**(1): p. 73-94.
83. Warren, G.A., et al., *On the Search for Nuclear Resonance Fluorescence Signatures of U-235 and U-238 Above 3 MeV.* Ieee Transactions on Nuclear Science, 2010. **57**(1): p. 317-322.
84. Warren, G.A., et al., *Nuclear resonance fluorescence of U-235 above 3 MeV.* 2007 Ieee Nuclear Science Symposium Conference Record, Vols 1-11, 2007: p. 2047-2049.
85. Warren, G.A., et al., *Nuclear Resonance Fluorescence of (235)U.* 2006 Ieee Nuclear Science Symposium Conference Record, Vol 1-6, 2006: p. 914-917.
86. Johnson, M.S., et al., *Applications of Photonuclear Physics for International Safeguards and Security.* Journal of the Korean Physical Society, 2011. **59**(2): p. 1414-1417.
87. Bertozzi, W., et al., *Accelerators for Homeland Security.* International Journal of Modern Physics A, 2011. **26**(10-11): p. 1713-1735.
88. Bertozzi, W., et al., *Imaging and Radiography with Nuclear Resonance Fluorescence and Effective-Z (EZ-3D (TM)) Determination; SNM Detection Using Prompt Neutrons from Photon Induced Fission.* Application of Accelerators in Research and Industry, 2009. **1099**: p. 559-564.
89. Bertozzi, W., et al., *Nuclear resonance fluorescence and effective Z determination applied to detection and imaging of special nuclear material, explosives, toxic substances and contraband.* Nuclear Instruments & Methods in Physics Research Section B-Beam Interactions with Materials and Atoms, 2007. **261**(1-2): p. 331-336.
90. Bertozzi, W. and R.J. Ledoux, *Nuclear resonance fluorescence imaging in non-intrusive cargo inspection.* Nuclear Instruments & Methods in Physics Research Section B-Beam Interactions with Materials and Atoms, 2005. **241**(1-4): p. 820-825.
91. Duderstadt, J.J. and L.J. Hamilton, *Nuclear reactor analysis*1976. Medium: X; Size: Pages: 563.
92. Watt, B.E., *Energy Spectrum of Neutrons from Thermal Fission U-235.* Physical Review, 1952. **87**(6): p. 1037-1041.
93. Tepel, J.W., *Ensdf - the Evaluated Nuclear-Structure Data File.* Computer Physics Communications, 1984. **33**(1-3): p. 129-146.
94. Malyshkin, Y., et al., *Neutron production and energy deposition in fissile spallation targets studied with Geant4 toolkit.* Nuclear Instruments & Methods in Physics Research Section B-Beam Interactions with Materials and Atoms, 2012. **289**: p. 79-90.
95. Guardiola, C., et al., *Geant4 and MCNPX simulations of thermal neutron detection with planar silicon detectors.* Journal of Instrumentation, 2011. **6**.
96. Othman, M.A.R., et al., *From imaging to dosimetry: GEANT4-based study on the application of Medipix to neutron dosimetry.* Radiation Measurements, 2010. **45**(10): p. 1355-1358.
97. Jamil, M., et al., *Simulation study using GEANT4 Monte Carlo code for a Gd-coated resistive plate chamber as a thermal neutron detector.* Radiation Measurements, 2010. **45**(7): p. 840-843.
98. Howard, A., et al., *Validation of Neutrons in Geant4 Using TARC Data - production, interaction and transportation.* 2008 Ieee Nuclear Science Symposium and Medical Imaging Conference (2008 Nss/Mic), Vols 1-9, 2009: p. 2160-2164.
99. Hanscheid, H., et al., *Muon-Capture Rates in U-233, U-234, U-235, U-236, U-238, and Np-237.* Zeitschrift Fur Physik a-Hadrons and Nuclei, 1990. **335**(1): p. 1-8.
100. Shin, K., et al., *Measurements of Ne-213 Response Functions to Neutrons of Energies up to Several 10s of Mev.* Nuclear Instruments & Methods in Physics Research Section a-Accelerators Spectrometers Detectors and Associated Equipment, 1991. **308**(3): p. 609-615.
101. Urone, P.P., N.S.P. King, and M.W. Mcnaughton, *Absolute Neutron-Detector Efficiency for Ne-213 from 11 to 50 Mev.* Bulletin of the American Physical Society, 1976. **21**(1): p. 109-109.
102. Drosg, M., *Accurate Measurement of Counting Efficiency of a Ne-213 Neutron Detector between 2 and 26 Mev.* Nuclear Instruments & Methods, 1972. **105**(3): p. 573-&.
103. Odell, A.A., C.W. Sandifer, and R.B. Knowlen, *Efficiency and Charged Particle Response of an Ne-213 Fast-Neutron Detector.* Bulletin of the American Physical Society, 1968. **13**(4): p. 559-&.
104. Miyadera, H., et al., *Imaging Fukushima Daiichi reactors with muons.* Aip Advances, 2013. **3**(5): p. 052133-7.

105. Brumfiel, G., D. Cyranoski, and A. Abbott, *Quake sparks nuclear crisis.* Nature, 2011. **471**(7338): p. 273-275.
106. Srinivasan, T.N. and T.S.G. Rethinaraj, *Fukushima and thereafter: Reassessment of risks of nuclear power.* Energy Policy, 2013. **52**: p. 726-736.
107. Stone, R., *Fukushima Cleanup Will Be Drawn Out and Costly.* Science, 2011. **331**(6024): p. 1507-1507.
108. Burns, P.C., R.C. Ewing, and A. Navrotsky, *Nuclear Fuel in a Reactor Accident.* Science, 2012. **335**(6073): p. 1184-1188.
109. Walker, J.S., *Three Mile Island: A nuclear crisis in historical perspective*2004: University of California Press.
110. Minato, S., *Feasibility of cosmic-ray radiography: a case study of a temple gate as a testpiece.* Mater Eval, 1988. **46**(11): p. 1468.
111. Tanaka, H.K.M., et al., *Radiographic measurements of the internal structure of Mt. West Iwate with near-horizontal cosmic-ray muons and future developments.* Nuclear Instruments & Methods in Physics Research Section a-Accelerators Spectrometers Detectors and Associated Equipment, 2005. **555**(1-2): p. 164-172.
112. Marteau, J., et al., *Muons tomography applied to geosciences and volcanology.* Nuclear Instruments & Methods in Physics Research Section a-Accelerators Spectrometers Detectors and Associated Equipment, 2012. **695**: p. 23-28.
113. Fehr, F. and T. Collaboration, *Density imaging of volcanos with atmospheric muons.* 12th International Conference on Topics in Astroparticle and Underground Physics (Taup 2011), Pts 1-6, 2012. **375**.
114. Nagamine, K., et al., *Probing the inner structure of blast furnaces by cosmic-ray muon radiography.* Proceedings of the Japan Academy Series B Physical and Biological Sciences, 2005. **81**(7): p. 257-260.
115. Lesparre, N., et al., *Geophysical muon imaging: feasibility and limits.* Geophysical Journal International, 2010. **183**(3): p. 1348-1361.
116. Malmqvist, L., et al., *Theoretical Studies of Insitu Rock Density Determinations Using Underground Cosmic-Ray Muon Intensity Measurements with Application in Mining Geophysics.* Geophysics, 1979. **44**(9): p. 1549-1569.
117. Borozdin, K.N., et al., *Scattering Muon radiography and its application to the detection of high-Z materials.* 2003 Ieee Nuclear Science Symposium, Conference Record, Vols 1-5, 2004: p. 3444-3444.
118. Hogan, G.E., et al., *Detection of High-Z Objects using Multiple Scattering of Cosmic Ray Muons.* Aip Conference Proceedings, 2004. **698**(1): p. 755-758.
119. Pesente, S., et al., *First results on material identification and imaging with a large-volume muon tomography prototype.* Nuclear Instruments & Methods in Physics Research Section a-Accelerators Spectrometers Detectors and Associated Equipment, 2009. **604**(3): p. 738-746.
120. Anghel, V., et al. *Performance of a Drift Chamber Candidate for a Cosmic Muon Tomography System*. in *11th International Conference on Applications of Nuclear Techniques ; 12-18 June 2011 ; Rethymnon, Greece*. 2011. USA: American Institute of Physics.
121. Borisov, A.A., et al., *A Muon Tomograph setup with a 3 x 3 m(2) area of overlapping.* Instruments and Experimental Techniques, 2012. **55**(2): p. 151-160.
122. Benton, C.J., et al., *Most probable trajectory of a muon in a scattering medium, when input and output trajectories are known.* Nuclear Instruments & Methods in Physics Research Section a-Accelerators Spectrometers Detectors and Associated Equipment, 2012. **693**: p. 154-159.
123. Wang, G., L.J. Schultz, and J. Qi, *Bayesian Image Reconstruction for Improving Detection Performance of Muon Tomography.* IEEE TRANSACTIONS ON IMAGE PROCESSING, 2009. **18**(5): p. 1080-1089.
124. Jonkmans, G., et al., *Nuclear waste imaging and spent fuel verification by muon tomography.* Annals of Nuclear Energy, 2013. **53**: p. 267-273.
125. Groom, D.E., N.V. Mokhov, and S.I. Striganov, *Muon stopping power and range tables 10 MeV-100 TeV.* Atomic Data and Nuclear Data Tables, 2001. **78**(2): p. 183-356.
126. Energy, U.S.D.o., *Integrated Data Base Report*, 1996. p. 1-8.
127. Green, J.A., et al., *Optimizing the Tracking Efficiency for Cosmic Ray Muon Tomography.* 2006 Ieee Nuclear Science Symposium Conference Record, Vol 1-6, 2006: p. 285-288.

128. Rios, R., et al., *Sealed drift tube cosmic ray veto counters.* Nuclear Instruments & Methods in Physics Research Section a-Accelerators Spectrometers Detectors and Associated Equipment, 2011. **637**(1): p. 105-108.
129. Shimizu, A., T. Onda, and Y. Sakamoto, *Calculation of gamma-ray buildup factors up to depths of 100 mfp by the method of invariant embedding, (III) - Generation of an improved data set.* Journal of Nuclear Science and Technology, 2004. **41**(4): p. 413-424.
130. Akers, D.W. and B.K. Schuetz, *Physical and Radiochemical Examinations of Debris from the Tmi-2 Lower Head.* Nuclear Safety, 1994. **35**(2): p. 288-300.
131. Schneider, U. and E. Pedroni, *Multiple Coulomb Scattering and Spatial-Resolution in Proton Radiography.* Medical Physics, 1994. **21**(11): p. 1657-1663.
132. Kaas, R., *Compound Poisson distribution and GLM's-Tweedie's distribution.* MATHEMATICS DAY, 2001: p. 3.

APPENDIX A

Imaging Fukushima Daiichi Reactors with Muons

The 9.0-magnitude earthquake followed by the vast tsunami on March 11, 2011, caused a nuclear crisis at Fukushima Daiichi [104, 105]. Damage of the reactor cores has attracted worldwide attention to the issue of the fundamental safety of atomic energy [106]. A cold shutdown was announced by the Japanese government in December, 2011, and a new phase of cleanup and decommissioning was started. However, it is hard to plan the dismantling of the reactors without any realistic estimate of the extent of the damage to the cores, and knowledge of the location of the melted fuel [107, 108]. In the case of Three Mile Island, it took more than 3 years before a camera could be put into the reactor, and about 10 years before the actual damage to the reactor could be assessed [109]. Since access to the reactor buildings is very limited due to high radiation fields, imaging the reactor cores from outside the buildings will be a valuable step, and can reduce the time required to dismantle the reactors significantly, resulting in cost savings and lower total worker radiation dose.

One technique for imaging the cores without access is muon imaging, which utilizes naturally occurring cosmic-ray muons to image large-scale objects. Cosmic-ray muons which have a sea-level flux of 10^4 $\mathrm{m}^{-2}\cdot\mathrm{min}^{-1}$ [53] are the results of hadronic showers high in the atmosphere. Since 1950s, imaging objects by measuring transmitted muons with a muon telescope has been applied to study mine overburden [9], an Egyptian pyramid [5], a temple gate [110], volcanoes [11, 111-113], a blast furnace [114] and caverns [115]. By measuring the attenuation of the muon flux, two-dimensional density maps are obtained. An approximation of muon attenuation in matter is given by:

$$-\frac{N}{\lambda}=\frac{dN}{dx}=\frac{dN}{dE}\frac{dE}{dx} \qquad \text{eq. 68}$$

Here, N is the number of muons, λ the attenuation length, $\frac{dN}{dE}$ the value of the muon energy spectrum at low energy, and $-\frac{dE}{dx}$ the mean energy loss rate. Since the attenuation arises by muon stop in material due to the energy loss, the transmission method is most sensitive to low atomic number (Z) materials where the specific energy loss is largest and the Coulomb scattering is smallest. In practical applications, muon transmission imaging often suffers from poor position resolution due to the continuous scattering along the muon path, and from low signal-to-noise ratio caused by low statistics because of small detection area (typically ~2 m^2) [115, 116]. Also, the muon flux incident on the object is of critical importance to determine the attenuation for transmission method, which is sometimes not easy to estimate.

A more sensitive technique, muon scattering radiography, was invented at Los Alamos National Laboratory [20, 29, 117, 118], and has been used by some other groups [119-121]. The scattering method uses two muon trackers to measure incoming and outgoing tracks of individual muons, where the region of interest is contained within the acceptance of the tracker pair. Combining the incoming and outgoing tracks provides better spatial resolution when compared to the transmission method where only the information from the scattered outgoing tracks is available. The multiple Coulomb scattering [54] is a stochastic process and the Gaussian width of the angle is given by [75]:

$$\theta_0 = \frac{13.6}{\beta c p}\sqrt{\frac{x}{X_0}}\left[1 + 0.038\ln\left(\frac{x}{X_0}\right)\right] \qquad \text{eq. 69}$$

Where β, c, and p are the velocity and momentum of the incident muon, and x and X_0 are the thickness and radiation length of the scattering medium. The radiation lengths for water, concrete, steel and uranium are 39.3, 11.6, 1.76 and 0.317 cm [53]. The muon momentum can be estimated by the muon scattering within the detector [18]. A method for calculating most probable muon trajectory and providing higher precision in density inferences has been presented [122]. Techniques used to reconstruct matter distributions are: the point of closest approach [18, 19]; maximum-likelihood / expectation-maximization [17]; Bayesian estimation [123]. The scattering method has high sensitivity to high-Z materials such as uranium, and is very useful for detecting them in a background of low-Z material. This method has been applied to scan trailers and shipping containers for special nuclear material [15]. It is also a promising technique for International Atomic Energy Agency's nuclear safeguards and non-proliferation [124]. To image Fukushima Daiichi reactors, a new analysis, displacement method, has been developed, which is described in the latter section.

A week after the Great East Japan Earthquake, we began to study applying the muon scattering technique to Fukushima Daiichi to assess damage of the reactor cores. Several groups in Japan and the US have suggested imaging the reactors with muon transmission method and compact detectors (~1 m^2). However, since uranium fuel and water give similar energy losses for muons, the fuel is difficult to distinguish from the overburden of water, concrete and steel with the transmission method. The energy loss of a muon through matter is given by:

$$\text{Energy loss} = -\frac{dE}{dx} \times \text{density} \times \text{length} \qquad \text{eq. 70}$$

The muon energy loss rate in uranium dioxide and water are 1.15 and 1.98 MeV·cm^2·g^{-1} for minimally ionizing particles respectively [125]. In a fuel rod, uranium dioxide pellets are packaged in a zirconium alloy tube, and the density of uranium fuel averaged over the active volume of the assembly is about 2.6 g/cm^3 [126]. Even with the whole assembly, an intact core attenuates the muon flux ~2% more than water does, which makes distinguishing the reactor core from water in the presence of the overburden difficult using the transmission radiography. In contrast, the fuel gives a distinct signal in scattering radiography, producing an image contrast of ~30% even through the same overburden. Also, the muon scattering and flux attenuation can be combined to distinguish materials [58]. Compared to conventional transmission radiography, scattering radiography improves the spatial resolution and the image contrast by an order of magnitude for imaging reactor cores [66].

In the summer of 2011, a reactor mockup was imaged using Muon Mini Tracker (MMT) at Los Alamos (altitude of 2,231 m). The MMT consists of two muon trackers each having effective detection area of 1.2 x 1.2 m^2 and consisting of 6-*x* and 6-*y* planes of sealed drift tubes. In the demonstration, cosmic-ray muons passing through a physical arrangement of material similar to a reactor were measured. The reactor mockup consisted of two layers of concrete shielding blocks with a thickness of 2.74-m each, and a lead assembly in between; one tracker was installed at 2.5-m height, and another tracker was installed on the ground level at the other side. Several arrangements of lead were studied to test specific features of the reactor imaging technique. One of the results is shown in Figure 88 where lead with a conical void similar in shape to the melted core of the Three Mile Island reactor was imaged through the concrete walls. It took 3 weeks to accumulate 8x10^4 muon events. The analysis was based on point of closest approach, where the track pairs were projected to the mid-plane of the target, and the scattered angle was plotted at the intersection. Even with an event rate of an order of magnitude smaller than what we expect at Fukushima Daiichi with proposed Fukushima Muon Tracker (FMT), we successfully imaged the lead cores.

A proposed plan for Fukushima Daiichi Unit 2 is shown in Figure 89. The plan includes installation of several muon trackers on the operation floor of turbine building (FMT-1) and in front of the reactor building (FMT-2). With this geometry, muons from the east can image the bottom region of RPV while muons from the west can image the original core region. The bottom of the reactor containment vessel can be imaged by installing FMT-2 below the ground level. Specifications of FMT-1 and 2 are shown in Table 10. They consist of gas-filled ionization drift-tube detectors made of aluminum [60], and have spatial and angular resolutions of 0.4 mm and 2 mrad (full width at half maximum) with tracking efficiency of close to 100%. The FMT system can measure muon scattering and flux attenuation simultaneously. Muon trackers of the similar sizes have been manufactured in the past with sealed drift tubes [127, 128], and the technique is mature. Advantages of the drift tube compared to other muon detectors are: less γ-ray sensitivity when compared to solid state detectors *e.g.* plastic scintillators; adequate spatial resolution; mechanical robustness; operational independence of tubes resulting in negligible inefficiencies of the muon tracker in case of failures; relatively low cost. Drift-tube pulses are amplified, discriminated and digitized at the detectors in field-programmable gate-array (FPGA) time-to-digital converters (TDCs). The data are transferred to data-acquisition computers on the Fukushima Daiichi site through a dedicated Ethernet link, converted into muon tracks for online analysis, and then further analyzed in detail.

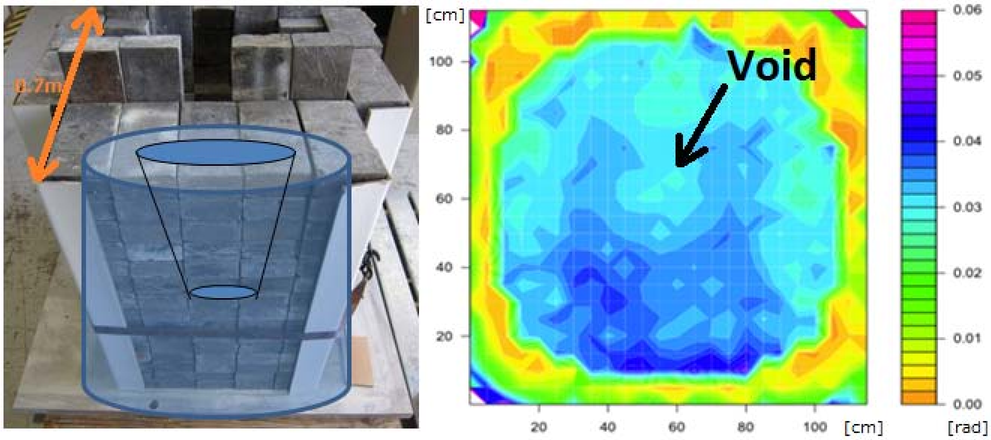

Figure 88 - Left – Lead reactor core with conic void. Right – Observed core where average scattering angles of muons are plotted. The void in the core is clearly imaged through two 2.74-m concrete walls. The lead core of 0.7-m thickness gives an equivalent radiation length to the uranium fuel in Unit 1, and gives a similar scattering angle. Hot spots at the corners are artifacts caused by edge effect of MMT.

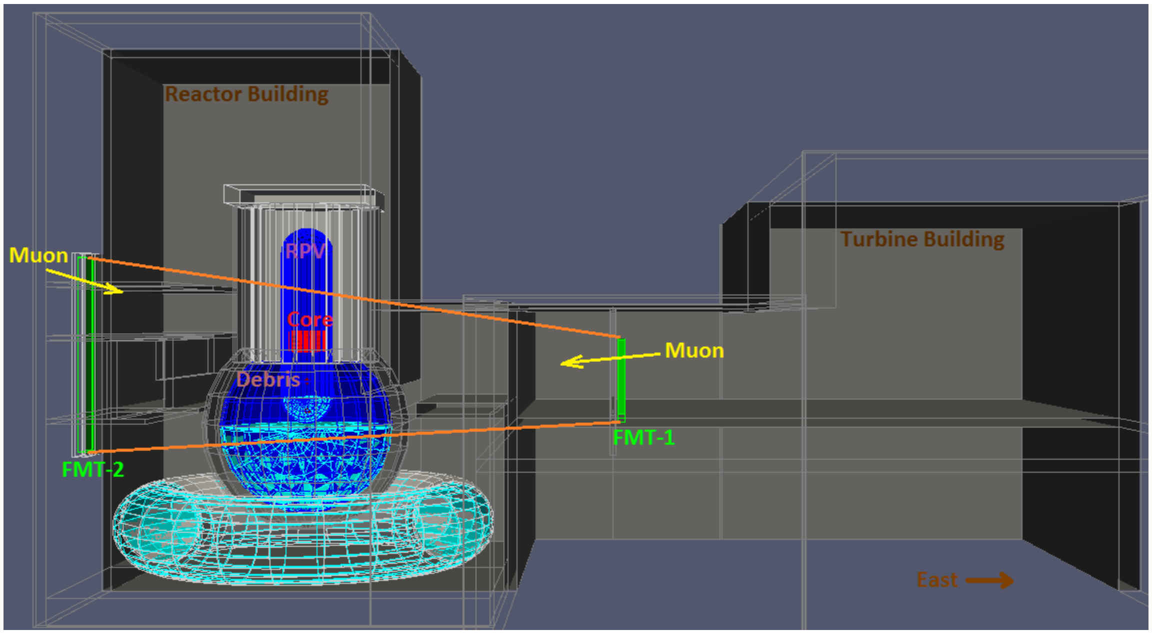

Figure 89 - Muon imaging setup for Fukushima Daiichi Unit 2. FMT-2 is installed inside a concrete radiation shield in front of the reactor building. Typical muon scattering angles are a few degrees.

	FMT-1	FMT-2
Detection area	$3.0\times3.0\text{m}^2$	$5.5\times5.5\text{m}^2$
Detector size	$3.3\times3.3\times0.6\text{m}^3$	$5.8\times5.8\times0.6\text{m}^3$
Drift tube	5-cm diameter, 12 layers (xx-yy…)	
Modules to be installed	3 – 15	2 – 4

Table 10 - Specifications of FMT-1 and 2. Measurement time scales inversely with the product of total area of FMT-1 and 2 at the lowest-order approximation. However, there is a strong angular dependence of muon flux ($\propto \cos^2\theta_z$, where θ_z is the zenith angle) [44].

The system is triggerless in the sense that tracks are built after the data have been digitized. The position calibration will be carried out in situ using the muon track data (auto calibration).

A major engineering challenge at Fukushima Daiichi is operation of the FMT in a high radiation environment. The site has radiation level of up to a few mSv/h near the reactor buildings of Units 1 - 3, which mostly consists of gamma rays from ^{134}Cs and ^{137}Cs. The gamma rays trigger drift tubes through Compton scattering which mostly takes place at their aluminum walls. Though most gamma-ray events can be discriminated by taking time coincidences between multiple drift-tube layers, average background rate of each drift tube must be kept below 20 kHz so as not to exceed the bandwidth of the Ethernet. On May 25, 2012, background rate in the 0.3-m long drift tubes was measured at Fukushima Daiichi in collaboration with Tokyo Electric Power Company (TEPCO) to estimate the shield requirement for the FMT-2. The radiation levels of the locations were 0.6, 0.7 and 1.2 mSv/h on the ground. The measured background rates were 950 kHz per 1 mSv/h (normalized to the 5.5-m length of the FMT-2 detector). Assuming the radiation level at the installation point to be 1 mSv/h, a concrete shield of 40- to 50-cm thickness will be needed to reduce the gamma-ray levels by a factor of 50 [129]. The radiation levels on the operation floor of turbine building are below 0.02 mSv/h at most locations in the case of Unit 2 (December 10, 2012), which allows FMT-1 to be operated without any radiation shield.

Simulation studies were performed with a geometry based on Fukushima Daiichi Unit 2 to test the feasibility of the proposed plan. Modeling studies on Unit 1 are described in the previous paper [66]. The Geant4 framework [31] was used and a cosmic-ray generator was implemented, which reproduces the correct energy spectrum of muons for different zenith angles in good agreement with known measurements [41]. The reactor model included all the major structures of Unit 2 as shown in Figure 89. The core in the simulation had an average density of 4.3 g/cm^3 over the volume and consisted of uranium dioxide (60.5%), zirconium (22%), stainless steel (2%) and water (15.5%) [126]; the debris has density of 8.2 g/cm^3 and consisted of uranium (70%), zirconium (14%), oxygen (13%) and stainless steel (3%), which is similar to nuclear debris found at the Three Mile Island accident [130]. For the image reconstruction, we have devised a new method that uses the displacement between the projection of the incoming trajectory to the exit detector from the measurement point as illustrated in Figure 90. When a muon goes through an object, it tends to be scattered more at the latter part of the trajectory because the scattering width scales inversely

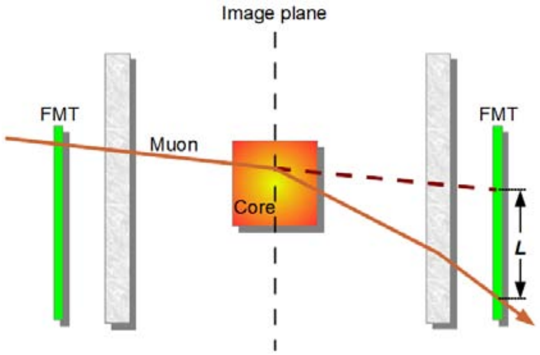

Figure 90 - Concept of image reconstruction with the displacement method. The incoming and outgoing tracks are projected to a plane at the center of the core, the intersection points are combined with weights chosen to optimize the position resolution, and a three-dimensional histogram of *x*, *y*, and the displacement length (*L*) is created. The largest weight (>80%) is placed on the incoming muon because it has higher energy and is scattered less in the intervening material between the detector and the core.

with the muon energy [131]. For the low energy part of the transmitted muon spectrum, most of the muon scattering can take place in the reactor core and in the concrete after the core. Since the contribution from each scattering source scales with the distance to the exit detector ($L_i = d_i\theta_i$), the latter part of the trajectory is less weighted.

The simulation results for Unit 2 with various core conditions (0 to 100% melted) analyzed with the displacement method are shown in Figure 91 where the reactor cores with conic voids were imaged through concrete walls and the steel RPV. The results correspond to 90 days of measurement with dimensions of 15x9 m^2 and 5.5x22 m^2 for FMT-1 and 2 respectively. A displacement threshold was selected to discriminate background from the water and concrete walls. Though detector resolutions are not included in the simulations, the scattered angle from the core is more than an order of magnitude larger than the detector resolution, thus they have little effect. In all cases, muon scattering is observed to provide detailed information about the reactor core allowing for quantitative assessment of the intact fraction. In addition, spherical debris of 20-, 30- and 40-cm radii can be distinguished. Figure 92 shows the image development with time (10 to 150 days) for the 50%-melted core with two debris of 20-cm radius. The estimated event rates are 12k and 70k per day for muons that pass through both FMT-1 and 2 from the east and west sides, respectively.

As a conclusion, feasibility of assessing the damage of the Fukushima Daiichi reactors with muon scattering imaging is shown. Muons are strongly deflected by high-Z materials such as uranium, which enables the scattering technique to spot them in a reactor. A few months of measurement will reveal the distribution of the reactor-core fuel materials, and can guide planning and execution of reactor dismantlement, potentially reducing overall project span by many years.

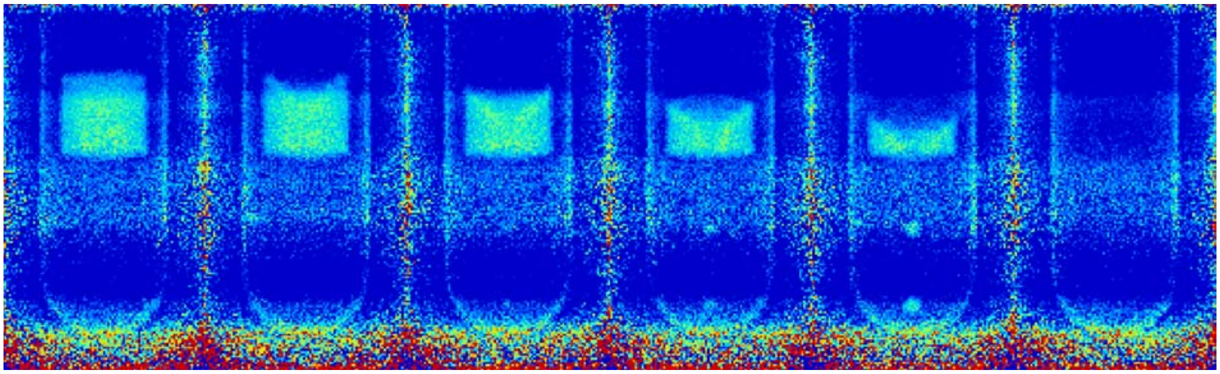

Figure 91 - Results of the GEANT4 simulations for Unit 2 with the geometry shown in Figure 89. The simulations were run with intact core (left), 10%-, 30%-, 50%-, 70%-melted core and no core (right). Two spherical debris of 10-cm (under 10%-melted core), 20-cm, 30-cm and 40-cm (under 70%-melted core) radii were placed in the lower region of RPV.

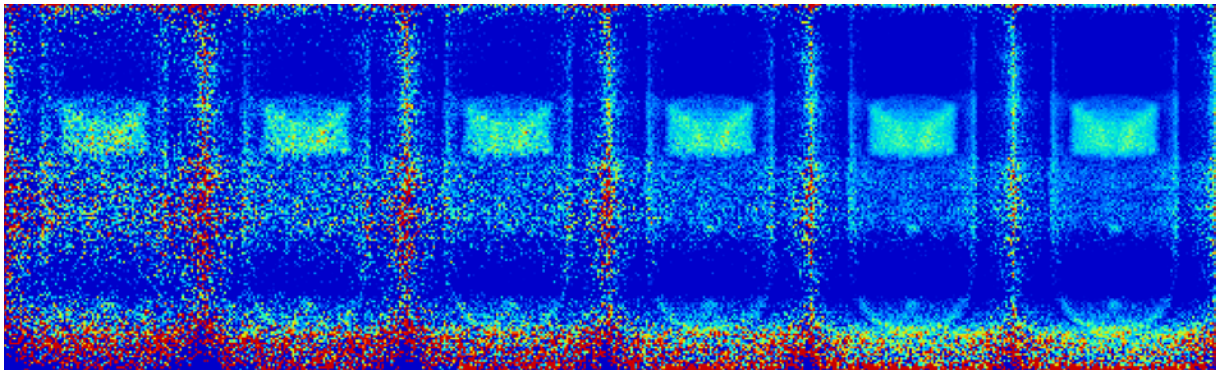

Figure 92 - GEANT4 simulations for 50%-melted core of Unit 2 with various measurement time spans. The simulation results correspond to measurement spans of 10 (left), 20, 30, 60, 120 and 150 days (right).

APPENDIX B

MMT Drift Tube Detector Performance in the Presence of a Radiation Field

From previous measurements, such as at the UNMRR and Fukushima, the presence of a high background radiation field negatively impacts the performance of our drift tubes. This decrease in performance occurs at either a high average count rate in a module of tubes (>300 Hz per tube) or a count rate of > 2 kHz in an individual tube. To counteract the high gamma-ray background that would be present for a Fukushima Daiichi measurement, the TDC firmware of the MMT was modified to include a coincidence between neighboring tubes. We imitated a high background radiation field by using ~60 kg of uranium spread throughout the imaging plane of the MMT. Two one hour measurements were orchestrated to examine the performance of the MMT with and without the coincidence firmware.

In Figure 93 and Figure 94, the MMT tube hit rates are shown before and after the implementation of the coincidence firmware respectively. The average tube hit rates without the coincidence firmware is ~400 Hz with several tubes exceeding 1 kHz. This overloads several of the TDC first-in first-out (FIFO) buffers which causes deadtime in the data acquisition and reduces the overall MMT efficiency. When the coincidence firmware is enabled, the tube hit rates drop by at least an order of magnitude. This function allows for better measurement of cosmic-ray muons in radiation fields.

Without an external radiation field, the MMT has an average tracking rate of ~70 Hz. By enabling the coincidence firmware, the tracking rate decreases to ~35 Hz, or a factor of two. However, this is an appropriate compromise when in the presence of external radiation, as the non-coincidence firmware also performs with a tracking rate proportional to the radiation field. For the measurement performed with the distributed uranium source, the non-coincidence firmware had a tracking rate of ~35 Hz, which is the same tracking frequency measured with the coincidence firmware. One important improvement, was the reduction of tube hits that otherwise overloaded the FIFO’s of the TDCs. Thus, our signal to noise ratio in the data stream significantly improved.

Four flux plots in the detector planes of the MMT are shown in Figure 95. The non-coincidence firmware is shown on the left and the coincidence firmware is shown on the right. The top supermodule

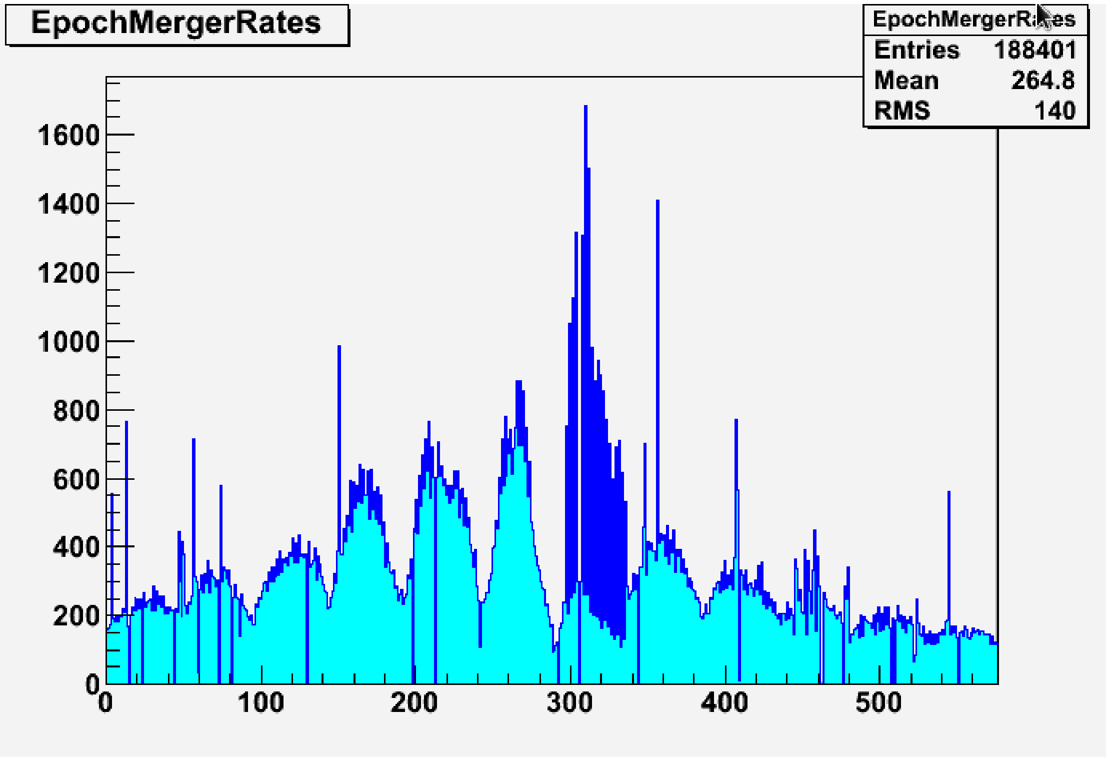

Figure 93 – Tube hit rate in the MMT per second with a distributed radiation field created by 60 kg of uranium. The hit rates are very high and overflow the data buffers in several of the TDC modules.

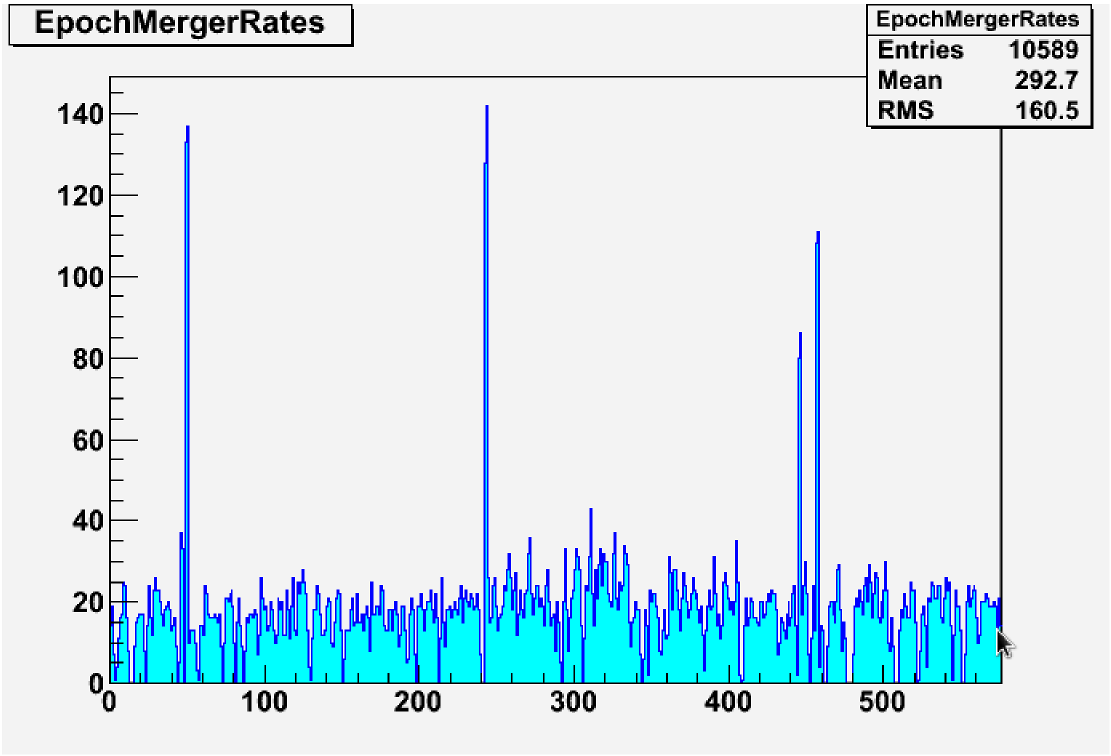

Figure 94 - Tube hit rate in the MMT per second with a distributed radiation field created by 60 kg of uranium. The rates drop by at least an order of magnitude following the implementation of the TDC coincidence firmware. This prevents the TDC first-in first-out buffers (FIFO) from overflowing.

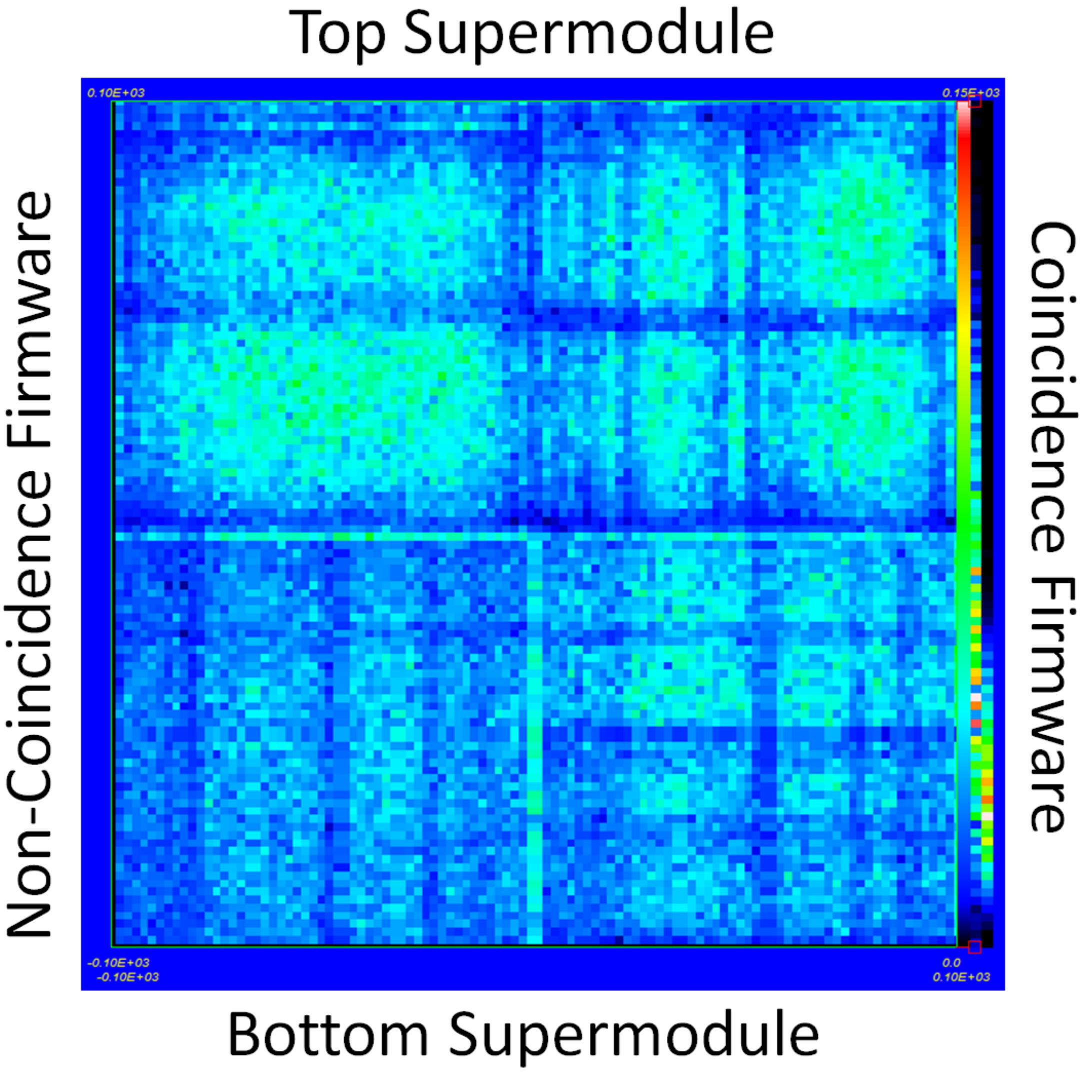

Figure 95 – Four flux plots in the detector planes of the MMT. The non-coincidence firmware is shown on the left and the coincidence firmware is shown on the right. The top supermodule flux is shown on the top and the bottom supermodule flux is shown on the bottom. The structure seen in the plots is due to dead or poorly performing tubes. The coincidence firmware amplifies this structure due to creating localized regions of inefficiency with the adjacent dead tube.

flux is shown on the top and the bottom supermodule flux is shown on the bottom. The structure seen in the plots is due to dead or poorly performing tubes. The coincidence firmware amplifies this structure due to creating localized regions of inefficiency with the adjacent dead tube. However, this defect seen in the detector planes does not noticeably affect our imaging capabilities. The image of the distributed uranium for the old and new coincidence firmware is shown in Figure 96. The distributed uranium source was measured with the MMT. Two uranium cubes and 4 uranium plates are clearly seen in the multiple scattering reconstructions. The data obtained by using the non-coincidence firmware is shown on the left, and the data obtained with the coincidence firmware is shown on the right. The ratio of the left image to the right image is shown in the middle. This ratio is flat indicating that the coincidence logic does not distort the image.

We will further test the coincidence firmware during the measurements in Japan which are mentioned in the future work section. We have learned that the efficiency of muon tomography in a radiation field can be increased by requiring coincidence, however; the coincidence amplifies the effect of the poorly performing tubes creating a dead tracking region. This can be addressed in the future by either repairing the dead tubes, or implementing different coincidence logic.

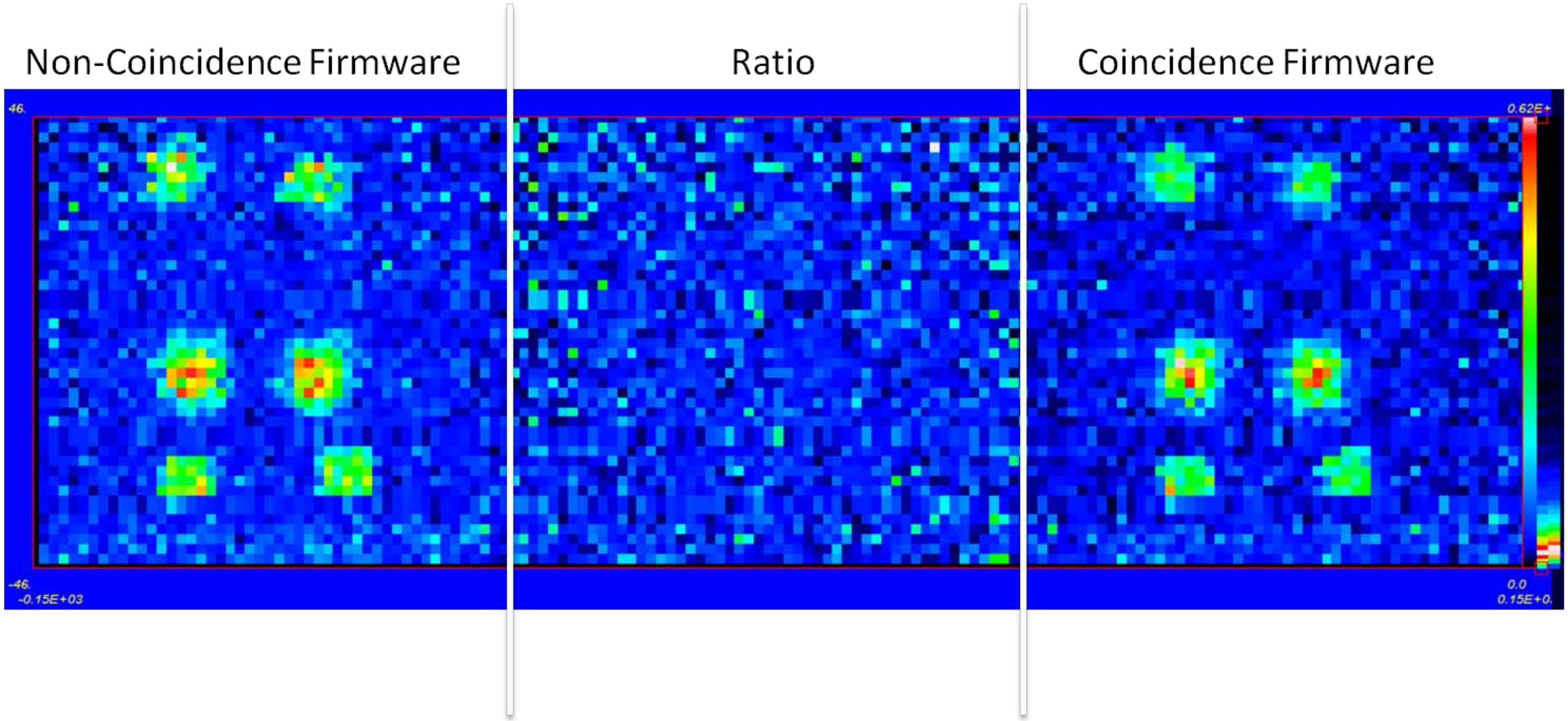

Figure 96 – The distributed uranium source was measured with the MMT. Two uranium cubes and 4 uranium plates are clearly seen in the multiple scattering reconstructions. The data obtained by using the non-coincidence firmware is shown on the left, and the data obtained with the coincidence firmware is shown on the right. The ratio of the left image to the right image is shown in the middle. This ratio is flat indicating that the coincidence logic does not distort the image.

APPENDIX C

The Lady: Measuring a Human Phantom with Muon Tomography

A medical path of research is being investigated by measuring the tissue density of a human phantom. The original goal of this research is to use cosmic-ray muons to measure the tissue loss in non-ambulatory patients over time. By measuring the phantom, we are establishing a baseline capability for muon tomography to be used in medical applications. Provided that resolution could be improved and sensitivity to low Z materials increased (through the use of carbon fiber drift tubes), an additional application of muon tomography is to measure the brain density of non-ambulatory patients for swelling near the skull following head trauma. If this were possible, it would provide a low dose alternative to multiple CTs of the brain following vehicular accidents.

A reconstruction of the human phantom is shown in Figure 97. Several body structures are recognizable including the skull, spinal column, and chest cavity. Different reconstruction techniques are being investigated for applications including measurement of the musculoskeletal components of the body and overall mass and density.

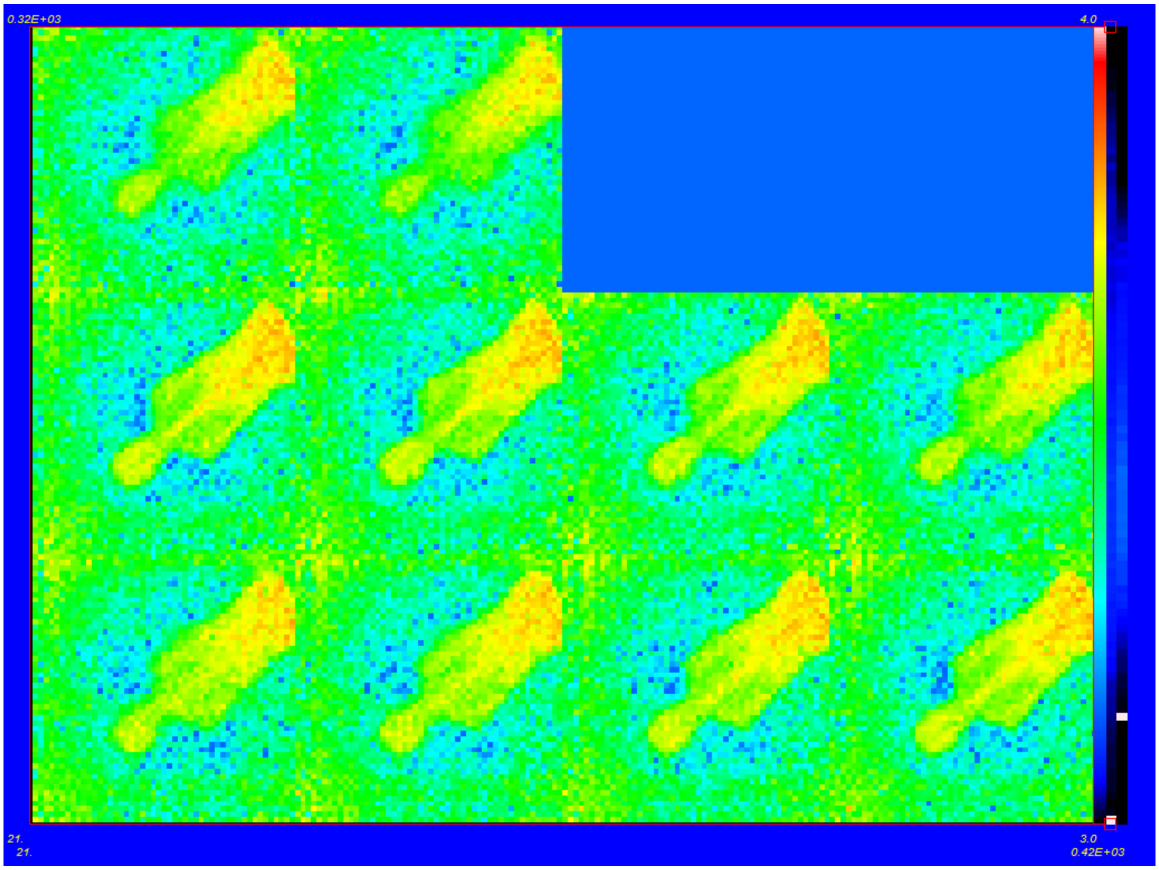

Figure 97 – The human female phantom imaged in the MMT. Several body structures are recognizable including the skull, spinal column, and chest cavity.

APPENDIX D

Fitting Data with a Log-Likelihood Function

The fitting of the data for the multigroup multiple scattering analysis and the time coincidence spectrum of the muon induced fission was performed by minimizing a model with log-likelihood. For example, a model was proposed to fit the background, prompt, and delayed component of the timing coincidence spectrum by combining a Gaussian, constant, and exponential decay curve:

$$y = B + Pe^{-\left(\frac{t-t_0}{\tau}\right)} + Ae^{-\frac{(t-t_0)^2}{2\sigma}} \qquad \text{eq. 71}$$

In order to fit the model to the data, a quasi-likelihood approach is used to estimate the fitting parameters [132]. The purpose of this model is to minimize the total deviation between the model and the data,

$$D = -2\phi \log(\Lambda) \qquad \text{eq. 72}$$

where D is the deviance, ϕ is the fixed dispersion parameter, and the likelihood ratio is defined by Λ. For a Poisson distribution the log-likelihood deviance is defined as:

$$D_1 = 2\sum_{1}^{n} w_i\left(y_i \log\left(\frac{y_i}{\mu_i}\right) - (y_i - \mu_i)\right) \qquad \text{eq. 73}$$

Where D_1 is the total deviance of the log-likelihood of a Poisson distribution, w_i is a weight associated with the dispersion of the data (assumed as 1 for our cases), y_i is a datum point, and μ_i is a model value. The parameters of the model (Gaussian, and exponential) were varied and the deviance was minimized using Excel's solver function. This allowed us to fit the data to a Poisson distribution.

APPENDIX E

Los Alamos Approval of Unclassified Release

This document has received approval for unclassified release from Los Alamos National Laboratory, LA-UR-13-24891.